Modeling of Continuous Physical Vapor Deposition
From Continuum to Free Molecular Flow

Vesper, J.E.

DOI
10.4233/uuid:828cef26-6fae-4a12-80a6-b83aed3a8e90

Publication date
2022

Document Version
Final published version

Citation (APA)
Vesper, J. E. (2022). *Modeling of Continuous Physical Vapor Deposition: From Continuum to Free Molecular Flow*. [Dissertation (TU Delft), Delft University of Technology]. https://doi.org/10.4233/uuid:828cef26-6fae-4a12-80a6-b83aed3a8e90

Important note
To cite this publication, please use the final published version (if applicable).
Please check the document version above.

MODELING OF CONTINUOUS PHYSICAL VAPOR DEPOSITION

From Continuum to Free Molecular Flow

MODELING OF CONTINUOUS PHYSICAL VAPOR DEPOSITION

FROM CONTINUUM TO FREE MOLECULAR FLOW

Dissertation

for the purpose of obtaining the degree of doctor
at the Delft University of Technology,
by the authority of the Rector Magnificus prof. dr. ir. T.H.J.J. van der Hagen,
chair of the Board of Doctorates,
to be defended publicly on Monday 17 October 2022 at 10.00 hrs

by

Judith Elin VESPER

Master of Science in Mechanics,
Technische Universität Darmstadt, Germany
born in Kassel, Germany.

This dissertation has been approved by the promotors.

Composition of the doctoral committee:

Rector Magnificus,	chair person
Prof. dr. ir. C. R. Kleijn,	Delft University of Technology, promotor
Prof. dr. S. Kenjereš, Dipl.-Ing.,	Delft University of Technology, promotor
Independent members:	
Prof.dr. V. Ayyaswamy,	University of California Merced, USA
Dr.ir. A.J.H. Frijns,	Eindhoven University of Technology
Prof.dr.ir. J.T. Padding,	Delft University of Technology
Prof.dr.ir. C. Vuik,	Delft University of Technology
Reserve members:	
Prof.dr. F. Scarano,	Delft University of Technology
Other members:	
Dr. R. Westerwaal,	Tata Steel Europe R&D, The Netherlands

This research was carried out under project number F22.3.13512 within the framework of the Partnership Program of the Materials innovation institute M2i (www.m2i.nl) and the Netherlands Organization for Scientific Research (www.nwo.nl). Some computations were carried out on the Dutch national e-infrastructure with the support of SURF Cooperative.

Keywords: Computational Fluid Dynamics, Rarefied Flow, Jet Interaction, Compressible, DSMC

Printed by: Ridderprint | www.ridderprint.nl

Front & Back: Mach number contours of interacting sonic plumes from an inviscid continuum solution.

ISBN 978-94-6384-378-2

An electronic version of this dissertation is available at
http://repository.tudelft.nl/.

It is sometimes rather unsatisfactory to obtain results without being able to see how things really work, so that in many respects it is often very convenient to complete a thermodynamical result with at least a rough kinetic interpretation.

Enrico Fermi [1]

CONTENTS

NOMENCLATURE

Greek Symbols

α	in Chapter 2: Thermal conductivity	$\mathrm{kg\,m^{-1}\,s^{-1}}$
α	in Chapter 3: Inclination angle	$^\circ$
α	in Chapter 4: Deflection angle exponent	-
α_t	Turbulent thermal conductivity	$\mathrm{kg\,m^{-1}\,s^{-1}}$
$\boldsymbol{\omega}$	Frequency	$\mathrm{s^{-1}}$
$\boldsymbol{\Sigma}$	Covariance matrix	
$\boldsymbol{\xi}$	Particle velocity	$\mathrm{m\,s^{-1}}$
χ	Species separation ratio	-
γ	Heat capacity ratio	–
Γ^+, Γ^-	Characteristics	
λ	Mean free path	m
μ	Dynamic viscosity	$\mathrm{kg\,m^{-1}\,s^{-1}}$
μ	in Chapters 3 and 4: Mach angle	$^\circ$
ν	Kinematic viscosity	$\mathrm{m^2\,s^{-1}}$
ν	in Chapters 3 and 4: Prandtl-Meyer angle	$^\circ$
ν	in Chapter 5: relaxation rate	$\mathrm{s^{-1}}$
ν_t	Turbulent viscosity	$\mathrm{m^2\,s^{-1}}$
Ω	Integration domain	
ω	Energy exponent	-
ϕ	Flow angle	$^\circ$
ψ_T	Isothermal compressibility	$\mathrm{J\,kg^{-1}\,K^{-1}}$
ρ	Density	$\mathrm{kg\,m^{-3}}$
τ	Mean collision time	s
Θ	angular component of polar coordinates	$^\circ$
φ	Flow angle	$^\circ$

Roman Symbols

$\boldsymbol{c} = \boldsymbol{\xi} - \boldsymbol{u}$	Fluctuational particle velocity	$\mathrm{m\,s^{-1}}$
$\boldsymbol{F}$	Deformation gradient tensor	$\mathrm{m^{-1}}$
$\boldsymbol{p}$	Pressure tensor	Pa
$\boldsymbol{q}$	Heat flux vector	$\mathrm{W\,m^{-2}}$
$\boldsymbol{R}$	Rotation matrix	
$\boldsymbol{r}$	Point vector	m

$\boldsymbol{u}$	Macroscopic velocity	$\mathrm{m\,s^{-1}}$
$\dot{m}$	mass flow rate	$\mathrm{kg\,s^{-1}}$
$\Im$	Imaginary component	
$\Re$	Real component	
A	Surface area	$\mathrm{m^2}$
$a = \sqrt{\gamma RT}$	Speed of sound	$\mathrm{m\,s^{-1}}$
c_p	Specific heat at constant pressure	$\mathrm{J\,kg^{-1}\,K^{-1}}$
c_v	Specific heat at constant volume	$\mathrm{J\,kg^{-1}\,K^{-1}}$
C_{dis}	Discharge coefficient	–
C_{ES}	Shakov	–
D	Length of inlet	m
d	Collisional diameter	m
dt	Time step size	s
dx	Typical cell size	m
e	Specific internal energy	$\mathrm{J\,kg^{-1}}$
E_{kin}	Macroscopic kinetic energy	J
E_{tot}	Total energy	J
f	Phase density	$\mathrm{s^6/m^3}$
f	in Chapter 2: Evaporation coefficient	–
h	Specific enthalpy	$\mathrm{J\,kg^{-1}}$
k	Kinetic turbulent energy	$\mathrm{J\,kg^{-1}}$
k_B	Boltzmann constant	$1.380\,649 \times 10^{-23}\,\mathrm{J\,K^{-1}}$
k_e	Kinetic energy	$\mathrm{J\,kg^{-1}}$
Kn	Knudsen number	-
L	Nozzle separation distance	m
M	Mach number	-
M	Molar mass	$\mathrm{kg\,mol^{-1}}$
m	Particle mass	kg
n	Number density	$\mathrm{m^{-3}}$
N_{cell}	Number of particles per cell	–
p	Pressure	Pa
p_{loss}	Fraction of loss deposition	-
R	Specific gas constant	$\mathrm{J\,kg^{-1}\,K^{-1}}$
R	Universal gas constant	$8.314\mathrm{J\,K^{-1}\,mol}$
S	Speed ratio	-
T	Temperature	K
t	Time	s
w	Regression weight	
y	Mole fraction	-

Superscripts

*	in critical section, i.e., $M = 1$

Subscripts

0	Quantity at stagnation conditions
Ag	Silver
g	Gas
He	Helium
HK	Hertz-Knudsen relation
in	Quantity at the inlet
is	isentropic relation
L	Lower jet
m	Melt
n	Nozzles
ref	Reference value
S	Stagnation quantity
S	in Chapter 2: Sutherland law
s	Static quantity
t	Total quantity
U	Upper jet
v	Vapor
VDB	Vapor Distribution Box

Dimensionless Numbers

Br	Brinkmann number	–
Kn_{GLL}	Gradient-length local Knudsen number	–
$Ma = \frac{\boldsymbol{u}}{a}$	Mach number	–
$Pr = \frac{\nu}{\alpha}$	Prandtl number	–
$Pr_t = \frac{\nu_t}{\alpha_t}$	Turbulent Prandtl number	–

SUMMARY

Physical Vapor Deposition (PVD) is the resublimation of a substance on a cold surface coating it with a thin solid layer. PVD coatings are utilized in industry to modify surface properties and appearance. Since the industrial process requires vacuum conditions, it has been mainly conducted in a batch process. Recently, PVD is considered a promising alternative coating technology to the hot-dip galvanization in order to apply a corrosion protective coating on steel. However, a continuous process is missing to manufacture protective coatings for strip steel on an industrial scale using PVD.

First approaches suggest the following process: The steel strip is pulled into a vacuum chamber through air-tight seals to ensure a non-reactive coating atmosphere and avoid impurities; then its surface is treated to obtain high adhesion during the coating process; afterwards it passes a Vapor Distribution Box (VDB) from which vapor jets (or plumes) emerge and coat the steel surface; eventually the strip leaves the vacuum chamber again via air-tight seals, is coiled and shipped.

To make this process usable on a large scale — or even superior to galvanization — multiple challenges need to be overcome: ensuring the tightness of the seals, cleaning the strip, preventing stray coating of the vacuum chamber, guaranteeing a uniform coating thickness, and providing a uniform high vapor mass flow to maintain a high speed of the production line. This thesis tackles the last challenge by modeling the vapor transport both inside the VDB and inside the vacuum chamber.

First the flow inside the VDB is modeled using a SIMPLE-/PISO-based algorithm for transsonic flows. To account for the evaporation at the melt surface, a boundary condition for the inlet pressure is implemented based on the Hertz-Knudsen equation. The total mass flow rate for different melt temperatures is compared to experimental values as well as an analytical, isentropic estimation. Furthermore, the sensitivity of the model to material properties and process conditions is studied. The total mass flow rate of the system is found to depend on evaporation and choking. With higher melt temperatures the total mass flow rate increases. The trend found in the simulations resembles the one from the experiment. Both yield only 33%–54% of the mass flow rate estimated by the analytical isentropic relation. This low efficiency improves with higher melt temperature. A comparison of the pressure loss across the VDB reveals that the main losses appear due to the viscous boundary layer in the nozzles connecting the VDB with the vacuum chamber. The simulation overpredicts the experimental result by a factor of 1.3. This may be due to the used assumption of an idealized value of unity for the evaporation coefficient; a value of approximately 0.3 would produce a better match between simulations and experiments. Impurities found in the experiment may cause this reduction of the evaporation coefficient.

When expanding from the nozzles into the vacuum chamber, the flow accelerates to supersonic speeds and rarefies. We study the interaction of two planar sonic plumes that causes a shock next to the interaction plane. This in turn produces peaks in deposition rate and thus in the coating. Direct Simulation Monte Carlo (DSMC) method is applied for the flow which ranges from continuum at the nozzles to rarefied and free molecular flow downstream. The results are compared to the analytical effusion solution and the inviscid continuum solution from a Riemann solver. The expansion and shock regions of the DSMC simulation are visualized by the Method of Characteristics (MOC). The mass flow distribution as a function of the degree of rarefaction, the nozzle-separation-distance and the inclination of the nozzles is studied. The DSMC result of plume interaction outside the VDB closely resembles the inviscid continuum solution at low degrees of rarefaction. The flow structure with expansions and shocks coincides, deviations are apparent in the actual number density, velocity and temperature especially in the shock region. With higher rarefaction, the shock structure diminishes and the flow field approaches the free molecular flow field. However, the rarefied flow field is not within the limits of the inviscid continuum and the free molecular flow field, but may exceed them in both deposition peaks and temperature peak in the shock region. Using the MOC for visualization reveals that with higher rarefaction the shock bends away from the interaction plane which can be explained by the increased temperature in the secondary expansion. While the shock location shifts with the nozzle-separation distance, it merges to one location when scaling it with the nozzle-separation distance. Bending the nozzle outlets towards each other produces a stronger shock starting further upstream, which in turn causes a stronger secondary expansion and thus smoother deposition.

In addition to studying the impact of geometry changes in the PVD setup, the effect of adding a light, inert carrier gas on the plume interaction and the resulting deposition uniformity is investigated. To this end, the carrier-gas mole fraction is varied at a given Knudsen number. Species separation focuses the heavy species along the primary axes, whereas the light inert carrier gas is scattered towards the periphery. Due to the higher mean molecular weight, the speed of sound decreases and consequently the interaction shock occurs farther downstream, is less bent and weaker producing a more uniform deposition profile. Desirable side effects of the carrier-gas are less stray deposition and a higher conductance of the coating material from the inlet nozzle.

The last part of the thesis focuses on the numerical method, since DSMC is accurate but computationally costly. The substitution of the collision step in DSMC with a kinetic relaxation using the Bhatnagar-Gross-Krook (BGK) operator is implemented in order to speed up the algorithm. The choice of the target distribution for the relaxation is crucial. The Maxwellian velocity distribution produces an incorrect Prandtl number; the Ellipsoidal-Stochastical BGK (ES-BGK) corrects for the Prandtl number by taking the stress into account; the Shakov model (S-BGK) corrects by considering the heat flux vector. The implemented models are verified against literature data and evaluated for their accuracy in simulating the interacting plumes case. In addition, we evaluated a hybrid coupling of the various kinetic relaxation models in dense, near-continuum regions with DSMC for rarefied and non-continuum regions. The switching criterion for the hybrid coupling was the gradient-length local Knudsen number. The implemented kinetic

models compare well to literature data for rarefied Poiseuille flow. The lower resolution criteria lower the computational cost to approximately 30% of the one of DSMC. For the planar jet interaction, the BGK model (using the Maxwellian target distribution) overestimates the shock strength, the S-BGK model overpredicts the diffusion of the shock, whereas the ES-BGK models results are in good agreement with the DSMC results. This indicates that the velocity sorting and breakdown of temperature isotropy in the expansions have a more significant influence on the flow field than the shock, which skews the velocity distribution. Coupling the kinetic models with DSMC in the highly rarefied regions improves the flow field for the BGK and S-BGK model, but not significantly.

In short, this thesis examines the influence of process conditions, geometry and carrier-gas use on the mass flow rate and deposition uniformity in continuous PVD for coating steel strips with anti-corrosive coatings. It provides modeling tools for the mass transport both inside and outside the VDB which can be used for further investigation and optimization.

SAMENVATTING

Fysisch opdampen, 'Physical Vapor Deposition' (PVD), is de resublimatie van een stof op een koud substraat die deze bedekt met een dunne vaste laag. PVD-coatings worden in de industrie gebruikt om de eigenschappen en het uiterlijk van oppervlakken te veranderen. Omdat het industriële proces vacuümcondities vereist, wordt het meestal in een batchproces uitgevoerd. Sinds kort wordt PVD als een veelbelovende alternatieve coatingtechnologie beschouwd voor het thermisch verzinken om een corrosiebeschermende laag op staal aan te brengen. Er ontbreekt echter een continu PVD proces om op industriële schaal beschermende coatings voor bandstaal te vervaardigen.
De eerste benaderingswijzen suggereren het volgende proces: De staalstrip wordt door luchtdichte afdichtingen in een vacuümkamer getrokken om een niet-reactieve coatingatmosfeer te waarborgen en onzuiverheden te vermijden; vervolgens wordt het oppervlak behandeld om tijdens het coatingproces een hoge hechting te verkrijgen; daarna passeert hij een dampverdeelkast, 'Vapor Distribution Box' (VDB) waaruit dampstralen (of pluimen) te voorschijn komen en het staaloppervlak coaten; tenslotte verlaat de strip de vacuümkamer weer door luchtdichte afdichtingen, wordt opgerold en verzonden.
Om dit proces op grote schaal bruikbaar te maken — of zelfs beter dan verzinken — moeten meerdere uitdagingen worden overwonnen: de dichtheid van de afdichtingen garanderen, de staalstrip reinigen, verdwaalde coating van de vacuümkamer voorkomen, een uniforme dikte van de coatinglaag garanderen, en zorgen voor een uniforme hoge dampmassastroom om de snelheid van de productielijn hoog te houden. Dit proefschrift gaat de laatste uitdaging aan het damptransport zowel in de VDB als in de vacuümkamer te modelleren.

Eerst wordt de stroming binnen de VDB gemodelleerd met behulp van een op SIMPLE/PISO gebaseerd algoritme voor transsonische stromingen. Om rekening te houden met de verdamping aan het smeltoppervlak, wordt een randvoorwaarde voor de inlaatdruk geïmplementeerd op basis van de Hertz-Knudsen-vergelijking. Het totale massadebiet voor verschillende smelttemperaturen wordt vergeleken met zowel experimentele waarden als met een analytische, isentropische schatting. Verder wordt de gevoeligheid van het model voor materiaaleigenschappen en procesomstandigheden bestudeerd. Er is gevonden dat het totale massadebiet van het systeem afhangt van verdamping en verstikking. Bij hogere smelttemperaturen neemt het totale massadebiet toe. De in de simulaties gevonden trend komt overeen met die van het experiment. Beide leveren slechts 33%–54% van het massadebiet op als geschat door de analytische isentropische relatie. Dit lage rendement verbetert met een hogere smelttemperatuur. Een vergelijking van het drukverlies over de VDB laat zien dat de belangrijkste verliezen optreden als gevolg van de viskeuze grenslaag in de spuitmondjes die de VDB verbinden met de vacuümkamer. De simulatie overschat het experimentele resultaat met een factor 1,3. Dit kan worden toegeschreven aan de gebruikte aanname van een geïdealiseerde waarde van 1

voor de verdampingscoëfficiënt; een waarde van ongeveer 0,3 zou een betere overeenkomst opleveren tussen de simulaties en experimenten. In het experiment gevonden onzuiverheden kunnen deze verlaging van de verdampingscoëfficiënt veroorzaken.

Wanneer de stroming vanuit de spuitmondjes in de vacuümkamer expandeert, versnelt de stroming tot supersonische snelheden en wordt ijler. We bestuderen de interactie van twee vlakke sonische pluimen die een schok veroorzaakt naast het interactievlak. Dit veroorzaakt op zijn beurt pieken in de afzettingssnelheid en dus in de coating. De Directe Simulatie Monte Carlo (DSMC) methode wordt toegepast voor de stroming die varieert van continuüm bij de spuitmondjes tot een ijle en vrije moleculaire stroming stroomafwaarts. De resultaten worden vergeleken met de analytische effusie-oplossing en de niet-viskeuze continuümoplossing van een Riemann-oplosser. De expansie- en schokgebieden van de DSMC-simulatie worden gevisualiseerd door de Method of Characteristics (MOC). De massadebietverdeling als functie van de mate van ijlheid, de onderlinge afstand tussen de spuitmondjes en de hellingshoek van de spuitmondjes wordt bestudeerd. Het DSMC-resultaat van pluiminteractie buiten de VDB lijkt sterk op de niet-viskeuze continuümoplossing bij lage graden van ijler worden. De structuur van de stroming met expansies en schokken valt samen, er zijn duidelijk afwijkingen in de daadwerkelijke getaldichtheid, snelheid en temperatuur, vooral in het schokgebied. Bij hogere mate van ijlheid neemt de schokstructuur af en benadert het stromingsveld het vrije moleculaire stromingsveld. Het ijle stromingsveld ligt echter niet binnen de grenzen van het niet-viskeuze continuüm en het vrije moleculaire stromingsveld, maar kan deze in het schokgebied in zowel depositiepieken als temperatuurpieken overschrijden.

Het gebruik van de MOC voor visualisatie laat zien dat bij hogere mate van ijlheid de schok wegbuigt van het interactievlak, wat verklaard kan worden door de verhoogde temperatuur in de secundaire expansie. Terwijl de locatie van de shock met de onderlinge afstand tussen de spuitmondjes verschuift, gaat zij op in één locatie wanneer zij met de onderlinge afstand tussen de spuitmondjes wordt geschaald. Door de spuitmondjes naar elkaar toe te buigen, ontstaat er een sterkere schok die verder stroomopwaarts begint, wat op zijn beurt een sterkere secundaire expansie en dus een gelijkmatiger afzetting veroorzaakt.

Naast het bestuderen van de invloed van veranderingen in de geometrie van de PVD-opstelling, wordt het effect van het toevoegen van een licht, inert draaggas op de pluiminteractie en de resulterende uniformiteit van de afzetting onderzocht. Hiertoe wordt de molaire fractie van het draaggas gevarieerd bij een bepaald Knudsen-getal. Soortenscheiding concentreert de zware soorten langs de primaire assen, terwijl het lichte, inerte draaggas naar het gebied aan de buitenkant wordt verstrooid. Door het hogere gemiddelde moleculaire gewicht neemt de geluidssnelheid af en treedt de interactieschok bij gevolg verder stroomafwaarts op, is minder krom en zwakker waardoor een gelijkmatiger afzettingsprofiel ontstaat. Gewenste neveneffecten van het draaggas zijn minder verstrooiing vanafzetting en een hogere geleiding van het coatingmateriaal vanuit de inlaatspuitmond.

Het laatste deel van het proefschrift richt zich op de numerieke methode, aangezien DSMC nauwkeurig maar rekenkundig kostbaar is. De vervanging van de botsingsstap in DSMC door een kinetische relaxatie met behulp van de Bhatnagar-Gross-Krook (BGK)

operator wordt geïmplementeerd om het algoritme te versnellen. De keuze van de doelverdeling voor de relaxatie is cruciaal. De Maxwelliaanse snelheidsverdeling levert een onjuist Prandtl-getal op; de Ellipsoïdaal-Stochastische BGK (ES-BGK) corrigeert voor het Prandtl-getal door rekening te houden met de spanning; het Shakov-model (S-BGK) corrigeert door rekening te houden met de warmtefluxvector. De geïmplementeerde modellen worden getoest aan data uit de literatuur en beoordeeld op hun nauwkeurigheid bij het simuleren van de casus van interagerende pluimen. Daarnaast evalueerden we een hybride koppeling van de verschillende kinetische relaxatiemodellen in gebieden die bijna een continuüm vormen met DSMC voor gebieden die ijl zijn en geen continuüm vormen. Het schakelcriterium voor de hybride koppeling was het op de gradiënt-lengte gebaseerde lokale Knudsen-getal. De geïmplementeerde kinetische modellen komen goed overeen met data uit de literatuur voor ijle Poiseuille stroming. De lagere resolutiecriteria verlagen de rekenkosten tot ongeveer 30% van die van DSMC. Voor de vlakke pluiminteractie overschat het BGK-model (gebruikmakend van de Maxwelliaanse doelverdeling) de kracht van de schok, overschat het S-BGK-model de diffusie van de schok, terwijl de resultaten van de ES-BGK-modellen goed overeenkomen met de DSMC-resultaten. Dit wijst erop dat de invloed van het sorteren van de snelheden en de afbraak van isotropie in de temperatuur in de expansies meer significant is op het stromingsveld dan de schok, die de snelheidsverdeling scheeftrekt. Het koppelen van de kinetische modellen met DSMC in de zeer ijle gebieden verbetert het stromingsveld voor het BGK- en S-BGK-model, maar niet significant.

Kortom, dit proefschrift onderzoekt de invloed van de procescondities, de geometrie en het draaggasgebruik op het massadebiet en de uniformiteit van de afzetting in continue PVD voor het coaten van staalstrips met corrosiewerende coatings. Het biedt modelleringstools voor het massatransport zowel binnen als buiten de VDB die voor verder onderzoek en optimalisatie gebruikt kunnen worden.

1

INTRODUCTION

1

Physical Vapor Deposition (PVD) is the process of a gas being deposited on a cold object and changing its phase directly to solid without passing the liquid state, i.e., being resublimated. Frost for example is PVD of water vapor onto cold plants and windows, on which it forms a thin uniform coating. This phenomenon from nature can be utilized to apply a protective, functional or aesthetic coating on a substrate, for example to protect steel against corrosion. For this purpose, most commonly zinc or zinc alloys are used, as they do not only build a barrier, but also give cathodic protection [2–6]. Compared to the deposition of frost encountered in nature, zinc coating by PVD requires well-designed devices, since the phase transition temperatures of zinc are much higher than the ones of water and chemical reactions have to be avoided. To exclude potential reactants, deposition processes of metals are implemented in vacuum chambers. Several PVD processes have been designed, which are characterised by their type of evaporation source. It can be thermal evaporation, e.g., in a crucible by induction coils [7] or by highly-energetic electron beams [8]. Another form is sputter deposition in which a plasma is generated in front of the source so that its ions strike the source material releasing single atoms into the vacuum, so that it is a non-thermal evaporation process. Since the plasma also benefits reactions, it is often used for the depositions of compounds, e.g., metal compounds in the semiconductor industry [9], (besides Atomic Layer Deposition, a sequential Chemical Vapor Deposition process and also commonly used for metal compounds). A further method is arc-PVD, in which the high kinetic energy of the electrons in an electrical arc release the source atoms. The produced films are very hard, which is why it is commonly applied for the coating of cutting tools [10].

The basic setup for thermal evaporation is the one shown in Figure 1.1. A Zinc (or other metal) source is placed in a vacuum chamber. The coating material is evaporated by means of an electro-beam or heating. The vapor spreads in all directions and coats both the substrate as well as the vacuum chamber. The latter stray deposition loss contaminates the chamber walls which entails cleaning of the chamber and consequently regular production downtimes. This traditional form of PVD is used in batch coating and involves long startup times, because the chamber has to be evacuated and refilled for each batch.

To make PVD also accessible for line production, continuous PVD setups were designed [7, 11, 12], which reduce stray deposition and can continuously operate without frequent shutdowns for refilling and maintenance. The layout of a continuous PVD line designed by Tata Steel is sketched in Figure 1.2. Instead of an open placement of the source in the vacuum chamber, the coating material is evaporated in a vapor distribution box, in which a higher pressure builds up than inside the vacuum chamber. The vapor is accelerated by the immense pressure ratio (up to speed of sound) generating jets directed towards the steel strip. The steel strip enters and leaves the vacuum chamber via vacuum locks guaranteeing a continuous line production. This setup ensures a higher deposition rate as well as a smaller stray deposition than in the traditional PVD setup. From the first promising concept to an efficient, high-quality setup many aspects have to be considered: the design of tight vacuum locks without introducing too much friction, continuous feed of liquid coating material, the adhesion behavior between resublimated zinc and steel and of course the mass transport in the system.

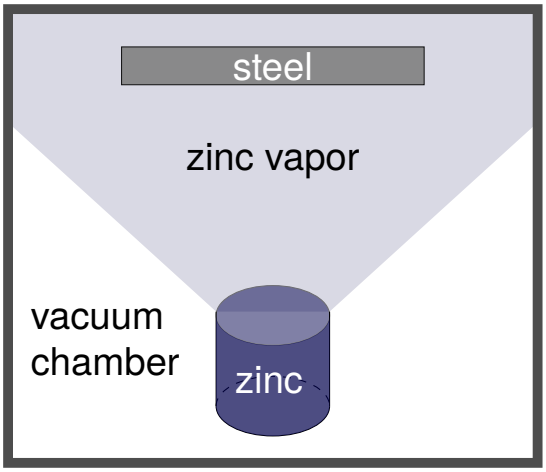

Figure 1.1: Principle of Physical Vapor Deposition (PVD) for steel coating as used in the traditional batch process. Zinc is evaporated from a source by either thermal or non-thermal means; it spreads into the vacuum chamber and coats the substrate, here steel, and as a side-effect also the chamber walls.

This thesis studies the latter, starting from the evaporation at the melt surface, the slow transport of dense vapor to the nozzles (incompressible continuum flow), the acceleration to supersonic flow inside the nozzles (compressible continuum flow) and the expansion of the flow into the vacuum chamber with a breakdown of equilibrium (rarefied flow).
Evidently, the continuous PVD line provides a variety of flow regimes which give rise to numerous modelling challenges justifying the curiosity-driven part of this research. Fortunately, we can use a plethora of possible approaches and models researched in the last centuries. The following section shortly outlines these developments in historical order, partially in their entangled form, as especially the early researchers studied more than one aspect of fluid mechanics. Often more than one researcher formulated a law or found a phenomenon at the same time or without knowing of the work of others. (Due to the language barriers of the author, the following section is biased towards texts available in English or German. The outline is based on information from the books by Anderson [13] and Lindley [14].)

1.1. SHORT HISTORY OF FLUID MECHANICS RELEVANT TO THE MODELLING OF A CONTINUOUS PVD PROCESS

In the classical and medieval periods, hydrodynamic principles were described which benefited the construction of buildings and ships such as Archimedes' principle [15] or explained daily life. These flows are mainly incompressible continuum flow, which means the ratio between the velocity u and the speed of sound a, i.e. the Mach number $Ma = u/a$, is low, and the field variables, e.g., pressure, velocity, temperature, can be expressed by a continuous function. Compressible flow behavior becomes first noticeable at speed differences above $Ma > 0.3$ corresponding to wind speeds of $\approx 100\,\mathrm{m\,s^{-1}}$

1

Chapter 3
Can design mitigate jet interaction shocks?
How applicable is inviscid continuum theory to describe jet interaction?

Chapter 4
Can a carrier gas reduce deposition non-uniformities?
Does species separation mitigate shocks?

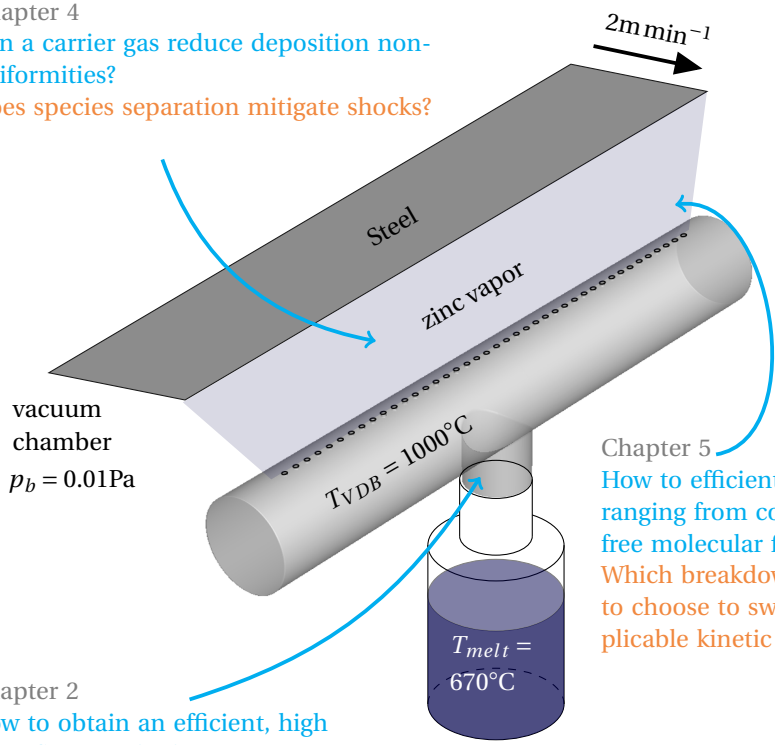

Chapter 5
How to efficiently model flow ranging from continuum to free molecular flow?
Which breakdown parameter to choose to switch to the applicable kinetic model?

Chapter 2
How to obtain an efficient, high mass flow inside the VDB?
How to model evaporation at the flow inlet?

Figure 1.2: Sketch of continuous Physical Vapor Deposition including the research questions of this thesis (the application-oriented research questions in blue, the curiosity-driven ones in orange). Zinc is evaporated from a crucible, from where it passes into the Vapor Distribution Box (VDB), which is heated to avoid condensation of the zinc, via small nozzles it flows into the vacuum chamber. Due to the choking inside the nozzles sonic plumes or jets emerge into the vacuum chamber, which may interact with each other. The zinc deposits onto a continuously moving steel stripe.

which exceeds the speeds of most cyclones. Hence, a human cannot experience or study compressible flow by direct means. Its wave-like character becomes clear only above $Ma = 1$, i.e., at supersonic speeds. Supersonic flow accelerates in a diverging cross section, whereas subsonic flow slows down. Rarefied flows require either vacuum, in which we cannot breathe and in which the boiling temperature is decreased, or very small scales in the order of the mean free path (≈ 65 nm at STP) which are only observable using a microscope. The correct description of incompressible fluid motion deducted

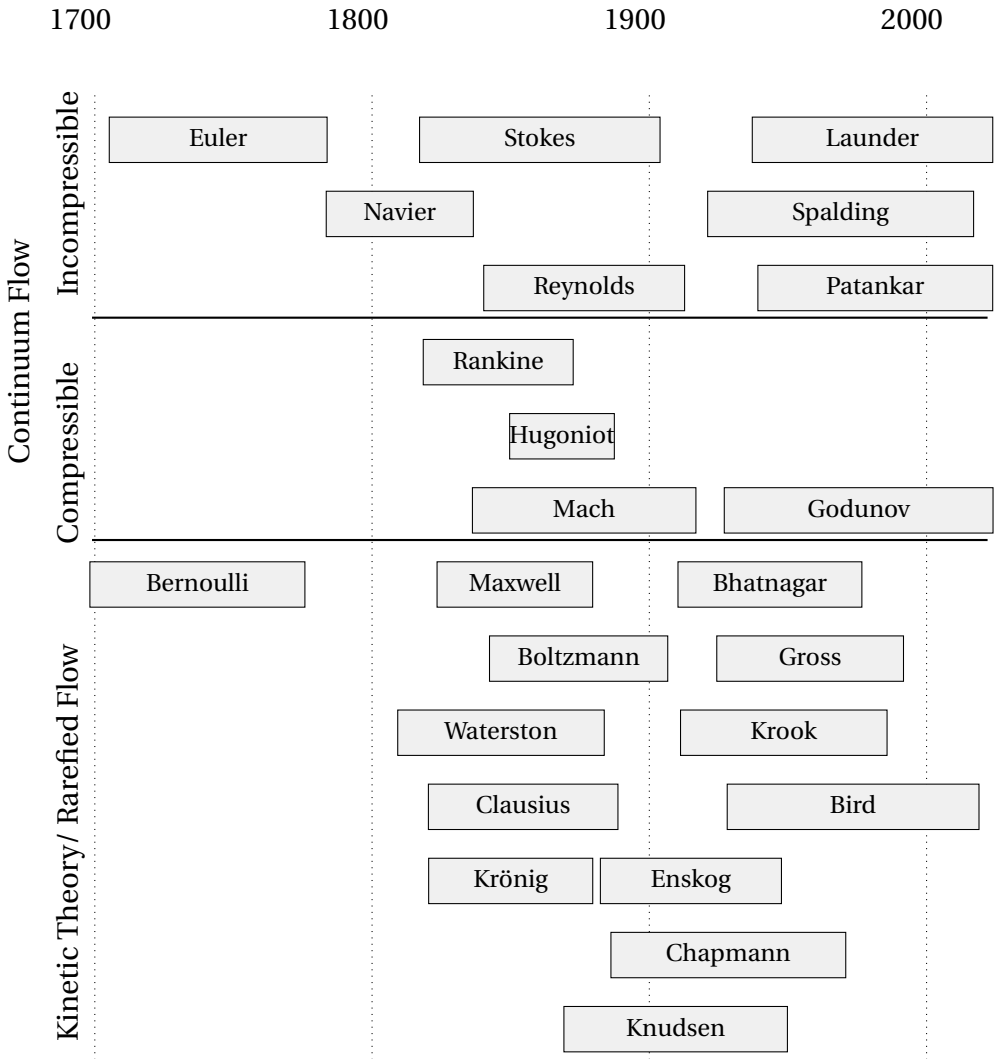

Figure 1.3: Time line of contributors to fluid mechanics theory and modelling classified by the field based on their contributions most relevant for the underlying thesis.

from observation and physical principles requires a great effort. But the prediction of both compressible and rarefied flow deducted from the observation of incompressible flows and thought experiments is intriguing, since we cannot experience these flows at first hand and their behavior often is opposite to the one known from incompressible continuum flow. Despite this, first sophisticated guesses about the nature of compressible flow and molecular movement were already made in the classical period: Vitruv wrote that “voice [...] moves [...] like the innumerably increasing circular waves which

appear when a stone is thrown into smooth water“ [16], which is information intended to benefit architects of theaters. Nowadays, we know how spot-on this describes sound waves, though at Vitruv's time it could only be a sophisticated guess. Similar hypotheses, impossible to prove at ancient times, but accepted to be correct in contempory times, concern the atomistic view on the world: Democritus (and his teacher Leucippus) are acknowledged to have first described the world to be founded on atoms and gave them their name 'atomos' - uncuttable. Lucretius meticulously interpreted this theory with regard to all daily phenomena and fabulated how small particles fly from an object to the eyes to make it visible or how water vaporizes from drying clothes and atoms fly into the surrounding air due to a kind of random movement [17]. Nowadays, we acknowledge this as coming close to truth in many (but not all) facets. However, Leukippos, Democrit and Lucretius had no obvious reason to assume the world to be made out of little atoms except perhaps for the incredibility of infinite sizes and continuous fields.

FLUID DYNAMICS IN MODERN TIMES

The extension of hydrostatics and -dynamics to a detailed description of fluid dynamics took mainly place after 1700. Figure 1.3 shows a timeline of researchers who contributed to the understanding of flow physics and / or its modelling relevant to this thesis. Leonardo da Vinci described the dynamics of fluid motion in sketches. Bernoulli recognized the relation between pressure and fluid velocity, nowadays known as Bernoulli's principle [18]. Euler undertook a first mathematical modelling of this phenomenon by giving the partial differential equation for the momentum conservation of inviscid fluids (despite that viscosity was described before by Newton) [19]. These so called Euler equations often describe external flows accurately as we will see for the plume interaction in Chapter 3. However, for internal flows that are affected by the shear in the boundary layers at the wall, viscous effects are dominant. The differential momentum equation including viscosity were derived independently by Henri Navier and George Gabriel Stokes [20], who gave the emerging Navier-Stokes equations their name, and others (Poisson and de Saint-Venant). Stokes suggested that molecules constitute fluid elements, but their fluctuational velocities are unimportant compared to the mean velocity from a macroscopic view [20]. In case of the compressible flows where thermodynamics affects the fluid dynamics, the continuity and momentum equation of both the Euler and the Navier Stokes equations have to be coupled with the energy equation, the Fourier equation. This set of equations describes the flow we can perceive with the naked eye, i.e. continuum flow.

Gas kinetics evolved parallel to continuum mechanics. The trigger for first quantitative kinetic models was the aim to describe gas behavior for an equation of state of gases. Next to the description of Bernouilli's principle, Bernoulli defined the pressure in terms of molecular motion in his Hydrodynamica [18]. John Herpath tried and John James Waterston managed to connect the molecular motion with heat and pressure [21]. In spite of its correctness, Waterston's derivation was only acknowledged after more famous physicists established the kinetic theory.

In 1856, August Krönig [22] — who is assumed to have read Waterston's work — presented the connection between the equation of state and molecular motion, stated that small molecules will move faster at the same temperature and described pressure-volume

work on a molecular level. It took Rudolf Clausius, who already built up his reputation with work on the connection between heat and work implicitly formulating the second law of thermodynamics, to make kinetic theory widely acceptable to the physics community. One year after Krönig's publication, he proposed in an essay with the apt title 'Über die Art der Bewegung, welche wir Wärme nennen' [23] (loosely translated 'On the kind of motion we call heat') that heat is movement, not only translational movement, but also rotational (since colliding bodies rotate) and vibrational (since he expected molecules to consist of multiple atoms with a not completely rigid connection). He drew fine distinctions which assumptions have to be fulfilled for a kinetic theory of gases: the volume of the molecule should be much smaller than the available space per molecule. The time of a collision should be negligible compared to the time between collisions and no intermolecular forces should play a role except for the collisions. He thus introduced the mean free path as the distance a molecule travels between two collisions. He connected the molecular movement to the heat and derived the specific heats.

Maxwell and Boltzmann took up kinetic theory from here and made it mathematically more sound. While considerations of big sample sizes and averaging played a role in the early kinetic theory, Boltzmann's revolutionary thought was the description of physics by statistical instead of deterministic laws. Thereby, he translated the discrete particle dynamics into a continuum equation, and as a consequence, brought abstract order into the confusing chaotic world of billions of particle movements and interactions. Thus not only trivial cases could be considered, but molecular motion of gases was comprehensively described including spatial changes and evolution in time. The resulting Boltzmann equation has seven dimensions: three in space, three in velocity space and one in time. When multiplying the Boltzmann equation with one or more molecular property (such as mass or particle velocity) and integrating afterwards over velocity space assuming a Maxwell velocity distribution, the known continuum conservation and transport equations such as for continuity, momentum and energy can be derived. This provides strong evidence for the correctness of the equation. Despite this, Ernst Mach (amongst others) was suspicious of the successfully emerging theories and severely criticized the change from empirical observation to thought experiments as the foundation of physical explanation, as he believed only empirically, directly measurable quantities should be used for the construction of physical laws.

Still, the proof that the Boltzmann equation reduces to the Euler equations in equilibrium and explains the (nearly) monotonic increase in entropy, made the statistical description too plausible to discard it. Further justification for molecular behavior was provided by Einstein in 1905: he described how fast a small particle would travel due to the uneven pressure distributions from the molecules colliding with the particle surface by statistical means [24]. Thus, he provided a quantitative method to connect molecular motion with a macroscopic observable phenomena, the Brownian motion.

Though the governing equations were found, i.e., the Boltzmann and the Navier-Stokes equations, their solutions for general cases were impossible. (Today the proof of the existence and uniqueness of a solution for the Navier Stokes equations is one of the millennium problems, not even including the solution itself.) Fluid dynamics had to restrain itself to special cases or the description of typical flow characteristics. Especially the latter is powerful if not to predict, but to understand flow and nowadays to evaluate

the plausibility of a result. Important concepts regarding this thesis are superposition in case of free molecular flow (Chapter 3,Chapter 4), hyperbolic character of supersonic flow (Chapter 3), and perturbation theory which addresses small non-linear deviations from linear behavior. Especially powerful was the reduction of problems by utilizing their similitude. Dimensional analysis (Buckingham-π theorem) leads to dimensionless numbers which sufficiently describe a flow, so that one result can be scaled to a flow which is similar in numbers. Furthermore, the dimensionless numbers facilitated the classification of flow regimes. This "law of similarity" and dimensionless numbers were popularized by and named after experimentalists. Three are meaningful for the present thesis (and will be defined in the coming sections): the Reynolds number, the Mach number and the Knudsen number.

In addition to the similarity, another level of abstraction was introduced by the use of moments. Reynolds — whose extensive studies of transition to turbulence in pipe flows made the Reynolds number popular for indicating the ratio of the inertial to the viscous forces, i.e., $Re = uL/\nu$, where u is the velocity, L the characteristic length and ν the kinematic viscosity — did not expect that it will be possible to describe the velocity fluctuations. Therefore, he split the flow into a mean and a fluctuational part, a procedure which was later called Reynolds decomposition [25]. Applying the Reynolds decomposition to the Navier-Stokes equations generates the Reynolds stress, i.e. a second-order moment of the fluctuational velocities which affects the mean velocity. It was found that not only turbulence, but also particle behavior can be described by moments and the lower the moment the less effort to either measure it, the easier to give a rough estimate under neglect of higher order moments and the higher the interest for engineering purposes. Consequently, in both kinetic and turbulent theory a bunch of modelling approximations were proposed to close the equation cascades, i.e. neglect higher-order terms or substitute a transport equation for a moment by an algebraic expression. A powerful simplification is the expression of the second-order moment, which corresponds to viscous stress, pressure and temperature in the kinetic theory and the Reynolds stress in turbulence, by the gradient of the first-order moment, which is velocity. This yields the stress incorporated in the Navier-Stokes equations in kinetic theory and Boussinesq's eddy viscosity hypothesis, which can be derived as the first-order truncation of a perturbation analysis (or by mixing length analogies). Launder and co-workers introduced the k-ϵ turbulence model which is based on the Reynolds decomposition and Boussinesq's eddy viscosity hypothesis [26]. The k-ϵ model is still commonly used and one version of it is applied in Chapter 2. While extremely useful for understanding the connection between molecular and macroscopic flows as well as simple efficient turbulence models, the assumption breaks for rarefied non-equilibrium and anisotropic turbulent flows. In the last decades, more accurate models were developed in both disciplines to account for this.

The early application-oriented research in kinetic theory was pursued by Martin Knudsen, who conducted several flow experiments in vacuum [27, 28] and also introduced the Knudsen cell [29], an effusion box connected to a vacuum chamber via a small orifice which may be seen as the first PVD apparatus designed by humans and exhibits a great similarity to the one depicted in Figure 1.2. The Knudsen number Kn, which was named after him, is the ratio between the mean free path λ and a characteristic

length L, so that it reads $Kn = \lambda/L$. It divides the flow regimes into the continuum regime for $Kn < 0.01$ (describable by Navier-Stokes equations), the slip flow regime for $0.01 < Kn < 0.1$ (Navier-Stokes equations in addition with slip boundary conditions), the transitional regime for $0.1 < Kn < 10$ (requirement to solve the Boltzmann equation) and the free molecular regime for $Kn > 10$ (the collision operator of the Boltzmann equation has negligible influence and an effusion solution is a sufficient description).

In kinetic theory, the work of Enskog [30] and Chapman [31] to approximate the Boltzmann equation by a perturbation series around the degree of rarefaction was groundbreaking and let to a description of phase space behavior easier digestible for the human mind. In 1916, Chapman detected four different forces acting on the species in a mixture of monatomic gases [32]: (i) Molecular diffusion counteracts concentration gradients; (ii) forced diffusion which appears only if the species react differently to a body force; (iii) pressure diffusion forces heavy molecules to high pressure regions and light molecules to low pressure regions and consequently enforces species separation due to molecular mass differences (an effect which will be utilized in Chapter 4 to mitigate shocks) and (iv) thermal diffusion (or thermophoresis), in which the thermal fluctuations of surrounding molecules push large molecules against the temperature gradient towards low temperature regions.

The drastic simplification of the collision operator of the Boltzmann equation into a relaxation by Bhatnagar, Gross and Krook transformed the integro-differential equation to a mere differential equation. Still, it did not tackle the entanglement of the movement and collision in the Boltzmann equation. Though not analytically solvable in general, this simplified equation allowed a solution for more special problems and was later the foundation for several numerical methods (one of which is implemented and used in Chapter 5).

COMPUTATIONAL FLUID DYNAMICS

The introduction of computers made the numerical solution of the equations, which tends with higher refinement of the discretization towards the correct solution, feasible. Hence, not only simple cases and qualitative flow behavior, but also accurate quantitative predictions became possible. However, the linear solution procedures for the non-linear equations came along with several obstacles: instability due to non-linear, stiff equations, the infinite equation hierarchy for the continuum equations, and the immense memory requirements for the six-dimensional Boltzmann equation.

Numerical mathematics emerged to find an approximate solution for differential equations. Bird introduced the Direct Simulation Monte Carlo (DSMC) in the sixties which provides an approximate solution to the Boltzmann equation [33, 34] by returning to its underlying physics, i.e., discrete particle dynamics. It splits the movement of molecules and their collision in distinct steps, thus decoupling both of each other which allows for a much coarser discretization than Molecular Dynamcis (MD). On the one hand, the consideration of molecular movement makes it applicable not only to continuum, but also non-equilibrium flow. On the other hand, the decoupling entails a fine discretization requirement limiting its use to a handful (i.e., a few millions) of molecules. Hence, it is mainly used for micro-fluidics and rarefied gases (DSMC will be used in chapters 3,4,5).

One of the most widely used algorithms for solving the Navier-Stokes equations is the

SIMPLE algorithms (or one of its derivatives) by Spalding and Patankar [35]. It solves the linearized governing equations in a decoupled serial algorithm with a momentum predictor and a pressure corrector step. Its derivative PISO uses two pressure corrector step which stabilizes the solution [36]. A combination of the two algorithms is used for the flow solution in Chapter 2. Sergei Gudonov introduced a numerical scheme to solve the Riemann problem which consists of a hyperbolic transport equation with a step function as initial condition [37], thus locally transforming the problem into an ordinary differential equation. This led to the development of approximate Riemann solvers, which can accurately predict hyperbolic flows such as supersonic flow including shocks (which will be used in Chapter 3).

Around the same time as the SIMPLE-based methods, lattice-gas automata and their these days thriving successor the Lattice Boltzmann method (LBM) were introduced [38]. The LBM solves the Boltzmann equation simplified by the substitution of the collisional operator by a relaxation operator. The simulation of local particle dynamics avoids an explicit pressure-momentum coupling and allows for local compressibility which produces a stable and highly parallizable algorithm. While different relaxation operators are possible, but the relaxation closure cannot correctly describe (large) deviations from equilibrium and algorithms for compressible flows were only introduced in the last years [39].

The vast variety of modelling approaches and the enormous extent of research provide the researcher with a ready-to-use toolbox. However, a good overview is required to choose the correct tool. The search for efficient accurate models and algorithms continues, especially for multi-regime flows as for example the one in the continuous PVD process (Figure 1.2): In the VDB the Mach number is low, corresponding to incompressible subsonic flow ($Ma < 0.3$); it increases inside the nozzles, first to compressible subsonic flow, then until the flow chokes ($Ma = 1$) and finally outside the nozzles, it reaches values above unity, corresponding to supersonic flow. At the same time, moderately high Reynolds numbers occur inside the VDB, which make flow separation, instabilities and low turbulence likely. The Knudsen number is low inside the VDB and at the nozzle outlet, justifying continuum assumptions; it rises in the expansion behind the nozzle outlet passing the transitional regime either reaching free molecular flow or — in case of jet interaction — being suddenly reduced by a shock. To tackle this multi-regime flow, it is split into two sections: The internal flow up to the nozzle outlet (Chapter 2) and the external flow region downstream from the nozzle (chapters 3, 4,5).

1.2. MOTIVATION AND OUTLINE

This thesis aims to model the flow inside a continuous PVD setup using Computational Fluid Dynamics (CFD). The goal is to predict mass flow rate and uniformity and maximize these for an optimal deposition. Each chapter has an application-oriented and a curiosity-driven motivation, where the weighting shifts from the former to the latter. Figure 1.2 depicts the region which each chapter treats as well as the corresponding application-oriented (in blue) and a curiosity-driven research questions (in orange). The outline is based on three main research questions.

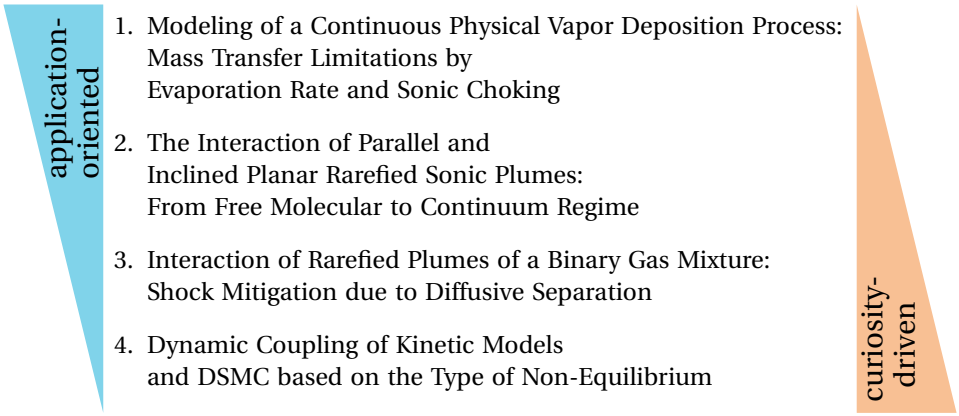

First, Chapter 2 aims to model the mass flow rate in the VDB of a continuous PVD setup accurately in comparison with experiments and maximize the mass flow rate. It addresses

> **Research question 1:** What limits the mass flow rate? How to obtain an efficient, high mass flow inside the VDB?

The mass flow is limited by two processes inside the VDB: Finite evaporation rate and choking inside the nozzles. Hence, the internal flow of the VDB is modelled, which is a continuum flow in the transonic regime, i.e., the flow ranges from sub- to supersonic flow. Besides accurate material properties, the numerical implementation of the Hertz-Knudsen boundary condition is crucial for the prediction of evaporated mass. After gaining some confidence in the modelling approach, the impact of process conditions on the flow rate and discharge efficiency are considered.

Chapters 3 and 4 both deal with the flow in the vacuum chamber after the nozzles. From the nozzles, free expanding plumes emerge. Upon interaction with each other shocks are induced causing an accumulation of density in the interaction plane. Subsequently, this yields undesired peaks in the deposition profile. Both chapters intend to mitigate the shocks and subsequent peaks in deposition. While Chapter 3 addresses geometry changes, Chapter 4 utilizes species separation effects. Chapter 3 addresses

> **Research question 2 a):** Can design changes mitigate jet interaction shocks? How does the rarefaction, the nozzle-separation distance and the inclination of the nozzles affect the flow and the deposition profile?

Chapter 3 approaches these questions first by considering the extreme cases of free molecular and inviscid continuum flow for planar jet interaction. Then the characteristics and shock region of the flow field are detected to compare the flow structure for different degrees of rarefaction. Eventually, it is investigated how the distance between the inlets and the tilting of the nozzles affect the deposition uniformity.

Chapter 4 extends the research question of the previous chapter by

> **Research question 2 b):** How does species separation affect shocks? Can a carrier gas reduce deposition non-uniformities?

To answer these questions, Chapter 4 evaluates how a light carrier gas affects the deposition rate, deposition uniformity and stray deposition in a jet interaction problem. The same tools as in the previous chapter are applied, again utilizing the explanatory power of inviscid continuum theory for the trends in rarefied supersonic flows.

Chapters 3 and 4 both use the DSMC method, which is widely acknowledged to be an accurate, but computationally costly method for rarefied flows, especially if both dense and rarefied regions exist in the flow field. This raises the question, how to speed up the simulation while maintaining an acceptable accuracy. Therefore, multiple new modelling approaches have been springing up in recent years. Several of them include a separation of the flow domain in a near-continuum and a rarefied region based on a breakdown criterion. Chapter 5 presents the implementation of particle-based kinetic relaxation models within the framework of OpenFoam to approximate the collision process. After its verification, different relaxation models are evaluated for modelling plume interactions. Eventually, criteria for switching between the target models for the relaxation are proposed. Chapter 5 discusses

> **Research question 3:** How to efficiently model flow ranging from continuum to free molecular flow? Can a substitution of the collision by a kinetic relaxation speed up the simulation? Which target distribution is applicable for interacting jets?

Conclusions and outlook are presented in Chapter 6.

2

Modeling of a Continuous Physical Vapor Deposition Process — Mass Transfer Limitations by Evaporation Rate and Sonic Choking

In recent years, Physical Vapor Deposition has been advanced to a continuous process which makes it amenable for in-line, high-quality and energy-efficient galvanization. To achieve the high and uniform mass flow required for in-line production, a Vapor Distribution Box is used, in which the zinc is evaporated. The zinc fills the Vapor Distribution Box at a relatively high pressure and leaves into the coating chamber via nozzles. A reliable modeling approach that can be used in the design and optimization of Vapor Distribution Boxes is as yet not available in the literature. The present paper analyses which phenomena play a major role and therefore have to be included in a simulation model of continuous Physical Vapor Deposition processes, and identifies process parameters which have a significant impact on deposition rate and uniformity.

To this end, a model for the flow and heat transfer is developed based on the numerical solution of the compressible Navier-Stokes-Fourier equations in combination with the Launder and Sharma low-Reynolds k-ϵ turbulence model, using the open-source CFD-library OpenFOAM. To account for the vapor mass flow to be limited by both evaporation and sonic choking, a novel inlet boundary condition is proposed based on the Hertz-Knudsen condition. Results from the CFD model are compared to those of analytical mod-

Published as Vesper, J. E., Obiji, C. S., Westerwaal, R., Boelsma, C., Kenjereš, S., & Kleijn, C. R. (2021). Modeling of a Continuous Physical Vapor Deposition Process: Mass Transfer Limitations by Evaporation Rate and Sonic Choking. Applied Thermal Engineering, 117099.

els based on isentropic flow, the influence of various modeling parameters is evaluated against experiments, and sensitivity of the process to various process parameters studied.

The proposed numerical model predicts mass flow rates with a much better accuracy than analytical models previously proposed in the literature. The latter overpredict the mass flow rate by a factor of 2.1–2.5, whereas the proposed numerical model overpredicts only by a factor of 1.3. Next to the novel Hertz-Knudsen boundary condition, the inclusion of viscous effects is found to be crucial to achieve this improvement, since viscous effects – especially in the boundary layer inside the nozzles – severely reduce the mass flow. The numerical model is shown to be only weakly sensitive to uncertainties in the evaporation coefficients and metal vapor viscosity. For the device studied, the mass flow discharge efficiency was found to be relatively low (≈ 40%). To increase this efficiency, viscous losses in the nozzle boundary layers have to be reduced, for instance by employing shorter or a bigger radius nozzles (possibly impairing nozzle-to-nozzle uniformity) or by employing a higher melt temperature and vapor pressure.

2.1. INTRODUCTION

Physical Vapor Deposition (PVD) is a coating technique commonly used in the automotive [40–42], turbomachinery [43, 44], textile [45], electronic [46] and solar energy industries [47, 48]. The manufactured coatings may improve structural and optical properties [49], act as thermal barriers [50] or protect steel from corrosion [51, 52]. In the last two decades, PVD was adapted to coat steel in a continuous process [7, 53, 54]. Its advantage over commonly used hot-dip galvanization [55, 56] and electro-galvanization processes [57] is that the heat impact which can change the steels structure is much lower [58]. In continuous PVD units, not only traditional zinc coatings can be applied, but also alloys such as zinc-magnesium-based coatings which provide a better protection against corrosion [2–6]. However, a reliable modeling approach that can be used in the design and optimization of continuous PVD units is as yet not available in the literature.

Traditional PVD processes are operated in batch mode and use physical means such as electro-beams or sputtering to evaporate coating material in a vacuum. The spreading atoms (or molecules) deposit on any object placed inside the chamber – including the chamber walls which consequently require regular cleaning. As a result, this diffuse distribution involves regular shut-downs of the PVD station, which is not feasible for a continuous production line. Furthermore, the evaporation rates reached by electro-beams and sputtering are quite low. A high mass flow directed towards the coating surface is necessary to integrate PVD in a strip production line. To achieve this, a continuous process was proposed in recent years [11]: The coating material, here zinc, is heated in a crucible and evaporates. The zinc vapor fills a Vapor Distribution Box (VDB), which is connected to the coating chamber via several small nozzles. Due to the high pressure ratio between the VDB and the coating chamber, which is under moderate vacuum, the vapor is drawn through the nozzles into the coating chamber. The zinc spreads into the vacuum at supersonic speed and eventually deposits onto the steel strip.

To the authors' knowledge, companies in South Korea, Belgium and the Netherlands are working on continuous PVD devices, but details are mostly not disclosed yet. A modification to the described setup was proposed by Banaszak et al. [12] who designed a VDB equipment with a longitudinal slot instead of nozzles and with a filter in front of the slot, which homogenizes flow speed and temperature before the vapor enters into the vacuum chamber. They also suggested using an induction heated filter consisting of a conductive material to avoid condensation. Zoestbergen et al. [7] heated the VDB wall to avoid condensation. While these measures are reasonable, the filter may hinder the flow and any heating inside the VDB decreases the metal vapor density which both lead to a decreased discharge.

While multiple shortcomings (e.g., stray deposition of coating material in the coating chamber and condensation at high mass flow rates) are yet to be remedied, this paper focuses on optimizing the process conditions to meet the most crucial requirement for continuous production: to obtain the required coating thickness within given tolerances at the typical speed of production lines, the mass flow has to be both high and uniform.

It is a major challenge to assess the effects of changes in design and process conditions. Measurements in high-temperature vacuum systems are difficult to perform and even simple geometry changes are costly. Theoretical predictions are complicated because the thermodynamic processes involved are highly non-linear and interwoven. Numer-

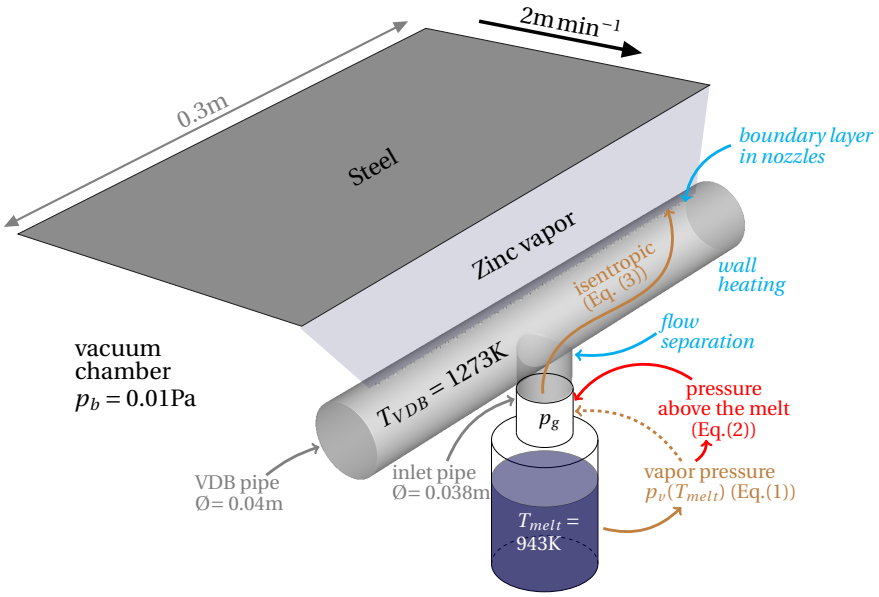

Figure 2.1: Sketch of Physical Vapor Deposition process. The simulated part of the Vapor Distribution Box is in gray. Brown denotes the modeling based on the Antoine vapor-pressure-equation and the isentropic relation, red the limitation of inlet pressure by the Hertz-Knudsen-equation, *italic cyan* the non-isentropic effects which require numerical modeling.

ical simulation methods, e.g., continuum Computational Fluid Dynamics (CFD) or rarefied gas simulation techniques such as Direct Simulation Monte Carlo (DSMC), enable us to shed some light on the processes involved, as it allows to account for and distinguish between the influence of non-ideal and non-linear phenomena.

The deposition rate and uniformity of batch PVD processes have been studied by using continuum CFD [59–62] or DSMC [8, 63–67]. Some studies also compared both methods [68–70]. Schmitz [53] developed a theoretical model for a continuous PVD process, in which he estimated the mass transfer from the VDB to the coated surface on the basis of isentropic and empirical relations. He approximated the jet vapor deposition process through a slot opening by splitting the flow into two parts: first, a continuum flow inside the VDB; second, a collisionless expansion outside the vacuum chamber. In the first part, he assumed a perfect, adiabatic gas flow with friction losses at the slot entrance and exit. Numerical simulation of a continuous PVD setup has so far been reported only as a subsidiary support of experiments [11, 12] to show the uniform velocity profile in a choking nozzle, but studies did not address the discharge efficiency or consider the limitation to the evaporation rate at the melt surface. The mass flow rate can be estimated by coupling the Hertz-Knudsen relation for evaporation with the isentropic relations for compressible flow, assuming choking in the nozzles. This estimate does not account for viscous effects. A reliable mass flow prediction to assess process modifications and optimize the process is missing.

A comprehensive numerical model of a continuous PVD process has to deal with vari-

ous phenomena that complicate numerical simulations, such as evaporation at the melt surface, the rapid increase in the Mach number of the vapor flow ranging from incompressible to compressible supersonic flow, the high pressure ratio between the VDB and the vacuum chamber (up to $\mathcal{O}(10^6)$) and the unknown thermodynamic, evaporation and transport properties of metal vapors. Furthermore, such a model has to account for multiple viscous phenomena, i.e., (i) viscous dissipation including heat generation [71], (ii) Fanno [72] and (iii) Rayleigh flow [73]. All of these phenomena may affect the discharge: (i) The dramatic velocity changes from zero-slip at the wall to supersonic velocity in the core result in high viscous dissipation, decreasing the pressure and possibly generating heat; (ii) in compressible subsonic flow, the pressure drop lowers the density and subsequently increases the velocity, whereas in supersonic flow, the pressure drop increases the density and decreases the velocity. The stagnation pressure and hence the mass flow decrease; (iii) The heating of the nozzles itself may give rise to a Rayleigh effect in the boundary layer which decreases the stagnation pressure and thus also the mass flow. It is unknown in the literature, and difficult to estimate a priori which of these phenomena significantly affect the flow and which can be neglected.

The present paper proposes important steps towards the development of such a model. To the authors' knowledge, it represents the first report on the development and assessment of a physically comprehensive numerical simulation model for continuous PVD coating processes that is validated against experimental data in an industrial setting. Various aspects of the numerical model discussed in this paper may not only benefit the emerging continuous Physical Vapor Deposition, but also other vacuum and turbomachinery technologies.

The present paper has two objectives: First, to evaluate which phenomena play a major role in the continuous PVD deposition process and have to be included in a numerical PVD model in order to capture all relevant physics. Second, to identify process modifications which have a significant impact on deposition rate and uniformity.

Gas flow and heat transfer in a pilot continuous PVD unit are modeled using the open-source CFD-library OpenFOAM [74]. To couple the limitation by the evaporation rate at the melt and the limitation the choking inside the nozzles, a novel boundary condition is implemented based on the Hertz-Knudsen equation and the isentropic relation. The numerical simulation results are validated with experimental results. First, the experimental pilot case setup is described, the thermodynamics involved is summarized and the isentropic expressions are listed which are required to estimate the mass flow rate. Then, the numerical methods are presented with a focus on the boundary condition that we implemented to capture the evaporation process correctly. Subsequently, the numerical method is verified and validated. In the results section, we present the flow field, mass flow rate and viscous losses. Finally, the results section discusses the applicability of isentropic equations to estimate the mass flow rate, the significance of the above-mentioned viscous phenomena and parameter uncertainties for numerical mass flow rate modeling and possible design improvements for a higher discharge efficiency.

2.2. EXPERIMENT

The studied equipment, its dimensions and the known process conditions are summarized in Fig. 2.1. Zinc is heated up in a crucible enclosed by induction coils to melt

Table 2.1: Specifications and sensitivities of used devices.

Device	Specification	Sensitivity
Thermocouple	Mantel Thermocouple type K	5 K
Vacuum pump	Pfeiffer Duo 125, oil diffusion, WKP 500 A	-
Eddy current thickness measurement	Fischer Phascope PMP10	0.5 µm

temperatures between 903 K – 943 K. The zinc vapor flows from the melt surface via an inlet pipe into the VDB, where a relatively high pressure builds up. The vapor leaves the VDB via 41 nozzles with a diameter of 2 mm and a length of 9.5 mm (nozzle-axis-to-nozzle-axis distance 6 mm). In the nozzles, the vapor is rapidly accelerated due to the large pressure difference between the VDB and the vacuum chamber (which is held at a background pressure $p_b = 0.01$ Pa). Subsequently, the flow chokes (i.e., it is limited to Mach numbers around one) at the nozzle outlet. Rarefied metal vapor jets emerge from the nozzles directed towards the moving steel strip, where the vapor solidifies upon impingement. The steel strip has a width $l = 0.3$ m and moves at a speed of 2 m min^{-1} (the speed of real line production is about 50 times higher). To avoid recondensation in the process, the wall of the VDB is kept at a temperature of about 1273 K by multiple resistance heating wires. Three thermocouples are placed to monitor the process: at the bottom of the crucible, in its center, and above the melt in the vapor. The coating thickness was measured using an eddy current device. The specifications and sensitivities of the devices are listed in Table 2.1. For each melt temperature $T = 903\,\text{K}, 923\,\text{K}, 943\,\text{K}$, two separate runs were conducted. The mass flow was determined by weighing the crucible before and after the run. A stray deposition rate between 8% and 11% was derived from mass flow rate and deposited film thickness.

2.3. MODEL

2.3.1. ISENTROPIC APPROXIMATION

Fig. 2.1 describes the thermodynamic relations and phenomena determining the flow. Neglecting all non-isentropic effects — such as flow separation, wall heating, viscous boundary layers — the mass flow rate can be estimated depending only on the melt temperature which is one of the few process conditions known from the experiment. Such an estimate is reasonable, (i) if the flow stays attached to the walls, which depends on geometry and Reynolds number, (ii) if the wall heat flux is not big enough to considerably heat the flow, and (iii) if the boundary layers are small compared with the bulk flow region. But even if this is not the case, an isentropic estimate is the best prediction available without a numerical simulation. In this section, we develop an ideal theoretical model assuming isentropic conditions. In addition, we assume that the pressure in the VDB is uniform, the gas inside the VDB is at stagnation conditions (i.e., the velocity is negligible) and the flow at the nozzle outlet is choked (i.e., $Ma = 1$) across the entire outlet cross section. All pressures used in this section are total pressures (i.e., static and dynamic pressure) and thus account for the flow dynamics. Fig. 2.1 shows the steps re-

Table 2.2: Antoine equation coefficients for Zinc [75].

A [K]	B	C	D [K^{-1}]	Temperature range in K
6883	9.418	-0.0503	-0.33	473 – 692.5
6670	12.00	-1.126	-	692.5 – 1000

quired for such a modeling. First, the saturation vapor pressure p_v has to be determined using the empirical Antoine equation which describes the pressure-temperature relation along the vapor-pressure curve as

$$\log_{10}\left(\frac{p_v(T_m)}{133.32}\right) = -\frac{A}{T_m} + B + C\log_{10} T_m + 10^{-3} D T_m, \tag{2.1}$$

where T_m is the melt temperature in K; the coefficients for zinc are listed in Table 2.2.

In a first approximate estimate it is assumed that the gas pressure p_g inside the VDB is the same as the saturated vapor pressure p_v. Isentropic relations can then be used to determine the mass flow rate as [73]

$$\dot{m}^*_{is} = p_g \sqrt{\frac{\gamma M}{R T_g}} A^*_n \left(\frac{\gamma+1}{2}\right)^{-\frac{1}{2}\frac{\gamma+1}{\gamma-1}}, \tag{2.2}$$

where A^*_n is the critical or sonic cross section of the nozzles (i.e., the outlet area where $Ma = 1$). As we neglect the subsonic viscous boundary layer, the sonic section corresponds to the total cross section $A^*_n = A_n$.

However, as the evaporation does not occur in a closed system, the actual gas pressure in the VDB adapts to a lower value than the vapor pressure used in Eq. (2.2). The actual vapor pressure p_g in the VDB determines both the mass flux evaporated from the melt and the outflow mass flux at the nozzles. The actual evaporation rate is proportional to the difference between the vapor pressure and the gas pressure p_g above the melt and is given by the Hertz-Knudsen equation [76, 77]

$$\dot{m}_{HK} = f A_m \left(p_v(T_m) - p_g\right) \sqrt{\frac{M}{2\pi R T}}, \tag{2.3}$$

where A_m denotes the melt surface area and the evaporation coefficient is often assumed to be $f = 1$. However, multiple studies report values around $f = 0.82$ for metal melts [78–80] and the mean value derived from zinc evaporation experiments conducted by Clair and Spendlove [81] was $f = 0.75$ when neglecting negative value outliers, or $f = 0.58$ when neglecting both negative values and values above unity.

By balancing the two mass flow rates from Eqs. (2.3) and (2.2), we obtain the actual value

for p_g and from this the mass flow rate limited by the Hertz-Knudsen condition

$$\dot{m} = \frac{f A_m \sqrt{\frac{M}{2\pi R T}}\, p_v(T_m)}{1 + \frac{f A_m}{A_n}\sqrt{\frac{1}{2\pi\gamma}}\left(\frac{\gamma+1}{2}\right)^{\frac{1}{2}\frac{\gamma+1}{\gamma-1}}}. \tag{2.4}$$

For numerical modeling (as described in the next section) it is useful to rewrite this equation in a form which has the mass flow rate on both sides of the equation

$$\dot{m} = \left[p_v(T_m) - \underbrace{\frac{\dot{m}}{f A_m}\sqrt{\frac{2\pi R T}{M}}}_{\text{limitation by HK}} \right] \cdot \sqrt{\frac{\gamma M}{R T_g}} A_n \left(\frac{\gamma+1}{2}\right)^{-\frac{1}{2}\frac{\gamma+1}{\gamma-1}}. \tag{2.5}$$

While the mass flow rate can be calculated explicitly from Eq. (2.4), Eq. (2.5) clearly illustrates the limitation of the mass flow rate due to the Hertz-Knudsen equation which shows that the gas pressure in the VDB is not equal to the vapor pressure, but rather reduced by the mass flow leaving the VDB, which in a steady system is the same as the evaporated mass flow. The higher the mass flux (e.g., due to a high outlet area A_n), the higher the limitation. High availability of the evaporated metal (e.g., due to a high melt area A_m or a high evaporation coefficient f) reduces the limitation.
In compressible flows through heated ducts, such as in the VDB nozzles, Rayleigh flow may occur which means that adding heat to the flow lowers the stagnation pressure [73]. Wall heating increases the thickness of the subsonic boundary layer and thus reduces the performance and mass flow rate of the nozzle. For a perfect one-dimensional flow this would reduce the stagnation pressure in the critical section, which would further decrease the mass flow rate to

$$\dot{m}_{Rayleigh,HK} = \frac{1}{\gamma+1}\left(\frac{\gamma+1}{2}\right)^{\frac{\gamma}{\gamma-1}} \dot{m} \tag{2.6}$$

and produce a discharge of $\dot{m}_{Rayleigh,HK} = 0.77\dot{m}$ for monatomic gases (for which $\gamma = 5/3$). In the process under consideration, the Rayleigh effect is expected to be considerably lower, as the heating only occurs at the nozzle walls and the nozzles are not long enough to allow heat conduction to the core.

Table 2.3: Boundary conditions.

Boundary	Pressure BC	Velocity BC	Temperature BC
Inlet	Total pressure or Hertz-Knudsen condition based on $p = p_v(T_m)$	Zero normal gradient	Total temperature based on $T_m = 943\,\mathrm{K}$
Outlet	Wave transmissive with $p_b = 0.01\,\mathrm{Pa}$ at a distance of 0.01 m	Outlet: zero normal gradient inlet: zero velocity convective	Constant temperature T_m
Wall	Zero normal gradient	No slip	Wall temperature $T_w = 1273\,\mathrm{K}$
Outlet Wall	Zero normal gradient	No slip	Zero normal gradient

2.3.2. NUMERICAL MODELING

GOVERNING EQUATIONS

The compressible Navier-Stokes-Fourier equations describe the flow by the conservation of mass, momentum and energy

$$\frac{\partial \rho}{\partial t} + \frac{\partial (\rho u_i)}{\partial x_i} = 0\,, \tag{2.7}$$

$$\frac{\partial (\rho u_i)}{\partial t} + \frac{\partial (\rho u_i u_j)}{\partial x_j} = -\frac{\partial p}{\partial x_i} + \frac{\partial}{\partial x_j} \underbrace{\left[(\mu + \mu_t) \left(\frac{\partial u_i}{\partial x_j} + \frac{\partial u_j}{\partial x_i} - \frac{2}{3} \frac{\partial u_k}{\partial x_k} \delta_{ij} \right) \right]}_{=\tau_{ij}}\,, \tag{2.8}$$

$$\frac{\partial (\rho e)}{\partial t} + \frac{\partial (\rho u_j e)}{\partial x_j} + \frac{\partial (\rho k_e)}{\partial t} + \frac{\partial (\rho u_j k_e)}{\partial x_j} = -\frac{\partial (p u_j)}{\partial x_j} + \frac{\partial}{\partial x_j} \left[\left(\alpha + \frac{\mu_t}{Pr_t} \right) \frac{\partial e}{\partial x_j} \right] + \frac{\partial \left(\tau_{ij} u_i \right)}{\partial x_j}\,, \tag{2.9}$$

where e is the internal energy and $k_e = \frac{1}{2} u_i u_i$ is the kinetic energy. Viscous effects dissipate momentum and generate heat. As the Brinkman number (i.e., the dimensionless ratio between heat generated by viscous dissipation and heat conducted away by thermal diffusion) was $Br = \mathcal{O}(1)$ in the nozzles, one simulation was run including heat generation due to viscous dissipation, which is the last term in the energy equation (Eq. (2.9)). However, the effect on temperature and the mass flow was negligible as the affected region was rather small. The difference in total mass flow rate was 0.3%. Therefore, heat generation by viscous dissipation was neglected in the simulations presented here.

Modeling of compressible flows in similar geometries revealed that it may be important to consider turbulent losses as well [82]. After initial laminar simulations, Reynolds number calculations indicated that turbulence may have an effect on the flow field. The Reynolds number based on local velocity, local viscosity and VDB pipe diameter was $Re = 2000$–4000 in wide regions of the inlet pipe and in the VDB pipe. Consequently, an eddy viscosity model was added. For further simulations, the turbulent viscosity μ_t was modeled by the Launder and Sharma low-Reynolds k-ϵ model [83] with a compression term based on rapid distortion theory (RDT) [84] (for brevity the turbulence model and corresponding boundary conditions are summarized in Appendix A.1). The turbulent Prandtl number was chosen as $Pr_t = 1$. Spontaneous nucleation and condensation may occur in the nozzle due to swift thermodynamic changes [85, 86] and was reported for continuous PVD processes especially for high pressures inside the VDB [7, 12]. Inspection of the regions of saturation (i.e., where $p > p_v(T)$) revealed, that supersaturation is reached inside the nozzles only and not to an extent which makes spontaneous nucleation probable [87]. Nor was condensation observed in the experiments which were run at moderate vapor pressures.

NUMERICAL SOLVER

A pressure-based compressible solver in the open-source library OpenFOAM ®-v1806 (i.e., *sonicFoam*) is used to solve the governing equations [88]. For a description of a similar solver, the reader is referred to [89]. Our verification and validation of the solver can be found in Appendices A.2.1 and A.2.2. This solver is suitable in the transonic regime which is central to the flow we studied. Its limitations in supersonic flows, e.g., regarding exact shock location prediction and adiabatic expansion treatment, are not relevant for the flow region under consideration (i.e., inside the VDB). As the flow at the nozzle outlet is supersonic (except for a small subsonic region in the boundary layer), the flow inside the VDB is not affected by the flow in the vacuum chamber. The Navier-Stokes-Fourier and k-ϵ-equations were discretized on a hexagonal mesh of 2.3 million cells in total and with 27 cells across the diameter of each nozzle. For a grid independence study we refer to Appendix A.2.3. The time integration was conducted using an implicit Euler scheme. The gradients were discretized by central differencing, the fluxes were discretized by a second-order Total Variation Diminishing scheme (Sweby limiter [90]), only the k and ϵ fluxes in the turbulence model were discretized by a first-order upwind scheme to stabilize the simulation (a second-order scheme would be preferable, but turbulence did not affect the flow significantly anyhow). The allowable maximum final residuals for the linear algebra solvers were set to 10^{-10} for pressure, turbulent kinetic energy and turbulent dissipation and 10^{-8} for velocity and energy. The mass flow rates at inlet and outlet were monitored; a solution was considered converged when the relative deviation of the two mass flow rates was below 0.5% (and no oscillations over time were observed).

CLOSURE OF THERMOPHYSICAL PROPERTIES

Since only the viscosity for alkali metal vapors has been reported in the literature, other metal vapor viscosities have to be approximated. We used the inverse-power-law-based method described by Fan et al. [8] first to estimate the collisional variable-hard-sphere diameter to be $\sigma_{VHS} = 5.684 \cdot 10^{-10}\,\mathrm{m}$ at a reference temperature of $T_{ref,VHS} = 2000\,\mathrm{K}$,

and then we applied the inverse power law to derive the temperature-dependent viscosity which we fitted with the Sutherland equation

$$\mu(T) = \frac{A_S\sqrt{T}}{1 + T_S/T}, \tag{2.10}$$

which gives $A_S = 1.008 \cdot 10^{-6}\,\mathrm{Pas}/\sqrt{\mathrm{K}}$ at a reference temperature $T_S = 400.9\,\mathrm{K}$. As temperature and pressure are far below the critical point, the ideal gas equation of state can be considered. The molecular weight of zinc is $M = 65.38\,\mathrm{g\,mol^{-1}}$, the specific heat at constant pressure $C_p = 317.901\,\mathrm{J\,K^{-1}\,kg^{-1}}$ and the Prandtl number $Pr = 0.7$.

BOUNDARY CONDITIONS

The simulated domain and its boundaries are depicted in Fig. 2.2, the boundary conditions applied are listed in Table 2.3. Based on the existing total pressure boundary condition in OpenFOAM [74], we implemented a Hertz-Knudsen pressure inlet boundary condition to obtain the correct mass flow. The total pressure p_t above the melt is limited by the maximum evaporation rate described by the Hertz-Knudsen equation (see Eq. (2.3)), where we set $\frac{\dot{m}}{f A_m} = \rho|U|$ and $p_t = p_g$ to obtain

$$p_t = p_v(T_m) - \frac{\rho|U|}{f}\sqrt{\frac{2\pi R T}{M}}, \tag{2.11}$$

where the temperature in the second term is the static gas temperature at the inlet, which for the sake of simplicity was equated with the melt temperature (as in our simulations the gas temperature deviated less than 2K from the melt temperature).
Furthermore, the computational domain does not start directly at the melt surface, but further downstream to reduce computational cost. The gap is bridged by assuming an isentropic acceleration of flow. Since it is in the incompressible flow regime (i.e., $Ma < 0.3$), the local static pressure $p_{s,in}$ evaluates depending on the calculated local inlet velocity U as

$$p_{s,in} = p_t - \frac{1}{2}\rho|U|^2. \tag{2.12}$$

The isentropic total temperature inlet condition is given by

$$T_{s,in} = \frac{T_t}{1 + \frac{\gamma - 1}{2\gamma}\psi_T|U|^2}, \tag{2.13}$$

where $\psi_T = \left(\frac{\partial\rho}{\partial p}\right)_T$ is the isothermal compressibility. The pressure boundary condition which is limited by both the Hertz-Knudsen relation and the isentropic relation was implemented in OpenFOAM. [1] At the outlet, a wave-transmissive pressure boundary condition was used to avoid numerically reflected shocks in front of the boundary [91].

[1] The implemented inlet pressure boundary condition is available at https://gitlab.tudelft.nl/evesper/HKLbc.

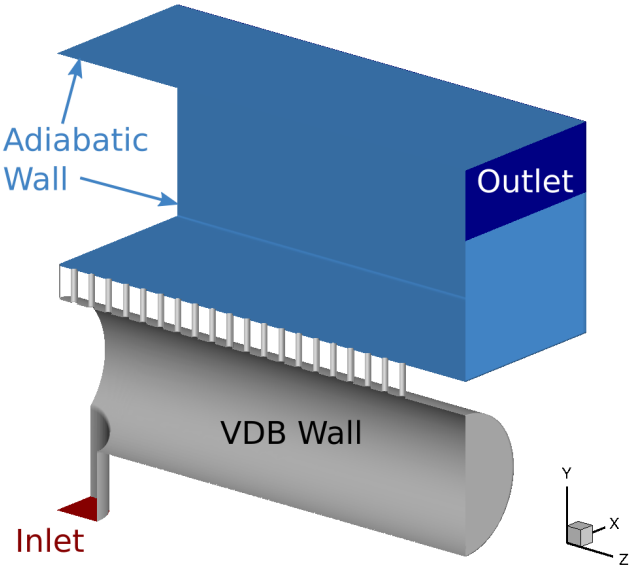

Figure 2.2: Boundaries of computational domain. The outlet boundary extends around the entire domain.

2.4. RESULTS AND DISCUSSION

2.4.1. FLOW FIELD INSIDE THE VDB

Fig. 2.3 shows the contours of the simulated velocity, pressure and temperature fields in the short and long cross-sections of the VDB. The values are clipped to best visualize the VDB part so that the drastic changes inside the nozzles are not captured (which will be discussed in section 2.4.3). The case shown applies to a melt temperature of 943 K and a wall temperature of 1273 K. In the simulation, a total pressure inlet boundary condition was used and the turbulence was modeled by means of the Launder and Sharma RDT-low-Reynolds k-ϵ model (if not mentioned otherwise, the Results section refers to this case). The velocity at the inlet adjusts to approximately 28 m s^{-1} (Fig. 2.3a). At the wall of the inlet pipe, a boundary layer develops, while the core flow accelerates. After the flow has entered the main part of the VDB, a shear layer forms between the jet and the surrounding vapor. On impinging onto the VDB wall, the flow stagnates, thus causing a local pressure rise. A wall jet emerges from the stagnation zone which is visible above the 4th to 6th nozzles from the left. The average static pressure at the inlet patch rises to 4171 Pa (Fig. 2.3b). This value remains similar in the entire VDB except for the stagnation region, where it is slightly higher, and the nozzle inlets where it drops dramatically (the pressure contours are clipped to values above 4100 Pa). The vapor temperature in the inlet pipe and the emerging jet is close to the melt temperature of 943 K (Fig. 2.3c). A thin thermal boundary layer forms at the pipe walls. In the rest of the VDB pipe, wall heating and the slow swirling motion result in a uniform temperature rise to approximately 1100 K. An additional insight in the flow dynamics can be gained from the streamlines shown in Fig.

2.4. While the streamlines are aligned with the wall in the inlet pipe, most of them swirl inside the VDB pipe at a lower speed, before accelerating rapidly when leaving via the nozzles (up to supersonic velocities).

2.4.2. VALIDATION AND MODELING

TOTAL MASS FLOW RATE

The total mass flow rate and the coating thickness over the strip width are known from the experiments and used for validating the model. Fig. 2.5 shows the mass flow rate as a function of the melt temperature. Both experimental runs are in good agreement with each other and show an increase in mass flow rate at higher melt temperatures. The analytic isentropic relation (Eq. (2.2)) overpredicts the mass flow by a factor of 2.5–3, the relation limited by the Hertz-Knudsen equation (Eq. (2.3)) by a factor of 2.1–2.5. The simulation with the total pressure boundary condition overpredicts the mass flow by a factor of 1.8, while that limited by the Hertz-Knudsen equation overestimates by a factor of 1.4 and after adding a turbulence model by a factor of 1.3. It should be noted that simulating half the domain instead of one quarter does not affect the mass flow rate. We also checked for the influence of applying a real gas model which, however, had no effect as most of the gas is not near the vapor pressure curve. To check the sensitivity to a wrongly predicted metal vapor viscosity, we ran one simulation with a viscosity increased by 50% which reduced the mass flow by only 8%.

INFLUENCE OF EVAPORATION COEFFICIENT

As discussed above, considering the evaporation-limitation is crucial for modelling the discharge. Limiting the possible mass flow from the melt surface by the Hertz-Knudsen Equation (Eq.(2.3)), even when assuming an evaporation coefficient at the theoretical upper limit $f = 1$, results in a considerable ($\approx 25\%$) drop in predicted mass flow rates. However, predicted mass flow rates are still 30–35% larger than experimental results. Assuming an evaporation coefficient f lower than 1 would further reduce the mass flow rate and could possibly explain the difference between experiments and simulations. In the literature, only few measurements of the evaporation coefficient were conducted for zinc [81] as well as for other metals [78–80]. The reported evaporation coefficients were in the range $f \in [0.58-0.82]$. We now discuss how the discharge depends on the evaporation coefficient. Before looking at the numerical results, we visualize in Fig. 2.6a, how the evaporation coefficient affects the slope of the Hertz-Knudsen equation (Eq. (2.3)) and its intersection with the isentropic relation (Eq. (2.2)). The intersection point is given by Eq. (2.4). For the range of reported values of f, a small change of the mass flow rate at the intersection point was found. Reducing the value of the evaporation coefficient from $f = 1$ to the smallest reported experimental value $f = 0.58$ reduces the mass flow rate by 12% only, thus still not explaining the 30–35% difference to our experimental data.
In Fig. 2.6b, the simulated mass flow rates are compared with those predicted by the theoretical relation (Eq. (2.4)). While the simulations produce a lower total mass flow rate, the relative dependence of the mass flow rate as a function of f is very similar in the simulations and in the theory. We may therefore use the theoretical curve to estimate the required reduction in f to reach a 35% reduction in the mass flow rate. suggests that the

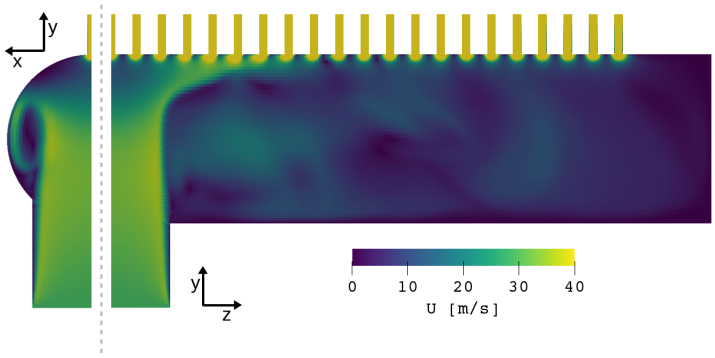

(a) Velocity magnitude, clipped to values below $40\,\mathrm{m\,s^{-1}}$.

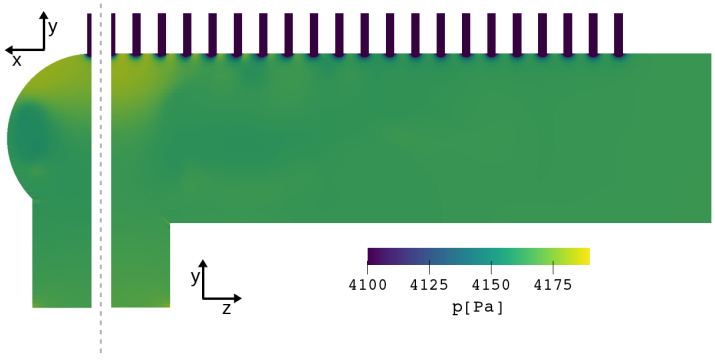

(b) Static pressure, clipped to values above 4100 Pa.

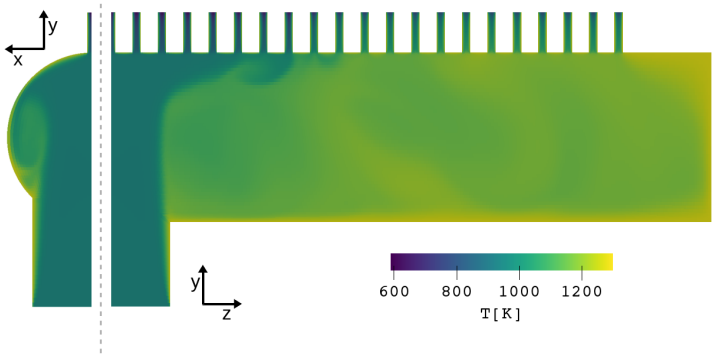

(c) Static temperature.

Figure 2.3: Contours of the instantaneous velocity magnitude, pressure and temperature in the short and long cross section. Both the velocity magnitude and pressure are clipped to better visualize changes within the VDB.

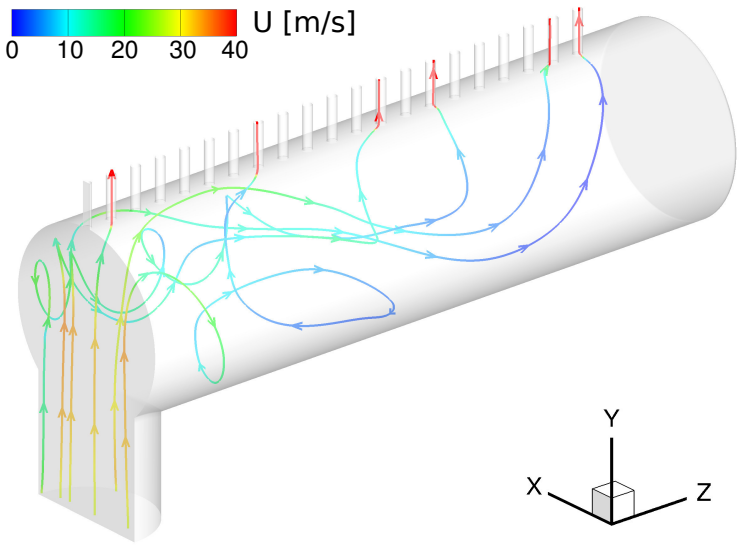

Figure 2.4: Streamlines colored by velocity magnitude, where values above $40\,\mathrm{m\,s^{-1}}$ are clipped.

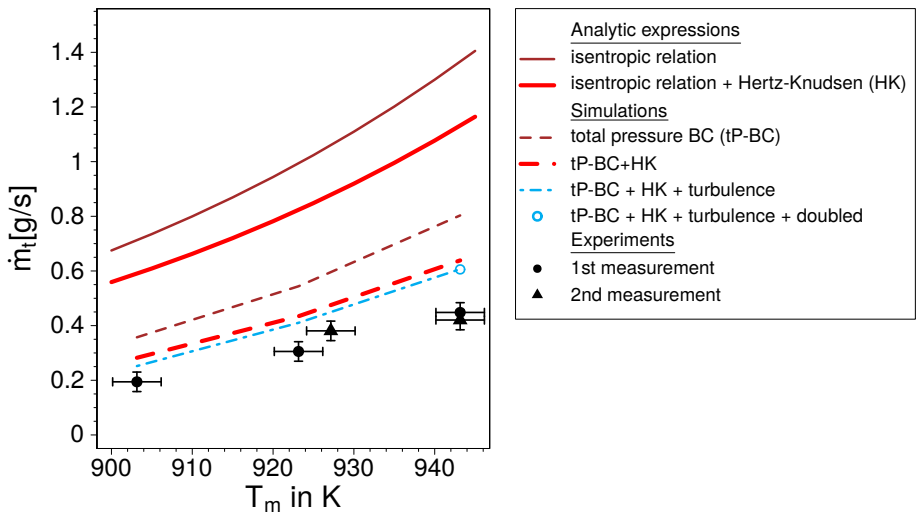

Figure 2.5: Mass flow rate over melt temperature: solid lines analytic expression, dashed lines simulations, black points measurements.

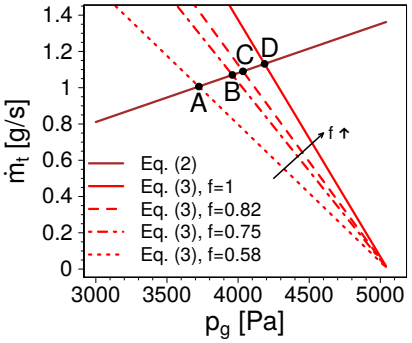

(a) Mass flow rate over the VDB gas pressure for the Hertz-Knudsen equation for several evaporation coefficients (Eq. (2.3)) and for the isentropic equation (Eq. (2.2)). The intersection points A, B, C, D correspond to Eq. (2.4).

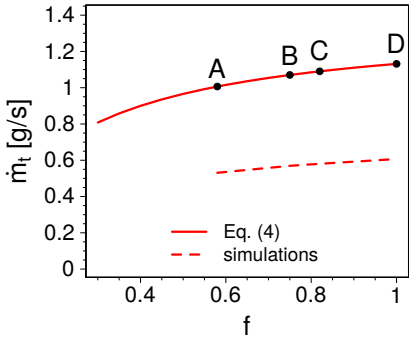

(b) Mass flow rate over evaporation coefficient f. The solid line denotes the analytic expression for the mass flow rate (Eq. (2.4)), the dashed line the simulated mass flow rate. The points A, B, C, D correspond to the intersection points in (a).

Figure 2.6: Influence of the evaporation coefficient on the mass flow rate modeling.

evaporation coefficient f would have to be as low as $f = 0.33$ in order for the numerical simulations to predict mass flow rates in agreement with the experimental data. Such an $f = 0.33$ value is much lower than reported experimental values. However, the experimental measurements of f were performed under process conditions ($T_m = 730 - 810\,\mathrm{K}$ and $p_g = 6 - 266\,\mathrm{Pa}$) that strongly deviate from those in the current PVD experiments. Moreover, the reported experimental values are for pure uncontaminated zinc. In the current experiments, dross was found to accumulate at the melt surface during the heat-up of the equipment and the run of the experiments. To further clarify this issue, an experimental evaluation under actual PVD process conditions may be required for a better estimate of f.

UNIFORMITY OF MASS FLOW

Fig. 2.7 shows the mass flow per nozzle. When connecting this to the pressure contour (Fig. 2.3), it is apparent that the mass flow rate is higher for the stagnation zone with a high pressure and low temperature compared to the sides of the VDB, where the pressure is lower and the temperature is higher (thus decreasing the density). The deviation in mass flux for different nozzles is approximately 8% for all cases, which is roughly the coating thickness variation in the experiments of 8 – 10%. However, the latter is in the same range as the inaccuracy of the measurement device.

2.4.3. OPTIMIZATION OF PROCESS CONDITIONS

ISENTROPIC OPTIMIZATION

For weak evaporation (i.e., small mass fluxes from the melt surface), the second term of

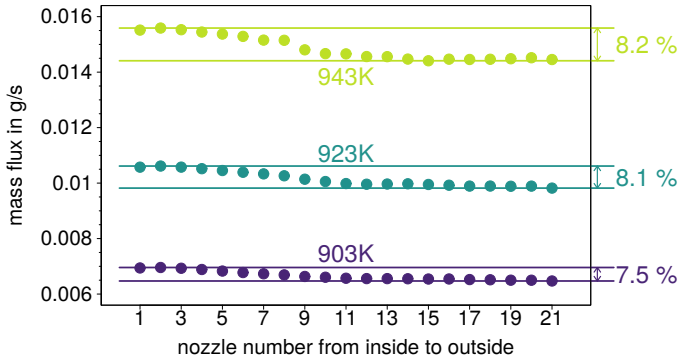

Figure 2.7: Mass flow rate per nozzle from simulations for different melt temperatures. The rate is given for the entire nozzle. The percentage on the right shows how much the maximum flow rate exceeds the minimum mass flow rate.

Table 2.4: Discharge coefficient $C_{dis} = \frac{\dot{m}_{actual}}{\dot{m}_{theoretical}}$, where the theoretical mass flow rate $\dot{m}_{theoretical}$ is from Eq. (2.4).

T_m	903 K	923 K	943 K
$C_{dis,sim}$	0.43	0.50	0.54
$C_{dis,exp}$	0.33	0.37	0.40

Eq. (2.5) is negligible and the mass flow rate is expected to vary proportionally to

$$\dot{m} \propto A_n \frac{p_t}{\sqrt{T_t}}, \tag{2.14}$$

where the total pressure p_t is approximately an exponential function of the melt temperature T_m, which is almost equal to the total temperature T_t at the VDB inlet. (It should be noted that while we used p_g and p_v to denote the total pressure at certain locations in section 2.3.1, here, we use the total pressure p_t to distinguish from the static pressure p which is required for the discussion of the flow dynamics as the dynamic pressure has to be taken into account.) Consequently, a higher melt temperature increases the term $\frac{p_t}{\sqrt{T_t}}$. Considering only this isentropic approximation, this leaves two options to increase the mass flow rate, a bigger critical nozzle outlet area A_n or a higher melt temperature T_m. However, both experiments and simulations show a much lower mass flow rate than the isentropic prediction. In the following subsection, we quantify the discharge efficiency and determine where the non-isentropic losses occur; we then describe the influence of the wall temperature and finally, explain why the discharge coefficient increases with the melt temperature.

NON-ISENTROPIC LOSSES

The discharge coefficient of the VDB, i.e. the ratio of the actual (experimental or simu-

Table 2.5: Total pressure and total temperature averaged across some z-planes.

	Total pressure p_t in Pa	Total temperature T_t in K
VDB inlet plane	4184	948
Nozzle inlet plane	4011	1144
Nozzle outlet plane	2796	1251

lated) discharge $\dot{m}_{actual}$ to the theoretical discharge $\dot{m}_{theoretical}$ (calculated by Eq. (2.5))

$$C_{dis} = \frac{\dot{m}_{actual}}{\dot{m}_{theoretical}},$$

is listed in table 2.4. For higher melt temperatures, the discharge coefficients increase for both the simulations and the experiments indicating a decline of non-isentropic effects. The total isentropic pressure p_t, which is the driving force, drops in the real process due to viscous and non-adiabatic losses, such as flow separation, turbulence or heating. This directly reduces the mass flow rate as can be seen in Eq. (2.14). The local total pressure (i.e., the pressure obtained by isentropically decelerating the flow to zero velocity) is calculated from the flow field as

$$p_t = p\left(1 + \frac{\gamma - 1}{2} Ma^2\right)^{\frac{\gamma}{\gamma - 1}}. \tag{2.15}$$

In addition, increases in total temperature reduce efficiency, though the total temperature has much less influence than the total pressure (refer to Eq. (2.14)). The total temperature is calculated from the flow field as

$$T_t = T\left(1 + \frac{\gamma - 1}{2} Ma^2\right). \tag{2.16}$$

Table 2.5 shows total pressure and total temperature averaged across certain z-planes to permit an estimation of the impact by different regions. Total pressure decreases by 4% between the VDB inlet and the nozzle inlet plane, but drops dramatically inside the nozzles by 30%. Total temperature rises by approximately 200 K between the VDB inlet and the inlet of the nozzles, inside the nozzles it only increases by approximately 100 K. If we use the values to compare the ratio $\frac{p_t}{\sqrt{T_t}}$ from the approximation in Eq. (2.14) at the nozzle outlet plane with the one at the VDB inlet plane, the estimated efficiency is 0.58, which is close to the actual simulated discharge coefficient of 0.54 (Table 2.5).
The losses — either due to a reduction in total pressure or an increase in total temperature — can be broken down into different contributions: (1) flow separation or turbulence in the VDB, (2) the viscous boundary layer in the nozzles and (3) the wall heating. The first two impact on the total pressure; the wall heating impacts both the total temperature and the total pressure. Since the pressure drop between the VDB inlet and nozzle inlet is small, we will not discuss (1) any further, but rather focus first on wall heating and then on the boundary layer.

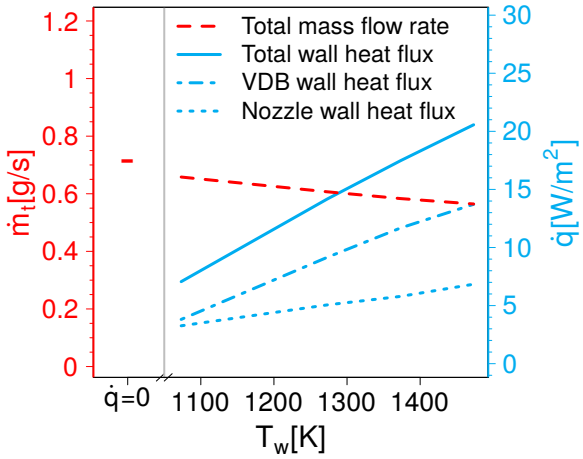

Figure 2.8: Mass flow rate and wall heat flux over wall temperature.

WALL HEATING

Wall heating is applied to prevent the metal vapor from condensing at the VDB walls. At the same time wall heating in compressible flow causes Rayleigh flow. This increases total temperature and reduces total pressure, both of which in turn lower the discharge coefficient.

Fig. 2.8 shows the total mass flow rate and the heat fluxes emerging from the VDB wall and the nozzle walls for different wall temperatures as well as for adiabatic walls. The introduced heat flux increases almost linearly with the wall temperature. The heat flux introduced by the VDB wall is approximately twice as high as that introduced inside the nozzles, in line with the 200 K temperature increase in the VDB versus 100 K in the nozzle, as listed in Table 2.5.

An increase in wall temperature by 100 K lowers the mass flow rate by approximately 4%. For the range under consideration, the relation is linear. Even adiabatic walls produce only a moderately higher mass flow. This indicates that other non-ideal effects, such as the viscous boundary layer in the nozzles, are responsible for the low discharge coefficient.

NON-ISENTROPIC LOSSES IN THE NOZZLE BOUNDARY LAYER

To determine the nozzle regions, where the drastic pressure drop occurs, Fig. 2.9 plots static pressure, total pressure, static temperature and total temperature across the nozzle diameter at the inlet, in the middle and at the outlet of the seventh nozzle. The (static) pressure is constant across and decreasing downwards of the nozzle, whereas the total pressure is at a constant high level in the inner core of the nozzle, but drops significantly next to the walls, which denotes losses due to both viscous effects and wall heating. The temperature drops in the core along the nozzle due to the transfer of heat to kinetic energy, while it tends towards the wall temperature directly next to the wall. The total temperature increases in the same near-wall region where the total pressure drops, while it stays nearly constant in the core. The increase in total temperature is caused by the

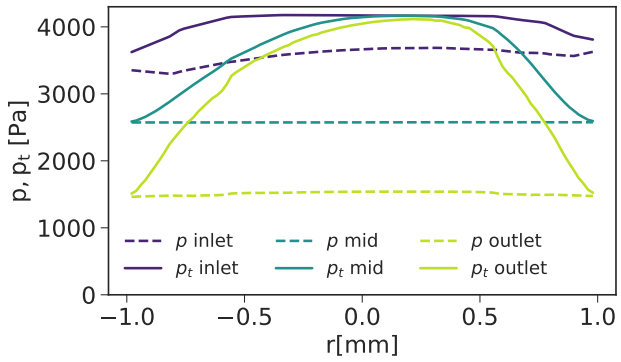

(a) Static pressure p and total pressure p_t.

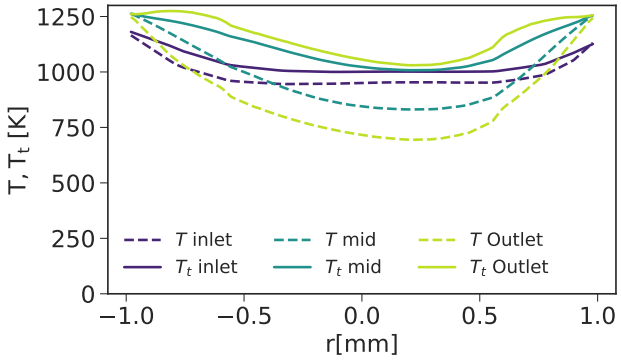

(b) Static temperature T and total temperature T_t.

Figure 2.9: Pressure and temperature profiles across the nozzle diameter at the inlet, half way downstream (mid) and outlet of the seventh nozzle.

Rayleigh flow only, whereas the observed pressure drop in the boundary layer can be accounted for by multiple phenomena: increased viscosity due to the high wall temperature, viscous dissipation, Rayleigh and Fanno effects. In the core of the nozzle flow these effects are negligible. It should be noted that due to the radial geometry the total impact is weighted by the radius, so that the pressure drop in the boundary layer has a large effect. This indicates that the easiest way to improve the mass flow discharge are bigger nozzle radii as the nozzle outlet area increases quadratically with nozzle radius, while the wall boundary increases only linearly. Another possibility would be shorter nozzles to reduce the boundary layer length and thickness. Design optimization of the nozzle shape (e.g., converging-diverging nozzles) may be another option, but the efficiency increase strongly depends on process conditions [92].

MELT TEMPERATURE

Earlier, we showed that the discharge coefficient increases with melt temperature. To analyze the influence of the melt temperature on non-isentropic losses in greater detail, Fig. 2.10 plots the Mach number for different melt temperatures as a function of the radius at the outlet of the seventh nozzle. As the nozzle inflow is not aligned with its axis, the profiles are asymmetric. The Mach number shows a plug profile with values above the speed of sound in the core region. However, the critical area (i.e., the area where $Ma > 1$) is significantly decreased by a substantial boundary layer (which we defined as the region where $Ma < 1$). The boundary layer for $T_m = 943\,\mathrm{K}$ matches the region of pressure loss in Fig. 2.9. Considering the radial geometry of the nozzle, the critical area is reduced by approximately a factor of four for a melt temperature of $T_m = 943\,\mathrm{K}$. For lower melt temperatures, the critical area is even smaller. A higher melt temperature produces a higher pressure in the VDB, which reduces the boundary layer thickness (in which the highest pressure drop appears) and expands the critical section, thus resulting in a higher discharge efficiency.
Hence it can be concluded, that a higher melt temperature improves the mass flow rate in two ways: The ideal isentropic mass flow rate increases and the non-isentropic losses become smaller.

2.5. CONCLUSIONS

A simulation model was developed to predict the total mass flux and mass flux uniformity in a continuous Physical Vapor Deposition apparatus. A crucial factor was the implementation of a new boundary condition, which considers the evaporation rate limitation by the Hertz-Knudsen relation. The simulations were validated by comparing the results with experiments and analytical approximations. The following conclusions can be drawn

1. For accurate modeling of continuous VDB processes:
    - The mass flow limitation by the Hertz-Knudsen boundary condition is crucial for predicting evaporating flows. However, the exact evaporation coefficient (within the range reported in the literature) is less decisive.
    - The influence of real gas models is negligible, the mass flow rate is not very sensitive to changes in viscosity.

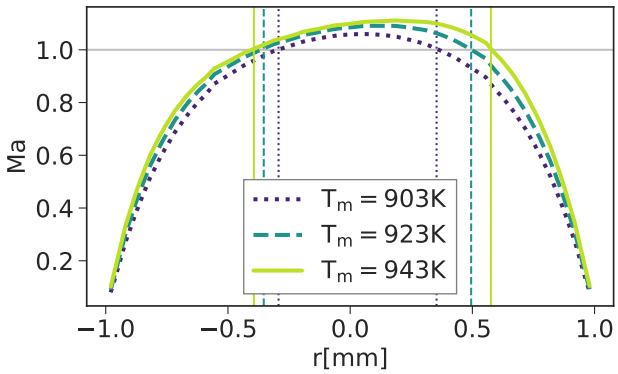

Figure 2.10: Mach number across the outlet of the seventh nozzle for different melt temperatures. The thin vertical lines mark the transition from sub- to supersonic flow.

- Despite the clear improvement in prediction quality, the computational results still overpredict the mass flow rate by approximately 30%. We suppose that either dross at the melt surface, which was detected subsequent to running the experiments, hampers the evaporation, or the evaporation coefficient considerably differs under the process conditions studied from that in the literature (due to different process conditions or melt contamination). To minimize these uncertainties, more measurements of the metal properties would be required.

2. For optimizing the continuous VDB processes:

   - The total mass flow rate depends mainly on melt temperature and nozzle geometry.
   - Since the flow is fast, the mass flow decrease due to wall heating is marginal.
   - For the device studied, the discharge efficiency (i.e., the ratio of actual to ideal mass flow rate) was low (0.33–0.4 in experiments and 0.43–0.54 in simulations). This is mainly due to the boundary layer within the nozzles. To increase the discharge efficiency the influence of the boundary layer has to be reduced (e.g., through shorter nozzles or a bigger nozzle radius). This, however, might impair nozzle-to-nozzle uniformity.
   - Higher melt temperatures and thus higher VDB pressures reduce the boundary layer thickness in the nozzles and result in a higher discharge coefficient.

3

THE INTERACTION OF PARALLEL AND INCLINED PLANAR RAREFIED SONIC PLUMES — FROM FREE MOLECULAR TO CONTINUUM REGIME

"Simple," said von Neumann. *"This can be solved by using the method of characteristics."*
"I am afraid I don't understand the method of characteristics."
"Young man, in mathematics you don't understand things. You just get used to them."

John von Neumann [1]

The interaction between rarefied vapor plumes can cause shocks and consequently distinct peaks in mass flux, which produce undesirable non-uniformities. To evaluate the impact of shock formation, we study pairs of interacting planar plumes, varying the degree of rarefaction and general geometric parameters, namely the nozzle-separation-distance and the mutual plume inclination. To consider the extremes of rarefaction, we give the analytic solution for free molecular flow, and simulate the inviscid continuum solution using an approximate Riemann solver. In the transitional flow regime, Direct Simulation Monte Carlo (DSMC) is applied. To detect the shock location, we make use of the Method of Characteristics. We conclude that, although the rarefied flow regime physically lies in between

Parts of this chapter have been published in Physics of Fluids, 33(8)[93].
[1] as paraphrased in Zukav, G. (2012). The dancing Wu Li masters: An overview of the new physics.[94], p.208

the free molecular and the inviscid continuum flow regimes, the peak value of mass flux in the transitional flow regime exceeds both the one of free molecular flow and the one of inviscid continuum flow (the latter by ≈ 10%). Rarefied flow exhibits a broader, but less strong secondary expansion after the shock than continuum flow. For planar jet interaction, the occurrence of the shock is rather insensitive to nozzle separation distance. Despite the intuitive expectation that inclining the plumes away from each other would lead to shock reduction and thus give a more uniform mass flux, the opposite is the case: Inclining the plumes towards each other leads to a stronger shock, but also to a stronger expansion, thus producing a more uniform mass flux with less stray mass fluxes.

3.1. INTRODUCTION

In recent years, clusters of rarefied vapor plumes (also sometimes called jets) have played an increasing role in both space and vacuum technology: The Reaction Control Systems of shuttle orbiters operate with multiple exhaust plumes. Micro satellites use plume clusters as well, and the number of launches has increased rapidly over the last decade [95]. Linear aerospike engines consisting of two planar plumes, which expand along the two sides of a spike and merge at the spike's end, are a promising rocket and micro-satellite thruster technology. This design of two interacting plumes can compensate for the decreasing atmospheric pressure and consequently suppress the increase in expansion at higher altitudes, allowing for single-stage-to-orbit space vehicles [96]. Recently, clusters of sonic zinc vapor plumes have been introduced as a novel technology to achieve a continuous Physical Vapor Deposition (PVD) apparatus for galvanizing steel [7, 97]. For all these technologies, the fluxes from the plumes are of importance. Shuttle orbiters operate next to space stations; the momentum flux and the heat flux from the exhaust plumes may cause damage when impinging on any sensitive structures, such as solar panels or optically-sensitive components [98, 99]. In coating technology, highly uniform coating is desirable which requires a uniform mass flux from the deposition plumes.

However, interacting plumes may cause a shock, which results in mass flow and temperature peaks around the interaction plane. The subsequent high-pressure region between the shocks leads to another expansion, called a 'secondary jet'. From the secondary jet a backflow may emerge, which for aerospikes and thrusters gives a pressure and heat load on the surface of the propelled space vehicle itself. In addition, recirculation in the interaction plane introduces viscous losses and may reduce efficiency of thrusters [100].

Single plumes are thoroughly studied due to their ubiquitous use as thrusters in aerospace [98, 101, 102]. Backflows appear for plume thrusters, especially for small Mach number, since then the expansion angle at the nozzle exit lip is obtuse and the flow is redirected towards the space vehicle. The resulting forces can disturb the space vehicle orientation and the heat flux and contamination may damage the vehicle's surface. Several researchers studied the backflow and suggested designs to minimize it [103–106]. Plume interaction may increase the backflow and the subsequent contamination of the space vehicle. Tools based on CFD, DSMC and approximations have been developed to predict the contamination, heat flux and disturbance forces due to plume impingement [107–110]. Recently extraterrestrial plumes were simulated and compared to their appearance in space [111–113].

Plume interaction has so far been much less studied. Since measurements in moderate or high vacuum conditions are difficult, only few experiments of plume interaction are reported in the literature, mainly considering space thrusters. Depending on process conditions, researchers found density peaks around the interaction plane [114, 115]. Some observed a small backflow [115]. To determine the occurrence of a shock and its strength under rarefied conditions, Koppenwallner [116] (as cited by Dagum et al. [117]) introduced the penetration Knudsen number Kn_p, as the ratio of the mean free path in the interaction plane and the path length between the interaction plane and the axis of the other plume. A few groups confirmed that the penetration Knudsen number is indeed a determining parameter for the occurrence of a shock under particular circum-

stances [118, 119]. However, Dagum and Zhu [117, 120] studied parallel plume interaction at different nozzle separation distances using the Direct Simulation Monte Carlo (DSMC) method and found that the penetration Knudsen number could not predict the shock impact on the flow field. For three interacting planar aluminium vapor plumes (aligned in one row), Venkattraman and Alexeenko [121] found that the deposition profile can be described by a superposition of the deposition of three single plumes at high Knudsen numbers, whereas at smaller Knudsen numbers the deviation due to the interaction peak is immense. Baby and Rajesh [122] studied jet interaction for two three-dimensional jets at a moderate pressure ratio ($r_p \approx 2500$–9500) and a background pressure of 5 Pa, which yields barrel shocks which inhibited the interaction between the jets. Although some simulations and experiments for specific designs and flow conditions were reported in the literature [123–125], a comprehensive evaluation of the sensitivity of the mass flux distribution to geometry and process conditions is missing. This knowledge is crucial for applications in propulsion systems, but also for coating technology, where non-uniformities caused by jet interaction deteriorate the product.

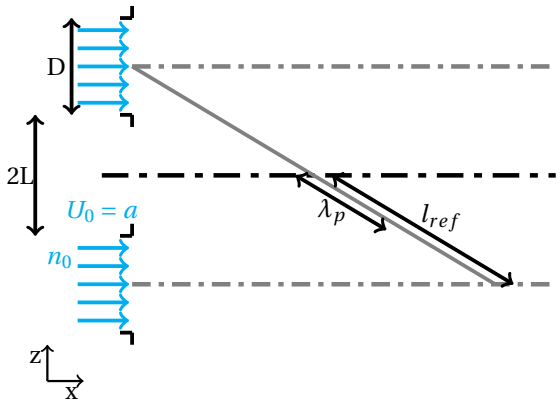

Figure 3.1: General flow setup: Plumes emerge from two inlets of length D at a nozzle separation distance $2L$. The domain extends infinitely in the third direction causing a planar problem. The penetration Knudsen number is defined as $Kn_p = \lambda_p / l_{ref}$.

To execute such a comprehensive evaluation, we study the onset, location and strength of the shock caused by two interacting planar sonic plumes of zinc vapor, as depicted in Figure 3.1, depending on geometry and process conditions, to make statements about the uniformity of mass flow at a most general level. The rarefaction ranges from the high Knudsen number free molecular to the low Knudsen number inviscid continuum flow limit.

In section 3.2, we introduce the solution methods, such as analytic equations for free molecular effusion flow, an approximate Riemann solver for inviscid continuum flow and Direct Simulation Monte Carlo (DSMC) for the transitional flow regime. The Methods section also describes the shock detection method, the far-field approximation and a discussion on the Penetration Knudsen number. The exact geometry, boundary conditions and thermophysical properties are discussed in section 3.3. In section 3.4, the flow fields for free molecular and continuum flow are compared to those for rarefied

flow. Afterwards, the shock location method is introduced and the effect of rarefaction on the shock location discussed. The shock location method is validated by analyzing the shock structure in relation to the detected shock location. To evaluate the influence of the shock on the mass flux distribution, mass flux profiles are compared for different degrees of rarefaction. Afterwards, shock location and line profiles are discussed for the other varied parameters, i.e., nozzle-separation distance and plume inclination. Finally, we compare the deposition uniformity for coating applications depending on these parameters.

3.2. METHODS

The phase density $f(\mathbf{r}, \mathbf{c}, t)$ describes the probability of finding a molecule at location $\mathbf{r}$ with velocity $\mathbf{c}$ at time t. The evolution of the phase density f is governed by the Boltzmann equation which, in the absence of body forces, reads as

$$\frac{\partial f(\boldsymbol{r},\boldsymbol{\xi},t)}{\partial t} + \boldsymbol{\xi} \cdot \nabla_{\boldsymbol{r}} f(\boldsymbol{r},\boldsymbol{\xi},t) = \left(\frac{\partial f(\boldsymbol{r},\boldsymbol{\xi},t)}{\partial t}\right)_{coll}, \tag{3.1}$$

where the left-hand side describes the convective transport and the right-hand side the collisions between particles. In section 3.2.1, only the left-hand side of Eqn. 3.1 is considered, giving us the collisionless or free molecular flow. In section 3.2.2, the local equilibrium case is described, which means that f in Eqn. 3.1 is replaced by the Maxwellian distribution f_0. Integrating the moments of this simplified equation over the velocity space leads to the Euler equations shown in section 3.2.2. For the steady-state Euler equations in the supersonic regime, the Method of Characteristics describes the flow field, which we used for the shock detection presented and which can be seen as the basis for approximate Riemann solvers. Section 3.2.3 describes how to solve Eqn. 3.1 for rarefied gases in the transition regime — where there are too many collisions to neglect the collision operator on the right-hand side, but too few to assume Maxwellian or Chapman-Enskog velocity distributions (which would yield the Euler and Navier-Stokes-Fourier equations, respectively). Section 3.2.4 sets out the far-field solution for the planar case (as the solutions given in the literature apply to a three-dimensional jet), which is used for the penetration Knudsen number described in section 3.2.5.

3.2.1. ANALYTIC COLLISIONLESS SOLUTION

The collisionless flow solution provides the extreme case of rarefaction as well as an insight into the non-equilibrium resulting from velocity sorting. The first analytical solution for free molecular flow from one slot was outlined by Knudsen [29] in 1909. He based his cosine law for the so called Knudsen cell on an equilibrium assumption and zero mean velocity at the slot outlet, which is not true for our case as the vacuum accelerates the flow and thus directs it along the jet axis, producing a higher density around the jet axis and a lower density far away from it. It was only in the 2000s that Cai and Boyd proposed an exact collisionless solution which includes both the spatial extension of the inlet and a non-zero inlet velocity [126]. We adapted their solution for a single straight jet to the two inclined jets by altering the integration domain and superposition, details are given in Appendix A.3.

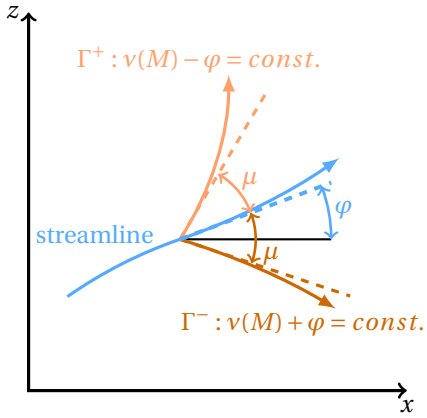

Figure 3.2: Schematic of characteristics.

3.2.2. CONTINUUM FLOW

Continuum flows are most commonly described by the Navier-Stokes-Fourier equations, which correspond to the first-order Chapman-Enskog approximation of the Boltzmann equation and include shear stress and heat flux. Yet for free expansions of supersonic plumes into vacuum, convective forces greatly surpass viscous forces (i.e., the Reynolds number tends to infinity, which yields a flow field similar to the inviscid limit) and no walls are present to form shear boundary layers. Since the velocity gradient is aligned with the flow direction in many parts of the flow field, the impact of shear stress is expected to be low. With the Prandtl number of gases $\approx 2/3$ being close to unity, also thermal conduction is expected to play a minor role in the energy equation compared to convection. Therefore viscous forces and conductive heat fluxes can be neglected in a first approximation (i.e., using a Maxwellian distribution instead of the first-order Chapman-Enskog expansion). The Navier-Stokes-Fourier equations then reduce to the Euler equations

$$\frac{\partial \rho}{\partial t} + \nabla \cdot (\rho \mathbf{u}) = 0, \tag{3.2}$$

$$\frac{\partial}{\partial t}(\rho \mathbf{u}) + \nabla \cdot (\rho \mathbf{u} \otimes \mathbf{u}) = -\nabla \bar{p}, \tag{3.3}$$

$$\frac{\partial}{\partial t}(\rho e) + \nabla \cdot \left[(\rho e + p)\mathbf{u}\right] = 0, \tag{3.4}$$

where the specific energy is $e = e_{int} + 0.5\mathbf{u}^2$ and the enthalpy is $h = e_{int} + p/\rho$ is used to calculate the temperature field. We close the equations by assuming a calorically perfect gas, i.e., $h = c_p T$ and $p/\rho = RT$.

METHOD OF CHARACTERISTICS

For purely supersonic flow, the Euler equations exhibit a hyperbolic behavior in space, which implies that information propagates in a wave-like manner. In a steady-state case as ours, the downstream solution depends only on the upstream solution and can be

deduced from it by using the Method of Characteristics (MOC). A proper derivation can be found in the book by Vos and Farokhi [127]; here we briefly sketch the underlying physics. In our case, the uniform inflow is homentropic and homenergetic, which according to Crocco's theorem entails that the flow field is irrotational [128]. This condition breaks inside the shock where the entropy increases and, consequently, the flow becomes rotational. The following qualitative visualization is confined to the planar, irrotational MOC and, strictly speaking, is therefore not applicable after the shock. The local velocity vector is sufficiently described by the local speed and flow direction expressed by the Mach number M and the flow angle φ. The local information propagates along the flow direction with the flow speed $a \cdot M$ and orthogonal to it with the speed of sound a. Therefore the domain of influence of each point is the Mach cone which expands around the streamline with the Mach angle

$$\mu = \sin^{-1}\left(\frac{1}{M}\right). \tag{3.5}$$

The left-running Γ^+- and right-running Γ^--characteristics span the Mach cone around the streamline as symmetry axis. Figure 3.2 sketches a streamline with the corresponding characteristics for one point. The Prandtl-Meyer function $\nu(M)$ indicates the angle, through which a sonic flow turns when it accelerates to a certain Mach number M greater than 1. A fluid element, which accelerates isentropically from Mach number M_1 to Mach number M_2, turns its direction by an angle $\nu(M_2) - \nu(M_1)$ (a compression proceeds inversely).
Along the characteristics Γ^+ and Γ^-, the following linear combinations of the flow angle and the Prandtl-Meyer-function are constant:

$$\nu - \varphi = \text{const. along } \Gamma^+ : \frac{dz}{dx} = \tan\left(\varphi + \mu\right), \tag{3.6}$$

$$\nu + \varphi = \text{const. along } \Gamma^- : \frac{dz}{dx} = \tan\left(\varphi - \mu\right), \tag{3.7}$$

where φ depends on the location as well as ν and μ, which are functions of the local Mach number.
Figure 3.3 shows the MOC solution for a sonic plume and a qualitative sketch of how the plume interaction modifies the solution (the non-isentropic process across the shock complicates a completely analytic solution and the presence of the subsonic region suppresses it entirely (see Zucrow on backward-facing step [129])). At the corners of the inlet, expansion fans arise, depicted by the characteristics emerging from the corners and spreading into the domain. The flow turns outward towards the vacuum and accelerates. It changes when crossing one of the depicted expansion fan lines, whereas within each of the polygons depicted in Figure 3.3, the Mach number and flow direction as well as density, pressure and temperature are approximated to be homogeneous (finer spatial discretization, i.e., more expansion fan lines emerging from the inlet corners, tends towards the correct solution). The flow direction is along the half angle between the Γ^+- and Γ^--characteristics and exemplary depicted by vectors in blue. In the core of the plume, the interaction of the characteristics deflects them, but their expansion character remains, i.e., the characteristics are diverging downstream. Due to the presence of an

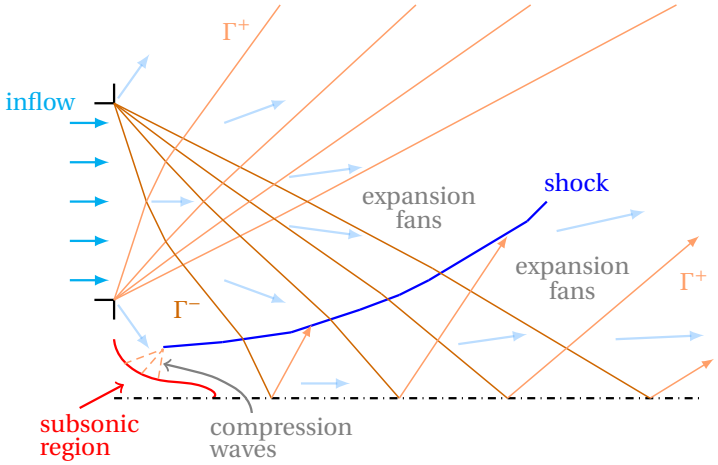

Figure 3.3: Qualitative sketch of plume interaction explained by Method of Characteristics. Expansion fans emerge from the inlet corners. The interaction between the flow and the subsonic region causes compression waves which induce a shock. The characteristics from the expansion bend when crossing the shock and get reflected at the symmetry.

identical second plume next to the first one in our problem, the case is symmetric. At the symmetry axis, the velocity normal to it has to be zero, and on the left side, immediately after the inlets, the velocity aligned with the symmetry axis is small, which results in a subsonic region. The flow from the expansion fan impinges on the concave part of the subsonic region causing compression waves which in turn induce a shock. Both the compression waves and the shock run along Γ^+-characteristics. The shock propagates through the velocity field. While around the subsonic region, the incoming flow is nearly orthogonal to the shock producing a (nearly) normal shock, further downstream the incoming flow has a significant tangential component to the shock resulting in an oblique shock. When crossing the shock, the Γ^--characteristics slightly bend towards the symmetry axis, where they are reflected and hit the shock a second time from its downstream side. Since the characteristics remain expansion waves both after crossing the shock and after the reflection at the symmetry, they bend the shock away from the symmetry axis [130].

Except for the subsonic region, the entire flow field is described by the Mach number M and the flow angle φ. The inviscid Euler solution is thus independent of the temperature and density (which can be deduced along the streamlines using isentropic relations), so that — except for a change in the shape of the subsonic region depending on density — the inviscid continuum flow field depends only on the nozzle separation distance and inclination.

DETECTION OF SHOCKS AND CHARACTERISTICS

Commonly, shocks are identified as regions with a high density of pressure isolines or with a pressure gradient magnitude above a specified value. However, the rapid expansions in the problem under consideration give rise to high pressure gradients before the

shock and consequently strongly varying shock strength along the shock (we use the common shock strength definition as the pre- to post-shock pressure ratio). This complicates shock detection based on the pressure field. A further obstacle is finite shock thickness, as a shock extends over several mean free paths ($\mathcal{O}(10)$) and the mean free path in rarefied flow is long [131]. Kanamori and Suzuki [132, 133] proposed to detect the shocks as a singularity in the characteristics field given by the local unit vectors in the direction $\mathrm{d}z/\mathrm{d}x$ from Eqns. 3.6 and 3.7. As shown in Section 3.2.2, the compression waves, which are $\mathbf{\Gamma}^+$-characteristics inclined towards each other, merge forming the shock. Anticipating the characteristics presented in Figure 3.8, we see that also other $\mathbf{\Gamma}^+$-characteristics inciding on the shock, merge with it, producing a local sink in the $\mathbf{\Gamma}^+$-field. Thus, a strong divergence in the $\mathbf{\Gamma}^+$-field indicates a shock. The broader shock in the transitional flow regime make the algorithm by Kanamori and Suzuki more difficult to apply. This is why, we base our implementation only loosely on their approach.
First, the deformation gradient tensor of the $\mathbf{\Gamma}^+$-field is calculated in all supersonic regions. Then the region with negative divergence of the $\mathbf{\Gamma}^+$-field, i.e., the sink, is extracted. From this subset, we extract regions where the deformation gradient tensor of $\mathbf{\Gamma}^+$ projected into the flow direction is negative. This second clipping is necessary, to exclude regions in which the divergence is negative due a gradient orthogonal to the streamlines (which occurs abundantly around the point where the sonic line cuts the symmetry) rather than along the streamlines. From this shock region, a shock line is derived by quartic regression weighted with the magnitude of the divergence of the $\mathbf{\Gamma}^+$-field. The shock strength — and with it the magnitude of the divergence of the $\mathbf{\Gamma}^+$-field — varies rapidly along the shock, since the incoming flow is highly non-homogeneous due to the upstream expansion. To account for this variation in weights, the weights were binned based on the x-coordinate and normalized per bin. This yields the following algorithm:

1. Calculate $\mathbf{\Gamma}^+$-characteristics vector field:
$$\mathbf{\Gamma}^+(\boldsymbol{r}) = \begin{bmatrix} \cos(\phi(\boldsymbol{r}) + \mu(\boldsymbol{r})) \\ \sin(\phi(\boldsymbol{r}) + \mu(\boldsymbol{r})) \end{bmatrix} \tag{3.8}$$
2. Calculate $\boldsymbol{F} = \nabla\mathbf{\Gamma}^+$ for regions where $M \geq 1$.
3. Extract $\mathrm{tr}(\boldsymbol{F}) = \nabla \cdot \mathbf{\Gamma}^+ < 0$.
4. Extract from this the subset $\hat{\mathbf{u}} \cdot (\boldsymbol{F}\hat{\mathbf{u}}) < 0$ as the shock region (where $\hat{\mathbf{u}}$ denotes the unit vector in flow direction).
5. Set the weight to $w = |(\mathrm{tr}(\boldsymbol{F}))| \cdot V_c$, where V_c is the cell volume.
6. Bin data per x-coordinate and normalize in each bin i the weights by dividing by the maximum weight, i.e.
$$\hat{w}_{i,j} = \frac{w_{i,j}}{\max\limits_{\text{j in bin i}} (w_{i,j})}$$
7. Determine shock line as quartic polynomial regression of z over x weighted with $\hat{w}_{i,j}$.

For shock detection in general, this procedure should be repeated for the Γ^--characteristics.

RIEMANN SOLVER

The Euler equations can be solved by using a conservative method called approximate Riemann solver, in which Eqns. 3.2, 3.3, 3.4 are locally diagonalized and split into ordinary differential equations for the fluxes. At each face in a finite volume mesh, the flux is calculated by solving local Riemann problems. An approximate Riemann solver (i.e., dbnsFoam of foam-extend 4.0 [134]) with the HLLC scheme [135] is used to calculate the inviscid continuum mechanical solution of the flow field. While approximate Riemann solvers can accurately solve supersonic regions, they possibly give rise to spurious wave modes in the subsonic region [136], which in the considered flow is the zone between the two jet inlets. A first-order HLLC flux construction was applied to avoid these spurious waves [137]. The temporal discretization is conducted by a fourth-order Runge-Kutta integration, which is explicit and therefore required small time steps to maintain numerical stability. A constant time step was chosen, so that the Courant-Friedrichs-Lewy number was below 0.3. A solver verification for a shock tube case is presented in Appendix A.4.

3.2.3. TRANSITIONAL FLOW REGIME

In the last decade, multiscale methods have been developed which give promising results at low computational effort for simple rarefied flows, such as the unified gas kinetic scheme [138, 139], discrete unified gas kinetic scheme (DUGKS) [140–142], kinetic relaxation models [143, 144] and the general synthetic iterative scheme [145]. Still, the simultaneously ongoing improvements of its algorithm [146] and its inherent numerical stability keep Direct Simulation Monte Carlo (DSMC) [34] the method of choice for accurate predictions of complex rarefied flows. Therefore, we applied it to study the plume interaction in the transitional flow regime between the two extreme cases of no collisions and local equilibrium. In DSMC, the gas is modelled by the movement and collision of molecules, represented as purely repulsive particles. The particle movement and collisions are decoupled — which mitigates the time step requirement as collisions do not have to be detected during the particle movement. After the movement, the particles are sorted into cells and collide randomly with other particles from the cell. Only the number density in the cell and relative velocity between particle pairs, but not their exact location, determine the collision probability. To further speed up the simulation, one simulation particle represents a large number of real molecules. To obtain accurate results despite these simplifications, the cell size has to be below $1/3\lambda$, the time step size below $1/10\tau$ and the number of particles per cell above 20 (to ensure enough collision partners) [34]. We fulfilled the listed resolution criteria in the entire flow field, except for the number of particles in the 'blind spot' by which we denote a small region above the inlet with an extremely low number density, so that collisions are improbable.
We used the dsmcFoam+ solver which is part of OpenFoam-2.4-MNF [147]. The collision partners were selected using the No-Time-Counter model. The collisions were calculated using the Variable-Hard-Sphere model.

3.2.4. FAR-FIELD SOLUTION

The far-field solution approximates the number density for continuum flow. It assumes a point source and a decrease of density proportional to the inverse of the distance in

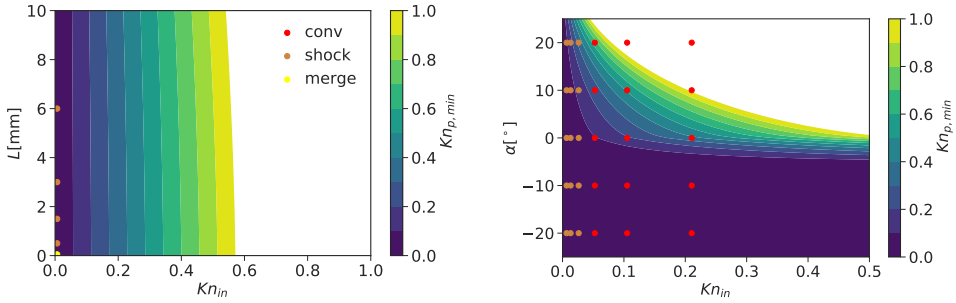

(a) $Kn_{p,min}$ depending on inlet-to-inlet distance L. (b) $Kn_{p,min}$ depending on inlet inclination α.

Figure 3.4: Minimum penetration Knudsen number maps (clipped to values below unity); (a) over Kn_{in} and L, (b) over Kn_{in} and α. Simulated cases are marked by points whose color indicates whether a shock ('shock') or only a region of converging Γ^+-characteristics ('conv') could be detected or whether the plumes merge ('merge').

radial direction for the two-dimensional case. Hence, in the far-field of a single plume, a self-similar azimuthal density distribution can be assumed. The density distribution can thus be split into a radial and azimuthal function

$$\frac{n(r,\Theta)}{n^*} = A\frac{R^*}{r}g(\Theta)\,, \tag{3.9}$$

where A is an integration constant and $R^* = D/2$. For outlet velocities above zero — which will occur due to the high pressure ratio between tank and vacuum — the flow does not spread in all directions at the outlet, but is constrained by the maximum turning angle Θ_{max}. Boynton fitted an azimuthal function to numerical solutions for a three-dimensional plume [148], which was afterwards commonly used. To adapt it for the two-dimensional case, the square-root of this function is considered which reads

$$g(\Theta) = \left[\cos\left(\frac{\pi}{2}\frac{\Theta}{\Theta_{max}}\right)\right]^{\frac{1}{\gamma-1}}\,, \tag{3.10}$$

where for a sonic outlet velocity, as we consider here, the two-dimensional Prandtl-Meyer expansion (PME) defines the maximum turning angle Θ_{max} and maximum velocity U_{max} which read

$$\Theta_{max} = \frac{\pi}{2}\left(\sqrt{\frac{\gamma+1}{\gamma-1}}-1\right), \tag{3.11}$$

$$U_{max} = \sqrt{\frac{\gamma+1}{\gamma-1}}U^*\,. \tag{3.12}$$

To ensure the mass flux conservation, A is determined by balancing the flux from the orifice with the mass flux integrated over the sphere of a certain radius r_c:

$$n^*U^*2R^* = 2\int_0^{\Theta_{max}} n^*U_{max}\frac{R^*}{r_c}Ag(\Theta)\,r_c\,\mathrm{d}\Theta\,, \tag{3.13}$$

which gives

$$A = \frac{U^* / U_{max}}{\int_0^{\Theta_{max}} g(\Theta)\, \mathrm{d}\Theta}, \tag{3.14}$$

which yields $A = 0.572$ for monatomic gas. The approximation tends to be incorrect near the inlet. In addition, the maximum velocity is based on the maximum velocity in a Prandtl-Meyer expansion, but considering that in a free expansion flow all thermal energy is expected to be transferred to kinetic energy, a maximum velocity of $u_{max} = \sqrt{2 c_p T_s}$ would be another reasonable estimate.

3.2.5. PENETRATION KNUDSEN NUMBER

To classify the strength of interaction, Koppenwallner [116] (as cited by Dagum et al. [117]) introduced the penetration Knudsen number Kn_p as

$$Kn_p(x) = \frac{\lambda_p(x)}{l_{ref}(x)}, \tag{3.15}$$

where λ_p is the mean free path at a position on the symmetry line based on the number density of the far-field solution, and l_{ref} the distance a particle could theoretically penetrate into the other jet from this symmetry line position (see also Fig.2.1). Koppenwallner assumed that the lowest penetration Knudsen number $Kn_{p,min}$ is appropriate to classify plume interaction into four different regimes: 1. For a very high minimum penetration Knudsen number, a free molecular flow occurs and consequently, penetration of molecules from one jet into the other jet; 2. if the mean free path is of the order of the characteristic flow length, collisions between the molecules of the two jets deflect their paths; 3. a further decrease of the penetration Knudsen number ($Kn_{p,min} < 0.2$) yields diffuse shocks slightly before the symmetry plane; after the shock, the flow direction of the molecules nearly aligns with the primary jet axis; 4. for very small Knudsen numbers ($Kn_{p,min} < 0.02$), a back flow may appear, which could interact with the upstream wall. Other research groups [117–120] used this definition to classify the interaction of plumes: Li and Ladeinde[119] tried to improve the definition by replacing the mean free path based on the number density only, by the one which accounts for the high relative velocity between the two jets. Holz et al. [118] studied the plume interaction experimentally and confirmed the appropriateness of penetration Knudsen number, which was, however, the more extreme case of $Kn_{p,min} = 0.045$.

Figure 3.4a depicts the minimum penetration Knudsen number $Kn_{p,min}$ map as a function of the inlet Knudsen number Kn_0 and the distance of the inlets for parallel jets. With an increasing inlet Knudsen number the minimum penetration Knudsen number increases proportionally (the proportionality factor is greater than unity). A higher distance between the jets increases the minimum penetration Knudsen number only marginally, which makes sense considering the estimations $\lambda_p \propto 1/n \propto r$ and $l_{ref} \propto r$ for the two-dimensional case. Figure 3.4b depicts the minimum penetration Knudsen number $Kn_{p,min}$ map as a function of the inlet Knudsen number Kn_0 and the inclination of the inlet streams for a constant inter-jet-distance $l = D/2$ (note, that l_{ref} does

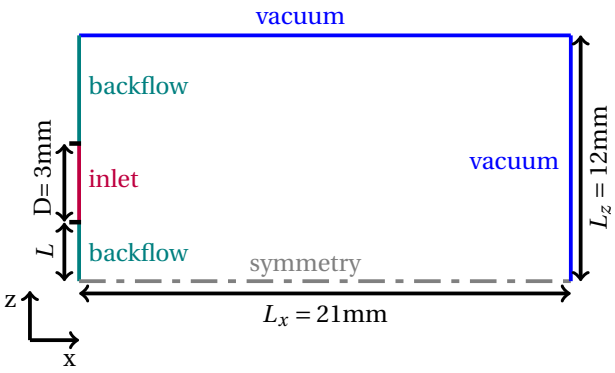

Figure 3.5: Geometry and boundary conditions for the DSMC simulation.

not only depend on the position of the symmetry line, but also on the jet inclination). When inclining the plumes towards each other — such as in a linear aerospike engine —, the penetration Knudsen number is below $Kn_{p,min} = 0.2$ even for high inlet Knudsen numbers, predicting a shock. For plumes inclined away from each other, the penetration Knudsen number rises rapidly, which makes it promising for avoiding shocks and the involved non-uniformities, e.g., in coating deposition.

3.3. CASE SETUP

DSMC Boundary Conditions

The computational domain and boundary conditions for the DSMC simulation are shown in Figure 3.5. To reduce the computational cost, only half of the domain is simulated using the symmetry in the interaction plane to split the domain. The computational domain is of size $L_x = 21\,\text{mm}$ and $L_z = 12\,\text{mm}$; the inlet of length $D = 3\,\text{mm}$ is positioned at distance L from the symmetry plane, so that $2L$ is the nozzle separation distance.
The assumed stagnation conditions, i.e., the conditions which are in the reservoir upstream the inlet in an experimental setup, are $T_s = 800\text{K}$ and varying values for n_s. The sonic inlet conditions are calculated by applying isentropic 1-D relations [73]

$$n^* = n_s \left(\frac{\gamma+1}{2} \right)^{\frac{-1}{\gamma-1}}, \tag{3.16}$$

$$T^* = T_s \left(\frac{\gamma+1}{2} \right)^{-1}, \tag{3.17}$$

which —with a specific heat ratio $\gamma = 5/3$ and molecular mass $m = 65.38\,\text{u}$ for zinc — yield an inlet temperature $T_{in} = T^* = 600\,\text{K}$ and an inlet velocity of $u_{in} = a(T^*) = \sqrt{\gamma k_B T^*/m} = 356.56\,\text{m s}^{-1}$. All other boundaries (except for the symmetry) have a vacuum outlet condition for DSMC, i.e., particles are removed from the simulation upon impingement. At the symmetry plane, inciding particles are specularly reflected. Likewise, the walls in the third homogeneous direction of our two-dimensional problem are specularly reflecting.

Table 3.1: Boundary conditions.

	DSMC	approximate Riemann solver		
		velocity	pressure	temperature
inlet	n_{in} drawn from Maxwellian with $T_{in} = 600\text{K}$, $u_{in} = 356.56\text{m}\,\text{s}^{-1}$	$u_{in} = 356.56\text{m}\,\text{s}^{-1}$	p_{in}	$T_{in} = 600\text{K}$
vacuum	delete particles	zero gradient	wave transmissive $p_o = 10^{-5}\text{Pa}$ at far distance $l_{inf} = 0.01\text{m}$	zero gradient
back flow	delete particles	if outlet: zero gradient if inlet: $u = \mathbf{0}$	if outlet: $p_o = 10^{-5}\text{Pa}$ if inlet: zero gradient	zero gradient
symmetry	reflect particles	symmetry	zero gradient	zero gradient

Riemann Solver Boundary Conditions

For the approximate Riemann solver, the outlet is split into a vacuum and a backflow boundary. The supersonic outflow at the vacuum may give rise to numerical shocks possibly distorting the upstream flow field. Hence, a wave-transmissive outlet boundary condition is applied at the vacuum outlets [91]. To stabilize the solution process, the backflow boundary condition was closed during the initialization. In the final solution, the backflow boundary condition distinguishes between outflow and inflow: for outflow, a pressure outlet $p_o = 10^{-5}\text{Pa}$ and zero velocity gradient are applied; for inflow, a zero pressure gradient and a zero convective velocity. (The density field is calculated from the ideal gas law.) An overview of the boundary conditions is given in Table 3.1. The discretization and a mesh independence study are presented in Appendix A.5.

Zinc Vapor Properties

As the intended main application is Physical Vapor Deposition, all simulations were conducted for zinc. As the viscosity of zinc vapor has not been studied yet, we applied the inverse-power-law approximation described by Fan et al. [8] to approximate the collisional properties. We chose potassium as reference metal which is in the same group as zinc and whose viscosity is reported in the literature [149]. The approximated Variable-Hardsphere collisional diameter of zinc is $5.684 \cdot 10^{-10}\,\text{m}$ and the viscosity parameter $\omega = 0.849$ at a reference temperature of $T_{ref} = 2000\,\text{K}$. The mass of the zinc molecule is set to $65.38\,\text{u}$. For the approximate Riemann solver, only the specific heat at constant pressure is required (as the inviscid equations are calculated), which is for zinc $c_p = 317.901\,\text{J}\,\text{kg}^{-1}\,\text{K}^{-1}$.

Table 3.2: Variation parameters: rarefaction Kn_s and corresponding inlet condictions, nozzle separation distance L, inlet inclination α. (p_{in} is only listed for cases which were calculated with the approximate Riemann solver.)

Kn_s	Kn_{in}	$n_{in}\left[\frac{10^{20}}{\mathrm{m}^3}\right]$	p_{in} [Pa]	L	α
$Kn_0 = 0.0047$	0.0066	232.09	192.264	$D/60$	$-20°$
$2Kn_0 = 0.0095$	0.0132	116.05	96.132	$D/6$	$-10°$
$4Kn_0 = 0.0189$	0.0263	58.02	–	$D/2$	$0°$
$8Kn_0 = 0.0378$	0.0526	29.01	24.033	D	$10°$
$16Kn_0 = 0.0756$	0.1052	14.51	–	$2D$	$20°$
$32Kn_0 = 0.1512$	0.2105	7.26	–		
$64Kn_0 = 0.3024$	0.4209	3.63	–		

3.3.1. PARAMETER VARIATION

The stagnation Knudsen number, describes the rarefaction in the pressure tank upstream of the inlet, which is required to compare to experiments, and reads $Kn_s = \lambda_s / D$, where D is the inlet width and λ_s the Variable-Hard-Sphere mean free path at the inlet, which is

$$\lambda_s = \left(\sqrt{2} \pi n_s d_{ref}^2 \left(\frac{T_{ref}}{T} \right)^{(\omega - 1/2)} \right)^{-1} . \tag{3.18}$$

For easier reference, the cases are addressed as a multiple of the smallest Knudsen number Kn_0. For the present simulations, which start at the inlet, it makes more sense to use the inlet Knudsen number $Kn_{in} = \lambda_{in}/D$. Kn_s can be converted into Kn_{in} using the isentropic relations in Eqns. 3.16, 3.17 and 3.18, which yields

$$Kn_{in} = Kn_s \left(\frac{\gamma + 1}{2} \right)^{\frac{1}{\gamma - 1} + \frac{1}{2} - \omega} . \tag{3.19}$$

The rarefaction, distance between the jets and their inclination away from one another were varied according to Table 3.2. In Figure 3.4, the different cases are marked by dots to illustrate the link to the penetration Knudsen number.

3.4. RESULTS AND DISCUSSION

In the first section of the results, the flow field for collisionless flow is presented for two parallel plumes and the analytical solution is verified (subsection 3.4.1), followed by the flow field of the Euler equations compared with a rarefied flow field (subsection 3.4.2). Section 3.4.3 shows the characteristics and shock detection for different degrees of rarefaction to visualize the impact of rarefaction on the shock location and understand the flow from another perspective. The last part focuses on the practical application: A comparison of estimated deposition profiles with the DSMC solution (subsection 3.4.4), an

analysis of the impact of nozzle separation distance and tilting on the shock location and deposition (sections 3.4.5, 3.4.6), and eventually a discussion of the non-uniformity of the mass flux (subsection 3.4.7).

3.4.1. COLLISIONLESS FLOW FIELD

Figure 3.6 shows the contours for various flow properties of the collisionless flow ($Kn_s \rightarrow$

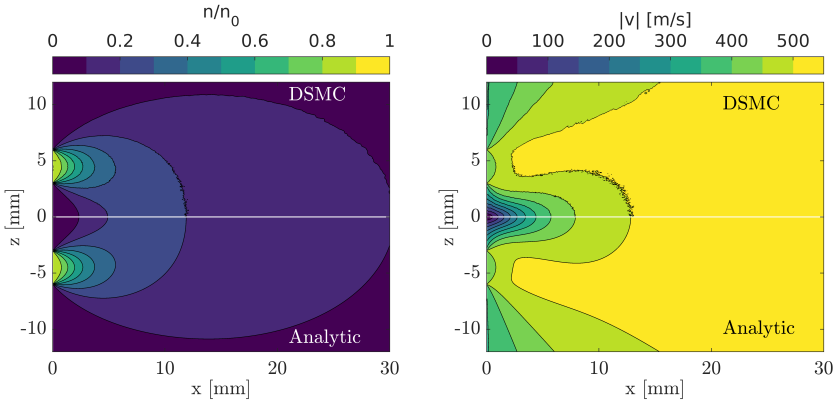

(a) Density

(b) Velocity magnitude

(c) Temperature

(d) Mach number

Figure 3.6: Flow field contours of collisionless flow ($Kn_s \rightarrow \infty$) for two parallel ($\alpha = 0°$) plumes at a nozzle-separation-distance $L = D$; (a) density, (b) velocity magnitude, (c) temperature and (d) Mach number. The upper half shows the DSMC solution and the lower half the analytic solution.

∞) for two parallel jets ($\alpha = 0°$) at a nozzle-separation-distance $L = D$. The collisionless DSMC is shown in the upper half and the analytic solution in the lower. They agree well in most regions. In the "blind spot" and far from the inlets, statistical noise begins to show in the DSMC solution due to the small sample size in these highly rarefied regions. The density normalized by the inlet density decreases behind the outlets (Figure 3.6a).

Around the symmetry plane, the superposition of the plumes produces an increased density. The velocity magnitude, shown in Figure 3.6b, increases downstream of the inlets due to "sorting" of the particles according to their velocity: While initially directed in several directions, particles align with the mean velocity the farther they travel away from the inlet. Therefore, the particles' velocities contribute increasingly to the mean velocity and decreasingly to the temperature. However, between the plumes the two fluxes from the inlets are counter-directed and the mean velocity cancels out yielding a low velocity region. The velocity sorting produces a low temperature in regions of high alignment between the particles' velocities and the mean velocity, e.g., in the expansions, as shown in Figure 3.6c. Between the two plumes, where the mean velocity cancels out, the immense relative velocities give a huge variance of particle velocities, and consequently a high temperature — even higher than at the inlet. The Mach number, shown in Figure 3.6d, depends strongly on the sorting of velocities, since both the velocity and the speed of sound ($a \propto \sqrt{T}$) are affected. The Mach number increases in the far-field to a value around $M = 1.8$. In the near-field of the flow, where a low velocity and high temperature prevail, a subsonic region occurs around the symmetry plane.

3.4.2. CONTINUUM FLOW AND TRANSITIONAL FLOW REGIME

The upper half of Figure 3.7 shows the flow field of two interacting plumes at $Kn_S = 2Kn_0$ ($L = D$, $\alpha = 0°$) solved by the approximate Riemann solver for the inviscid Euler equations. As in the collisionless case, the flow expands downstream from the inlet. Density, temperature and pressure decrease, whereas the velocity increases with increasing distance from the inlet. The isolines form ellipses, that are symmetric about the jet axis, which implies that the primary expansion is well protected against any influence from the other jet. The temperature drops to a lower level than for collisionless flow, tending towards zero; and the velocity rises higher, with values above $U = 600\,\mathrm{m\,s^{-1}}$. Both phenomena are caused by an expansion which is not diffuse as in the collisionless case, but directed by the pressure gradient which in the presence of collisions efficiently transforms thermal energy into kinetic energy. Please note that thermal energy is also transferred from the homogeneous direction (i.e., here the y-direction) into kinetic energy in the planar flow plane thus enhancing the acceleration, which is impossible in collisionless flow. Around the symmetry plane a sharp discontinuity occurs for all flow variables. Density and temperature rise, the velocity drops. The discontinuity traverses through the entire flow field in a shape similar to a Laval nozzle. The flow variable extrema in the inter-shock region are close to the "throat" (i.e., the narrowest section), and from there they mitigate in both directions, i.e., in the back flow and the so-called secondary expansion. The temperature values are highest next to the symmetry plane, which increases the pressure; this in turn will keep the number density in the center of the inter-shock region lower than near the shocks.

The lower half of Figure 3.7 shows the flow field of same two interacting plumes ($L = D, \alpha = 0°$, $Kn_S = 2Kn_0$) solved by DSMC. The flow exhibits a higher similarity with the continuum case in the upper half of Figure 3.7 than the collisionless case (Figure 3.6), since its rarefaction is low. However, the shielding of the shock does not hold anymore, and the high number density of the inter-shock region diffuses into the primary expansion. The increase in velocity and decrease in temperature are mitigated, as missing

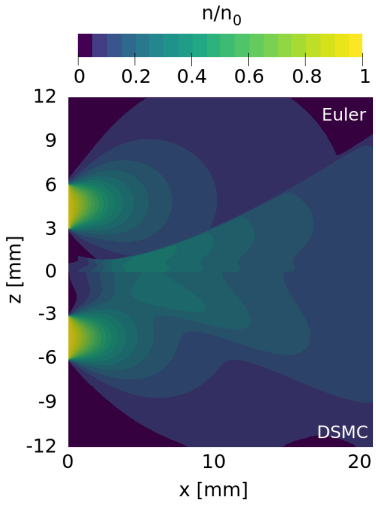

(a) Density.

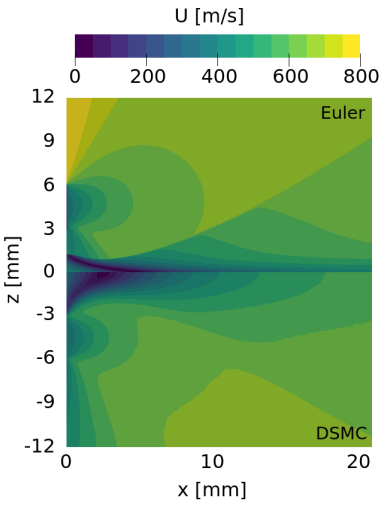

(b) Velocity magnitude.

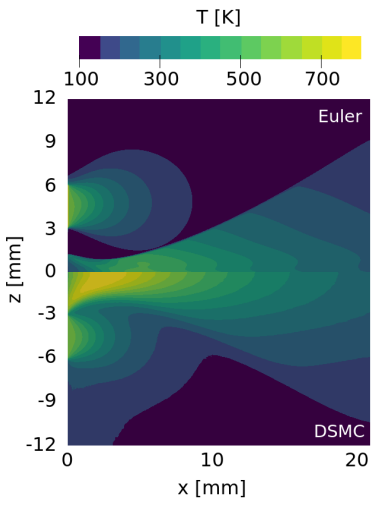

(c) Temperature.

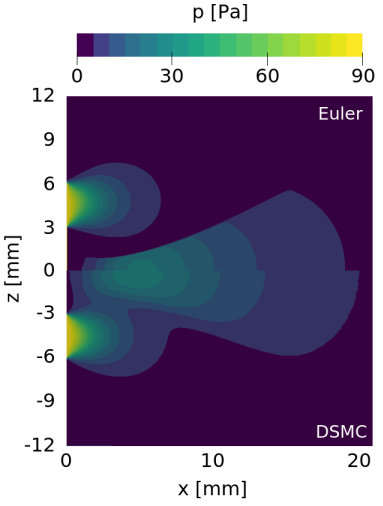

(d) Pressure.

Figure 3.7: Flow field contours of two parallel $\alpha = 0°$ interacting plumes at a nozzle-separation-distance $L = D$ for a stagnation Knudsen number of $Kn_s = 2Kn_0$; (a) density, (b) velocity magnitude, (c) temperature and (d) pressure.

collisions imply less efficient transfer of thermal energy to macroscopic kinetic energy. This entails a delayed expansion as can be observed in the velocity contours. In the inter-shock region, the temperature exceeds both the collisionless and the continuum flow. While the shock — typical of low rarefaction — accumulates the energy behind the shock, the diffuse behavior due to rarefaction keeps more energy in the thermal than in

the macroscopic kinetic mode. The higher temperature increases the effect of keeping the number density around the symmetry plane lower than directly behind the shocks. The shock location — which for continuum flow was obvious and consistent between all contours — is not clearly determinable for the rarefied solution, which is why we use the MOC to identify the shock location in the next section.

3.4.3. VISUALIZATION BY METHOD OF CHARACTERISTICS

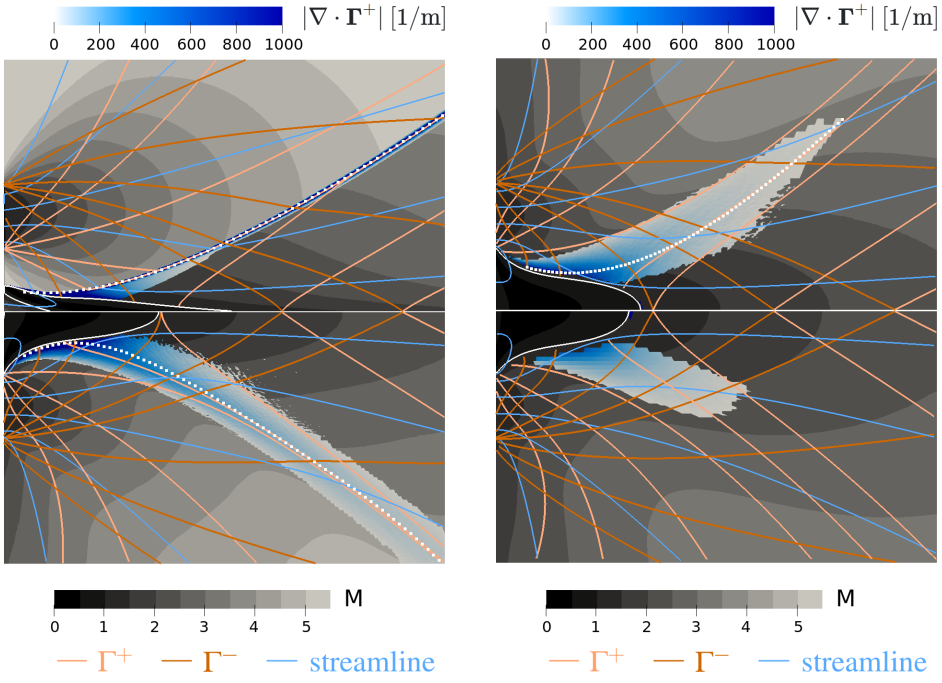

(a) $Kn_s = 2Kn_0$. The upper half depicts the Euler solution, the lower half the DSMC solution.

(b) The upper half depicts the DSMC solution for $Kn_s = 4Kn_0$, the lower half the DSMC solution for $Kn_s = 8Kn_0$.

Figure 3.8: Characteristics and shock detection (a) for $Kn_s = 2Kn_0$, in the upper half the Euler solution is shown, in the lower half the DSMC, (b) for DSMC solutions for $Kn_s = 4Kn_0$ in the upper half and $Kn_s = 8Kn_0$ in the lower half. The gray, banded contours in the background show the Mach number, the blue, continuous contours represent the region detected as shock region and are colored by $|\nabla \cdot \Gamma^+|$, clipped at 1000m^{-1}. The blue lines are streamlines, the brown lines Γ^- characteristics, and the beige lines Γ^+ characteristics (in the lower part the characteristics are mirrored). The white dotted line is the shock line detected from the regression of the shock region; the white solid line is the sonic line, i.e. $M = 1$.

Visualization by the Method of Characteristics shifts the view from the descriptive character of the macroscopic thermodynamic properties to the hyperbolic character, which determines the inviscid continuum flow behavior and to a large extent still the one in the transitional flow regime for the considered case, since a sufficient number of collisions occurs in crucial parts such as the inlet region and the shock to approach continuum

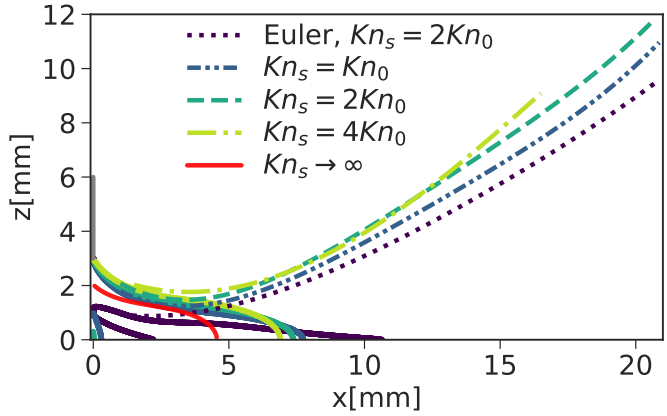

Figure 3.9: Shock location (dashed or dotted line) and sonic lines (solid) for different degrees of rarefaction. The vertical gray line denotes the inlet, the red dots the sonic line for free molecular flow.

flow behavior (from a large-scale point of view). Figure 3.8 depicts the characteristics of the flow fields as well as the detected shock region in continuous blue contours; the gray, banded contours in the background represent the Mach number. Figure 3.8a shows the inviscid continuum case (with an inlet density based on $Kn_s = 2Kn_0$) in the upper half and the corresponding DSMC solution in the lower half. For the inviscid continuum case, the Γ^- expansion fan unfolds around the upper corner of the inlet, the Γ^+ expansion fan around the lower corner. When crossing each other, their interaction causes the characteristics to bend slightly. The streamlines, depicted in blue, run along the half angles. In the shock, the Γ^+-characteristics turn sharply and merge with the shock, while the Γ^--characteristics cross the shock with only marginal bending. The streamlines turn accordingly. Upon impingement on the subsonic region or the symmetry, the Γ^--characteristics are reflected and turn into Γ^+-characteristics. Initially the reflection angle is wide and the post-shock Γ^+-characteristics hit the shock from downstream and thus bend it upwards. However, further downstream the Γ^+-characteristics are parallel to the shock or tend already away from it and so will not hit it and bend it further. (If, in a thought experiment, we extrapolate the characteristics before the shock to the very far-field, the streamlines will align more and more with the shock, until they do not cross it anymore. At an infinite distance, the shock transforms into a contact discontinuity, i.e., the velocity is parallel to the discontinuity, but state variables such as density and temperature are discontinuous across the shock.)

In the following discussion of the transitional flow regime, please keep in mind that with rarefaction the characteristics lose their ability to exactly describe the mechanisms determining the local solution. Yet the qualitatively similar flow behavior allows a meaningful visualization using the characteristics. For the DSMC solution of the $Kn_s = 2Kn_0$ case (Figure 3.8a lower half), the Γ^+-characteristics exhibit a pattern comparable to the Euler solution, but bend earlier and more smoothly, merging gradually with the shock. The subsonic region is bigger reaching to the corners of the inlet and, in particular, exhibits a bigger concave region, from which the shock region starts. The shock region

passes the computational domain at a rather constant, large width. However, the $|\nabla \cdot \Gamma^+|$ values are lower than for the continuum case and rapidly decrease when passing through the domain. Even when considering its broad domain, the shock region distinctly bends more outward than in the Euler solution. So the secondary expansion is wider, but the increase in Mach number is less steep which would be a contradiction in pure inviscid continuum flow. The underlying reason is that the secondary expansion maintains a higher pressure, temperature and hence speed of sound in the transitional flow regime (refer to Figure 3.7). On the one hand, the information that there is a shock travels further upstream due to the higher speed of sound (another equivalent line of argument is that the expansion experiences the shock, when its pressure is equal to the one behind the shock, which happens earlier for higher pressures in the secondary expansion). On the other hand, the high thermal fraction of energy leaves less for the macroscopic kinetic energy which in combination with the high temperature gives a lower Mach number. Appendix A.6 compares the shock structure with the detected shock location to validate the applied shock detection method.

Figure 3.8b shows the DSMC solution for $Kn_s = 4Kn_0$ in the upper and the one for $Kn_s = 8Kn_0$ in the lower half. With increasing rarefaction, the Mach number rises more slowly in the expansions, as fewer collisions transfer thermal energy into macroscopic kinetic energy. For a low number density, the characteristics bend more, especially in the "blind spot". The Γ^+-characteristics bend well before the shock region aligning gradually with the shock. Consequently, the shock region is much broader than for $Kn_s = 2Kn_0$, but the strength of the divergence $|\nabla \cdot \Gamma^+|$ is lower. The shock does not pass through the entire domain, but dissolves earlier. At $Kn_s = 8Kn_0$, the shock region is even smaller and a detection of a shock line is not feasible anymore.

Figure 3.9 compares the shock location and sonic line for several degrees of rarefaction. For higher degrees of rarefaction, the subsonic region becomes thicker (i.e., it extends more into the primary expansion) and shorter, indicating an earlier rise of velocity due to an earlier onset of expansion. This agrees with the shift of shock line, which moderately shifts upstream for higher rarefaction. 3

3.4.4. DEPOSITION PROFILES

After the location detection of the shock, its impact on the deposition is quantified. To this end, Figure 3.10 compares the profiles for different solutions methods. Both the free molecular solution and the far-field approximation are superpositions of two single plumes and exhibit two peaks in number density around the inlet positions (Figure 3.10a). The far-field approximation is in reasonable agreement with the Riemann solution outside the interaction region. Between the inlet peaks, the far-field approximation predicts a smooth uniform plateau, whereas the inviscid Euler solution produces symmetric profiles about the inlet axis, which means that the plumes are shielded from each other. However, two sharp peaks occur close to the symmetry plane marking the shock locations with high density accumulation in between. Compared to the approximations, the number density of the transitional flow regime is qualitatively a blending (Figure 3.10b): At a low Knudsen number, the impact of the shock is severe and the profile resembles the Riemann solution, but with higher peaks and a deeper trough in between. This may be explained with the higher temperature and consequently higher

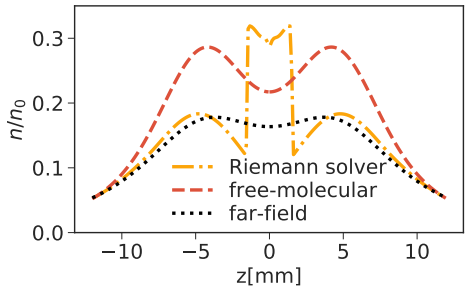

(a) Normalized number density

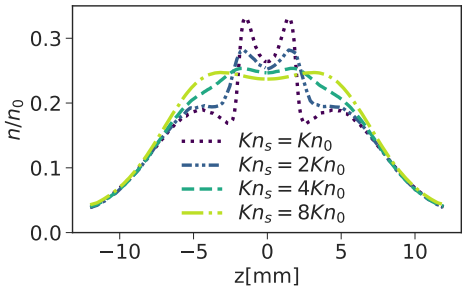

(b) Normalized number density

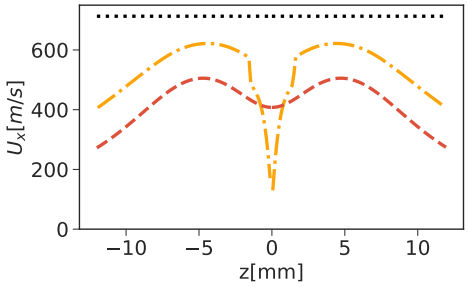

(c) x-component of velocity

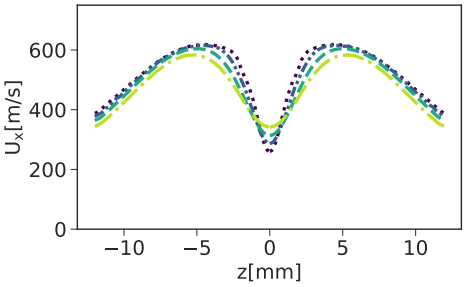

(d) x-component of velocity

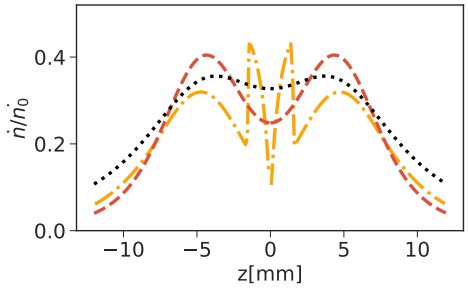

(e) Normalized deposition rate

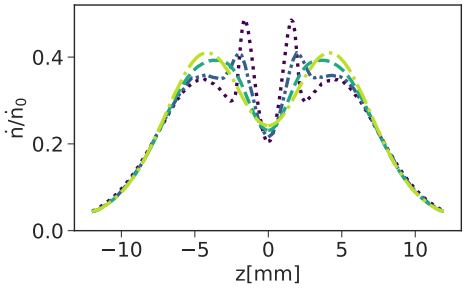

(f) Normalized deposition rate

Figure 3.10: Profiles of normalized number density, velocity in x-direction and normalized deposition rate at $x = 6$ mm for the inviscid continuum flow (Riemann solver, inlet density corresponds to $Kn_s = Kn_0$), free molecular flow and the far-field approximation ((a),(c), (e)) and in the transitional flow regime (DSMC) at different degrees of rarefaction ((b),(d),(f)).

pressure at the symmetry plane (refer to Figure 3.7c and Figure 3.7d), which deters particles from the symmetry. With increasing rarefaction, the density peak due to the shock diminishes and the rise due to the shock becomes less sharp. The spread outside the interaction region remains similar to those of the far-field and continuum solutions, as it is determined by the collisions right after the inlets, which still play a major role for the degrees of rarefaction considered.

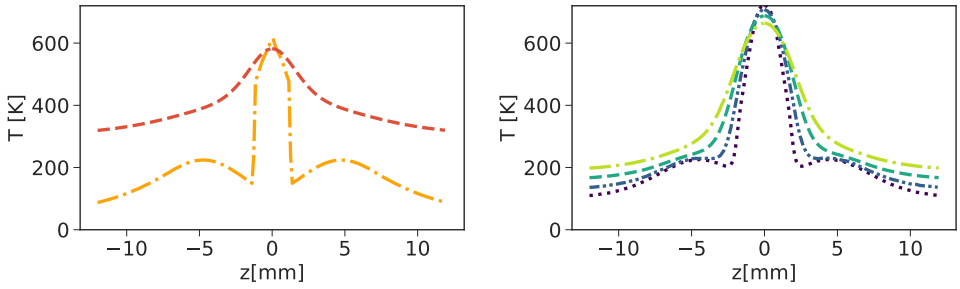

(a) Temperature

(b) Temperature

Figure 3.11: Temperature profiles for (a) inviscid continuum flow (Riemann solver) and free molecular flow; (b) for the transitional flow regime (DSMC) at different degrees of rarefaction.

The axial velocity outside the shock region is higher for the continuum flow than for the free molecular one (Figure 3.10c), as in continuum the temperature is actively transformed into kinetic energy, while in free molecular flow the energy transfer from thermal to kinetic energy is caused by particle velocity sorting which is diffuse and not targeted. In the shock region, velocity drops severely for the continuum solution. The velocity profile in the transitional flow regime (Figure 3.10d) is as smooth as the free molecular one, but reaches a maximum velocity as high as the continuum flow (since the collisions after the inlet are responsible for accelerating the flow), and rather small values around the symmetry plane (since there are still enough collisions to form a shock).
The deposition profile is estimated as the product of number density and axial mean velocity (for perfect sticking the actual deposition could deviate marginally due to velocity fluctuations, i.e., temperature). As the peak in density coincides with the trough in velocity, the deposition profiles have a higher agreement for different methods and degrees of rarefaction than the density profiles. When comparing the deposition profile, it is striking that the peaks for the lowest rarefaction in Figure 3.10f exceed the ones in the Riemann solution in Figure 3.10e by approximately 10%. The reason is that due to the diffusive nature in the transitional flow regime the density rises in a region where the velocity is still high, whereas the sharp discontinuity in continuum flow keeps high density and high velocity regions distinctly apart. (Consequently the peaks in deposition are marginally shifted outside compared to the peaks in number density.)
The temperature for the continuum solution is about three times lower than the inlet temperature outside the shock region (Figure 3.11a). The temperature peak inside the shock region is as high as the inlet temperature. For free molecular flow, the temperature is approximately one half of the inlet temperature, except for the region around the symmetry plane where it peaks at a modest level. The high temperature for free molecular flow is the counterpart to its low velocity, both stemming from the diffuse distribution of translational energy in the absence of collisions. In the transitional flow regime, the temperature profile (Figure 3.11b) has a shape between those of continuum flow and free molecular flow, but its peak temperature surpasses theirs, because the high energy accumulation inside the shock as seen in the continuum flow interferes with the diffuse

movement of particles typical of transitional flow. This higher temperature is responsible for the deeper trough in number density at the symmetry plane. Despite the described differences between the Riemann solver solution for the Euler equations and the DSMC solution, the Riemann solver gives an estimate of local deposition rates within engineering precision (≈ 10%) for very low Knudsen numbers such as $Kn_s = Kn_0$, whereas the free molecular solution fulfils this for $Kn_s > 8Kn_0$. In between these Knudsen numbers, DSMC is required to accurately predict the impact of the interaction. We hypothesize that the validity range of the Riemann solution could be enlarged by solving the Navier-Stokes-Fourier equations rather than the Euler equations. This would add the diffusive character due to viscosity (which increases with temperature and independent of other variables such as density [150]), but not the one due to rarefaction (which is expected to be considerably higher). However, further research is needed to test this hypothesis.

3.4.5. DISTANCE

Figure 3.12 shows the subsonic region and shock location (Figure 3.12a) and number density contours (Figs. 3.12c, 3.12d, 3.12e, 3.12f, 3.12g) for different distances between the inlets. For higher nozzle separation distances, the shock line smoothly follows the concave part of the subsonic region, before it turns away due to the expansion. The smaller the nozzle separation distance, the smaller and more convex the subsonic region. The shock wave strongly bends away from the symmetry line for $L = D/6$. This is caused by the high mass flow into the subsonic region and across the shock which forces a higher pressure in the secondary plume which results in a strong expansion. For the even smaller nozzle separation distance of $L = D/60$, the subsonic bubble has a maximum half height of 0.02mm or about 10 times the local mean free path. The jets merge and no shock is detectable anymore. The shock does not disappear for high nozzle separation distances (at least in the considered range) — which is in agreement with the discussion of the penetration Knudsen number for planar plumes in subsection 3.2.5—, but its impact on the deposition changes. Figure 3.12b shows the shock location scaled by half the nozzle-to-nozzle distance L. The scaling shifts the shock location to collapse to the same line. Figure 3.12i plots the deposition profile at $x = 9\,\text{mm}$ for different nozzle separation distances. For $L = D/60$, only one peak is visible, which splits into two for $L = D/6$. For higher distances, the peaks from the primary plumes and the interaction shocks become distinguishable. While at a high nozzle separation distance of $L = 2D$, the peaks due to the shock are similar to the peaks from the primary expansions, the non-uniformity is still high and the deposition per length is small. Figure 3.12i evaluates whether the similarity previously found for the shock location also holds for the deposition by plotting the normalized deposition rate at $x/L = 3$ over z/L. Clearly the deposition peak positions also conincide after scaling, but the deposition profiles itself vary significantly from each other. It may play a role, that the inlet is of constant finite size for all considered cases.

3.4.6. TILTING

Figure 3.13a shows the shock location and sonic line for several jet inclinations. Tilting the jets more towards each other (i.e., $\alpha = -10°$ and $\alpha = -20°$) reduces the subsonic region. It does not extend that far into the primary plume, as the high density caused by

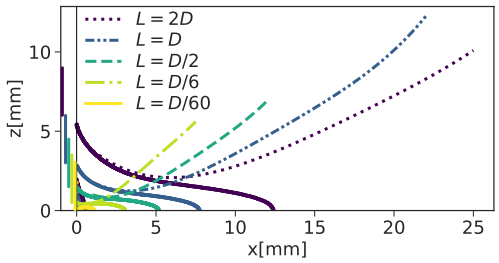

(a) Shock location (dashed or dotted lines) and sonic line (solid) for different nozzle separation distances. The vertical solid lines on the left mark the inlet location.

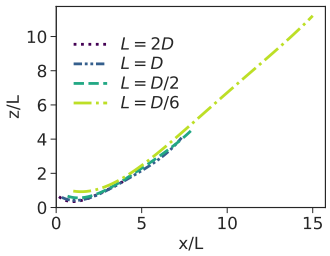

(b) Shock location for different nozzle separation distances scaled by the nozzle separation distance L.

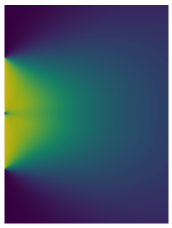

(c) $L = D/60$

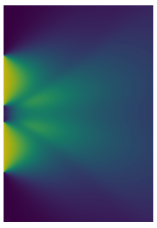

(d) $L = D/6$

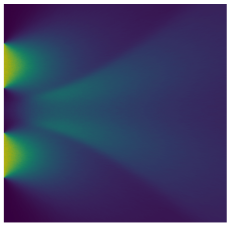

(e) $L = D/2$

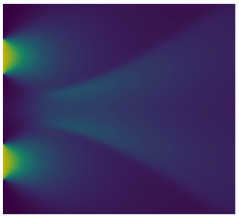

(f) $L = D$

(g) $L = 2D$

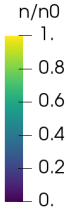

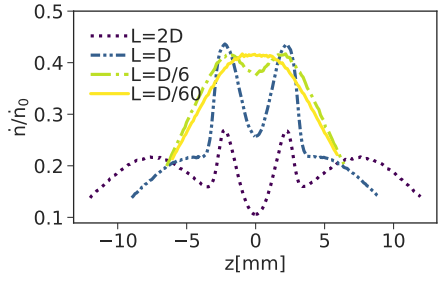

(h) Normalized deposition rate at $x = 9$mm

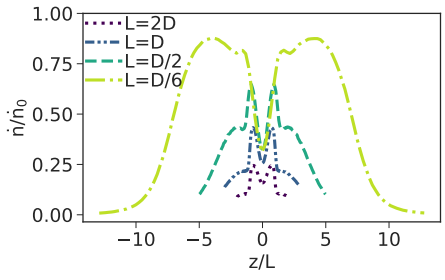

(i) Normalized deposition rate at $x/L = 3$

Figure 3.12: Influence of nozzle separation distance for parallel plumes at $Kn_s = Kn_0$. (a) Comparison of shock locations, (b) shock location spatially scaled by the nozzle separation distance (c)-(g) number density contours, (h) deposition profile, (i) deposition profile spatially scaled by the nozzle separation distance.

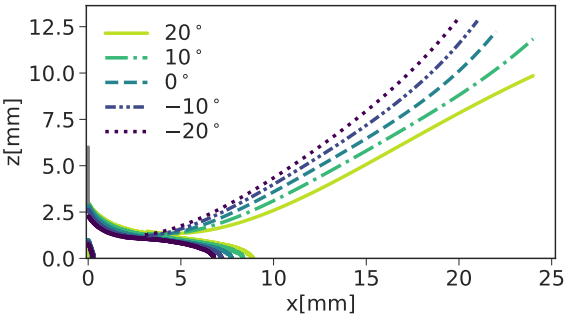

(a) Shock location (dashed or dotted lines) and sonic line (solid) for different angles of tilting of the inlet velocity.

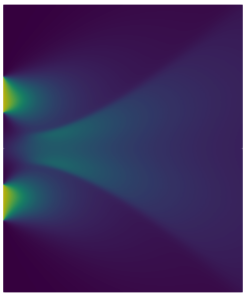

(b) $\alpha = -20°$

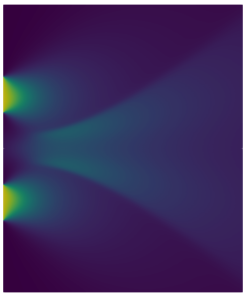

(c) $\alpha = -10°$

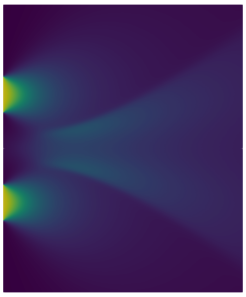

(d) $\alpha = 0°$

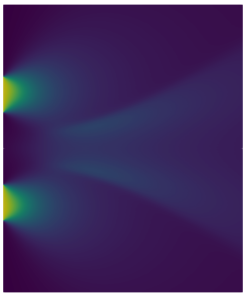

(e) $\alpha = 10°$

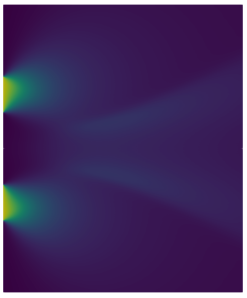

(f) $\alpha = 20°$

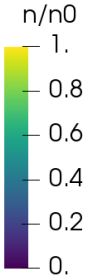

Figure 3.13: Influence of tilting the inlet velocity ($Kn_s = Kn_0$ and $L = D$). (a) Comparison of shock location and subsonic region, (b)–(f) number density for several degrees of inclination.

tilting it towards the symmetry plane shields the first plume from particles penetrating from the other primary plume. On the other hand, the high number density crossing the shock increases the pressure after the shock, which drives the secondary expansion, thus enforcing the latter. Consequently, the expansion bends the shock line more away from the symmetry plane and the flow expands faster, producing a smaller subsonic region. (The same phenomenon can also be explained in terms of characteristics: as the expansion fan from the inlet is more inclined towards the symmetry plane, the reflected

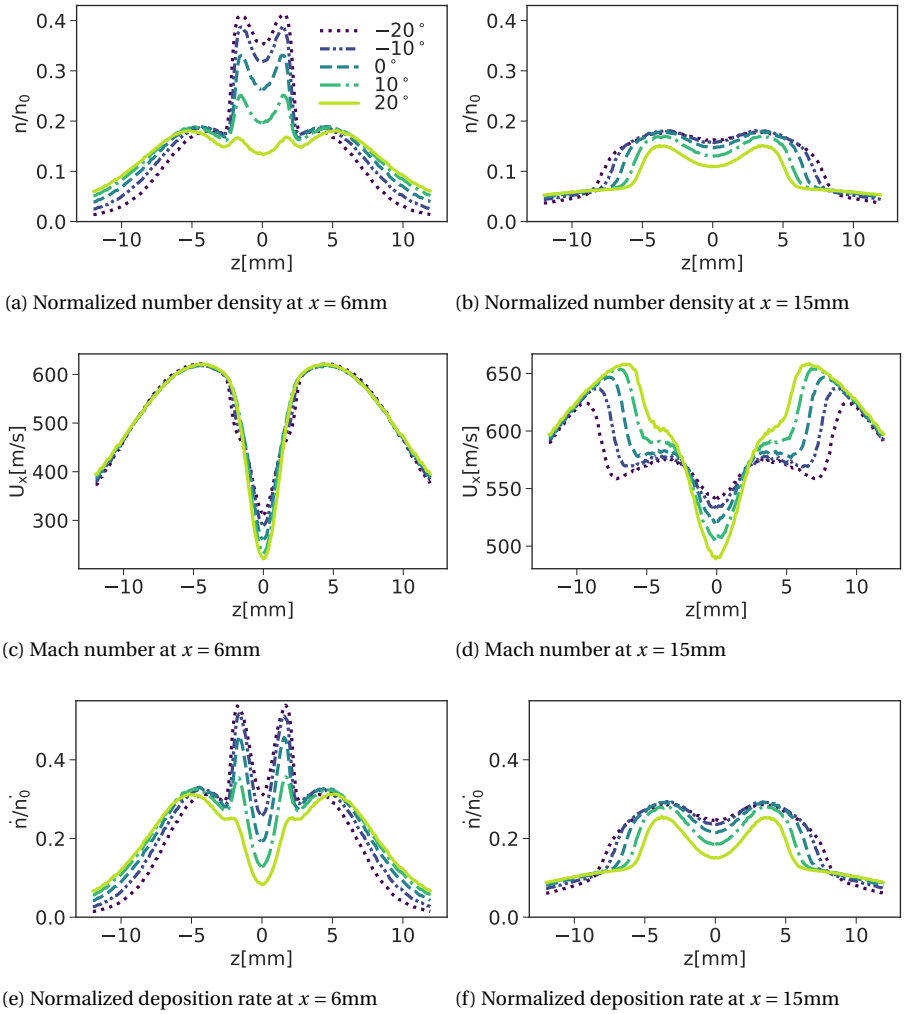

(a) Normalized number density at $x = 6$mm

(b) Normalized number density at $x = 15$mm

(c) Mach number at $x = 6$mm

(d) Mach number at $x = 15$mm

(e) Normalized deposition rate at $x = 6$mm

(f) Normalized deposition rate at $x = 15$mm

Figure 3.14: Normalized density, Mach number and normalized deposition profiles for several inclination angles (a)–(c) at $x = 6$mm and (d)–(f) at $x = 15$mm.

Γ^+-characteristics impinge onto the shock at wider angles and thus cause a stronger expansion. Consequently, the shock bends more away from the symmetry plane.) By tilting the inlet streams away from each other (i.e., $\alpha = 10°$ and $\alpha = 20°$) the opposite effect occurs. The subsonic region starts slightly further upstream, fewer particles cross the shock producing a weaker secondary expansion. For the inclinations and Knudsen numbers under consideration, it was decided based on the detected shock region, whether it is feasible to draw a shock line or whether the region can be neglected as a compression region not strong enough to cause a shock. The results are marked in Figure 3.4b. In-

dependent of the inclination of the jets, a shock was detected for stagnation Knudsen numbers up to $4Kn_0$; above $8Kn_0$ only a compression region emerged around the subsonic region. However, the deposition profiles do depend on the inclination.
Figure 3.14 shows the profiles for the number density, normalized by the inlet density, the velocity component parallel to the jet axis and the deposition rate normalized by the inlet flow rate over the z-coordinate at $x = 6$mm (Figs. 3.14a, 3.14c, 3.14e) and $x = 15$mm (Figs. 3.14b, 3.14d, 3.14f) at $Kn_S = Kn_0$ for different inclination angles. At $x = 6$mm the shock is at the same position for the different inclinations (Figure 3.13a), which is reflected by the same location of the two peaks in the density profile. However, the height of these peaks is negligible for $\alpha = 20°$ and immense for $\alpha = -20°$, as with the latter a much higher number density flux already crossed the shock. The velocity profiles (Figure 3.14c) at this position approximately match for the different inclinations and exhibit a low value in the shock region, which mitigates the impact of the shock in the deposition profile (Figure 3.14e). Further downstream, at $x = 15$mm, the two broad peaks from the shocks dominate the density profile (Figure 3.14b). They have a similar maximum value, but the stronger expansion for cases inclined towards each other broadened the peaks farther over the domain. In addition, the density trough around the symmetry is smaller yielding a flatter, more uniform density profile than for plume inclinations away from the symmetry. The velocity profiles (Figure 3.14d) resemble each other in shape with an undisturbed accelerated flow at the edges of the domain, a small trough at the start of the shock and a deeper one in the center. The main difference between the inclinations being that for plumes inclined to each other the low Mach number region between the shocks extends farther and the expansion already began which reaccelerates the flow between the shocks and mitigates the velocity trough in the center. The overall deposition (Figure 3.14f) in the depicted segment is considerably higher for plumes tilted towards each other, since less mass flow leaves the domain. This reduction in stray deposition is a desirable side effect for coating technology. The non-uniformity in the deposition rate profile is mitigated compared to the upstream profile. This applies in particular to $\alpha = -20°$, which had (perceptibly) the highest deposition non-uniformity at $x = 6$mm and the lowest at $x = 15$mm. To provide a more general overview of non-uniformity, we quantify it in the next section.

3.4.7. DEPOSITION UNIFORMITY

A major objective was to determine the effect of nozzle tilting and rarefaction on the uniformity of the deposition. While small variations in coating thickness may be tolerable, strong deviations should be avoided. Based on this consideration, we chose the minimum square deviation from a constant height c as a measure of non-uniformity

$$A_{dev} = \min_{c\in\mathbb{R}} \int_{z=0}^{z_{60\%}} \left(\frac{\dot{n}-c}{c}\right)^2 \mathrm{d}x, \tag{3.20}$$

where $z_{60\%}$ is the position where 60% of the influx would be deposited. The choice of such a cut-off coordinate is required to exclude the long thin tail of deposition (which can also not be captured by the finite computational domain). For a perfectly uniform deposition, $A_{dev} = 0$; the stronger and more numerous the deviations, the higher A_{dev}. Figure 3.15 plots A_{dev} over different degrees of rarefaction and nozzle-to-plate distances,

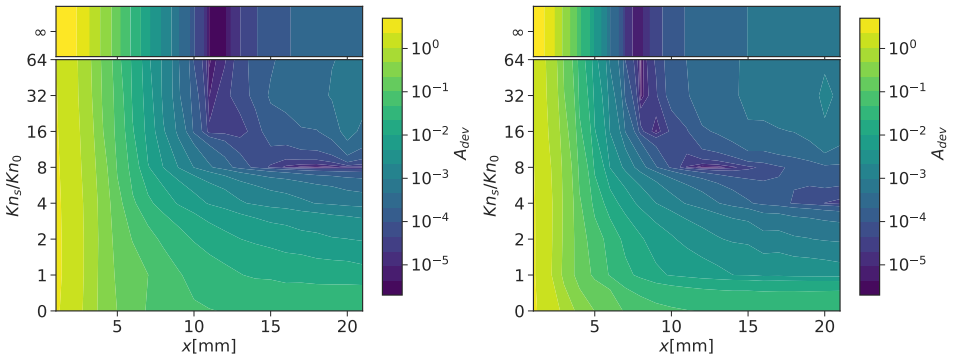

(a) Parallel jets, i.e., $\alpha = 0°$.

(b) Jets inclined by $\alpha = -20°$.

Figure 3.15: Non-uniformity A_{dev} over different degrees of rarefaction and nozzle-to-plate distances for two (a) parallel and (b) inclined jets at a nozzle separation distance $L = D$. The inlet number density for the inviscid continuum solution at $Kn_s = 0$ is the one for $Kn_s = Kn_0$. The free molecular solution is kept separate. The underlying grid of the contour plot is $20x8$.

using a logarithmic scale. For very short nozzle-to-plate distances, the non-uniformity is high and nearly independent of the rarefaction, since it captures the non-uniformity from the two jet inlets only. Non-uniformity decreases with the distance to the inlets. A strong mitigating effect of rarefaction sets in around $x = 6$mm, which corresponds to the start of the shock. For high rarefaction equal to or greater than $Kn_s = 16Kn_0$ and for free molecular flow, the minimum non-uniformity is reached around $x = 12$mm and increasing again afterwards. While the two plumes superposed each other before, they merge into one single plume further downstream, which increases non-uniformity. For lower rarefaction (i.e., equal to and below $Kn_s = 8Kn_0$), non-uniformity monotonically decreases with the distance to the inlet (for the region considered), thus exhibiting lower non-uniformity at high distances than the higher rarefied cases. This is the result of the interaction shock which "fills" the trough between the two primary plumes, producing a broad plateau in the deposition profile. When the jets are tilted towards each other (Figure 3.15b), the non-uniformity decreases faster with increasing distance from the inlet. The minimum for free molecular flow is reached closer to the inlet than for parallel jets, since the density peaks merge earlier to form a plateau and then a single density peak. For long distances from the inlet, the minimum occurs for a rarefaction of $Kn_s = 4Kn_0$ compared to $Kn_s = 8Kn_0$ for the non-inclined case.

3.5. CONCLUSIONS

We have investigated the interaction of two sonic, rarefied, planar plumes — either parallel or inclined to each other. The extreme cases of a collisionless analytic flow solution and an inviscid continuum solution calculated by an approximate Riemann-solver were presented. In the transitional flow regime, multiple DSMC simulations were conducted. To analyze the flow field, we detected the characteristics and used their divergence to detect the shock location.

For free molecular flow, the expansion stems purely from sorting of particles' velocities, producing only a moderate increase in velocity and a small decrease of temperature compared to collisional flow. The inviscid continuum solution gives strong expansions, with rapid increases in velocity and drops of density and temperature. The interaction causes sharp shocks passing through the flow domain, which is reflected in two severe peaks in the deposition profile. Common to both flow regimes is a high temperature in the symmetry plane. The behavior in the transitional flow regime is a blend of free molecular flow and continuum flow. However, some flow variables and fluxes lie outside the limits of these two extreme cases. In and behind the subsonic region, the temperatures exceed both the free molecular and the continuum solution. On the one hand, this results from the high particle and thus energy accumulation due to the shock which is typical of continuum/collisional flow, on the other hand, a lack of collisions compared to the continuum case enables diffuse particle movement and hinders the energy transfer from temperature to macroscopic kinetic energy. The latter phenomenon yields a wider, but less strong secondary expansion bending the interaction shocks apart. The mass flux peak values in the transitional flow regime exceed the ones of continuum flow.

A shock can be perceived up to very small nozzle separation distances. Only when the distance is of the order of $\mathcal{O}(10)$ mean free paths or less, a shock region cannot be detected anymore and the two plumes merge into one single plume. Tilting the plumes towards each other shifts the onset of the shock further upstream and as a result of the higher flux crossing the shock enhances the secondary expansion compared with parallel plumes. This causes steep density peaks at small distances from the inlet. On the other side, the increased pressure enhances the expansion, resulting further downstream in a more homogeneous density and mass flux, while decreasing stray deposition. The non-uniformity in the deposition decreases with distance from the inlets for high rarefaction, and minimizes approximately at the coordinate, where the subsonic region ends. When inclining the plumes towards each other, the distance, at which the minimum non-uniformity is reached, decreases.

Our findings can support the design of vacuum technology such as Physical Vapor Deposition to obtain homogeneous mass, momentum and energy fluxes. In addition, they may help in analyzing backflows of multithrusters and their potential structural damage on space vehicles such as micro satellites.

We studied the planar case of interacting plumes, which in the broadest sense is representative of linear aerospike nozzles. Especially in aerospace applications, three-dimensional clusters are common, the simulation of which involves significantly higher computational costs for a well-resolved DSMC. For three-dimensional plume clusters, a mitigation of shock effects is expected, as the gas can escape the shock region in another direction, while for three-dimensional toroidal aerospikes [151] an increase of the shock effect is expected, since a higher mass flux enters the interaction region.

4

DIFFUSIVE SEPARATION IN RAREFIED PLUME INTERACTION

In the present study, we propose the use of a light, inert carrier gas to support deposition uniformity and rate in continuous Physical Vapor Deposition, in which closely spaced slots or nozzles are required to achieve a sufficiently high deposition rate. Interaction shocks between the emerging rarefied plumes cause undesired non-uniformities in the deposited coating. The present work evaluates the effect of adding a carrier gas on the interaction shock. We study the interaction between two sonic plumes consisting of a binary mixture, i.e., silver as coating material and helium as light inert carrier gas, by Direct Simulation Monte Carlo. While the inlet Mach and Knudsen numbers were kept constant, the fraction of carrier gas was varied to single out the effect of species separation. The influence of rarefaction on species separation was also studied. Species separation produces a high carrier-gas fraction in the periphery and an accumulation of the heavier species in the jet core. The resulting change in speed of sound alters the local expansion characteristics and thus shifts the shock location and weakens the shock. These phenomena intensify with degree of rarefaction. It is shown that adding a light carrier gas increases deposition rate, may enhance uniformity, and reduces stray deposition.

This chapter has been accepted for publication in the *Journal of Vacuum Science & Technology B.*

4.1. INTRODUCTION

In thin-film deposition processes from the gas phase, such as Physical Vapor Deposition (PVD), varying the inert and reactive gas mixture composition is used to influence the layer growth mode [152], enhance uniformity [153], or to produce compounds such as titanium nitride which requires a nitrogen atmosphere [154]. Several experimental and numerical studies analyzed the effect of adding an inert background or carrier gas onto the film thickness and distribution in batch deposition processes, mainly finding a smoothing of the deposition profile and a decrease of deposition rate due to an enhanced number of collisions [65, 68, 153, 155, 156]. Directed vapor deposition processes [157, 158] were developed which utilize light carrier gases to enhance the deposition rate and reduce deposition loss (i.e., fraction of evaporated material not being deposited on the substrate). The latter diminishes production down times due to cleaning and maintenance in continuous lines. Inert carrier gases were used to foster the transport of coating material to undercuts, since otherwise PVD is a line-in-sight technology [159–161]. In chemical deposition processes, carrier gases are utilized to suppress early reactions and control the reactant ratio to achieve the desired morphology of the deposited film [152]. It was shown that light carrier gases benefit the conductance of material through pipes and orifices and thus the possible deposition rate [162, 163]. In summary, the use of background and carrier gases decisively influences the film growth in thin-film and coating technology.

Recently, continuous PVD lines were introduced which overcome the disadvantages of batch processes, i.e., a low deposition rate and production down times due to maintenance. A sufficient evaporation rate for coatings is typically reached via a thermal source [7], whereas maintenance is reduced by avoiding stray deposition using plumes (or jets) directed towards the substrate emerging from multiple closely spaced nozzles or slots [12, 97]. In these plume clusters, the initially free expansion interacts with neighboring plumes producing shocks [121]. This causes mass flow non-uniformities, which are especially undesirable in thin film deposition [93, 164]. The higher the mass flow rate and the smaller the nozzle-to-nozzle distance the higher the peaks in deposition. However, a high and uniform deposition is required in continuous coating technology to keep the coating process step at the general line speed and to obtain a high-quality coating.

The successful use of adding light carrier gases to heavy reactant gases in batch PVD and other coating processes indicates a good chance that this may also improve continuous PVD processes.

An important effect to be taken into account when utilizing mixtures of heavy and light gases is the spatial separation of the various species. This may be caused by various physical mechanisms, such as differences in body forces in centrifugal flows [165–167], thermodiffusion effects in non-isothermal flows [168, 169] and pressure gradients in confined microflows [170, 171]. Gas species separation occurs in microelectromechanical systems (MEMS) [172, 173], radiometric pumps [174, 175], Knudsen pumps [176, 177] and aerospace applications [101, 178, 179]. For the latter, pressure-driven species separation has a severe influence, since both high pressure gradients and long mean free paths occur, and the separation increases with both.

Because of its relevance to aerospace applications in for instance (micro)thrusters, free expansions of rarefied plumes or jets have been comprehensively studied. Several ana-

lytic [180], experimental [178, 181, 182] and numerical [162, 183, 184] studies on multi-species gas plumes found that the heavier species accumulates around the jet axis. In contrast, the fraction of the lighter species is high in the backflow region and regions farther away from the jet axis. Simulations of species separation of an argon-helium mixture at small Knudsen numbers were performed by Riabov [183]. He found that the decoupling of the streamwise and the circumferential temperatures, the so called "freezing" which is an indication for continuum breakdown, takes place further upstream for the heavier species. Wu et al. studied experimentally and numerically the interaction of two three-dimensional hydrogen-oxygen thrusters at small separation distances with a focus on the interaction shock and its possible effect on a backflow[185]. The latter may damage the spacecraft using multiple thrusters. The effect of species separation on the flow field was not in the focus of the study.

Species separation effects are also reported for flows involving shocks, but it is difficult to establish the same generality as for free expansion flows due to the multitude of possible geometries and shock types. Rothe [186] experimentally studied the species separation effect in bow shocks. He found an earlier number density increase for the lighter species than the heavier one, which implies a staggered onset of the shock. Ramos et al. [182] analyzed this separation of species for a nitrogen-hydrogen mixture in supersonic jets with and without a shock-wave structure. In the former case, the authors found a steep increase of the heavier species in the jet core right after the nozzle where the pressure gradient is highest. In the shock-wave structure, Ramos et al. [187] found separation across the shocks (yielding an accumulation of lighter species slightly before and inside the Mach and Barrel shock). Additionally, background gas penetrated into the jet core after the first Mach disk, which was increased for light background gas. The authors also addressed the rotational-translational energy transfer as well as the energy transfer between species.

In summary, there exists a good understanding in literature of species separation in free expansions of a single rarefied plume. However, the knowledge of the influence of shocks on species separation as available in literature is limited to some specific, generally non-rarefied, gas flow configurations. To the authors' best knowledge, species separation in interacting free expansion rarefied gas plumes with downstream interaction shocks, as it appears in plume clusters of a continuous PVD line, has not been described in literature.

The present paper studies the species separation in planar plume interaction of a binary mixture of silver and helium and its impact on the location and strength of the shock. We aim to answer the question how the mutual influence between shocks and species separation have an impact on mass flux magnitude and uniformity. We show how the addition of a light carrier gas influences this mutuial interaction and consequently the deposition rate, deposition uniformity, and deposition loss. The involved phenomena are unravelled on the one hand by considering the free molecular flow to evaluate species separation effects and on the other hand by visualizing the flow field plotting the characteristic curves. With the latter also the downstream shift of the shock location and the weakening of the shock with helium fraction and degree of rarefaction is presented.

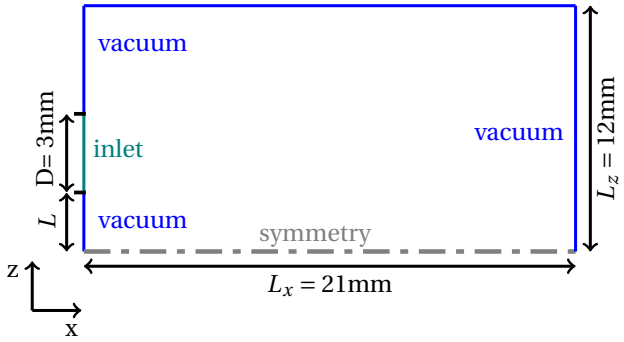

Figure 4.1: Geometry and boundary conditions for the DSMC simulation.

4.2. METHODS

We simulate the interaction between two parallel, planar sonic plumes by Direct Simulation Monte Carlo (DSMC) method [34]. The plumes emerge from two inlet slots of width $D = 3\,\text{mm}$ at a separation distance $2L = 6\,\text{mm}$ (the distance between the edges of the nozzles). Due to the symmetry, we simulate only the upper half of the geometry. The computational domain (Figure 4.1) is planar and spans $21\,\text{mm} \times 12\,\text{mm}$. Except for the inlet and the symmetry plane, all other boundaries are vacuum boundary conditions. The inlet mixture composition at the orifice is assumed to be uniform. The mass ratio of silver and helium is $m_{Ag}/m_{He} = 26.94$. At the inlet, a free stream boundary condition is applied with a mixture of silver and helium at a temperature of $T_{in} = 2000\,\text{K}$ at a velocity corresponding to $M = 1$, which corresponds to a stagnation temperature of $T_s = 2600\,\text{K}$. The inlet density depends on the Knudsen number, which was chosen as a multiplicity of $Kn_0 = 0.0125$, i.e., $Kn \in [Kn_0, 2Kn_0]$, and the carrier-gas fraction, i.e., the mole fraction of helium, which takes the following values $y_{He} \in [0, 0.1, 0.3, 0.5, 0.7, 0.9, 1]$. The inlet velocity is the speed of sound, which depends on the mixture composition. To determine the inlet number density from the inlet Knudsen number $Kn_{in} = \lambda/D$, the mean free path of the binary mixture needs to be evaluated as [34]

$$\lambda = \frac{1}{n\pi}\left[\frac{y_{He}}{\sqrt{2}d_{He}^2 y_{He} + \sqrt{1+\frac{m_{He}}{m_{Ag}}}d_{He,Ag}^2 y_{Ag}} + \frac{1-y_{He}}{\sqrt{1+\frac{m_{Ag}}{m_{He}}}d_{He,Ag}^2 y_{He} + \sqrt{2}d_{Ag}^2 y_{Ag}}\right], \tag{4.1}$$

where the collisional diameter for each species varies with temperature according to the Variable Hard Sphere model [34] as follows

$$d = d_{ref}\left(\frac{T_{ref}}{T_{in}}\right)^{\left(\frac{\omega}{2}-\frac{1}{4}\right)}, \tag{4.2}$$

Table 4.1: Modeling parameters for Variable Soft Sphere [188] model for helium [34] and silver (approximated by inverse-power law [8]).

	m $[10^{-27}\,\mathrm{kg}]$	d_{ref} $[10^{-10}\,\mathrm{m}]$	ω	α	T_{ref} [K]
He	6.65	2.3	0.66	1.26	273
Ag	179.12	8.31	0.853	1.92	273

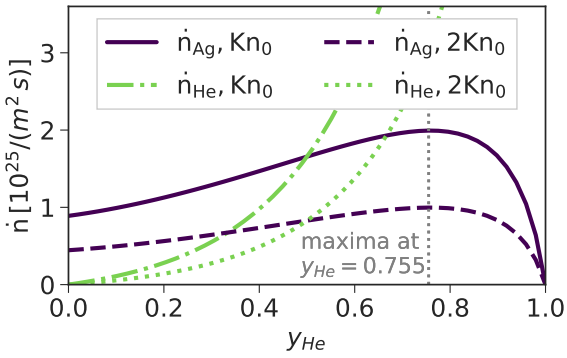

Figure 4.2: Inlet number density fluxes depending on carrier-gas fraction.

where the energy exponent ω and reference diameter d_{ref} are given in Table 4.1. The collisional diameter between atoms of different species is given as

$$d_{He,Ag} = \frac{1}{2}\left(d_{He} + d_{Ag}\right). \tag{4.3}$$

The inlet speed, i.e., the speed of sound of the mixture, is given by

$$a = \sqrt{\gamma \frac{k_B T_{in}}{\left(y_{He} m_{He} + (1 - y_{He}) m_{Ag}\right)}}. \tag{4.4}$$

DSMC requires a thermodynamic closure for the collisions to match the macroscopic transport properties. For this, the Variable Soft Sphere model [34] is applied, since the viscosity and binary diffusivity can not be correctly modelled by simpler models. The properties of helium and silver are listed in Table 4.1. The reference diameter and viscosity parameter of silver are estimated by the inverse-power-law approximation described by Fan et al. [8]. The reference metal for the inverse-power law was rubidium which is in the same group as silver and whose viscosity is reported in the literature [149]. The data for helium are the ones reported by Bird [34]. To obtain accurate results despite the decoupling applied in DSMC, a time step smaller than one tenth of the mean collisional time has to be maintained, i.e., $dt < \tau/10$, and a cell size smaller than one third of the local mean free path is required. Since we use eight sub-cells per cell this requirement can be loosened to $(dx < 2\lambda/3)$. To have enough unbiased collision partners, at least 20 representative particles are required per cell. All these requirements were fulfilled, except for the highly rarefied region (i.e., in the “blind spot" of the plume where the collision

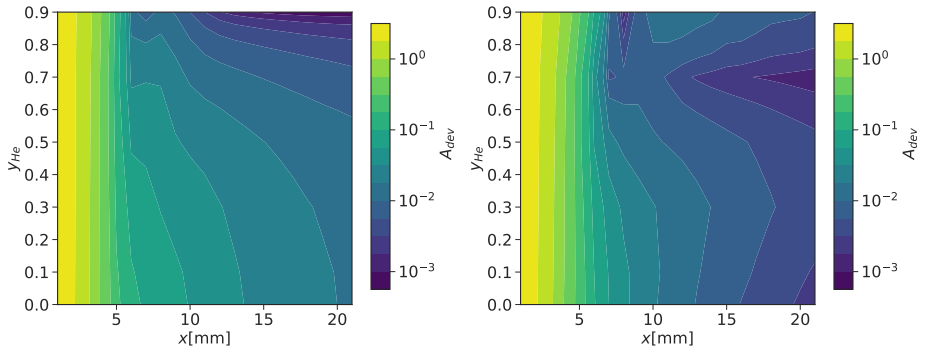

(a) Deviation from uniformity for $Kn = Kn_0$.

(b) Deviation from uniformity for $Kn = 2Kn_0$.

Figure 4.3: Non-uniformity A_{dev} depending on carrier-gas fraction and nozzle-to-plate distances for two plumes at a nozzle separation distance $L = D$.

probability is low anyway), which justifies our approach. To fulfill the spatial resolution criteria, first a simulation on a coarse grid was performed and based on the local mean free path refined before starting the actual simulation. The time step was also adapted and kept constant throughout the simulation. This procedure was conducted for each case, as the resolution requirements differ depending on both Knudsen number and carrier-gas fraction. Exemplary a time step, mesh and particle number independence study was conducted for the case $Kn_{in} = 2Kn_0$ and $y_{He} = 0.5$, the results show that the resolution is (more than) sufficient (refer to Appendix A.7). The *dsmcFoamPlus* solver was used, which was implemented in *OpenFoam 2.4* and extensively verified by White et al.[147].

4.3. RESULTS

Three main criteria regarding mass flow are desirable in coating technology: (i) a high total deposition rate, (ii) a uniform deposition and (iii) an avoidance of stray deposition. We use the deposition profiles of silver, i.e., $\dot{n}_{Ag}$, to comprehensively quantify these criteria depending on the mixture composition. First we evaluate (i) the total deposition rate by plotting the inlet number density fluxes over the carrier-gas fraction y_{He} for $Kn_{in} = Kn_0$ and $Kn_{in} = 2Kn_0$ as shown in Figure 4.2. With increasing carrier-gas fraction, the silver mass flux — which we are eventually interested in — rises up to its maximum at $y_{He} = 0.755$. This increase may seem counter intuitive, since the silver fraction decreases with higher helium fraction. Nevertheless, the silver inlet velocity increases, since the speed of sound is inversely proportional to the square root of molecular mass, i.e., $a \propto 1/\sqrt{m}$. It should be noted that the addition of a lighter carrier gas increases viscosity with $1/\sqrt{m}$, which may increase the boundary layer in the slot or nozzle and thus reduce the outflow. The present study does not consider this effect. Comprehensive studies on the conductance and species separation from orifices and through pipes of finite lengths were published in recent years [162, 163, 189]. However, as the higher vis-

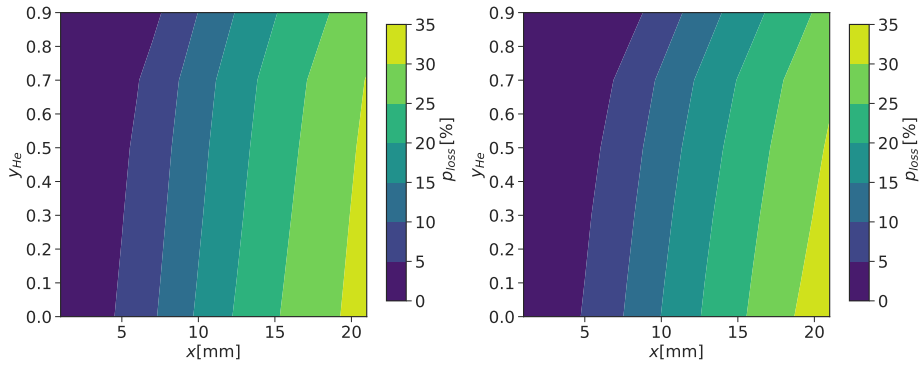

(a) Stray deposition loss for $Kn = Kn_0$.

(b) Stray deposition loss for $Kn = 2Kn_0$.

Figure 4.4: Stray deposition loss p_{loss} depending on carrier-gas fraction and nozzle-to-plate distances for two plumes at a nozzle separation distance $L = D$.

cosity affects only the boundary and not the bulk flow, the effect is assumed to be small. To quantify (ii) the uniformity of the deposition, the minimum squared deviation of silver deposition (i.e., minimized with respect to c, a number from the set of real numbers) is calculated, which reads

$$A_{dev} = \min_{c \in \mathbb{R}^+} \int_{z=0}^{z=12\,\mathrm{mm}} \left(\frac{\dot{n_{Ag}} - c}{c} \right)^2 \mathrm{d}z. \tag{4.5}$$

$A_{dev} = 0$ corresponds to perfect uniformity, whereas higher A_{dev} indicates non-uniformity. Figure 4.3a (for $Kn = Kn_0$) and Figure 4.3b (for $Kn = 2Kn_0$) show the non-uniformity measure A_{dev} over the nozzle-to-plate distance and molar fraction of helium y_{He}. The non-uniformity is highest directly after the inlet, where the spreading of species starts, and decreases rapidly with increasing distance. The non-uniformity starts to differ for different molar fractions of helium at a nozzle-to-plate distance of $x \approx 5\,\mathrm{mm}$. For $Kn = Kn_0$, adding more carrier gas monotonically enhances uniformity, whereas for $Kn = 2Kn_0$ the non-uniformity decreases up to a minimum approximately at $y_{He} = 0.7$ before increasing again. While the exact minimum value can be expected to depend on the geometry and process conditions, it indicates that high fractions of carrier gas may mitigate shock-induced non-uniformities. Figure 4.4a and Figure 4.4b show (iii) the stray deposition which is the coating material fraction p_{loss} which does not reach the substrate (assumed to stretch over the range $z = \pm 12\,\mathrm{mm}$), but leaves the computational domain (i.e., coats the vacuum chamber). With higher nozzle-to-plate distance the loss deposition increases. The stray deposition loss is slightly higher for $Kn = Kn_0$ (Figure 4.4a) than for $Kn = 2Kn_0$ (Figure 4.4b). The higher the carrier-gas fraction, the smaller the deposition loss, e.g., at $x = 10\,\mathrm{mm}$ only 10% are lost for $y_{He} = 0.9$ compared to 15% for no carrier gas for the case of $Kn = 2Kn_0$ (Figure 4.4b). Thus, adding a light carrier gas improves the coating deposition regarding all three evaluated criteria.
To explain these results, Figure 4.5 shows the line profiles of the normalized silver number density, silver velocity and normalized silver deposition along z-direction for differ-

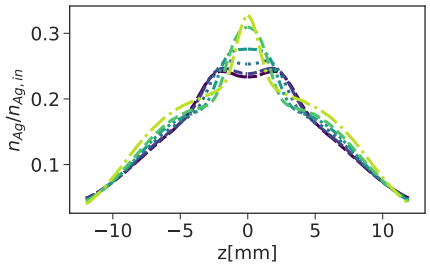

(a) Normalized number density at $x = 8\,\text{mm}$.

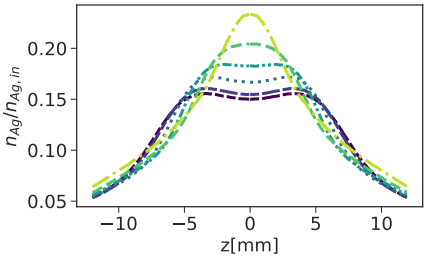

(b) Normalized number density at $x = 15\,\text{mm}$.

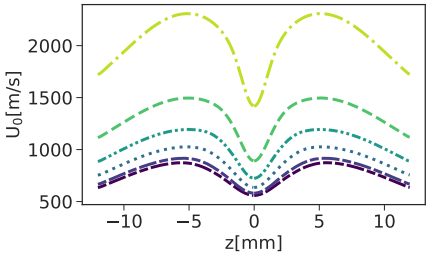

(c) Velocity in x-direction at $x = 8\,\text{mm}$.

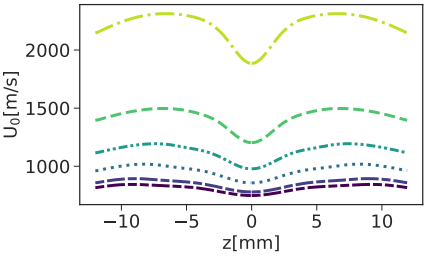

(d) Velocity in x-direction at $x = 15\,\text{mm}$.

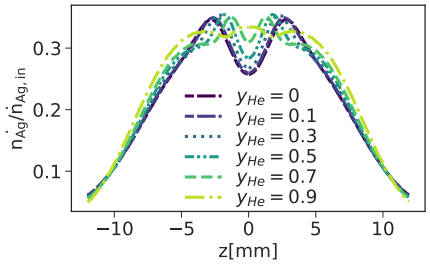

(e) Normalized number density deposition at $x = 8\,\text{mm}$.

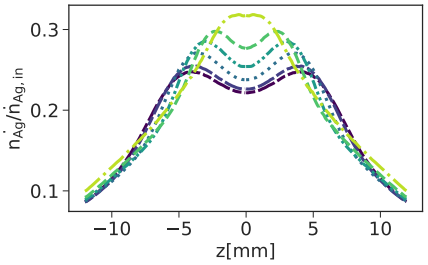

(f) Normalized number density deposition at $x = 15\,\text{mm}$.

Figure 4.5: Line profiles of the flow of two interacting plumes for $Kn = 2Kn_0$ and for several carrier-gas fractions along z-direction. (a), (d) show the silver number density normalized by the silver inlet number density, (b), (e) the silver velocity in x-direction, (c), (f) the silver number density flux normalized by the silver inlet number density flux. (a), (b), (c) are at a nozzle-to-plate distance of $x = 8\,\text{mm}$ and (d), (e), (f) at a nozzle-to-plate distance of $x = 15\,\text{mm}$.

ent mole fractions of carrier gas y_{He} for $Kn = 2Kn_0$. At $x = 8\,\text{mm}$, the normalized number density profile for the pure silver mixture, i.e., $y_He = 0$, (Figure 4.5a) linearly increases towards the symmetry and shows two elevated peaks on each side of the symmetry plane. With increasing carrier-gas fraction, the two distinct peaks merge into one and the rest of the profile is more curved. All velocity profiles depict two broad peaks and a trough at the symmetry, but with higher carrier-gas fraction y_{He} the velocity magnitude significantly increases (Figure 4.5c). The normalized silver number deposition profile, which

is the product of the normalized number density and the velocity (divided by the silver inlet velocity), i.e., $\dot{n}_{Ag}/\dot{n}_{Ag,in} = (n_{Ag}u_{Ag})/(n_{Ag,in}u_{Ag,in})$, is shown in Figure 4.5e. It increases nearly linearly from the outer side towards its peaks and shows a considerable trough in between for the pure silver mixture. With increasing helium mole fraction, the profile becomes curved and broad peaks are visible around the inlet positions and one or two peaks occur at or next to the symmetry plane. The velocity trough at the symmetry trenches a deposition trough for the low carrier-gas fractions and compensates for the number density peak for high carrier-gas fractions, thus smoothing the deposition profile. This illustrates the smaller non-uniformity when adding carrier-gas in moderate amounts (in this case $y_{He} \in (0.4, 0.8)$). At higher nozzle-to-plate distance of $x = 15\,\text{mm}$, the number density is plug-like for small carrier-gas fractions y_{He} and forms a triangle profile with a high peak for high y_{He} (Figure 4.5b). The velocity profiles (Figure 4.5d) flatten out producing a deposition profile which strongly resembles the number density profile. With higher helium fraction, the peaks merge into one narrow high peak. This explains the increase of non-uniformity with carrier-gas fraction above $y_{He} = 0.7$ previously observed in Figure 4.3b.
The underlying flow behavior can be split into two phenomena to understand the effect of the carrier gas, namely

1. species separation due to rarefaction, and subsequent change of speed of sound with molecular weight,

2. subsequent change of Γ^+- and Γ^--characteristics.

While the species separation requires rarefied flow conditions, since it is proportional to the mean free path, the definition of speed of sound and the characteristics make sense only in (near) continuum flows — as observed in the shock and at the beginning of the expansions.

4.3.1. FREE MOLECULAR FLOW

To visualize phenomenon 1, we consider the extreme case of free molecular flow ($Kn \to \infty$) where species separation is purely based on the difference of the velocity standard deviations. Figure 4.6 plots free molecular flow of two parallel plumes, each of them has a carrier-gas fraction of $y_{He} = 0.5$. At the inlet, silver and helium are in equilibrium, i.e., $T_{Ag} = T_{He}$. The variance of the velocity distributions is $k_B T/m$, so that silver has a narrower velocity distribution than helium, which affects the spreading of the species. Figure 4.6a shows the emerging number density field for silver in the upper and helium in the lower half, respectively. The silver number density decreases with distance from the inlet, mildly along the jet axis and more rapidly in the offside, producing isocontours in the form of ellipses. In contrast, for the lighter helium, the number density decreases rapidly in all directions causing nearly circular isocontours. The mean velocity of the mixture in x-direction (in the upper half of Figure 4.6b) increases with distance to the inlet and takes values around $900\,\text{m}\,\text{s}^{-1}$, whereas the one in z-direction is highest in the peripheral regions (shown in the lower half of Figure 4.6b). Figure 4.6c shows the slip velocity of helium $\Delta\boldsymbol{u} = \boldsymbol{u_{He}} - \boldsymbol{u}$, which qualitatively resembles the mean velocity field, but helium exceeds the mean velocities of the mixture by two to three times in both x-

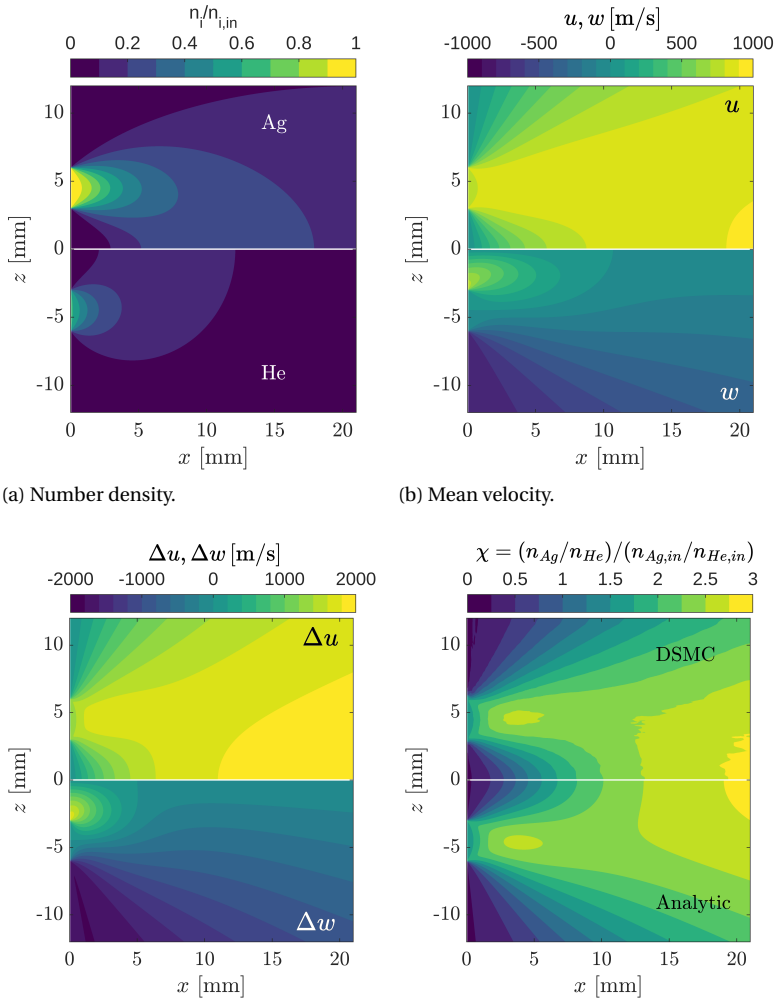

(a) Number density.

(b) Mean velocity.

(c) Slip velocity of helium.

(d) Species separation.

Figure 4.6: Contours of free molecular flow of two interacting plumes of a homogeneous binary gas mixture with a carrier-gas fraction of $y = 0.5$. (a) shows number density of silver in the upper and the one of helium in the lower half; (b) depicts the mean velocity of the mixture and (c) the slip velocity of helium, in the upper half is the x-component, in the lower half the z-component; (d) presents the species separation ratio χ calculated by DSMC in the upper half and calculated from an analytic solution in the lower half.

and z-direction. Figure 4.6d plots the resulting species separation ratio, i.e., the species ratio compared to the species ratio at the inlet

$$\chi = \frac{n_{Ag}/n_{He}}{n_{Ag,in}/n_{He,in}}.$$

The upper half shows the DSMC solution for the mixture; the lower half shows the analytic solution given by Cai et al. [108, 126], which describes the entire flow field for a planar plume as a function of the speed ratio at the inlet $S_{in} = U_{in}/\sqrt{2k_BT/m}$. It can be seen that the DSMC results are in good agreement with the analytical solution. The species separation ratio is above unity in most regions indicating the predominance of silver especially around the jet axes, whereas helium prevails only in the peripheral region. Silver, the heavy species, which exhibits moderate speeds, has a higher number density fraction along the jet axis, whereas the light helium swiftly leaves the computational domain. Farther downstream, the superposition of the two plumes produces an even higher fraction of silver around the symmetry plane. On the one hand, this behaviour explains the small stray deposition of silver in Figure 4.4a and Figure 4.4b. On the other hand, the prevalence of silver and its high molecular weight lets it dominate other flow fields such as the temperature (and consequently the local speed of sound).

4.3.2. RAREFIED FLOW FIELD

When considering collisions, the high slip velocities between silver and helium diminish. The contours in Figure 4.7 compare the flow fields for the case for $y_{He} = 0.1$ in the upper half with the case for $y_{He} = 0.9$ in the lower half, both for $Kn = 2Kn_0$. The normalized number density (Figure 4.7a) decreases in the primary expansion, but increases around the symmetry plane further downstream before expanding again. The interaction shock is expected to lie between the primary and secondary expansion. For the higher carrier-gas fraction, the entire structure is elongated which indicates that the helium focuses the heavy silver first around the primary jet axis — producing a shock further downstream — and then around the secondary jet axis, i.e., symmetry plane. Figure 4.7b shows the slip velocity of helium in x-direction. Please note, that high gradients at some edges of the computational domain can be accounted to the vacuum boundary condition and the higher scattering for $y_{He} = 0.1$ comes from the lower number of helium particles. The slip velocity is an order of magnitude smaller than in the case of free flow (upper half of Figure 4.6c), but still positive in the majority of the flow field. In the shock region, the slip velocity is smaller and for $y_{He} = 0.9$ even partially negative which indicates an earlier shock of the lighter species. Figure 4.7c plots the slip velocity of helium in z-direction. The helium escapes in both direction away from the jet axis downstream of the inlet as for the free molecular flow. The z-velocity slip increases in the shock region and is everywhere directed away from the symmetry plane in the secondary expansion. An especially high local slip Δw_{He} can be found in the shock region for $y_{He} = 0.9$, which coincidences with the negative streamwise slip velocity Δu_{He}. Both indicate that the light helium is ejected out of the shock region by the collisions with the heavy silver.

The resulting species separation ratio (Figure 4.7d) is in most regions above unity as was already the case for free molecular flow. However, in the shock region the smaller or even reversed helium slip velocities compared to the free molecular case cause a dip in species separation. For higher carrier-gas fraction, the species separation is stronger in the expansions, but also the zone of less species separation around the shock is larger which is in agreement with the higher impact of the shock region on the slip velocities. The prevalence of silver comes along with a higher local mass, thus (given a certain temperature) a smaller standard deviation of fluctuational velocities and hence a lower speed

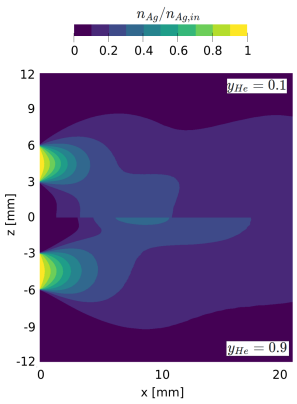

(a) Normalized silver density.

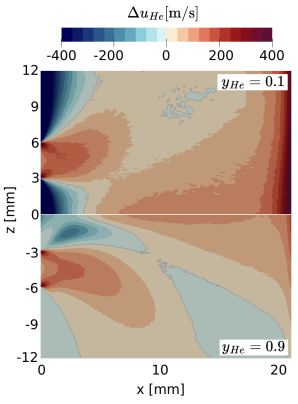

(b) Helium slip velocity in x-direction.

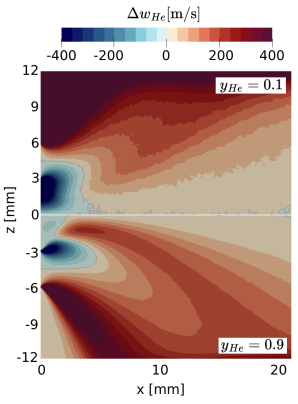

(c) Helium slip velocity in z-direction.

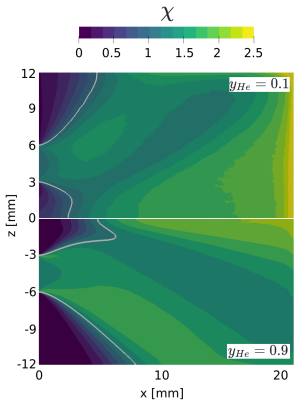

(d) Species separation ratio.

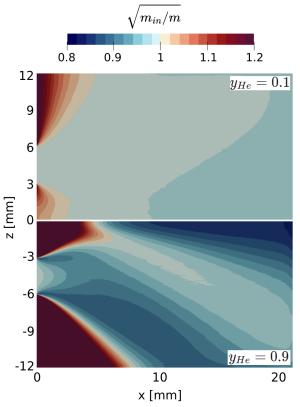

(e) Square root of the inverse of the molecular mass scaled by the inlet molecular mass.

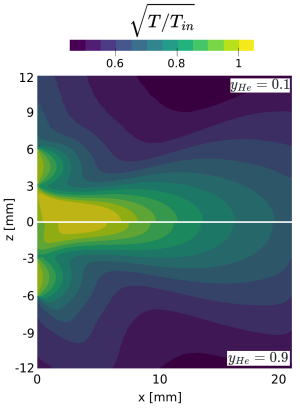

(f) Square root of the temperature scaled by the inlet temperature.

Figure 4.7: Contour plots of two interacting jets of a binary gas mixture for $Kn = 2Kn_0$, in the upper half for a carrier-gas fraction of $y_{He} = 0.1$, in the lower half for a carrier-gas fraction of $y_{He} = 0.9$. (a) shows the silver number density normalized by the inlet silver number density, (b) the helium slip velocity in x-direction, (c) the helium slip velocity in z-direction, (d) the species separation ratio χ where the gray line marks $\chi = 1$, (e) the contribution factor of molecular weight to the change of speed of sound, (f) the contribution factor of temperature to the change of speed of sound. The contour plots are clipped to the range of the corresponding color bar.

of sound, which varies with $a \propto \sqrt{T/m}$. The factors with which local weight and temperature alter the speed of sound can be separated. Figure 4.7e plots the factor due to change of local weight which is the square root of the inverse of the molecular mass normalized by the inlet molecular mass, i.e., $\sqrt{m_{in}/m}$. This factor is close to unity for the majority of the flow field for $y_{He} = 0.1$ implying negligible impact of species separation on the speed of sound, except for the peripheral highly rarefied regions where the factor

reaches high values. For $y_{He} = 0.9$, the molecular mass factor is up to 14% lower in the primary expansion than at the inlet, and up to 18% lower in the secondary expansion. In the shock region, the molecular mass factor ratio rises to values close to unity. The corresponding temperature factor $\sqrt{T/T_{in}}$ is shown in Figure 4.7f. While species separation is directly reflected in a molecular mass factor which deviates from unity, the temperature factor mainly drops due to the expansion and rises due to the interaction at the symmetry plane (which also occur in a pure mixture case). Differences due to species separation are noticeable when comparing the cases of different carrier-gas fractions. However, these mainly occur in the highly rarefied regions, e.g. the peripheral region above the inlet and the early interaction region with high temperatures. In these almost free molecular flow regions, the definition of the speed of sound is pointless. In the core of the expansions and in the shock region, the temperature factor exhibits symmetrical behavior for $y_{He} = 0.1$ and $y_{He} = 0.9$. Hence, it can be concluded that the speed of sound changes because of the change in local molecular mass due to species separation (and changes in temperature are not relevant).

4.3.3. CHANGE OF Γ^+ AND Γ^- CHARACTERISTICS

Due to the previously decribed reduction of speed of sound by the species separation, a fluid element has a narrower domain of influence which is the Mach cone whose half-cone aperture is the Mach angle $\mu = \arcsin\left(\frac{1}{M}\right)$ that decreases for lower speeds of sound. The corresponding envelopes are the Γ^+- and Γ^--characteristics, so that the impact of local species separation on the flow field can be visualized by these characteristics. The course of the characteristics Γ^+ and Γ^- can be expressed by the local flow angle φ and the Mach angle μ and reads

$$\Gamma^+ : \frac{dz}{dx} = \tan\left(\varphi + \mu\right), \tag{4.6}$$

$$\Gamma^- : \frac{dz}{dx} = \tan\left(\varphi - \mu\right). \tag{4.7}$$

(Please note, that the description by characteristics is only strictly applicable for inviscid continuum flow and in the here considered rarefied flow, it aids the understanding since the deviation from equilibrium is small. For more details on the characteristics of supersonic inviscid continuum flows refer to the literature [127].)
Figure 4.8 plots the Mach number field as banded grayscale contours, streamlines in blue and characteristics in brown and beige. The case for a carrier-gas fraction of $y_{He} = 0.1$ is shown in the upper half and the one for $y_{He} = 0.9$ in the lower half. In both cases, the Mach number increases in the primary expansion, decreases when crossing the shock and again increases in the secondary expansion. For the high carrier-gas fraction, the Mach number increases faster — since the stronger species separation cumulates the heavy silver as was shown in Figure 4.7 — and therefore the characteristics form a more acute angle with the streamline. This narrower expansion affects the shock location. The shock region is detected based on the divergence field of the Γ^+-characteristics and marked by the blue continuous contours. While the shock region traverses nearly the entire computational domain for $y_{He} = 0.1$, it fades early for $y_{He} = 0.9$ and bends away

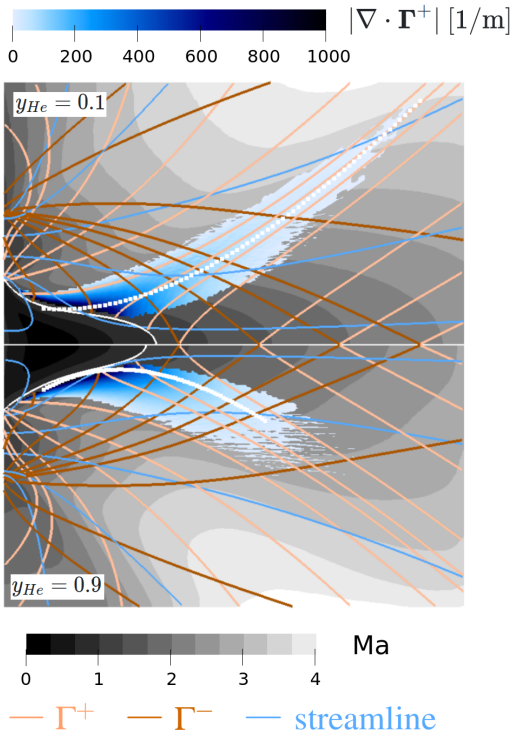

Figure 4.8: Characteristics and shock detection for $y_{He} = 0.1$ in the upper half and $y_{He} = 0.9$ in the lower half at inlet Knudsen number $Kn = 2Kn_0$. The gray, banded contours in the background show the Mach number, the blue, continuous contours represent the region detected as shock region and are colored by $|\nabla \cdot \Gamma^+|$, clipped at 1000m^{-1}. The blue lines are streamlines, the brown lines Γ^- characteristics, and the beige lines Γ^+ characteristics (in the lower part the characteristics are mirrored). The white dotted line is the shock line detected from the regression of the shock region; the white solid line is the sonic line, i.e. $M = 1$.

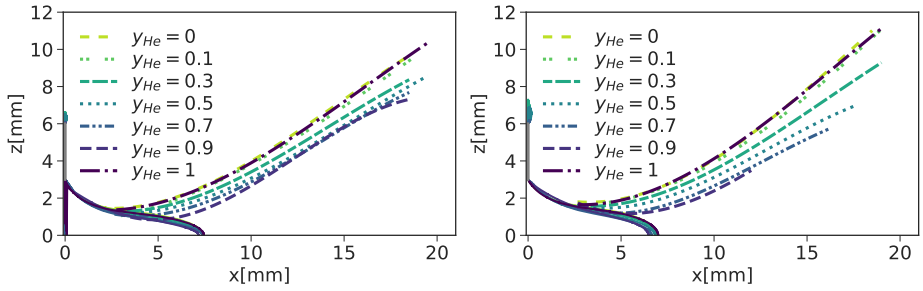

(a) $Kn = Kn_0$.

(b) $Kn = 2Kn_0$.

Figure 4.9: Shock location (dashed or dotted) and sonic line (solid) depending on the carrier-gas fraction for (a) $Kn = Kn_0$ and (b) $Kn = 2Kn_0$.

less from the symmetry plane. (Details of the shock detection method were described in a previous publication [93]. Its benefit over the commonly used isobars [190] or pseudo-Schlieren [191] is that it does not loose its validity when the pre-shock condition is highly inhomogeneous in pressure and density along the shock, which is the case in the present study due to the expansion flow.)
Figure 4.9 plots the shock location and sonic line for different carrier-gas fractions for $Kn = Kn_0$ and $Kn = 2Kn_0$. The subsonic region (marked by solid lines) changes only insignificantly with carrier-gas fraction. For pure helium and pure silver the shock location matches — which is expected due to similarity which depends only on the Mach number and marginally on the Knudsen number [93], which were kept the same for all cases. A small carrier-gas fraction of $y_{He} = 0.1$ has only a negligible impact on the shock location. However, the shock location shifts downstream for higher carrier-gas fractions and the divergence region becomes shorter so that the shock does not traverse through the entire domain but diffuses before. This greater deviation corresponds to the higher change of local mean molecular mass due to species separation. Hence, the information that an interaction takes place can not travel as far upstream, producing a later shock. In addition, the shock region is broader and weaker for the higher carrier-gas fraction, which can be accounted to a more oblique shock due to the shift. The shift of the shock and its weakening is more prominent for a higher degree of rarefaction, i.e. $Kn = 2Kn_0$ in Figure 4.9a, since for longer mean free paths atoms can move a longer distance without collisions thus enhancing species separation [32]. The narrower shock region and weaker shock explain the smaller distance between peaks and smaller peak height observed in the deposition profiles for high carrier-gas fractions. The fading of the shocks reveals why at high carrier-gas fractions and rarefaction the deposition profile seems to resemble the merging of the two plumes (Figure 4.5f) and consequently produces a higher non-uniformity than at lower carrier-gas fractions (Figure 4.3b).

4.4. CONCLUSIONS

We investigated the use of a light carrier gas to support continuous Physical Vapor Deposition processes of a heavier species, in which plume interactions (otherwise) would cause shocks. To evaluate the effect of species separation, we kept the Mach number and the Knudsen number constant, while varying the carrier-gas fraction.
At the inlet, the addition of a carrier gas increases the speed of sound and consequently the mass flow of the coating material from a sonic inlet. In the expansion flow, a higher carrier-gas fraction produces a stronger separation of species that pushes the light species to the offside and focuses the heavy species along the axis. Consequently, stray deposition reduces monotonically with carrier-gas fraction. In the region with a high fraction of heavy species, the Mach number increases more compared to cases with lower carrier-gas fractions. This shifts the transformation of information into a smaller Mach cone which in turn produces a less bent and more oblique, weaker shock. Therefore, the impact of the shock on the deposition profile is reduced. This improves deposition uniformity up to the point at which adding more carrier gas causes a merging of the two plumes into one and uniformity decreases. A higher rarefaction enhances the merging of the plumes.
Thus, the three main requirements concerning the mass flow — high mass flow rates,

low stray deposition and high uniformity — are all facilitated by adding a lighter carrier gas (up to a certain carrier-gas fraction). While we showed these beneficial outcomes only for planar plume interaction with a very specific geometry, the same effects can be expected for other nozzle geometries and three-dimensional interacting plumes. A simplification made in the current study is that the influence of the actual substrate is not considered. The applied vacuum condition removes the gases and does not allow backflow. For the applied metal, i.e., silver, this is may be an appropriate assumption, since the majority of it is expected to stick on the substrate surface. The carrier-gas, i.e., helium, rebounds from the substrate and may affect the upstream flow. Further studies (with the precise geometry) would be necessary to evaluate this affect. The carrier gases will not only impact the transport to the substrate, but also the growth of the film. The exact effect depends on the deposited material, process conditions and desired film morphology. Experiments would be required for a comprehensive evaluation of carrier gas use in continuous PVD.

5

HYBRID COUPLING OF KINETIC MODELS AND DSMC

Jedes Gasmolekül fliegt mit der Geschwindigkeit einer Kanonenkugel und stößt innerhalb einer Zeitsekunde viele millionen mal auf ein anderes. Wer könnte sich da nur ein angenähertes Bild von dem wirren Treiben der Elemente der Körper machen, aber die durchschnittlichen Resultate kann man mit derselben Einfachheit durch kombinatorische Analysis finden, wie die des Lottospiels.

Ludwig Boltzmann [192]

The modelling of interacting gas jets emitted into vacuum is a challenge due to the flow expanding from a continuum state to rarefied flow and dropping back to a continuum state at the interaction shock. The classical approach of coupling a Navier-Stokes-Fourier solver with the particle-based Direct Simulation Monte Carlo technique suffers from stochastical noise at the coupling interface, especially when the flow direction is from the rarefied to the continuum regime. Alternatively, particle-based approximations of the Boltzmann equation such as mimicking the collision process by relaxation models can be used to avoid accuracy loss at the interface. The corresponding models using the Bhatnagar-Gross-Krook (BGK), Ellipsoidal-Stochastical Bhatnagar-Gross-Krook (ES-BGK), Shakov (S-BGK) and Unified-BGK (U-BGK) distributions as target of the relaxation were implemented in the open-source library OpenFOAM. The models were tested on a Poiseuille flow, a thermally-driven cavity flow and Couette flow in the rarefied regime. At the same time, the connection between the local type of equilibrium breakdown, i.e., a high anisotropy of standard deviation or a high skewness in the velocity distribution, and the performance of the models were discussed. To classify the type of equilibrium breakdown, the real and imaginary part of the Fourier-transformed deviation of the local velocity distribution from equilibrium were considered. They were tested for free-molecular and rarefied Couette-Fourier

flow and applied to two interacting jets. However, no clear picture has been found of what type of equilibrium breakdown predominates. For the interacting jet problem, the ES-BGK model performed best giving a perfect match with DSMC for all considered degrees of rarefaction. The BGK predicted a stronger shock, the S-BGK model a more diffuse shock. A hybrid coupling between DSMC and the kinetic model based on a gradient-length local Knudsen number breakdown criterion brought only little improvement.

5.1. INTRODUCTION

Modeling of rarefied flows is a necessity for analyzing gas emitted from comets [193, 194], for sophisticated design of space vehicles [179, 195] and vacuum technology processes [121, 196]. The Boltzmann equation describes the transport of moving and colliding particles in the phase space. The numerical solution of the Boltzmann equation comes at a high computational cost, since it requires a discretization in seven dimensions. To overcome this obstacle Bird introduced the Direct Simulation Monte Carlo (DSMC) method [34], a particle-based method in which the movement and collision of the Boltzmann equation are decoupled. The particles representing the molecules are initially allocated a position and a velocity according to the initial density and velocity conditions. In each iteration of the algorithm, first, the particles move with their current velocity. Second, the particles are binned based on a superposed grid and particles within each bin may (or may not) collide depending on the local collision probability. DSMC is nowadays generally accepted to accurately predict rarefied flows when two conditions are fulfilled. First, a correct closure for the collision probability and the scattering angle has to be applied which ensures the correct macroscopic transport as coefficients empirically perceived and is species dependent. Second, the decoupling of the movement and collision necessitates sufficiently fine spatial and temporal resolutions, and the collision partner selection via the binning requires enough collision partners per bin (or cell) to avoid biased collision processes [34]. These high resolution requirements make DSMC still costly and restrain it to small problems, i.e., at relatively high Knudsen numbers.

Several research groups aim to reduce its computational effort by either improving the computational implementation and underlying computational architecture, e.g., using GPUs, or by altering the model itself. The latter often involves the identification of near-equilibrium regions in which a phenomenological closure at a higher level is possible, e.g., solving the Navier-Stokes-Fourier equations in these regions and coupling with a particle-based solver for rarefied regions [197, 198]. However, the coupling between a continuum and a particle-based method always suffers from difficulties transferring the information from one into the other [198]. This approach works quite well, when the transfer is one-directional from the continuum domain to the particle-based solver. For example in expansion flows in which the initial high density allows for a Navier-Stokes-Fourier solution and the velocity at the coupling interface is directed into the DSMC domain and well above the speed of sound, so that particle crossings from DSMC to continuum domain are unlikely. However, if further downstream the number density rises, e.g., due to shocks, a transfer of the particle information back to Navier-Stokes-Fourier variables suffers from statistical noise.

The loss of information at the model interface can be avoided by restricting the flow solution to particle-based methods in the entire field. Since a sufficient description of a (near-)equilibrium physical state requires considerably more particles than the same description by macroscopic variables, the memory requirement is high as well as the processing of the particle behavior in each time step. To not fall back on DSMC in continuum regions, but to compensate for the higher computational cost, the collision procedure can be replaced by a kinetic relaxation as described by Bhatnagar, Gross and Krook (BGK) [199] with the so called BGK operator. Instead of resolving the collision kinetics to determine the velocity distribution of the next time step, the current velocity

distribution is relaxed towards a target distribution to a degree which depends on the local collision probability. Since it is known that in near-equilibrium regions a sufficient number of collisions relax the velocity distribution towards a target (near-) equilibrium distribution, a kinetic relaxation is a short-cut to model the collision process. This allows for less strict resolution requirements and hence reduces the computational effort in near-equilibrium regions. In highly rarefied regions the DSMC collision step still has to be conducted, as the velocity distribution is too far from a target distribution. These fully particle-based approaches avoid the trouble of transferring information between different descriptions.

The pivotal point for kinetic relaxation is the choice of the target distribution, since it determines the thermodynamic closure and hence the macroscopic transport properties. The classical BGK operator relaxes towards equilibrium, i.e., towards a Maxwellian velocity distribution [199]. This yields a Prandtl number of unity, whereas the correct Prandtl number of gases is approximately 2/3. To obtain the correct Prandtl number different alternative target distributions where introduced, of which two are promising: (i) the Ellipsoidal statistical BGK distribution (ES-BGK) [200], which takes into account the pressure tensor and relaxes towards a velocity distribution which is a Maxwellian transformed by a symmetric positive-definite tensor, (ii) the Shakov distribution (in combination with the BGk operator denoted as *S-BGK* in this Chapter) [201], which considers the heat flux and thus introduces skewness into the target distribution. Multiple researchers applied these models as relaxation to several problems. Roughly speaking, thermally driven and expansion flows — whose velocity distributions exhibit a high anisotropy in standard deviation — are accurately represented by the ES-BGK relaxation model [202–204], while flows with a high skewness in their velocity distribution such as shocks and shear-driven flows can be adequately modeled using the Shakov BGK model (S-BGK) [143, 205]. It can be concluded that it is problem dependent which of the target distributions is well-suited. To obtain more generality, Chen et al. [143] proposed a blending of the two models, the so called Unified BGK model (U-BGK). Its drawback is that for each problem a blending parameter has to be determined, and even small changes of the problem necessitate readjustment. In addition, if the flow is more complicated than rather homogeneous test cases such as Couette-Fourier-Flows, a single global parameter underfits the problem.

Broadly speaking, the ES-BGK model considers non-isotropy of the standard deviation, that is reflected in an even moment, and the Shakov model considers skewness, which is an odd moment. We calculate the real and imaginary part of the local Fourier transform of the particle velocities and compare it with the one for the Maxwellian velocity distribution. Our hypothesis is that, if the real part of Fourier transform deviation is high, the ES-BGK model is more applicable, whereas, if the imaginary part is high, the Shakov model should be used. In free expansion flows, for example, the velocities sort when particles scatter away from each other and stop colliding: the particle velocity component parallel is maintained producing a standard deviation in parallel direction similar to the one initially assigned, whereas the orthogonal component decreases, since non-aligned particles switch their "ray“ until alignment. Thus, a non-isotropy of the standard deviation arises making the ES-BGK model a suitable candidate. On the other hand, inside a shock in a continuum flow, fast particles at a comparatively low temperature from the

pre-shock state mingle with slow particles at a higher temperature from the post-shock state. This causes a bi-modal velocity distribution with a skewness, which indicates that the S-BGK model may be a suitable candidate for modelling. These considerations work well as long as the problems are isolated. However, in the interacting jet problem studied in Chapters 3 and 4 both expansions and shocks occur making the choice of a target distribution for the relaxation more difficult.
This chapter aims at finding a suitable target distribution for modelling the interacting jet problem with a kinetic relaxation model. To this end, we present our implementation of the BGK, ES-BGK, S-BGK and U-BGK model within the dsmcFoamPlus solver of OpenFoam [147]. Then we show the verification of the models for a rarefied Poiseuille flow and a Couette flow. Afterwards we aim at a better understanding of the 'type' of non-equilibrium by considering a free-molecular and rarefied Couette-Fourier flow and a thermally driven flow in a cavity. We use this to analyse the non-equilibrium of the jet interaction. Eventually the BGK, ES-BGK and S-BGK models are applied to the interacting jet problem, once in their pure form and once coupled with DSMC in the rarefied regions.

5.2. NUMERICAL METHOD

Gas flow can be modelled by the Boltzmann equation

$$\frac{\partial f(\boldsymbol{r},\boldsymbol{\xi},t)}{\partial t} + \boldsymbol{\xi}\cdot\nabla_{\boldsymbol{r}} f(\boldsymbol{r},\boldsymbol{\xi},t) = \left(\frac{\partial f(\boldsymbol{r},\boldsymbol{\xi},t)}{\partial t}\right)_{coll}, \tag{5.1}$$

where $f(\boldsymbol{r},\boldsymbol{\xi},t)$ describes the probability density to find at time t a particle at location $\boldsymbol{r}$ with a velocity $\boldsymbol{\xi} = \boldsymbol{u} + \boldsymbol{c}$, which can be split in the local mean particle velocity $\boldsymbol{u}$ and the fluctuational part $\boldsymbol{c}$. The equation describes the temporal and convective change of phase density on its left-hand side and the change due to collisions on its right-hand side. Standard finite difference solution methods suffer from to the high memory requirement for discretizing the six-dimensional phase space. Approaches drastically reducing the space in their discretization such as Lattice-Boltzmann Method (LBM) [206] may sufficiently cope with continuum flows at low Mach number, but are not applicable for high-speed, rarefied flows. Bird [34] utilized the principles underlying the Boltzmann equation — particle movement and collision — to develop the nowadays most common method for rarefied flow, Direct Simulation Monte-Carlo (DSMC). In DSMC, gas molecules are represented by a high number of particles, whose movement and collision are decoupled. While the movement is clearly described, the collision modeling requires a collision probability and scattering to close the equation, which are normally phenomenologically determined, i.e., they are chosen to match empirically available data on viscosity and diffusivity. To obtain an accurate result despite the decoupling and the boxing in parcels, three criteria have to be fulfilled:

1. the cell size dx should be considerably lower than the mean free path λ: $dx < \frac{\lambda}{3}$,
2. the time step size dt should be much smaller than the time between collisions τ: $dt < \frac{\tau}{10}$,

3. the number of particles N_{cell} per cell should be sufficiently large: $N_{cell} > 20$.

These high resolution requirements make DSMC costly particularly at low Knudsen numbers. This is why Gallis and Torczynski [207] and Macrossan [208] replaced the collision operator of the method by a relaxation towards a target distribution following an approach first described by Bhatnagar, Gross and Krook described in the next section.

5.2.1. KINETIC RELAXATION MODELS

The Bhatnagar-Gross-Krook (BGK) collision operator [199] mimics the behavior of the actual collision operator in the Boltzmann equation by relaxing the current velocity distribution f towards a target distribution f_0 at a frequency ν according to

$$\left(\frac{\partial f(\mathbf{x},\mathbf{v},t)}{\partial t}\right)_{coll} = \underbrace{-\nu\left(f - f_0\right)}_{\mathbf{S}:=}. \tag{5.2}$$

The relaxation frequency ν is related to the viscosity. To ensure 'physical' results, the following basic physical laws and properties should be fulfilled by the collision term $\mathbf{S}$ [150]:

1. Mass, momentum and energy shall be conserved

$$m\int \mathbf{S}\,\mathrm{d}\mathbf{c} = 0 \tag{5.3a}$$

$$m\int \mathbf{c}\mathbf{S}\,\mathrm{d}\mathbf{c} = \mathbf{0} \tag{5.3b}$$

$$\frac{m}{2}\int \mathbf{c}^2\mathbf{S}\,\mathrm{d}\mathbf{c} = 0 \tag{5.3c}$$

2. The second law of thermodynamics has to hold, i.e., entropy increases.
3. In equilibrium, the velocity distribution is the Maxwellian distribution f_M.
4. The Prandtl number is close to 2/3.

It depends on the target distribution f_0 whether these criteria are met.

Bhatnagar-Gross-Krook Model (BGK)

The natural choice is to relax towards perfect equilibrium yielding the classical Bhatnagar-Gross-Krook (BGK) relaxation model [199], with the Maxwellian as target distribution

$$f_0^{BGK} = f_M = \left(\frac{m}{2\pi k_B T}\right)^{\frac{3}{2}} \exp\left(-\frac{m\mathbf{c}^2}{2k_B T}\right), \tag{5.4}$$

and the relaxation frequency ν is determined from the dynamic viscosity as

$$\mu = \frac{n k_B T}{\nu} \quad . \tag{5.5}$$

However, the BGK model suffers from over-predicting the Prandtl number to be always unity meaning that the heat transport is underpredicted. To overcome this major drawback in the modeling of rarefied compressible flows, some common modifications of the Maxwellian distribution exist.

Ellipsoidal Statistical BGK Model (ES-BGK)
The Ellipsoidal Statistical BGK-Model [200] (ES-BGK) is applying a stress-dependent distortion tensor to the velocity distribution

$$f_0^{ES} = \frac{1}{\sqrt{\det \mathbf{A}}} \left(\frac{m}{2\pi k_B T} \right)^{3/2} \exp\left(-\frac{m}{2k_B T} \mathbf{c}^T \mathbf{A}^{-1} \mathbf{c} \right) \text{ with} \tag{5.6a}$$

$$\mathbf{A} = \mathbf{I} + \frac{1-Pr}{Pr} \left(\frac{3\mathbf{p}}{tr(\mathbf{p})} - \mathbf{I} \right), \tag{5.6b}$$

where $\mathbf{p} = \langle m\mathbf{c} \otimes \mathbf{c} \rangle$ is the pressure tensor and $\mathbf{I}$ the identity matrix. The relaxation frequency ν_{ES} is determined from

$$\mu = Pr \frac{n k_B T}{\nu_{ES}} \quad . \tag{5.7}$$

With the transformation of the target distribution the correct Prandtl number can be achieved. The ES-BGK target distribution fulfills all requirements for a well-posed kinetic distribution, but does not perform well in non-equilibrium flows in which the distribution is skewed such as in shocks [205].

(Since $\mathbf{A}$ is symmetric positive-definite, it can be split into $\mathbf{A} = \mathbf{BB}$, where $\mathbf{B} = \mathbf{Q}\sqrt{\Lambda}\mathbf{Q}^T$ with the $\mathbf{Q}$ as the orthogonal basis consisting of the eigenvectors of $\mathbf{A}$ and Λ the diagonal matrix of eigenvalues. This is a useful property in the latter implementation.)

Shakov BGK Model (S-BGK)
The Shakov distribution is modifying the velocity distribution based on the heat flux vector $\mathbf{q}$ [201]

$$f_0^S = f_M \left(1 + (1-Pr) \frac{2(\mathbf{c}\cdot\mathbf{q})}{5(k_B T)^2 p} \left(\frac{m\mathbf{c}^2}{k_B T} - 5 \right) \right), \tag{5.8}$$

where $p = tr(\mathbf{p})/3$ and $\mathbf{q} = \langle (m/2\mathbf{c}\cdot\mathbf{c})\mathbf{c} \rangle$. The relaxation frequency is determined by Equation 5.5. The S-BGK model achieves the correct Prandtl number by scaling the resulting heat flux. The S-BGK model considers the skewness of the velocity distribution and hence is suitable for shocks and shear driven flows, but fails to accurately predict thermally driven or expansion flows. Furthermore, it may assume negative values and does not fulfill the second law of thermodynamics.

Unified BGK-Model (U-BGK)
Chen et al. [143] proposed a blending of the ES-BGK and the Shakov model resulting in

Table 5.1: Fulfillment of basic criteria for kinetic models.

	Mass, momentum and energy conservation	2. Law of Thermodynamics	$f_{eq} = f_M$	$Pr \approx \frac{2}{3}$
BGK	✓	✓	✓	✗
ES-BGK	✓	✓	✓	✓
S-BGK	✓	✗	✓	✓
U-BGK	✓	✗	✓	✓

the Unified BGK model (U-BGK), which reads

$$f_0^U = f_0^{ES*} + f_0^{S*} \quad \text{where } Pr = \frac{C_S}{1 - C_{ES}} \text{ and} \tag{5.9a}$$

$$f_0^{ES*} = \frac{n}{\sqrt{\det \mathbf{A}}} \left(\frac{m}{2\pi k_B T} \right)^{3/2} \exp\left(-\frac{m}{2k_B T} \mathbf{c}^T \mathbf{A}^{*-1} \mathbf{c} \right) \text{ with} \tag{5.9b}$$

$$\mathbf{A}^* = \mathbf{I} + C_{ES} \left(\frac{3\mathbf{p}}{tr\mathbf{p}} - \mathbf{I} \right) \text{ , and} \tag{5.9c}$$

$$f_0^{S*} = f_M (1 - C_S) \frac{2(\mathbf{c} \cdot \mathbf{q})}{5(k_B T)^2 p} \left(\frac{\mathbf{c}^2 m}{k_B T} - 5 \right) . \tag{5.9d}$$

The relaxation frequency ν_{UBGK} is determined from

$$\mu = \frac{n k_B T}{(1 - C_{ES}) \nu_{UBGK}} \quad . \tag{5.10}$$

C_{ES} and C_S are the parameters known from the ES-BGK and S-BGK distribution, the achieved Prandtl number depends on them as follows: $Pr = \frac{C_S}{1 - C_{ES}}$. To obtain $Pr = 2/3$, only one of the parameters can be chosen , e.g., C_{ES}, which consequently results in $C_S = 2/3\,(1 - C_{ES})$. The U-BGK inherits the properties of the ES-BGK and S-BGK, fulfilling most criteria for kinetic models except for the second one. Chen et al. claim that it is able to predict all kind of flows in the transition regime fairly accurately — assuming a fitting of the model constant for the studied problem.

The extent to which the kinetic models meet the criteria defined before is listed in Table 5.1. Table 5.2 lists in the first two columns how the collision operator of a certain model modifies the resulting shear stress and/or heat flux to obtain the correct Prandtl number. Afterwards an overview is given for which kind of flows the model is suitable. The last column describes the possible sampling methods, which will be discussed later.

Table 5.2: Properties of kinetic models in respect to the flow. The first two columns are based on information from Chen et al. [143].

	τ	$\mathbf{q}$	Good at	Sampling
BGK	$\tau_{\mathbf{BGK}}$	$\mathbf{q}_{\mathbf{BGK}}$	Equilibrium	Box-Muller transform
ES-BGK	$Pr \cdot \tau_{\mathbf{BGK}}$	$\mathbf{q}_{\mathbf{BGK}}$	Thermally driven, expansion flows [202–204]	Box-Muller transform / Metropolis-Hastings
S-BGK	$\tau_{\mathbf{BGK}}$	$\frac{1}{Pr}\mathbf{q}_{\mathbf{BGK}}$	Shear driven flow, shocks [143, 205]	Metropolis-Hastings
U-BGK	$\frac{1}{1-C_{ES}}\tau_{\mathbf{BGK}}$	$\frac{1}{C_S}\mathbf{q}_{\mathbf{BGK}}$	$Kn < 0.1$ [143]	Metropolis-Hastings

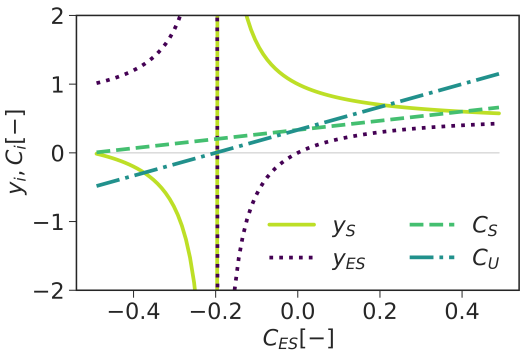

Figure 5.1: The mole fractions and model parameters of the substitute model for the U-BGK distribution (Eqn. 5.15) as a function of the ES-BGK parameter C_{ES}.

PHYSICAL INTERPRETATION OF U-BGK

The U-BGK model promises an elegant blending of ES-BGK and S-BGK model to adapt the relaxation to different types of non-equilibria while maintaining most criteria for kinetic models, especially the Prandtl number criterion. To obtain a rough physical interpretation beyond its mathematical soundness, we rewrite the U-BGK distribution as an allocation of particles either to the ES-BGK or the S-BGK model. First, we use an approximation, proposed by Chen et al. [143] in a different context, to split the ES-BGK distribution in its Maxwellian part and its anisotropic part

$$\tilde{f}_0^{ES} = f_0^M \left(1 + \frac{1}{2}\left(\frac{m}{k_B T}\right)^2 \mathbf{c}^T \mathbf{A}^D \mathbf{c}\right), \tag{5.11}$$

where $\mathbf{A}^D$ denotes the deviatoric part of Eqn. 5.9c. This approximation exhibits the same standard deviation as the ES-BGK distribution. Replacing the first terms of the U-BGK distribution with Equation 5.11 yields

$$\tilde{f}_0^U = f_0^M \left[1 + \frac{1}{2}\left(\frac{m}{k_B T}\right)^2 \mathbf{c}^T \mathbf{A}^D \mathbf{c} \tag{5.12}$$

$$+ (1 - C_S)\frac{2(\mathbf{c}\cdot\mathbf{q})}{5(k_B T)^2 p}\left(\frac{\mathbf{c}^2 m}{k_B T} - 5\right)\right], \tag{5.13}$$

which can be split again in the original parts (we set $Pr = 2/3$, so that $C_S = 2/3(1 - C_{ES})$)

$$\begin{aligned}\tilde{f}_0^U = f_0^M & \\ \cdot \Bigg[& \underbrace{\frac{3C_{ES}}{1+5C_{ES}}}_{y_{ES}} \left(1 + \underbrace{\frac{1+5C_{ES}}{3}}_{C_U} \frac{1}{2}\left(\frac{m}{k_B T}\right)^2 \mathbf{c}^T \mathbf{A}^D \mathbf{c}\right) \\ & + \underbrace{\frac{1+2C_{ES}}{1+5C_{ES}}}_{y_S} \left(1 + \underbrace{\frac{1+5C_{ES}}{3}}_{C_U} \frac{2(\mathbf{c}\cdot\mathbf{q})}{5(k_B T)^2 p}\left(\frac{\mathbf{c}^2 m}{k_B T} - 5\right)\right)\Bigg],\end{aligned} \tag{5.14}$$

where y_i denotes number fractions of particles. By changing the approximation back to the approximate ES-BGK and the S-BGK distributions we obtain

$$\tilde{f}_0^U = y_{ES}\tilde{f}_0^{ES}(C_{ES} = C_U) + y_S f_0^S(C_S = C_U). \tag{5.15}$$

We plot the number fractions y_i and the model parameters C_i over C_{ES} in Figure 5.1. In the range $C_{ES} \in (-0.5, -0.2)$, the number fraction y_{ES} is above unity and correspondingly, y_S is negative in this range. Approximately at $C_{ES} \approx -0.2$ a singularity occurs. Between $C_{ES} \in (-0.2, 0)$, the number fraction y_S is above unity and correspondingly, y_{ES} is negative. Above $C_{ES} = 0$ the fractions are within bounds, but one should note that this region is rather an over-relaxation towards the Shakov distribution for which the ES-BGK compensates by inverting its target distribution. Despite these dubious properties, Chen et al. showed that the U-BGK model produces in certain flows a better agreement with

DSMC than the ES-BGK or the S-BGK models [143]. Namely, the authors found that for both Poiseuille flow and shock flows a model parameter of $C_{ES} \approx 0.25$ produces good results — which does not lie between the ES-BGK ($C_{ES} = -0.5$) and S-BGK model ($C_{ES} = 0$), but over-tunes towards giving a heat flux higher than for any of the pure models.

5.2.2. EQUILIBRIUM BREAKDOWN CRITERION

From a macroscopic view point, non-equilibrium occurs for a high degree of rarefaction, i.e., either low density, and/or steep gradients. In a microscopic sense, this corresponds to the prevalence of the left-hand side of the Boltzmann equation, i.e., the phase density transport, over its right-hand side, which would force the phase density distribution back to equilibrium. The criteria proposed to detect equilibrium breakdown are based either on macroscopic quantities or the phase density distribution.

The former has the advantage that it can be applied to continuum solvers without underlying information on the velocity distribution. Hence, multiple breakdown parameters were suggested related to the development of Navier-Stokes-DSMC-coupled solvers [209–214]. Garcia proposed that the deviation between the local Maxwellian and local first-order Chapman-Enskog approximation may be used as breakdown criterion [211]. The Chapman-Enskog factor, which multiplied with the Maxwellian, gives the Chapman-Enskog distribution reads

$$\Gamma(\mathbf{c}) = 1 + \left(\mathbf{q}^* \cdot \mathbf{c}\right)\left(\frac{2}{5}|c|^2 - 1\right) - \mathbf{c} \cdot \tau^* \cdot \mathbf{c}, \tag{5.16}$$

where $\mathbf{q}^*$ is the normalised heat flux and τ^* the normalised stress from the Navier-Stokes-Fourier equations, e.g., the heat flux is calculated according to Fourier's law from the temperature gradient and not from the local particle velocity distribution. An evaluation therefore requires the calculation of the gradients of velocity and temperature [210]. Garcia [211] chose the breakdown criterion as $B = \max\left(\max_{i,j}(\tau_{ij}), \max_i(q_i)\right) > 0.1$. It should be noted, that this criterion is not Galilean invariant.
Most commonly used is the Gradient-Length Local Knudsen number Kn_{GLL}, which was introduced by Boyd et al. [215] and reads

$$Kn_{GLL} = \max_{\phi \in \{\rho, T, |\mathbf{u}|\}} \left(\frac{\lambda}{\phi}\left|\nabla\phi\right|\right). \tag{5.17}$$

The equilibrium breaks for $Kn_{GLL} > 0.05$ [215]. The velocity and temperature gradient are directly related to the Navier-Stokes-Fourier stress and heat flux like for the criterion by Garcia, but the decisive difference is to relate the gradient to the mean free path. These kind of gradient-based criteria work quite well with continuum methods, since the fields are sufficiently smooth, whereas in statistical methods such as DSMC, the macroscopic field suffers in each cell from statistical fluctuations which are (almost) independent of that in the next cell, which may cause significant gradients just due to statistical fluctuations. For both continuum and particle-based modelling approaches, the gradient of the variables needs to be evaluated, making it a non-local procedure and consequently introducing an idle time for most threads in a parallelized algorithm.
Hence, for particle-based methods the deviation of the local velocity distribution from

equilibrium seems to be a natural choice. Kumar et al. [212] proposed the local Kolmogorov-Smirnov parameter as a measure for this deviation, i.e., the maximum of the deviation between the actual and the equilibrium cumulative density function. Their work suggested that for a Kolmogorov-Smirnov parameter above 1%, the near-equilibrium breaks down. The method suffers from the uncertainty how to best choose bins for calculating the cumulative density function and a high requirement for the sample size (one million velocity samples still gave significant statistical scatter).
Alamatsaz and Venkattraman used the Fourier transform to characterize the deviation of the actual velocity distribution from the corresponding Chapman-Enskog distribution [213]. One beauty of this algorithm is that neither a sampling of macroscopic variables nor a gradient calculation is necessary. Therefore, we investigate this parameter for our case. Instead of considering the deviation from the Chapman-Enskog equation as in the original formulation, we consider the deviation from the Maxwellian and split the deviation in its real and imaginary part. This is motivated by the different applicability of the kinetic models as described in Section 5.2.1. A high real part of the Fourier-transformed deviation from the Maxwellian indicates a good performance of the ES-BGK model, a high imaginary one of the S-BGK model.
The general trivariate normal distribution with a zero mean and a covariance matrix $\mathbf{\Sigma}$ reads

$$f(\mathbf{c}) = \frac{1}{\sqrt{(2\pi)^3}\sqrt{|\mathbf{\Sigma}|}} e^{\left(-\frac{1}{2}\mathbf{c}^{\mathrm{T}}\mathbf{\Sigma}^{-1}\mathbf{c}\right)} \tag{5.18}$$

and its Fourier transform is

$$\circ\!\!- \quad \hat{f}(\boldsymbol{\omega}) = \int_{-\infty}^{\infty}\int_{-\infty}^{\infty}\int_{-\infty}^{\infty} f(\mathbf{c}) e^{-i\boldsymbol{c}\cdot\boldsymbol{\omega}} \,\mathrm{d}c_1\mathrm{d}c_2\mathrm{d}c_3 = e^{-\frac{1}{2}\boldsymbol{\omega}^T\mathbf{\Sigma}\boldsymbol{\omega}} . \tag{5.19}$$

The covariance matrix for the Maxwellian distribution reads

$$\mathbf{\Sigma} = \begin{pmatrix} \frac{k_B T}{m} & 0 & 0 \\ 0 & \frac{k_B T}{m} & 0 \\ 0 & 0 & \frac{k_B T}{m} \end{pmatrix}, \tag{5.20}$$

which eventually yields for the Fourier-transformed Maxwellian

$$\hat{f}_M(\boldsymbol{\omega}) = e^{-\frac{1}{2}\frac{k_B T}{m}\boldsymbol{\omega}^2} = e^{-\frac{1}{2}\tilde{\boldsymbol{\omega}}^2} , \tag{5.21}$$

where the normalized frequency is $\tilde{\boldsymbol{\omega}} = \boldsymbol{\omega}/\sqrt{m/k_B T}$. The Fourier transform of the Maxwellian is entirely in real space and has no imaginary component.
The Fourier transform of a general velocity distribution reads

$$\circ\!\!- \quad \hat{f}(\boldsymbol{\omega}) = \int_{-\infty}^{\infty}\int_{-\infty}^{\infty}\int_{-\infty}^{\infty} f(\mathbf{c}) e^{-i\boldsymbol{c}\cdot\boldsymbol{\omega}} \,\mathrm{d}c_1\mathrm{d}c_2\mathrm{d}c_3 \tag{5.22}$$

$$\approx \underbrace{\sum_{k=1}^{N} \cos(\boldsymbol{c}_k\cdot\boldsymbol{\omega})}_{\Re\left(\hat{f}(\omega)\right)} - \underbrace{i\sin(\boldsymbol{c}_k\cdot\boldsymbol{\omega})}_{\Im\left(\hat{f}(\omega)\right)} , \tag{5.23}$$

where $\Re\left(\hat{f}(\omega)\right)$ denotes the real part of the Fourier transform and $\Im\left(\hat{f}(\omega)\right)$ the imaginary one.
Then, the real and imaginary component of the deviation from the Maxwellian are

$$\Delta\Phi_{\Re} = \int_{-\infty}^{\infty} \left|\Re\left(\hat{f}(\boldsymbol{\omega})\right) - \hat{f}_M(\boldsymbol{\omega})\right| \mathrm{d}\boldsymbol{\omega} \tag{5.24}$$

$$\Delta\Phi_{\Im} = \int_{-\infty}^{\infty} \left|\Im\left(\hat{f}(\boldsymbol{\omega})\right)\right| \mathrm{d}\boldsymbol{\omega}\,. \tag{5.25}$$

The numerical integration is conducted using a Gauss-Hermite integration of second order, with sample points $\omega_{1,2} = \pm\frac{1}{\sqrt{2}}$ and weights $W = \frac{\sqrt{\pi}}{2}$, so that

$$\Delta\Phi_{\Re} \approx W^3 \sum_{k=1}^{2}\sum_{l=1}^{2}\sum_{m=1}^{2} \left|\Re\left(\hat{f}(\omega_k,\omega_l,\omega_m)\right) - \hat{f}_M(\omega_k,\omega_l,\omega_m)\right| \tag{5.26}$$

$$\Delta\Phi_{\Im} \approx W^3 \sum_{k=1}^{2}\sum_{l=1}^{2}\sum_{m=1}^{2} \left|\Im\left(\hat{f}(\omega_k,\omega_l,\omega_m)\right)\right|\,. \tag{5.27}$$

The sampling of these data is time consuming, especially since they do not coincide with data which are commonly sampled from a DSMC simulation anyway.

5.2.3. IMPLEMENTATION

The collision step in the dsmcFoamPlus solver of OpenFoam-2.4.0-MNF was substituted by a relaxation step, keeping the remaining algorithm the same as shown in Figure 5.2a. This enables us to use the kinetic models in the high density and DSMC in the rarefied regions. The details of the relaxation step for the particles in one cell can be found in Figure 5.2b: First the algorithm loops over all particles to sum up their pre-collision momenta and kinetic energies. In case of using the Metroplis-Hastings-algorithm (used for ES-BGK, Shakov and U-BGK) a burn-in for the cell velocity distribution is conducted, sampling a certain number of velocities from the distribution without using them. Afterwards it is looped over the particles again deciding whether a relaxation takes place or not based on the cell density and the collisional diameter (which is temperature dependent). If a collision takes place, a new velocity is sampled (in case of the Metropolis-Hastings algorithm again ten samples are not used to decorrelate the samples) and assigned to the particle. The post-collisional momenta and kinetic energies are summed up. Eventually the velocities are shifted and scaled based on the ratio of the pre- to post-collisional momenta and kinetic energies to conserve momentum and energy.
The speed-up of the kinetic models comes on one side from the higher accuracy when loosening the resolution criteria for cell and time step size by a factor two theoretically leading to a speed-up by a factor 4 in two-dimensional cases and by a factor 8 in three-dimensional cases, on the other side from limiting the number of operations to the number of particles in the cell, which may have especially in dense regions a major effect. Kumar et al. reports a speed-up of factor two for a two-dimensional rarefied case [216] and Pfeiffer a speed-up about 17 for a three-dimensional case [217]. This model is feasible for near-continuum regions of the flow which in the studied case is the region after the nozzle, in rarefied regions DSMC will be used. To switch between the regions the gradient length local Knudsen number is used.

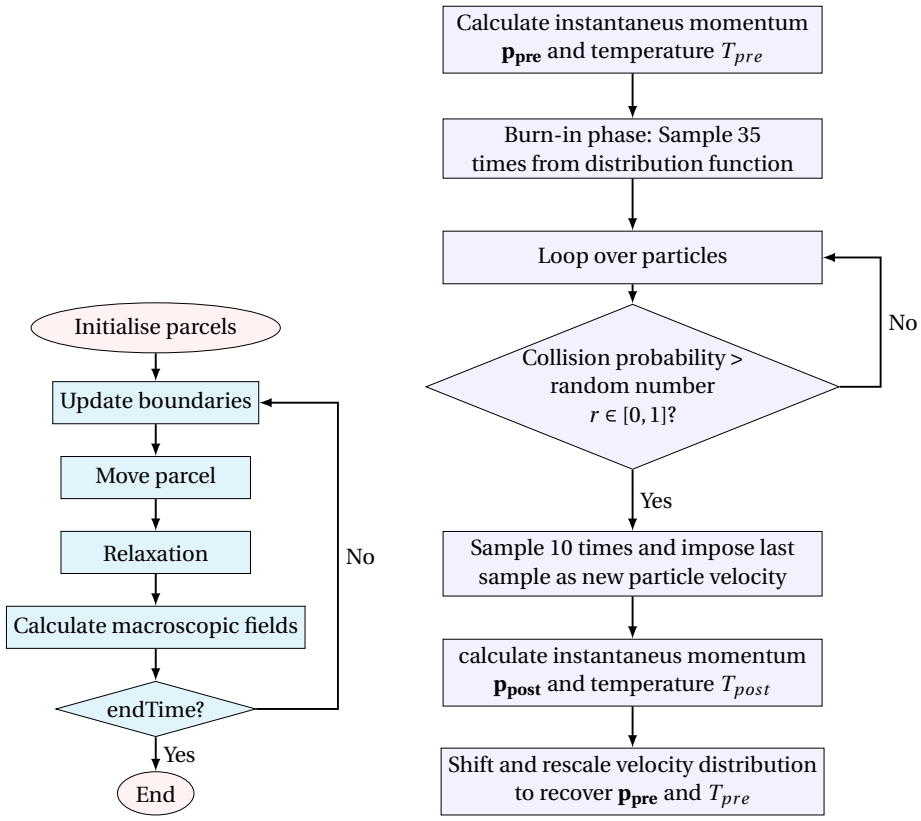

(a) Kinetic Model. (b) Metropolis-Hastings algorithm.

Figure 5.2: Flow charts of (a) DSMC algorithm adapted to use kinetic relaxations instead of collisions and (b) Metropolis-Hastings algorithm to sample velocities from a target distribution.

5.3. RESULTS

VERIFICATION BY A POISEUILLE FLOW

To verify the setup we use Poiseuille flow as described by Chen et al. [143]. The case is dimensionless. We set the channel height $L = 1$, the initial conditions at $T_0 = 1$, $p_0 = 1$, $\rho_0 = 1$, $S_0 = \sqrt{2k_BT/m} = 1$. The considered monatomic gas was modelled by the Hard-Sphere model, i.e., $\omega = 0.5$. The Knudsen number reads

$$Kn = \sqrt{\frac{\pi}{2}} \frac{\mu_0 \sqrt{k_B T/M}}{p_0 L}$$

and was set to $Kn = 1$.

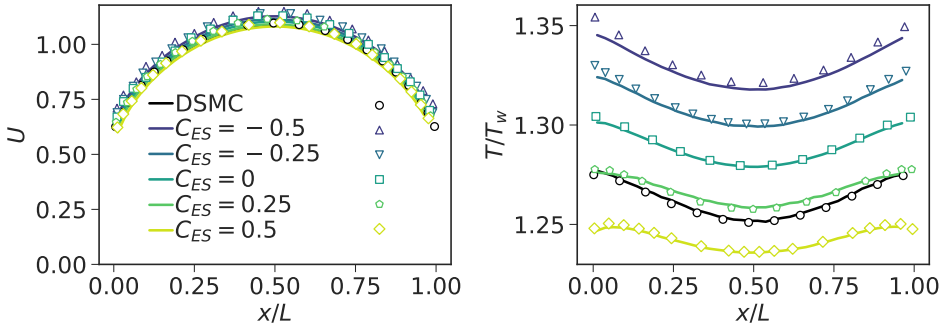

(a) Velocity (b) Temperature

Figure 5.3: Line profiles for a Poiseuille flow at $Kn = 1$ and $G = 1$. The results from the implemented U-BGK model is denoted by solid lines, results by Chen et al. [143] are denoted by symbols.

With the viscosity of the Hard-Sphere model, i.e.,

$$\mu = \frac{5}{16}\sqrt{\frac{k_B T/m}{\pi}}\frac{m}{d^2}, \tag{5.28}$$

the molecular diameter is

$$d = \sqrt{\frac{5k_B}{16\sqrt{2}}} \tag{5.29}$$

The mass of the species is set in a manner that the speed ratio $S = \sqrt{2k_B T/m}$ equals unity.
The dimensionless gravity is set to 1. For the non-dimensionalization:

$$g = g^* 2k_B T_0 d = g^* 2k_B \sqrt{\frac{5k_B}{16\sqrt{2}}} \tag{5.30}$$

Figure 5.3 shows the velocity and temperature over the channel height obtained by DSMC and the U-BGK model with several values for C_{ES} compared to results by Chen et al. [143] for validating of the implementation. The velocity (Figure 5.3a) exhibits a parabolic profile and a high slip at the walls. The ES-BGK model (i.e., $C_{ES} = -0.5$) gives the highest velocity. With higher C_{ES} the velocity marginally decreases. The temperature (Figure 5.3b) is approximately 1.3 of the wall temperature with a dip in the region of low shear, i.e., in the center, and a temperature jump at the walls. The results of the code are in good agreement with the solution by Chen et al. [143]. The profile best matching with DSMC is the one for $C_{ES} = 0.25$ which does not lie between the ES-BGK and the S-BGK model, but beyond the Shakov limit, meaning that the heat flux appears to be considerably higher than the one predicted by a BGK model.

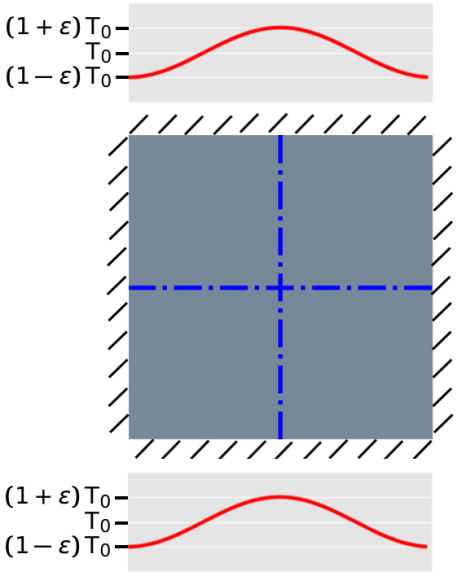

Figure 5.4: Geometry and temperature boundary condition of the thermal cavity flow, with adiabatic vertical walls and a sinusoidal temperature profile at the horizontal walls. The dashed blue lines denote symmetries, so that is it sufficient to simulate one quarter of the domain.

5.3.1. THERMAL CREEP FLOW IN A CAVITY

In 1879, Maxwell predicted thermal creep flow for rarefied gases, which is caused "by inequalities of temperature at the surface of the solid, which give rise to a force tending to make the gas slide along the surface from colder to hotter places" [218]. It is highest for $\lambda \approx \nabla T/T$. We consider a standard thermal creep flow case in a cavity as depicted in Figure 5.4, whose lower and upper wall are kept at a spatially varying temperature profile

$$T(x) = T_0\left(1 - \epsilon\cos\left(\frac{2\pi x}{L}\right)\right),$$

where $T_0 = 300\,\mathrm{K}$ and $\epsilon = 0.5$. The side walls are isothermally at $1 - \epsilon T_0$. The Knudsen number is $Kn = 1$ and the medium is argon. Owing to vertical and horizontal symmetries, the case can be reduced to one quarter, which is chosen to be the lower left one. Figure 5.5 shows scaled temperature contours $T_\epsilon = 1/\epsilon(T/T_0 - 1)$ in the left, lower quarter of the cavity for different models. In Figure 5.5b, the DSMC solution predicts a low temperature in the left corner and a high temperature on the right, which induces a strong flow along the lower wall marked by velocity vectors. A large counter-clockwise circulation occurs with an overall transport of hotter gas from the hot wall region towards the cold wall region. The scaled temperature varies rapidly along the wall, where the particles assume the wall temperature after wall collisions. The temperature variations are also high where the recirculation leaves or arrives at the heated wall. In the upper half, the temperature changes are more moderate. For the kinetic models, the scaled temperature contours are shown with the isotherms in black and the corresponding isotherms

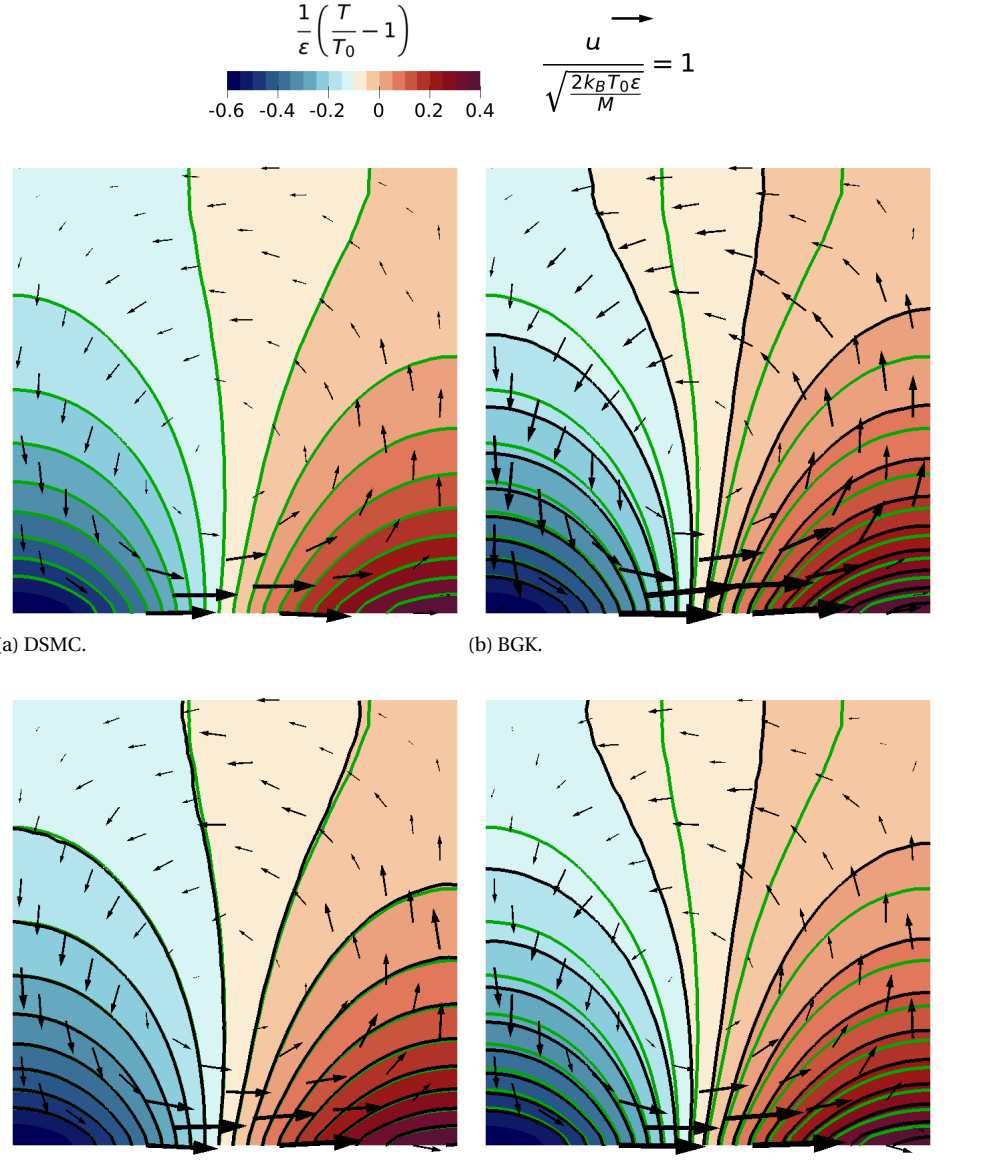

(a) DSMC.

(b) BGK.

(c) ES-BGK.

(d) S-BGK.

Figure 5.5: Scaled temperature contours in a temperature-driven cavity flow for (a) DSMC, (b) BGK, (c) ES-BGK and (d) S-BGK. The black arrows depict the velocity field (the reference vector is plotted next to the legend). The green solid lines denote the isotherms of the DSMC solution and indicate thus the deviation from the isotherms of the different relaxation models shown by black solid lines.

for the DSMC in green. The BGK model, presented in Figure 5.5b, gives qualitatively the same picture, but the isotherms are shifted downstream compared with the DSMC solution, which is in agreement with the higher velocities. The ES-BGK model's thermal isocontours (Figure 5.5c) as well as the velocity field match the ones of the DSMC. The S-BGK model (Figure 5.5d) produces a temperature and velocity field similar to the BGK overpredicting the downstream transport of temperature.
The velocity distribution of this simple looking flow field is more complex than the previous one of the Poiseuille flow. The velocity distributions (for the DSMC) were sampled for points along a streamline starting at the top of the computational domain and once cycling through the flow domain (Figure 5.6a). A typical velocity distribution at the marked red point is shown in Figure 5.6b. It is clear that it deviates from the equilibrium function and that the standard deviation is non isotropic and the skewness is non zero. The normalized temperature per direction

$$\Theta_i = \frac{1}{\epsilon}\left(\frac{T_i}{T_0} - 1\right)$$

(Figure 5.6c) and the skewness of the velocity distribution μ_i (Figure 5.6d) are plotted over the streamline coordinate s. At the top ($s = 0$), the temperatures have the same value and the skewnesses are zero. The normalized temperatures decline on the path along the adiabatic wall, with the one in x-direction having a higher value and the one in y-direction a lower value than the mean temperature. At the same time, the skewness in y-direction becomes negative, whereas the one in x-direction stays at zero. Along the bottom wall, the normalized temperatures coincide with each other and steeply climb from a value near $\Theta = -0.5$ to $\Theta = 0.3$. Also the skewness in y-direction rises from negative to positive values, whereas the skewness in x-direction is negative. Afterwards the temperatures separate again, where the normalized temperature in y-direction this time exceeds the one in x-direction. The skewness is positive and falls to zero at the top of the computational domain. The temperature deviations at the beginning and end of the streamline can be explained with the direction the high velocity particles have in a certain region: particles which collided with the hot region of the bottom wall, i.e., close to $x = 0.5\,\text{mm}$ exhibit a higher standard deviation than the ones which collided with the cold region. If they move to the adiabatic wall, they travel horizontally and their high standard deviation introduces a higher temperature in x-direction than y-direction, whereas if they move up vertically they contribute to the high temperature in y-direction in the center of the cavity. All particles colliding with the bottom wall adopt a velocity according to the temperature of the wall which explains the good agreement of all temperatures and their rise along the wall. Particles which collide with a symmetric wall, i.e., either the one at the symmetry line or the adiabatic wall, will switch only their sign of wall normal velocity, thus suppressing any skewness in x-direction. The particles colliding with the bottom wall have a wide range of velocities when approaching the wall, either a very low standard deviation of velocity when leaving the cold wall and a high one when leaving the hot wall, thus introducing a negative skewness in y-direction upstream the bottom wall and a positive one downstream the bottom wall. At the bottom wall, the temperature gradient drives the flow by accelerating the slower incoming particles to high velocities. This consideration illustrates how complicated the velocity distribution can become even in small test cases and how fast the kind of non-equilibrium can

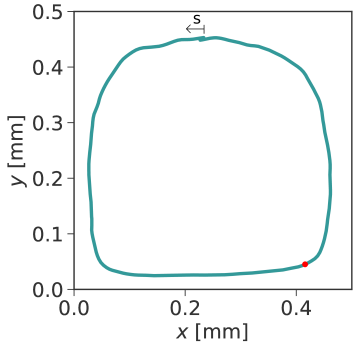

(a) Streamline.

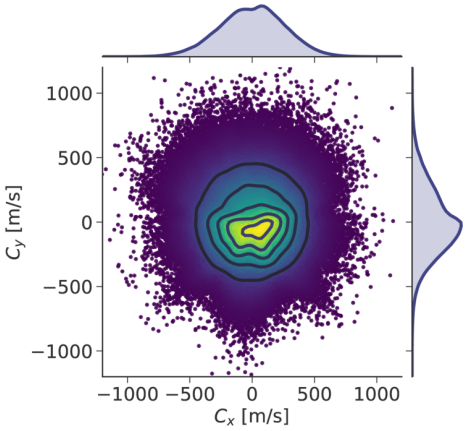

(b) Velocity distribution.

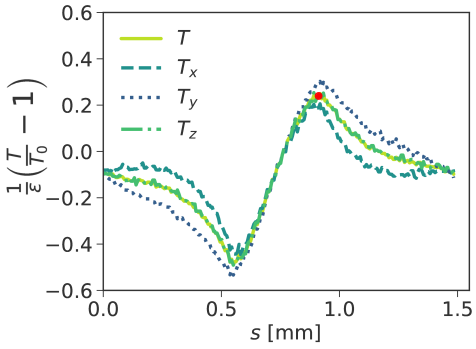

(c) Temperature.

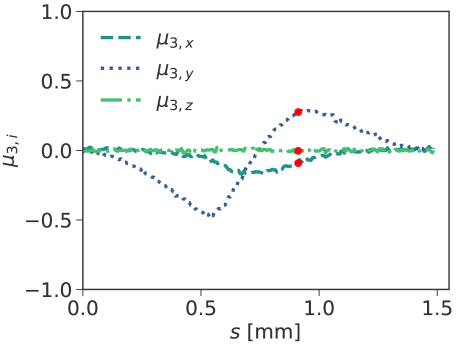

(d) Skewness.

Figure 5.6: Velocity distribution along the circulation in the thermally-driven cavity flow. (a) Considered streamline in the lower left quarter of the cavity; (b) Scatterplot of the velocity distribution at a point marked in red in (a); (c) temperatures along streamline; (d) skewness of the velocity distribution along streamline.

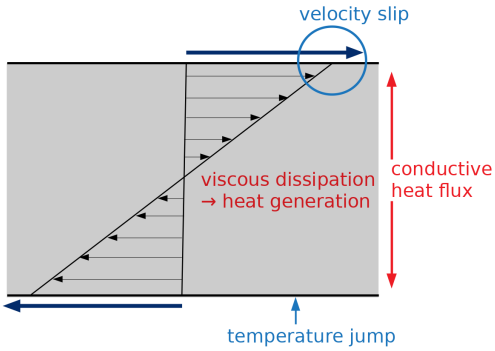

Figure 5.7: Sketch of physical phenomena appearing in rarefied Couette flow.

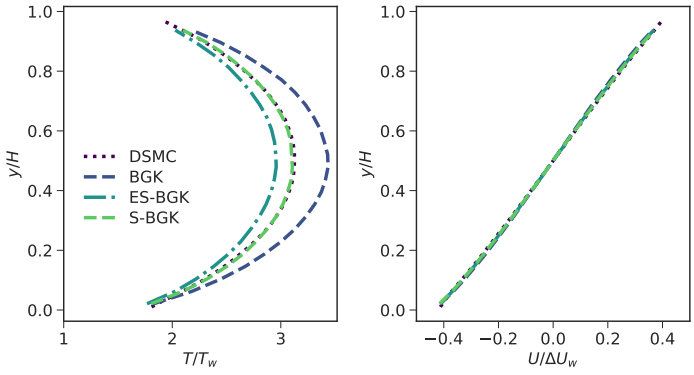

(a) Temperature profile (b) Velocity profile.

Figure 5.8: Line profiles for a Couette flow of argon at a Knudsen number of $Kn = 0.14$, wall temperatures at $T_w = 273\,\mathrm{K}$ and a wall velocity difference of $\Delta U_w = 1500\,\mathrm{m\,s^{-1}}$; (a) shows the temperature profile, (b) the velocity profile along the channel width.

change — owing the good match of the ES-BGK model more to a serendipity than a sophisticated choice.

5.3.2. SHEAR-DRIVEN FLOW — COUETTE FLOW

Another simple test case to explore the behavior of the kinetic models is a rarefied Couette flow as sketched in Figure 5.7. Two infinitely extended isothermal plates force a shear flow on the confined Argon gas by moving in opposite direction. The rarefaction yields an incomplete transfer of momentum and temperature from the walls to the fluid resulting in a velocity slip and a temperature jump. The heat generation due to the viscous dissipation and the limited transfer of heat to the walls due to the rarefaction give rise to a parabolic temperature profile along the wall normal direction. The amplification of the temperature profile depends on the Prandtl number, the ratio of viscous

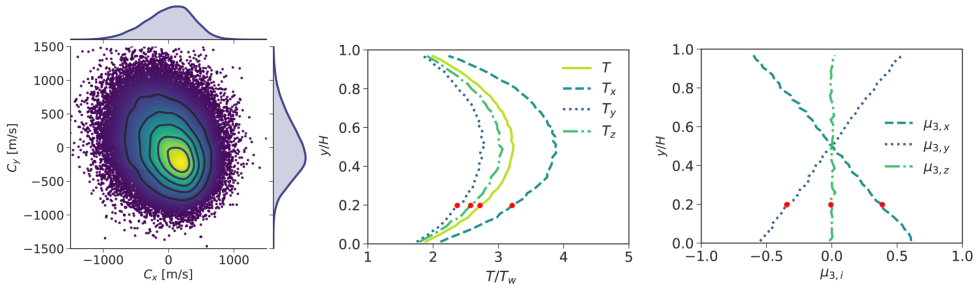

(a) Velocity distribution. (b) Temperatures. (c) Skewness of velocity distribution.

Figure 5.9: Velocity distribution for a Couette flow of argon at a Knudsen number of $Kn = 0.14$, wall temperatures at $T_w = 273\,\mathrm{K}$ and a wall velocity difference of $\Delta U_w = 1500\,\mathrm{m\,s^{-1}}$; (a) shows a typical velocity distribution at $y/H \approx 0.2$; (b) the temperatures in different directions along the channel width; (c) the skewness along the channel width.

diffusion to thermal diffusion. The effects of velocity slip, temperature jump and temperature overshoot increase for higher Knudsen numbers and are a good indicator in which regions the models are applicable.

A Couette flow of argon at a Knudsen number $Kn = 0.14$ (based on the channel height) was simulated using the BGK, ES-BGK, S-BGK models as well as DSMC. The wall temperature was isothermally kept at $T_w = 273\,\mathrm{K}$ and the difference between the wall velocities was $\Delta U_w = 1500\,\mathrm{m\,s^{-1}}$. For the temperature DSMC predicts a jump of 0.6 of the wall temperature and a temperature build-up at the channel centre of 3.4 times the wall temperature. The velocity profile is linear with a small wall velocity slip of 0.1 of the applied wall velocity difference. As expected, the BGK model overpredicts the temperature overshoot. The ES-BGK model slightly underpredicts the temperature around the channel centre. The S-BGK model matches the DSMC perfectly. This is in agreement with the properties of the models as described in Section 5.2.1, since rarefied shear-driven flows produce a skewed velocity distribution. This can be exemplary seen in Figure 5.9a where a typical distribution of the fluctuational particle velocities at $y/H \approx 0.2$ is depicted. A broad, wide tail of high velocities in negative x- and positive y-direction occurs giving rise to a positive skewness in x-direction and a negative one in y-direction. Also the temperatures equilibrium is broken, which is better visible in Figure 5.9c which shows the temperatures per direction accros the channel height. The temperature in x-direction T_x rises to $T/T_w \approx 3.9$, since the high shear introduces large velocity differences in this direction and particles mingle between layers due to the rarefaction. Whereas particles with a high y velocity component quickly collide with the wall leveling off the temperature T_y. The skewness linearly changes across the channel being positive in x-direction and negative in y-direction at the bottom, to the opposite at the top. These measures may seem arbitrary as they depend on the choice of directions and multiple measures have to be considered to gain an understanding of the non-equilibrium. Therefore, in the next section we explore an alternative way to classify equilibrium breakdown.

The speed-up of the rarefied Couette flow simulations for the kinetic model compared to the DSMC is shown in table 5.3 for the BGK, ES-BGK and S-BGK model. The BGK speeds

	comp. cost (scaled by DSMC)	time frac. spent in move	time frac. spent in collide or relax	Total No. of particles	No. of cells along x-axis	No. of cells along y-axis	time step size in 10^{-5} s
DSMC	1	93.74%	2.19%	192843	10	200	3.5
BGK	0.167	79.26%	7.21%	92289	5	100	7
ES-BGK	0.224	64.13%	18.32%	92289	5	100	7
S-BGK	0.225	70.08%	13.77%	92289	5	100	7

Table 5.3: Computational cost (scaled by the one of the DSMC), fraction of time spend in move and collide or relax functions and the resolution for the DSMC and the kinetic models for Couette flow at $Kn = 0.14$.

up the simulation by a factor of ≈ 6 and the ES-BGK and S-BGK model by a factor of ≈ 4.5. The latter matches the speed-up stated by Kumar et al. [216], who contributed the main effect to the loosened resolution criteria. Since the cell length is twice as long as for DSMC, but the required number of particles per cell is 40, the total number of particles halves (in a planar flow). In addition, the allowed time step size doubles. This produces an expected speed-up of 4.

Approximately 94% of the computational time is spent on the movement of particles for the DSMC, and only approximately 2% in the collision step. Note that in less rarefied flow, the proportions would shift to the collisions. For the kinetic models, the time spent in the relaxation step is between 7% for the BGK and 18% for the ES-BGK model. The higher overhead for the ES-BGK can be explained on the one hand by the requirement to sample the stress tensor and on the other by the use of the Metropolis-Hastings algorithm compared to the Box-Muller transform for the BGK model. While the S-BGK model needs to use a sampling algorithm, the decomposition stated in Section 5.2.1 could transform the BGK distribution to an ES-BGK distribution eliminating the efficiency loss due to rejected velocities occurring in a Metropolis-Hastings algorithm.

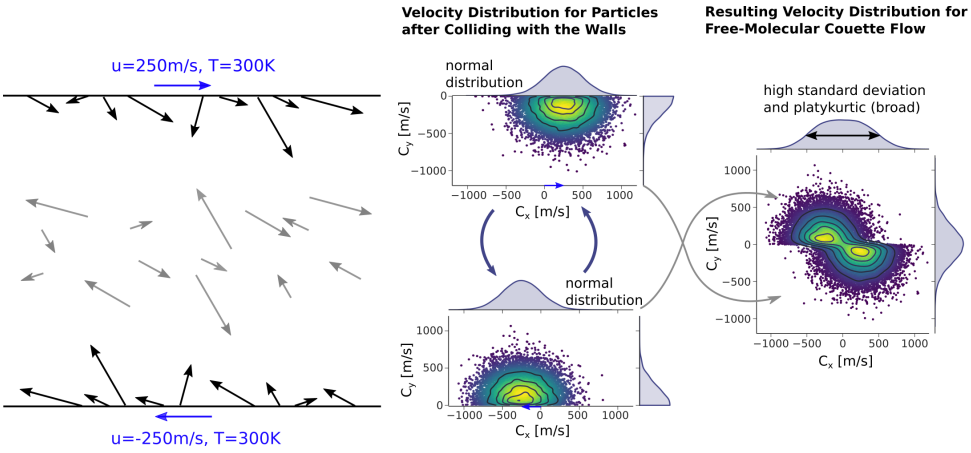

Figure 5.10: Free molecular Couette flow at a $\Delta u = 500\,\mathrm{m\,s^{-1}}$ and $T = 300\,\mathrm{K}$. The flow domain and boundary conditions are shown on the left together with a qualtitative sketch of the particle velocities of the particles after collision with the wall (black) and in the bulk region of the channel (gray). The quantitative particle distributions after colliding with the wall are shown in the center, their superposition, which it the total velocity distribution in the free molecular Couette flow, is shown on the right.

5.3.3. COUETTE-FOURIER FLOW

The previous section showed the applicability of the Shakov distribution in shear-driven rarefied flows with the comment that the occuring velocity distributions are skewed. To understand the produced velocity distributions better we consider free molecular and rarefied Couette-Fourier flows. Couette-Fourier flows occur between two infinitely extended plates, that move with differing velocities, producing a Couette flow, and / or are kept at differing temperatures, producing Fourier Flow. Without collisions the distribution of fluctuational velocity does not depend on the location and is the superposition of the two half normal distributions from the wall collisions, weighted with the particle flux colliding with the wall. This simplicity in combination with the vast variety of producible velocity distributions makes it an ideal candidate for evaluating the breakdown (without considering the use of the kinetic models as neither collision nor relaxation is applied).

COUETTE FLOW

The setup and velocity distribution of a free molecular Couette flow case is depicted in Figure 5.10. Both walls are kept at 300 K and move with a velocity of $250\,\mathrm{m\,s^{-1}}$ in opposing directions. When a particle collides with the upper (lower) wall, it will get a x-velocity assigned from a Maxwellian distribution, whose mean is shifted to $250\,\mathrm{m\,s^{-1}}$ ($-250\,\mathrm{m\,s^{-1}}$), and a y-velocity from a half Maxwellian distribution. The y-velocities determine how fast particles cross the channel and collide with the the other wall. Since both half Maxwellian distributions are for the same temperature, i.e., they have the same standard deviation, the exchange between velocity distribution is at the same speed, so that the total velocity distribution is Maxwellian in y-component.The x-velocity distribution has a higher standard deviation and the kurtosis is lower than that of a Maxwellian.

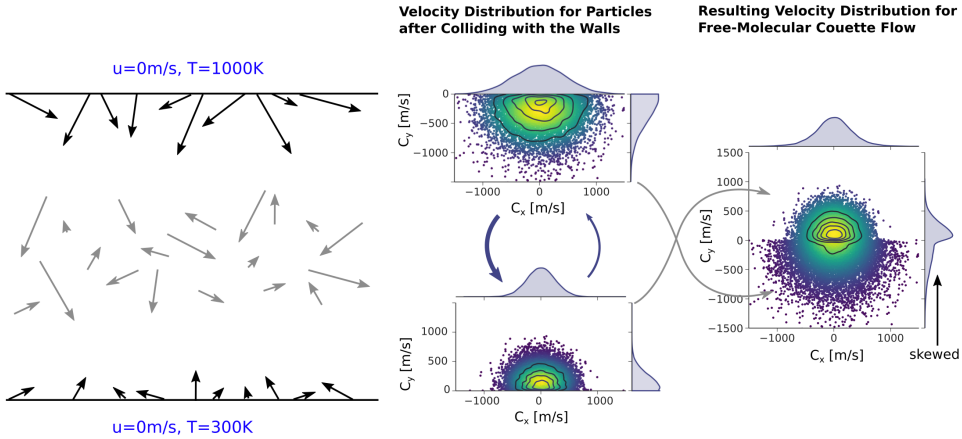

Figure 5.11: Free molecular Fourier flow at $\Delta T = 700\,\mathrm{K}$. The flow domain and boundary conditions are shown on the left together with a qualtitative sketch of the particle velocities of the particles after collision with the wall (black) and in the bulk region of the channel (gray). The quantitative particle distributions after colliding with the wall are shown in the center, their superposition (weighted with the number of wall collisions per time), which it the total velocity distribution in the free molecular Couette flow, is shown on the right.

FOURIER FLOW

For the considered Fourier flow in Figure 5.11, both walls are kept still, but the upper wall has a higher temperature of 1000 K, whereas the lower wall has a temperature of 300 K. Both velocity distribution for the populations from a wall are Maxwellian, but the standard deviation is much higher for the warmer wall. The on average higher y-velocities from the upper wall feed the population of the lower wall much faster than the other way round. In the total velocity distribution, the y-velocity distribution is therefore skewed, with more particles moving up. In addition, the kurtosis of the x-component changes, but less significantly than the skewness of the y-velocity.

COUETTE-FOURIER MAP

The real, the imaginary and total Fourier transform deviation from equilibrium is shown in Figure 5.12 for a range of Couette-Fourier flows. The equilibrium case is at $T_0 = 300\,\mathrm{K}$ and zero wall velocity, so that both the real and imaginary part are zero. For a higher difference in wall velocities, the real deviation (Figure 5.12a) increases, which denotes a change in the even moments, for example a higher kurtosis or different standard deviations in different directions. This change also depends on the wall temperature, with a slower smaller of the real deviation for moderately high wall temperatures and a faster increase for moderately low all temperatures)compared to 300 K, for wall temperatues close to zero high valus of real deviations are reached (the lowest included wall temperature is $T_w = 10\,\mathrm{K}$, since the time until reaching a steady state otherwise takes to long). However, the dependence on the wall velocity difference prevails over a significant range the one on the wall temperature difference. With deviating wall temperatures, the imaginary deviation increases (Figure 5.12b). It is worth noting that the increase of the imaginary part is symmetric around the equilibrium temperature, when scaling the temper-

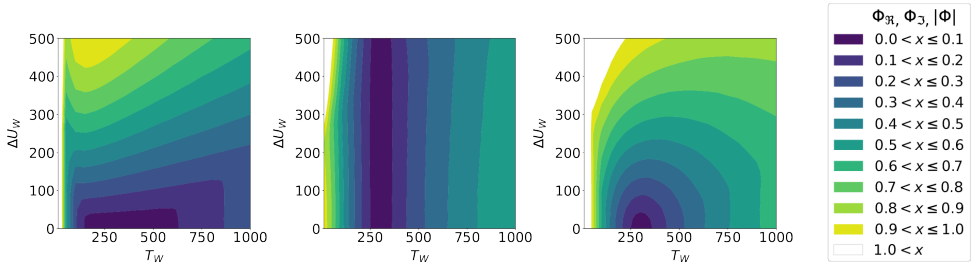

(a) Real deviation $\Phi_{\Re}$ (b) Imaginary deviation $\Phi_{\Im}$ (c) Total deviation $|\Phi|$ (L2-norm)

(d) Real deviation $\Phi_{\Re}$ (e) Imaginary deviation $\Phi_{\Im}$ (f) Total deviation $|\Phi|$ (L2-norm)

Figure 5.12: Fourier maps for the deviation of the velocity distribution from a Maxwellian for a Couette-Fourier flow. (a)–(c) for free molecular flow, (d)–(e) for $Kn = 0.5$; (a), (d) real part of deviation, (b), (f) imaginary part of deviation, (c), (g) L2-norm deviation.

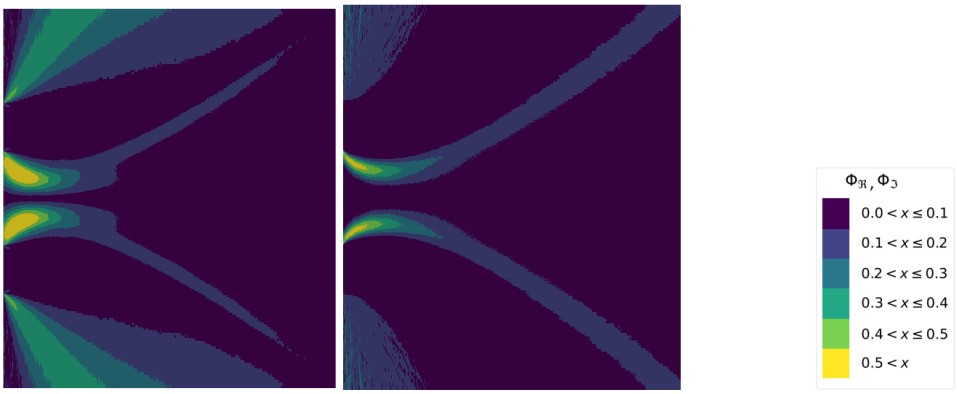

(a) Real deviation $\Phi_{\Re}$ (b) Imaginary deviation $\Phi_{\Im}$

Figure 5.13: Fourier transform maps for the deviation of the velocity distribution from a Maxwellian for interacting jets with inlet stagnation Knudsen number $Kn_0 = 0.13$.

ature as $\sqrt{(T_w / T_0)}$. Also the real deviation marginally increases. The L2-norm depicted in Figure 5.12c shows a smooth increase when moving away from the equilibrium conditions.

Figures 5.12e–5.12f show the same measures for a rarefied flow at $Kn = 0.5$. The qualtitative behavior corresponds to the free molecular case, but the values are significantly lower. With a further decrease in Knudsen number, the flow field becomes less homogeneous — e.g., the shear-driven Couette flow at $Kn = 0.14$ (Section 5.3.2) showed an extreme increase in temperature around the center plane producing a heat flux from the bulk towards the walls. In such a case, an average value of $\Phi_{\Re}$ and $\Phi_{\Im}$ for the entire flow field does not make sense. In summary, the kind of equilibrium may be determined at a local level, but global statements for a flow are difficult to make.

5.3.4. INTERACTING JETS

DEVIATION FROM EQUILIBRIUM

Our eventual aim in developing rarefied gas dynamics solvers is to be able to solve more complex cases, in which different kinds from deviations of equilibrium occur such as the interaction of jets previously discussed in Chapter 3. Two effects introduce non-equilibrium in this kind of flow: (1.) the breakdown of thermal isotropy due to the velocity sorting in the expansion, (2.) the bimodal velocity distribution in the shock region due to the steep gradient in temperature in combination with a long mean free path. In (1.) the free expansion, the particles align their path to the direction of the velocity they attained in their last collision. Assuming several beams emerging from a point source, a particle whose velocity is not aligned with the beam will leave this beam and cross the other beams until it ends on the beam which is aligned to the particle velocity. Thus, the orthogonal temperature $T_\perp$ will decline rapidly when leaving the source, whereas the parallel temperature $T_\parallel$ after an initial decline will retain its value. Hence,

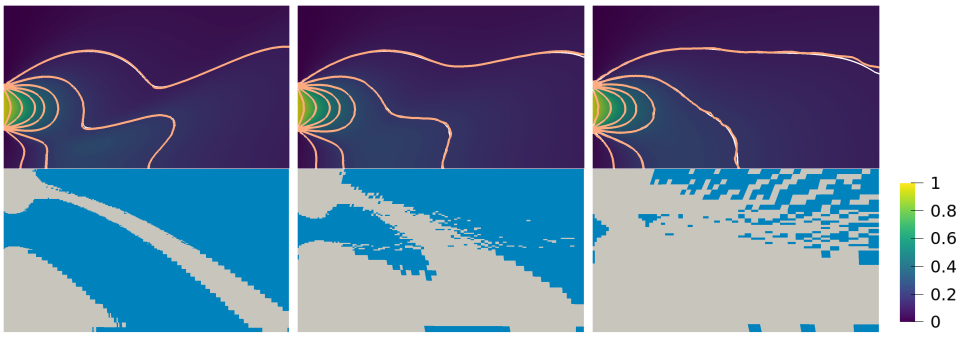

(a) $Kn_0 = 0.013$ (b) $2Kn_0$ (c) $4Kn_0$

Figure 5.14: Normalized number density contours of two interacting jets calculated with the hybrid ES-BGK-relaxation-DSMC coupled in the upper half and the regions in which the ES-BGK relaxation was applied (blue) or the collisions were resolved by DSMC (gray) in the lower half at an inlet stagnation Knudsen number of (a) $Kn_0 = 0.013$, (b) $2Kn_0$ and (c) $4Kn_0$. The applied breakdown criterion was $Kn^*_{GLL} = 0.1$.

the standard deviation of the velocity distribution will not be isotropic corresponding to a non-spherical pressure tensor or a high $\Phi_{\Re}$. The high alignment leads to high mean velocities, which in the (2.) shock will be confronted with the high temperature, small mean velocity particles from behind the shock. This leads to a bimodal velocity distribution with a skewness, corresponding to a non-zero heat flux or a high $\Phi_{\Im}$. The Fourier transform of the deviation from the Maxwellian is shown in Figure 5.13. The real part (Figure 5.13a) assumes high values exceeding $\Phi_{\Re} = 0.5$ in the offsides of the inlet with a large region above $\Phi_{\Re} = 0.1$. While the deviation is higher in the subsonic region, with values above $\Phi_{\Re} = 0.5$, the deviation diminishes when entering the shock. At the shock itself, a small stripe of $\Phi_{\Re} > 0.1$ occurs; downstream from the shock the deviation fades. The imaginary part of the deviation (Figure 5.13b) is small in the offside and only comprises a small region in the extreme offside. The imaginary part of the deviation is high at the sonic line, but not inside the subsonic region. At the shock, the imaginary part of the deviation is $\Phi_{\Re} > 0.1$ in a broader stripe, which transverses the entire computational domain.

Therefore both the even and odd moments will deviate in this flow from the equilibrium distribution, which makes it a good candidate for testing the capabilities of the target distributions for the relaxation.

KINETIC MODELS AND HYBRID COUPLING

Figure 5.14 shows the interacting planar jets solved by a hybrid ES-BGK-DSMC solver at different degrees of rarefaction. The number density contours are plotted in the upper half with thin white lines depicting isolines from a DSMC simulation and thin beige lines for the same isolines for the hybrid ES-BGK-DSMC solution. Since the results are in very good agreement the white DSMC lines are rarely visible. This is true for all three considered degrees of rarefaction, which range from a clear shock interaction (Figure 5.14a) to an almost diffuse superposition of plumes (Figure 5.14c). The lower half depicts regions

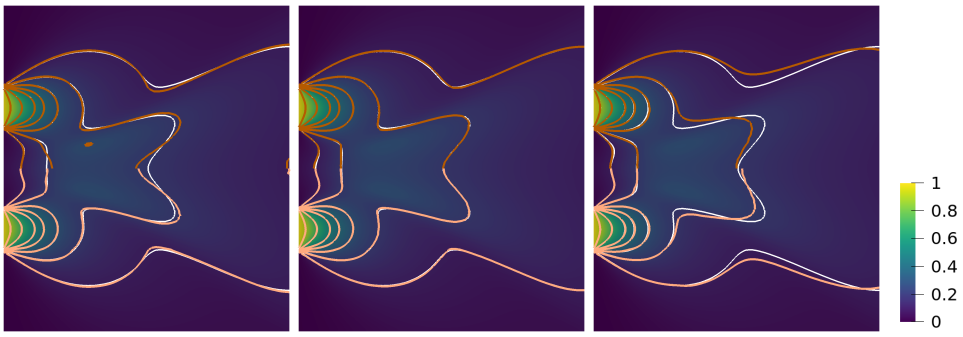

(a) BGK (b) ES-BGK (c) S-BGK

Figure 5.15: Normalized number density contours of two interacting planar jets at $Kn_{in} = Kn_0$ calculated with the (a) BGK, (b) ES-BGK and (c) S-BGK distribution for the relaxation.

in which the ES-BGK relaxation was applied in blue, and those in which the DSMC solution was applied in gray based on a breakdown criterion of $Kn^*_{GLL} = 0.1$. For the lowest Knudsen number of $Kn_{in} = Kn_0 = 0.013$, the ES-BGK solver is applied in most regions except for the shock region and the 'blind spot' in the periphery. For $Kn_{in} = 4Kn_0$, on the other hand, DSMC is required in the majority of the flow field. (Please note that a few cells at the vacuum boundary are unexpectedly not recognized to be out of the equilibrium range, since zero normal gradient boundary conditions diminish the calculated total gradients.)

The excellent agreement (in combination with the audaciously high breakdown limit) raises the question how well the pure kinetic model without hybrid coupling compares to the hybrid-coupled models. The performance of the BGK, ES-BGK and S-BGK model is assessed in Figure 5.15 for $Kn_{in} = Kn_0$, where the number density contours of the pure model are presented in the upper and the one of the corresponding hybrid solvers in the lower half. Isolines are marked in white for DSMC, in brown for the pure kinetic model and in beige for the hybrid model. The BGK model slightly overpredicts the shock intensity (Figure 5.15), i.e., the shock shields the primary expansion more and the number density level behind the shock is higher, whereas the S-BGK model underpredicts it, i.e. the number density distribution is more diffuse both in the primary and secondary expansion. This is in so far surprising as it implies that incorporating the heat flux decreases the accuracy compared to solely using the Maxwellian as target distribution.

Figure 5.16 compares line profiles of normalized number density, velocity and temperature at $x = 5\,\text{mm}$ for the different kinetic models with the DSMC solution. The BGK model overpredicts the secondary peaks in the number density which are caused by the shock and the temperature peak in the center plane. Except for these deviations, which indicate an underprediction of diffuse behavior, the BGK model is in good agreement with the DSMC solution. The ES-BGK exhibits no significant deviations from the DSMC solution. The S-BGK model predicts lower secondary peaks in number density, higher primary peaks and a smooth transition without the deep troughs predicted by the other models and the DSMC method. Also the velocity trough and temperature peak at the

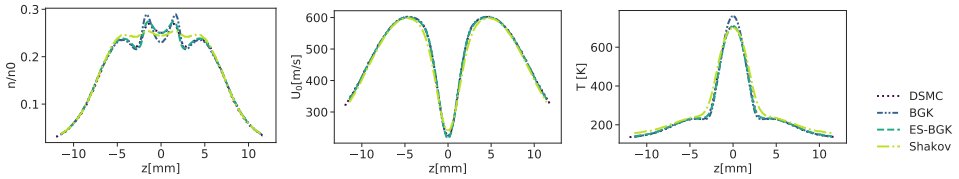

(a) Number density (b) Velocity (c) Temperature

Figure 5.16: Profiles of (a) normalized number density, (b) velocity and (c) temperature at $x = 5\,\text{mm}$ for interacting jets with inlet stagnation Knudsen number $Kn_s = 2Kn_0$.

center plane extend farther outwards indicating a more diffusive character of the S-BGK model.

Table 5.4: Computational cost for the simulation of two interacting planar jets for different kinetic models, compared to the costs of DSMC, accompanied by the number of used particles and the number of grid cells.

	computational cost (normalized by DSMC)	time step size in s	particle number in 10^6	grid cells
DSMC	1	$8 \cdot 10^{-9}$	14	23744
BGK	0.274	$16 \cdot 10^{-9}$	7	6527
ES-BGK	0.298			
S-BGK	0.279			

Table 5.4 compares the computational cost, i.e. the CPU time, normalized by the one of the DSMC simulation for the pure relaxation simulations. The use of the solver saves for all target distributions approximately 70% of the CPU time. This can be explained by the decreased resolution criteria, which allow a twice higher temporal and spatial resolution, but demand a twice as high number of particles per cell. Ideally, this would speed up the simulations by a factor of four. Further improvements in the relaxation may accelerate the solver further. In a three-dimensional flow, the (ideal) speed up of the relaxation compared to the resolved collisions would be even increased by a factor of eight.

5.4. CONCLUSION

We implemented the BGK, ES-BGK, S-BGK and U-BGK kinetic relaxation models in the OpenFoam dsmcFoamPlus solver.

The physical meaning of the U-BGK model was illustrated by splitting the distribution in an approximate manner into a subset of velocities obeying an ES-BGK and another obeying the S-BGK distribution. This indicated that the blending procedure in accordance with the two-third Prandtl number criterion yields an inversion of the distributions for large ranges of the model parameter C_{ES}.

The implementation of the kinetic relaxation models was verified for a rarefied Poiseuille flow showing good agreement with results in the literature. We studied the behavior of the models and the velocity distributions of a rarefied thermally-driven cavity flow and a rarefied Couette flow showing that even simple problems exhibit a broad variety of how

equilibrium is violated.
We analysed the types of non-equilibrium by splitting the Fourier-transformed deviation of the velocity distribution from the Maxwellian distribution in its even and odd part using the real and imaginary part of the velocity distribution's Fourier transform. We explored these measures for several free-molecular and highly rarefied Couette-Fourier flows which indicated that the parameters were able to clearly separate between the even part of the deviation due the applied velocity difference and the odd part due to temperature differences. With less rarefaction, the amplitude of the measures decreased, but the qualitative behavior remained the same.
Applying the Fourier transform deviation measures to interacting jets showed a high deviation in the real part at the peripheries of the inlets which indicates a significant velocity sorting in these regions. In addition, a deviation of the real part was visible in the shock region. An odd deviation appeared mainly in the shock region. As the regions of real and imaginary part of the deviation overlapped to a great extent, a sophisticated guess for which target distribution would perform best was difficult.
When applying the kinetic relaxation using different target distributions, it turned out, that the BGK performed well, but overpredicted the effect of the shock, whereas the ES-BGK model showed perfect agreement with DSMC, and the S-BGK model underpredicted the effect of the shock producing a more diffuse number density field. A hybrid coupling between the relaxation to a target distribution and DSMC with the gradient-length local Knudsen number as switching criterion, brought only small accuracy improvements. It can be concluded that for the studied case of interacting planar plumes the ES-BGK yields good and sufficient results. However, this statement is restricted to this special case. First ideas were outlined for a breakdown criterion which selects the applicable target distribution that need a broader consideration to make it work.

6

Conclusion

6.1. CONCLUDING REMARKS

This thesis addresses the modelling of the transport processes in a continuous Physical Vapor Deposition (PVD) process and recommended design approaches with a focus on deposition uniformity as well as efficient energy and material use.

The simulation of the Vapor Distribution Box (VDB) in Chapter 2 demonstrated the potential of CFD for modeling and optimizing industrial gas flow applications by addressing

> **Research question 1:** What limits the mass flow rate? How to obtain an efficient, high mass flow inside the VDB?

The simulated Navier-Stokes-Fourier equations together with the empirical laws such as the Antoine equation and the Hertz-Knudsen equation predicted the same trends as the experiments for the mass flow rate. Both simulation and experiments were in good agreement with a theoretical approximation considering the Hertz-Knudsen limited evaporation and the choking in the nozzles as limiting factors. The quantitative results were off, e.g. the mass flow rate was overpredicted by 30%, most likely due to: (1) a lack of accurate information on the material properties, namely the evaporation coefficient of zinc at a high melt temperature and a high pressure above the melt; (2) the expectation that the zinc in the VDB contains impurities which may further affect the coefficient. This illustrates that the prediction quality of the well-known thermo- and fluid dynamic laws, often validated for water or air experiments, highly depends on the availability and use of correct material properties, which are partially lacking for other materials (or their non-pure form). Still — while an accurate quantitative prediction is desirable — for the engineering design, trends as a function of system and process parameters as well as the localization of the dissipation losses are the crucial knowledge. The studied VDB system can be summarized as "following the Hertz-Knudsen and isentropic relation, but with a discharge efficiency of only 40–50%". This first and most important result may not be surprising, since the underlying equations and involved phenomena have been known for a long time. In addition, experiments already revealed the low efficiency. However, the present computer aided engineering reveals opportunities for energy saving and efficiency increase which we are otherwise ignorant of, as we cannot pinpoint the exact location of the loss based on engineering rules and experiments and are uncertain whether it is avoidable at all. This study provided first hints for optimized process conditions and geometry: the efficiency rises with higher pressures inside the VDB and a tremendous efficiency gain is expected for larger and shorter holes, as the main loss occurs in the boundary layers of the holes. These recommendations may seem to be of secondary priority when aiming for a process to work in the first place. But in face of climate change, energy (and material) efficient processes are crucial, especially if planned for continuous lines. The developed CFD model can be applied to assess these design options and spare the cost of producing and testing multiple VDB geometries experimentally.

Zooming in on the vapor plumes emitted from the VDB, Chapter 3 studied the interaction of two sonic, planar jets with a focus on the emerging deposition peaks, as they are undesirable for coatings. It addressed

> **Research question 2 a:** Can design changes mitigate jet interaction shocks? How does the rarefaction, the nozzle-separation distance and the inclination of the nozzles affect the flow and the deposition profile?

First, the chapter demonstrated how different theoretical frameworks can explain flow behavior in terms of elementary phenomena. The free molecular flow framework is based on a simple concept, still the arising expressions are difficult to comprehend. The results depict the breakdown of equilibrium and velocity sorting typical in rarefied flow in its purest form. On the other hand, the framework of the inviscid continuum flow reduces the flow problem to a system of hyperbolic equations, which allows for a first qualitative solution with pen, paper and ruler. Furthermore, applying the concept of the Method of Characteristics proved to be powerful in the visualization of the plume interaction in the transitional regime (which was simulated by DSMC). This is all the more important since the staggered change of flow variables within the shock as well as the high pressure gradients in both the expansions and the shock make it difficult to localize flow features based on conventional methods. Not only could the shock position be detected, but also similarity could be analyzed to scale the position of the shock based on the distance between the plume inlets. Thus, the location of the deposition peaks caused by the shocks can be predicted for different scales. However, the overall deposition profile and the location of highest peaks clearly depends on the ratio between inlet width and distance between the inlets highlighting the limits of simple scaling laws. The transitional flow is based on a combination of phenomena found in the free molecular and the inviscid continuum flow. However, the resulting flow fields do not lie in between the bounds of those two limiting flow solutions. Rather, the temperature and deposition peaks exceed both solutions. With higher degrees of rarefaction the shocks tended to be bent away form the symmetry plane.

A question was how geometry changes may benefit the deposition uniformity. Two first hypotheses came up: (1) A closer nozzle spacing should prevent the expansions from a high speed-up before the shock and the plumes could merge, (2) when tilting the jets away from each other less mass would reach the interaction plane and thus cause less mass to enter the shock region. Both hypotheses turned out to be partially true, but still do not hold the expectations placed in them: (1) The merging of the plumes only occurred when the spacing of the plumes was in the order of a few mean free paths, which is not feasible for the manufacturing of the required tools. (2) The tilting of the plumes away form each other caused a weaker shock, but also meant that two peaks from the primary expansions caused a severe non-uniformity in deposition (when the nozzle-to-plate distance was reasonable long). Unexpectedly, a tilting of the plumes towards each other turned out to actually improve the deposition uniformity. While the shocks initially are indeed stronger and cause higher peaks in the mass flux, further downstream the high mass in the interaction plane in combination with the stronger expansions smoothens the deposition profile. In addition, the tilting towards each other reduced the stray deposition, which is highly desirable in the continuous PVD process, as it reduces maintenance time.

Chapter 4 extends the previous chapter by evaluating whether the use of a light inert carrier gas benefits the deposition, in particular answering

> **Research question 2 b):** How does species separation affect shocks? Can a carrier gas reduce deposition non-uniformities?

To answer the question, several simulations of interacting sonic, planar silver vapor plumes with varying helium carrier-gas mole fractions were conducted. Due to the similarity of the flow field for same inlet Mach numbers, the same flow field is predicted for pure silver and pure helium plumes respectively (at same inlet Knudsen numbers). However, if instead a binary mixture is used, species separation occurs and the heavier species focuses at the axis of the primary plume, whereas the lighter species is pushed to the periphery. The speed of sound increases in regions, in which the lighter species prevails. Unsurprisingly, the Mach angle decreases and consequently the interaction shocks are mitigated. Furthermore, adding a light carrier gas enhances the conductance at the inlet and reduces stray deposition. All these effects are beneficial for deposition processes. Adding a carrier gas has a higher flexibility than geometry changes, since the carrier gas flow rate could be adjusted during the run. However, there are additional costs for the carrier gas. Helium, which is the obvious choice for a carrier gas, is in high demand in other sectors, and its price on the world market varies. Recycling of the used helium (or another carrier gas) could make it feasible one day to use carrier gas for an improved deposition and a better process control.

Chapter 3 and Chapter 4 used the Direct Simulation Monte Carlo method for solving the rarefied flow problem, which is computationally very costly, especially in the dense vapor regimes, as they occur in the inlet region and downstream from the shock. Chapter 5 therefore addressed

> **Research question 3:** How to efficiently model flow ranging from continuum to free molecular flow? Can a substitution of the collision by a kinetic relaxation speed up the simulation? Which target distribution is applicable for interacting jets?

A relaxation method based on the Bhatnagar-Gross-Krook operator was implemented in the open-source library OpenFOAM to replace the collision step in DSMC. Since the equilibrium target distribution, viz. the Maxwellian velocity distribution, does not accurately model the relation between the shear forces and heat flux, other distributions that do so were implemented as well, one which scales the shear stress tensor and one which scales the heat flux. Three different target functions were thus evaluated: the Maxwellian velocity distribution as in the original Bhatnagar-Gross-Krook model (BGK), the Ellipsoidal-Stochastical BGK distribution (ES-BGK) and the Shakov distribution (S-BGK). The ES-BGK considers the local shear stress (an even deviation from equilibrium) in the target distribution, whereas the S-BGK model considers the local heat flux (an odd deviation from equilibrium). Hence, the ES-BGK model performed well for thermally-driven flows and expansion problems, whereas the S-BGK performed better in the prediction of shear-driven flows or shocks. The ES-BGK also performed best in the simulation of interacting vapor jets, where the primary and secondary expansion extend over the majority of the computational domain, whereas the shock is confined to a small region.

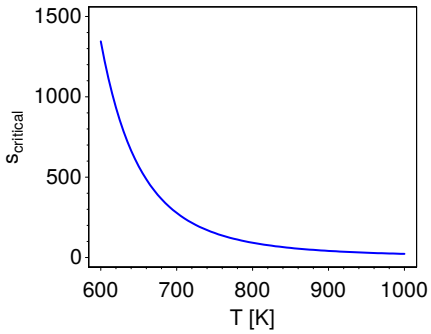

Figure 6.1: Critical nucleation pressure ratio over temperature for Zinc vapor.

6.1.1. IMPLICATIONS FOR CONTINUOUS PHYSICAL VAPOR DEPOSITION OPTIMIZATION

The application-oriented part of this thesis aimed for a high, uniform deposition rate while maintaining a high efficiency. To achieve this, the pressure inside the VDB should be high to reduce the viscous boundary layer thickness inside the nozzles. A reduction of the viscous boundary layer, e.g., by reducing the nozzle length or increasing the nozzle diameter, benefits the efficiency. If multiple nozzle rows are used, a tilting of the nozzles towards each other benefits uniformity and reduces stray deposition. To control the deposition and smoothen deposition peaks due to plume interaction, the use of a carrier gas is beneficial.

For the model based design and optimization of continuous PVD, one modelling method alone will not suffice (at the present time). A pressure-based solver is most suited for the internal flow up to choking. In the vacuum chamber, the flow is rarefied and a DSMC simulation is most appropriate. However, for first estimates of shock locations at low or moderate Knudsen numbers, the Riemann solver solution, which approximately solves the Navier-Stokes-Fourier equations, is sufficient. The reason is that the overall dominating flow effects, i.e., the expansions and the interaction shocks, take place near-continuum regions. This also explains the good approximation of the flow field when using kinetic models which relax the velocity distribution towards a target instead of resolving the collisions. Especially, the ES-BGK model showed good results, as it is able to represent the typical velocity sorting occurring in rarefied expansion flows.

6.2. RESEARCH OPPORTUNITIES

6.2.1. CONDENSATION IN THE EXPANSION FLOW

Experiments revealed shiny spots on the PVD coating for certain process conditions, which indicate a not perfect resublimation, but a liquid phase. One possible source of liquid droplets would be condensation inside the nozzle or the downstream expansion flow[219]. This effect can be used to produce metal nano particles [220]. However, in a PVD coating it is undesirable. For condensation to occur, nuclei have to be present, which may either be particulates from a different material or droplets which form spon-

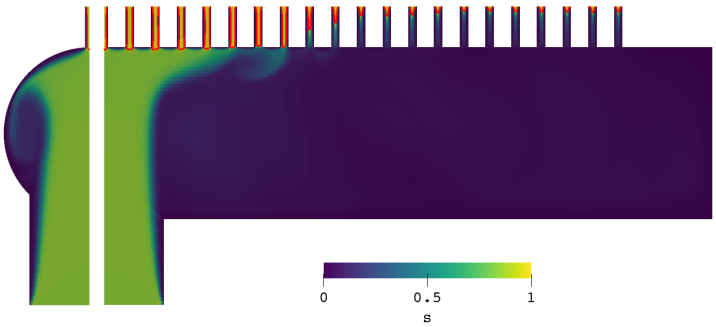

(a)

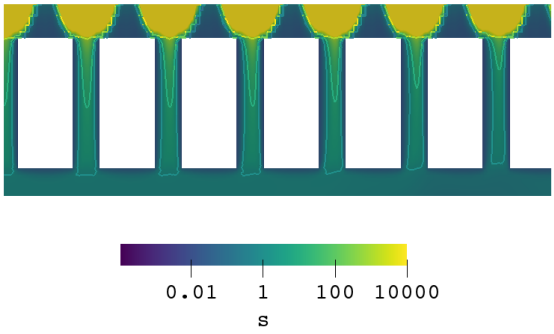

(b)

Figure 6.2: Contours of saturation ratio $s = \frac{p}{p_v(T)}$ for (a) the short and long cross section of the VDB, and (b) a detail for the inner seven nozzles. Note the different scales. The isoline $s = 1$ is marked red in (a), the isolines $s = 1, 10, 1000$ are marked by a light color in (b).

taneously from the vapor phase. For the former, saturation is required, for the latter, a highly supersaturated state of the liquid has to be reached, which can be achieved by rapid cooling as it appears in nozzle flows [87]. In a high-pressure-ratio nozzle flow, heat is transformed into kinetic energy at a high rate and consequently pressure and temperature drop rapidly yielding a high supersaturation. For condensation of zinc vapor in converging nozzles, Bayazitoglu et al. [85] found that higher melt temperatures and consequently higher inlet pressures result in more and bigger particles; shorter nozzles yield less and smaller particles. In addition, they observed that a smaller convergence angle of the nozzle yields a less rapid change in thermodynamic properties and thus a later onset of nucleation and thus less particles.

The supersaturation pressure is the ratio between the static pressure p divided by the vapor pressure from Eqn. 2.1:

$$s = \frac{p}{p_v(T)}.$$

The nucleation rate, J, is given by [85]

$$J = n_v^2 \Omega \sqrt{\frac{2\sigma(T)}{\pi m}}\, s^2 \exp\left(-\frac{16\pi\sigma(T)^3\Omega^2}{3(k_B T)^3}\frac{1}{(\ln s)^2}\right), \tag{6.1}$$

where Ω is the molecular volume, $\sigma(T)$ the surface tension, which is a linear function of temperature, and n the number density in a saturated gas calculated by $n_v = \frac{p_v(T)}{k_B T}$. The critical supersaturation pressure (i.e., the pressure above which we expect an onset of nucleation), is defined as the one for which the nucleation rate is equal to $1\,\mathrm{cm}^{-3}\,\mathrm{s}^{-1}$ [85]. Figure 6.1 shows the the critical saturation pressure ratio over the temperature range typical for flows in continuous VDB devices.
Figure 6.2 shows the regions of saturation (i.e., where the actual pressure exceeds the vapor pressure calculated from the local temperature) in the VDB. A few regions inside the VDB show saturation, mainly in regions with a small flow velocity. In and behind the nozzles, the gas is saturated. The supersaturation, as can be seen in Figure 6.2b, reaches the critical state ($s^* = \mathcal{O}\left(10\text{–}10^3\right)$) at the end of the nozzles or in the free expansion. (Please note that the coarse resolution of the mesh behind the nozzles was justified, because we considered this as a supersonic outflow region not of interest for the mass flow calculations. The mesh would need to be refined for a proper investigation of the condensation in this region.)
It should be noted that the presence of supersaturation and also critical supersaturation does not necessarily imply immediate condensation, since it is a kinetic process [221]. The high velocities inside the nozzle and the expansion flow could transport a supersaturated fluid element reaching the supersaturated state fast enough to a rarefied region and thus avoid the onset of condensation. It is worth mentioning that the presence of a carrier gas as proposed in Chapter 4 affects condensation in a complex manner. On the one hand, a carrier gas removes heat generated during the condensation, on the other hand, pressure volume work is conducted against the carrier gas hindering the condensation process [222].
Further research could address whether the source of the shiny spots are indeed droplets, whether these form in the nozzles or the expansion and how to avoid them. This certainly includes continuum simulations to obtain the exact thermodynamic state, but may be extended to molecular dynamic simulations to obtain a more accurate prediction of nucleation, growth and aggregation of droplets, since the above mentioned nucleation rate method showed significant deviations from experiments [223].

6.2.2. DYNAMIC COUPLING OF KINETIC MODELS

For a more general hybrid kinetic-relaxation-DSMC model, it would be preferable if the switching criterion would (i) indicate which model to use in which region based on the type of deviation found and (ii) be based on the local particle velocity distribution rather than on the macroscopic variables (which need to be sampled and whose gradient has to be calculated in a non-local manner, both of which slow down the algorithm). While the splitting in the real and imaginary part of the Fourier transform may be a first attempt to achieve this, this also requires a time-consuming sampling step which except for the switching criterion brings no benefit. A more sophisticated switching criterion

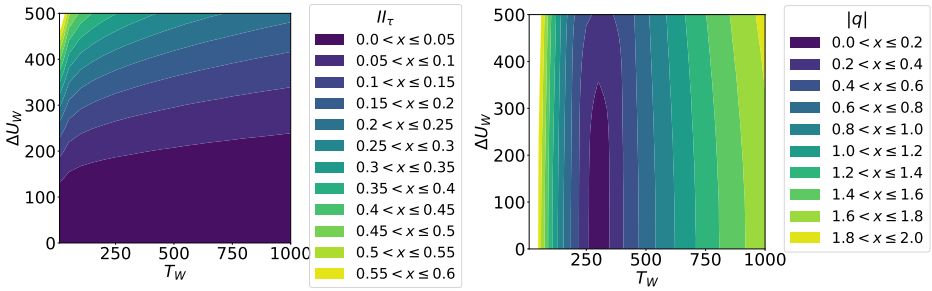

(a) Second invariant of the shear stress tensor I_2. (b) Invariant of the heat flux vector $|q|$

Figure 6.3: Maps of (a) the second invariant of the stress tensor and (b) the invariant of the heat flux vector, i.e., its magnitude, for Couette-Fourier flow at $Kn = 0.5$ as a function of the applied wall temperature T_w at the top wall and the wall velocity difference ΔU_w. The temperature of the bottom wall is 300 K

could be based on the stress tensor and the heat flux vector as those can be reused in the target distributions for the kinetic relaxation models. Chen et al. [143] derived for a one-dimensional bi-modal distribution consisting of two delta functions, that

$$C_{es} = -\frac{(q/\rho)^2}{(P_{11}/\rho)^3} \,. \tag{6.2}$$

Despite its unboundedness, this function yielded a significant improvement compared to constant C_{es} for a shock calculation. In addition, they state that for a thermally-driven flow with two distinct peaks, C_{es} should recover the ES-BGK model.
To reach a physically meaningful switching criterion it should be Galilean invariant. The invariants of the pressure tensor and the heat flux vector would be the natural choice. The total pressure tensor is the correlation matrix between momentum and velocity

$$\mathbf{p} = \langle m\mathbf{c} \otimes \mathbf{c} \rangle \,, \tag{6.3}$$

which can be normalized by division with its own trace, i.e., $\tilde{\mathbf{p}} = \mathbf{p}/\mathrm{tr}(\mathbf{p})$. $\tilde{\mathbf{p}}$ can be split into its isotropic contribution $\tilde{p} = \mathrm{tr}(\tilde{\mathbf{p}})/3 = 1/3$ and deviatoric part $\tilde{\tau} = \tilde{\mathbf{p}} - (1/3)\mathbf{1}$. Since the isotropic part of the pressure tensor is taken care of by the temperature ($T \propto p$), the distribution is described up to the second order by the deviatoric part of the pressure tensor, i.e., the stress. The first invariant is $I = \mathrm{tr}(\tau) = 0$ for any deviatoric (i.e., traceless) tensor. The second and third invariant read

$$I_2 = \frac{1}{2}\left[\overbrace{(\mathrm{tr}(\tau))^2}^{=I_1=0} - \mathrm{tr}\left(\tau^2\right)\right] = \lambda_1\lambda_2 + \lambda_2\lambda_3 + \lambda_3\lambda_1 \,, \tag{6.4}$$

$$I_3 = \det(\tau) = \lambda_1\lambda_2\lambda_3 \,, \tag{6.5}$$

where I_2 is a measure for the anisotropy of the tensor and I_3 measures the change of volume, if the tensor would be applied to a unit sphere. Therefore, especially I_2 shall be considered to be most relevant for describing the anisotropy of the pressure. To explore the invariants we reconsider the rarefied Couette-Fourier flow at $Kn = 0.5$ covered

in Section 5.3.3. The second invariant of the stress tensor is shown as a function of the top wall temperature T_w and the applied velocity difference ΔU_w in Figure 6.3a. For pure Fourier flows, the second invariant vanishes. With increasing velocity difference it rises. As for the real part of the deviation of the Fourier-transformed velocity distribution from the Maxwellian distribution, the second invariant also increases higher for higher temperatures. In opposite to the former, the second invariant does not show the sharp increase for extreme wall temperature ratio. Figure 6.3b shows the magnitude of the heat flux vector. Its sensitivity to the applied velocity difference is small. In contrast, it increases rapidly for changes of the top wall temperature. The qualitative behavior of these two invariants compare quite well to the real and imaginary part of the deviation of the Fourier-transformed velocity distribution from the Maxwellian. Compared to the latter, these invariants have the advantage that the pressure tensor needs to be sampled for the ES-BGK and the heat flux vector for the Shakov model. Thus the expected overhead due to sampling for the switching criterion is expected to decrease significantly.
Generalizing the one-dimensional function given by Chen (Equation 6.2) to multiple dimensions it seems to be natural to chose

$$C_{es} = -\frac{\left(\frac{|\mathbf{q}|}{\rho}\right)^2}{f\left(\left(\frac{I_2}{\rho}\right)^{3/2}, \frac{I_3}{\rho}\right)} \text{ bounded by } C_{es} \in [-0.5, 1)\,, \tag{6.6}$$

where $f(\cdot)$ is a function to be determined. Its exact form may be explored by systematic parametrization and machine learning.

6.2.3. ALTERNATIVE TARGET DISTRIBUTIONS IN KINETIC MODELS

Alternatively the relaxation function could be replaced with the first-order Chapman-Enskog expansion which considers both stress and heat flux producing results as accurate as the Navier-Stokes-Fourier equations. This reduces the requirement of switching mechanism to the choice between a kinetic relaxation model and resolved DSMC collisions. A drawback is that the easy Box-Muller transform, which can generate typical velocities for BGK and ES-BGK, would need to be replaced by a sampling algorithm, e.g., Acceptance-Rejection or Metropolis algorithms [211], which often have a small yield of accepted sampled velocities. As the acceptance rate depends on the local velocity distribution, no sound statements on the computational cost can be made beforehand.

6.3. FUTURE OUTLOOK

The governing equations for fluid dynamics are well known. The validity or viability of solution methods are often confined to certain flow regimes, which makes it necessary to chose the method based on the problem at hand. In multiscale problems or problems with varying qualitative behavior (i.e., elliptic, parabolic, hyperbolic), a coupling is required. Generally applicable solution methods such as DSMC, which are able to solve problems independent of the qualitative behavior, are not fast enough to use them in this wide range. This makes it necessary to manually chose the method for the problem at hand and to further develop the used models and algorithms. On the horizon, a transition is becoming apparent from classic solution methods based on con-

tinuum equations, i.e., Finite-Volume-Method (FVM), Finite-Difference-Method (FDM), towards particle-based methods, such as Lattice-Boltzmann-Method (LBM), Spherical Particle Hydrodynamics (SPH) or DSMC. A driving force for this transition is the local nature of these methods, which allows them to utilize the massive parallelization capacities of Graphics Processing Units (GPUs) and thus speed up the solution process. Moreover, the local nature diminishes numerical instabilities and consequently facilitates conducting simulations.
Even after a suitable modelling is found, the lack of accurate material data often hampers a quantitatively correct solution. This may either be lacking information on a pure substance, or missing information on the amount of impurities and their effect on the material properties. Therefore, computational fluid dynamics remains a field, where either a validation with an experiment is required, or one has to confine oneself to statements on trends and extreme outcomes rather than accurate quantitative results. Despite its shortcomings and still-ongoing developments, CFD is a powerful tool for better understanding of flows in nature and industry, from understanding climate change to optimizing production processes.

ACKNOWLEDGEMENTS

Firstly, I thank my promoters **Chris** and **Sasa** for giving me the opportunity to work on a topic completely new to me and comprising a wide range of physics. In the project, I learned a lot about rarefied gases, compressible flow and the applicable numerical methods. Thank you for co-supervising my students and your input into this thesis. I much appreciated your detailed finetuning of my introductions, Chris. Being teaching assistent in your course taught me a different view on transport phenomena, Sasa. **Edzo**, thanks for having the idea that CFD modeling may help with this particular challenge in metallurgical process technology and initiating the project.

What promoted me most was the interest others took in my work and endorsement which helped me overcome internal and external doubts. Thanks, **Ruud**, for asking questions, organising my visits at Tata and constantly supervising me. The hands-on experience on the actual PVD apparatus was essential. **Daniel**, you not only listened to me, but also proposed several interesting, constructive ideas and commented the plume interaction paper meticulously. **Luis**, the best way to get absorbed into a topic was discussing with you. From particle-turbulence interaction, binary diffusion, moments or eddy detection criteria. Besides this we share an enthusiasm for borrel endless discussions on freedom. **Stephan Hickel**, **Ferry Schrijer** and **Ingrid Wysong**, I met all of you only once, but the openness you considered my problems with and hints you gave were crucial to me and my work.

The best supervison came from my students, they discovered any inconsistency by notorious questioning and brought fresh ideas. **Anne**, you were my first Bachelor student, with your curious, straight-forward mind you sparked the work on VDB modeling. **Chibuikem**, your stubborn desire to use OpenFOAM for continuing Anne's work led us to a trying struggle with the software, but also to nice results. **Theo**, the maverick theoretical discussions with you were a highlight of my PhD days. **Wouter H.**, thanks for taking commendable care not only of your own work but also our co-supervised LO1 project. **Joëlle**, I admire your diligence, presentation skills and analytical ability. **Wouter V.** your persistence in speaking Dutch with me helped my integration process enormously. **Sebastian**, delving back into good old LES with you and exploring buoyant flows was a great experience.

Manu, I will keep our small adventures in good memory: your search for vegetarian food in Udine, our failed attempt to hitch-hike from Noordwijk to Leiden (1st time I ignored snow warnings of Nederlandse Spoorwegen) and co-supervising Sebastian. Working with you on LES taught me the benefits of a different style of work and supervision.

Annekatrien, dank je wel voor al de Nederlandse literatuur: van artikelen, recepten, magazinen tot makkelijke boeken. Onze lockdown wandelingen en discussies over koetjes en kalfjes genoot ik zeer. Hartelijk bedankt voor de snelle vertaling van mijn samenvatting en stellingen.

Matheus, I learned a lot from you about Brazil and real-world problems in process engineering and control. I miss your dry humour, our cooking evenings and bicycle trips.
Ruud, Erwin, Christiaan, you introduced me to Emily and supported my playground PVD experiments on it, but also taught me "roddelen". **Erwin**, thanks for giving me a ride to Amsterdam (2nd time I ignored snow warnings of Nederlandse Spoorwegen).
Romana, sharing rooms with you in Veldhoven, Lunteren and Eindhoven brought many good discussions about god and the world. **Rense**, ice-skating, bouldering and meals at your fraternity brought me closer to Dutch society. **Xiaolin**, I enjoyed the many hot pots at your place, our trip to monumenten dag and discussions about society and culture.
Debasish, your many layers of worldly wisdom and empathy made it a joy to speak with you. Thanks, for guiding me to Tagore's work, I became a big fan. **Manas**, thanks for all the tips for NWO PhD life and the activities you organised for Young Delft. **Christiaan**, you were the first to insist on speaking Dutch and took the time to explain its subtleties in detail. **Thijs, Mohammed** and **Chih-Chia**, thanks for being active part of the OpenFOAM user group and liven things up.
My office mates shaped my daily work. **Amith**, the way you used your soulfulness to deal with difficult situations was a paragon I still aim to live up to. **Wenjie**, thanks for introducing me to DSMC in your last and my first days at TP. **Kevin**, your openness and pragmatic weighing of pros and cons were my biggest cultural shocks. I enjoyed having you as office mate and am still fascinated by your teaching skills. **Iman**, you were the never-present, most courteous office mate. **Fei**, our Friday post-biology-group-meeting-pre-borrel discussions were long and brought new insights. **Artem**, I will miss our complaining about the drawbacks of OpenFOAM (by now I know they are pretty small by comparison). **Dimitrios**, your enthusiasm to understand each term in k-ϵ-model as well as the updates on Ingrid were fabulous. **Brice**, thanks for your kindness and constant interest in my work. **Saikat**, you made me remember Gymkhana park, the rice fields of Kharagpur and Indian politics.
I enjoyed the time spent with the rest of TP during lunch, coffee breaks and of course long office evenings. I would especially thank for the discussions and time with my fellow colleagues **Hrushikesh, Cees, Sid, Maulik, Ewert, Lorenz, Jorrit, Costa, Nathalie, Minu**.
I much appreciate the help by **Anita, Jennifer** and **Sandra** in all bureaucratic processes.
A big thank to **Gabrie Meesters** for giving indispensable moral support as my Mentor.
Many shaped the time I didn't spend on the dissertation, of whom I want to acknowledge the most remembered: **Peter**, for marvelous Dutch lessons, **Joeri**, for organising informative discussions on books, **Poernima**, for great Bharatanatyam lessons.
I want to thank my friends, who kept me going, tolerated me revising or simulating during joint activities or just cheered me up.
Thanks to my family for their continuous support and love before and during the PhD time. Special thanks to **Jutta**, who in addition improved my manuscripts immensely by language corrections.
Johannes, thank you for listening to me, correcting texts and discussing things which were not your métier. You unconditionally supported my decisions, lifted my mood when needed and appealed to my perseverance.
Finally, I would like to thank **Viridis**. Your beauty has accompanied me all these years and will certainly continue to do so in the future.

A

APPENDIX

A.1. TURBULENCE MODEL

The turbulent viscosity μ_t is modeled by the Launder and Sharma low-Reynolds k-ϵ model [83] with a compression term based on rapid distortion theory (RDT) [84], which is available in OpenFOAM ®-v1806, as $\mu_t = \rho C_\mu \frac{k^2}{\epsilon}$ where the turbulent kinetic energy k and the dissipation rate ϵ are described by the following transport equations:

$$\frac{\partial(\rho k)}{\partial t} + \frac{\partial(\rho k u_j)}{\partial x_j} - \frac{\partial}{\partial x_j}\left[\rho\left(\nu + \frac{\nu_t}{\sigma_k}\right)\frac{\partial k}{\partial x_j}\right] = \rho G - \rho\epsilon - \rho D - \frac{2}{3}\rho\frac{\partial u_i}{\partial x_i}, \tag{A.1}$$

$$\frac{\partial(\rho\epsilon)}{\partial t} + \frac{\partial(\rho\epsilon u_j)}{\partial x_j} - \frac{\partial}{\partial x_j}\left[\rho\left(\nu + \frac{\nu_t}{\sigma_\epsilon}\right)\frac{\partial \epsilon}{\partial x_j}\right] = \left(C_{\epsilon,1}P - C_{\epsilon,2}f_2\rho\epsilon\right)\frac{\epsilon}{k} + \rho E - \frac{2}{3}C_{\epsilon,1}\rho\frac{\partial u_i}{\partial x_i}\epsilon, \tag{A.2}$$

where the turbulence generation term is

$$G = \nu_t \frac{\partial u_k}{\partial x_k}\left(\frac{\partial u_i}{\partial x_j} + \frac{\partial u_j}{\partial x_i} - \frac{2}{3}\frac{\partial u_l}{\partial x_l}\delta_{ij}\right)$$

the near-wall source terms and the near-wall damping functions are

$$D = 2\nu\frac{\partial\sqrt{k}}{\partial x_i}\frac{\partial\sqrt{k}}{\partial x_i} \text{ and } E = 2\nu\nu_t\frac{\partial^2 u_i}{\partial x_j\partial x_k}\frac{\partial^2 u_i}{\partial x_j\partial x_k}$$

$$f_2 = 1 - 0.3\exp\left(-R_t^2\right) \text{ and } f_\mu = \exp\left(-\frac{3.4}{1+\frac{1}{50}R_t}\right)$$

$$\text{where} \quad R_t = \frac{k^2}{\nu\epsilon}.$$

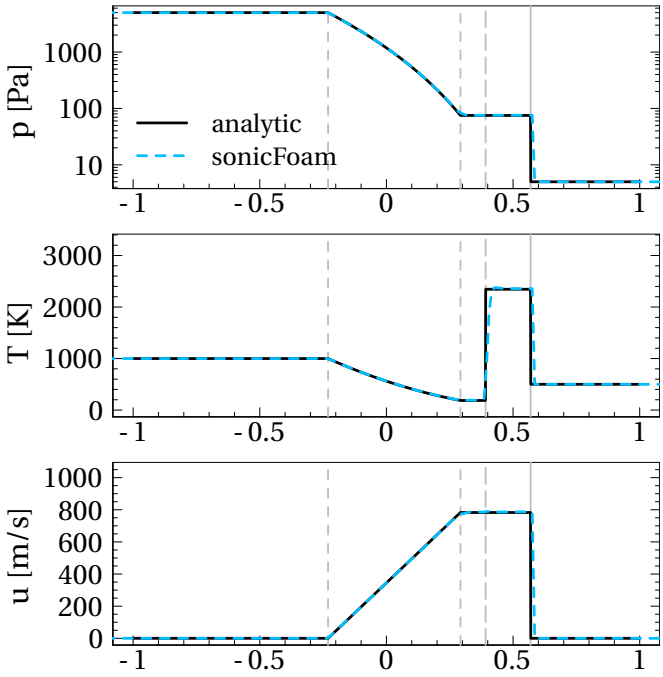

Figure A.1: Pressure, temperature and velocity in the shock tube at $t = 0.0005\,\mathrm{s}$. Comparison of analytic and *sonicFoam* solutions. The thin vertical gray lines mark from left to right: the expansion head, the expansion tail, the slip surface and the shock.

The coefficients are $C_\mu = 0.09$, $C_{\epsilon,1} = 1.44$, $C_{\epsilon,2} = 1.92$, $C_3 = 0$, $\sigma_k = 1$ and $\sigma_\epsilon = 1.3$. Based on the Reynolds number of a laminar test simulation $Re = 2000$, the inlet turbulent intensity was estimated to be $I = 0.085$ [224], which corresponds to an inlet turbulent kinetic energy $k \approx 9.75\,\mathrm{m^2\,s^{-2}}$ and an inlet turbulent dissipation rate of $\epsilon \approx 1880\,\mathrm{m^2\,s^{-3}}$ [225].

A.2. VERIFICATION, VALIDATION AND MESH INDEPENDENCE

A.2.1. SHOCK TUBE VERIFICATION

The used solver, i.e., *sonicFoam*, is verified with a shock tube, which is a one-dimensional pipe that is initially split into a driver section at a high uniform pressure and a driven section at a low uniform pressure. When starting the simulation (or in an experiment when destroying the separating membrane), a shock is induced and travels into the driven section. Shock tubes are meaningful verification cases for compressible flow solvers, since on one hand, important compressible flow phenomena occur, such as shock, contact discontinuity and expansion. On the other hand, the simplicity allows for an analytic solution [73]. To stay close to the nozzle flow inside the VDB, the thermodynamic prop-

Table A.1: Boundary conditions for the Sajben transonic diffuser.

	pressure	velocity	temperature	kinetic energy	turbulent dissipation
inlet	static pressure $p_{in} = 116.77\,\text{kPa}$	$152.45\,\text{m}\,\text{s}^{-1}$ ($Ma = 0.46$)	static temperature $T_{in} = 273.3\,\text{K}$	$54.4\,\text{m}^2\,\text{s}^{-2}$	$21\,966\,\text{m}^2\,\text{s}^{-3}$
outlet	static pressure 110.66 kPa	zero gradient	zero gradient	zero gradient	zero gradient
walls	zero gradient	no slip	adiabatic	wall function	wall function

erties of zinc were used. No initial velocity or inlet velocity was applied. To verify the solver for the immense pressure drop across the domain, the pressure ratio was set to $r_p = 1000$. The initial conditions at $t = 0$ are:

- driver section: $p = 5000\,\text{Pa}$, $T = 1000\,\text{K}$ for $x < 0$
- driven section: $p = 5\,\text{Pa}$, $T = 500\,\text{K}$ for $x > 0$

The grid has 20000 equidistant cells. Figure A.8 compares analytic and flow solver solutions at $t = 5 \cdot 10^{-4}\,\text{s}$. The vertical gray lines mark from left to right the start and end of the expansion region, the contact discontinuity, across which temperature and density are discontinuous, but velocity and pressure are constant, and the shock. The shock speed is marginally overpredicted by *sonicFoam*, which results in a very small shift of the discontinuity in the profiles to the right. The numerical solver is in good agreement with the analytical solution.

A.2.2. SAJBEN TRANSONIC DIFFUSER VALIDATION

The solver *sonicFoam* and the turbulence model were validated with a transonic converging-diverging diffuser flow, which was experimentally studied by the group around Sajben [227] for multiple pressure ratios. The steady-state cases have been widely used for validation of compressible CFD codes [226, 228–230] and are part of the NASA verification and validation archive [231]. Since we apply the solver later to flows without shocks, we chose the 'no-shock' case with a pressure ratio of $r_p = 0.862$ for the validation. The two-dimensional diffuser geometry is visible in Figure A.2a; its throat height is $h_{th} = 44\,\text{mm}$ and other details were described by Bogar et al. [227]. We used a grid of 94 cells in wall-normal direction with a strong vertical refinement towards both walls and 380 cells in streamwise direction with a progressive horizontal refinement towards the throat region with a grid-expansion ratio of $1.002 - 1.003$. The cell centers in direct neighborhood to the wall had a distance less than $y_1^+ = 0.9$ to the wall. A total pressure of $p_s = 135\,000\,\text{Pa}$ and total temperature of 285 K is assumed. For the simulations, the isentropic relations were applied to obtain pressure, temperature and velocity for $Ma = 0.46$. The inlet turbulence intensity was set to $I = 0.04$. At the outlet, the pressure was set

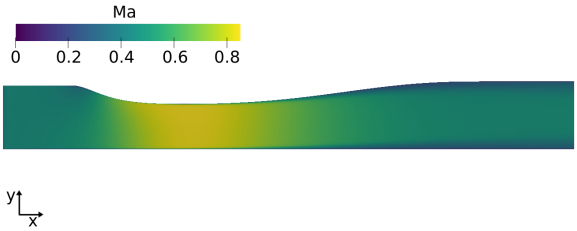

(a) Mach number contours.

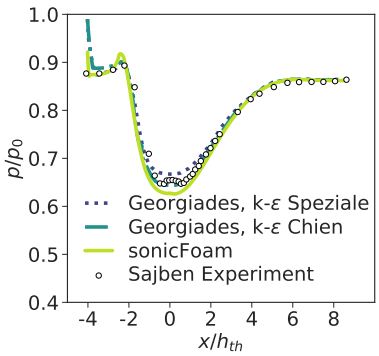

(b) Pressure along the top wall.

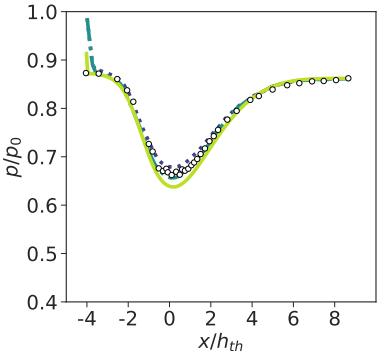

(c) Pressure along the bottom wall.

Figure A.2: Sajben transonic diffuser validation case. Contours and pressure profiles along the walls from sonicFoam compared to experimental results (data from [226])and simulations by Georgiades et al. [226].

to $p_o = 116770\,\text{Pa}$. The boundary conditions are listed in Table A.1. The fluid was air with a specific heat ratio $\gamma = 1.4$, a molecular mass of $M = 28.9\,\text{g mol}^{-1}$, specific heat at constant pressure $c_p = 1005\,\text{J kg}^{-1}\,\text{K}^{-1}$ and Prandtl number $Pr = 0.72$. The Sutherland law was applied in the form of Eq. 2.10 with a coefficient $A_S = 1.7219 \cdot 10^{-6}$ at a reference temperature of $T_0 = 288.167\,\text{K}$. The solver, discretization schemes and turbulence model were the same as described in Section 2.3.2. The previously described Launder and Sharma low-Reynolds k-ϵ model with RDT term was applied.

The Mach number contours are shown in Figure A.2a. The subsonic, turbulent inflow accelerates in the nozzle and reaches a maximum Mach number of $Ma = 0.85$ close to the throat and afterwards decelerates. Figure A.2b and Figure A.2c compare pressure normalized by the inlet stagnation pressure along the bottom and top wall from the experiments, the simulations by Georgiades [226] using the Speziale k-ϵ and Chien k-ϵ turbulence models and the solver used in the present study, called *sonicFoam*. At the top wall (Figure A.2b), the pressure normalized by the inlet stagnation pressure drops to $p/p_0 = 0.85$ at the inlet, reaches its maximum where the converging section starts, drops in the throat to its minimum and rises afterwards to the outlet pressure. The simulation by Georgiades using the Chien k-ϵ turbulence model matches the experimental data well, the one using the Speziale k-ϵ turbulence model reports a higher pressure in the trough, *sonicFoam* predicts here a marginally lower pressure. The profile at the bot-

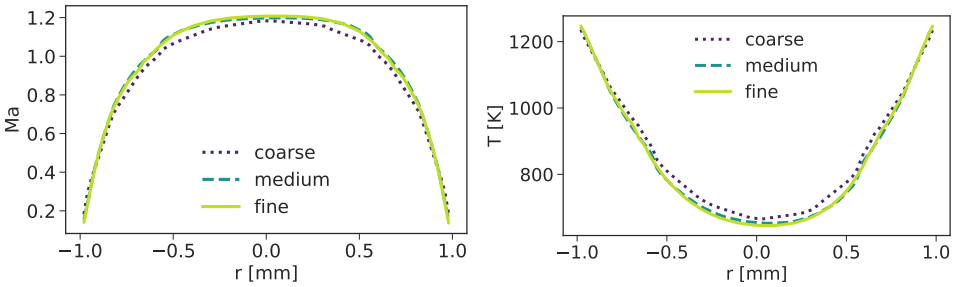

(a) Mach number.

(b) Mach number.

Figure A.3: Mach number and temperature profile at the outlet of the second nozzle for different grids (see Table A.2).

Table A.2: Grids, number of cells and mesh quality criteria.

	total no. of cells in Mio	no. of cells along one nozzle diameter	max. non-orthogo-nality	mean non-orthogo-nality	max. aspect ratio	max. skewness
coarse	0.75	13	62.01	12.90	12.06	2.03
medium	2.32	27	67.10	12.50	13.02	2.26
fine	4.47	36	70.5921	14.69	52.64	2.52

tom wall is similar to the one at the top wall except for the first small rise in pressure and the fact that the pressure drop is smaller. These differences occur, since the geometry changes only at the top wall and thus affects the pressure at the bottom wall less. *sonicFoam* again matches the experimental data well except for a small underprediction in the throat. Overall, a reasonable agreement is reached between experiment and *sonicFoam*.

A.2.3. GRID INDEPENDENCE STUDY

In compressible flows, adequate meshing is important for both the numerical stability and the accuracy of the result. The grid dependence of the solution was studied (for the standard case at a melt temperature of 943 K) on three meshes listed in Table A.2. As the gradients are expected to be highest within the nozzles, the resolution inside the nozzles is crucial. Fig. A.3 shows the Mach number and temperature profile at the outlet of the second nozzle. While for the coarse mesh both Mach number and temperature deviate from the results of the finer meshes, the medium and fine mesh results are in good agreement. This is why we chose the medium mesh for further calculations.
To speed up the simulations, two symmetry planes were used and only a quarter of the VDB was simulated. This particularly constrains the swirling motion along the long extension of the VDB. To study the influence on the viscous losses, half of the VDB was also simulated for the standard case. Neither the total nor the local mass flow rate changed

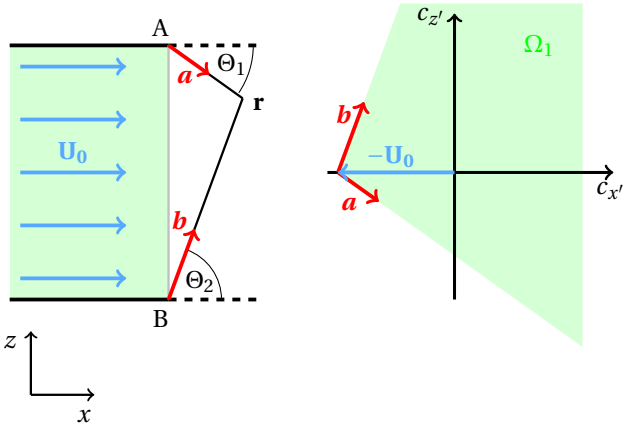

Figure A.4: Single straight jet. On the left, there is a sketch of the jet geometry in real space, on the right the velocity domain as introduced by Cai and Boyd [126]. To obtain the solution at point **r** the velocity space is integrated over the region bounded by vectors a and b which connect the outlet with point **r**.

notably, which justifies the use of the quarter geometry.

A.3. EQUATIONS FOR COLLISIONLESS FLOW SOLUTION

The velocity ξ of each particle is split into a local mean velocity **u** and a fluctuational velocity **c**, i.e., $\xi = \mathbf{u} + \mathbf{c}$. Equilibrium and a non-zero mean velocity are assumed to prevail at the outlets of the nozzles, so that the particle velocity distribution results from a Maxwellian distribution $f_0(\mathbf{c})$ shifted by the mean inlet velocity $\mathbf{U_0}$. For each point in the flow domain, Cai and Boyd [126] integrated the moments over a region in velocity space bounded by the velocity vectors, for which particles leaving from the two utmost points of the inlet reach the studied point (the corresponding bounding vectors are **a** and **b** in Figure A.4). For a planar, sonic, non-inclined jet, the moment $M_\Psi \in [n, v_x, v_z, e]$ of an invariant $\Psi \in [1, \xi_x, \xi_z, 1/2\mathbf{c}^2]$ can be obtained by integrating over the invariant weighted with the phase density, which gives

$$M_\Psi(\mathbf{r}) = \iiint_\Omega \Psi f_0(\mathbf{c})\,\mathrm{d}\mathbf{c}, \tag{A.3}$$

where the kinematic relation

$$\Omega : \frac{z - \frac{D}{2}}{x} < \frac{c_z}{c_x + U_0} < \frac{z + \frac{D}{2}}{x} \tag{A.4}$$

bounds the integration over velocity space to those velocities which may reach the point **r**. The corresponding domain is shown in Figure A.4 on the right. Cai and Boyd transformed the integration domain over the velocity space to polar coordinates with the velocity magnitude $|\boldsymbol{V}| = \sqrt{(U_0 + c_x)^2 + c_z^2}$ as the radial component and the angle Θ which is formed by the jet axis and the vector connecting the studied point with a point on the

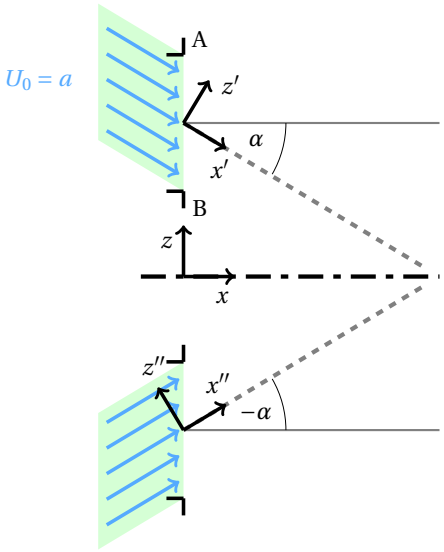

Figure A.5: Coordinate transformation for jets inclined at angle α.

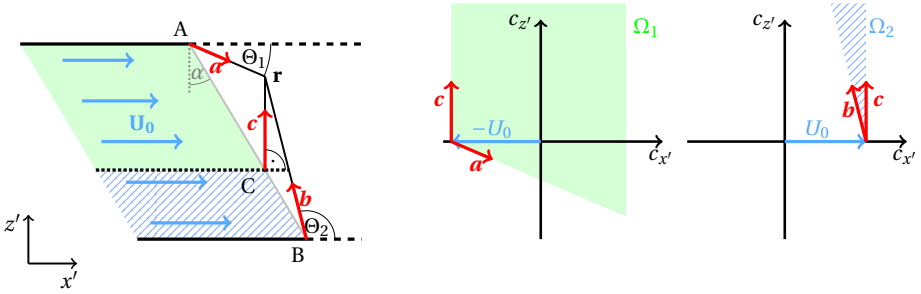

Figure A.6: Single jet. On the left, there is a sketch of the jet geometry in real space, on the right, there are the two velocity domains compared to Figure A.4. To obtain the solution at point **r** the integration domain is split into a part where the mean inlet velocity is directed towards **r** (uniform green area) and one where the mean inlet velocity is directed away from **r** (hatched in blue area).

inlet boundary, as the angular component. The corresponding integration element is $d\xi = |\mathbf{V}|d|\mathbf{V}|\,d\Theta$. The transformed integration reads as

$$M_\Psi(\mathbf{r}) = \iiint_\Omega \Psi f_0(\xi)\,|\mathbf{V}|d|\mathbf{V}|d\Theta, \tag{A.5}$$

$$\text{where } \Omega : \frac{z-\frac{D}{2}}{x} < \tan(\Theta) < \frac{z+\frac{D}{2}}{x}, \tag{A.6}$$

$$\text{and } 0 < |\mathbf{V}| < \infty. \tag{A.7}$$

This integration produces the solution for a single, straight jet with the mean inlet velocity U_0. The final expressions for density, velocity and temperature can be found in the work of Cai and Boyd [126].

Similar effusion problems can be solved by altering the integration domain Ω. As described below, we adapt the solution for a single straight jet to (i) a single inclined jet and then (ii) two inclined jets next to each other.

(i) Single Inclined Jet

To evaluate the number density of an inclined jet, the coordinate system needs to be rotated to align the jet axis with the direction of the inlet velocity (Fig. A.5) using the rotation matrix

$$\mathbf{R} = \begin{pmatrix} \cos(\alpha) & -\sin(\alpha) \\ \sin(\alpha) & \cos(\alpha) \end{pmatrix}, \tag{A.8}$$

where α is the inclination angle of the jet. The local coordinate transformation for integration for the upper jet is $\mathbf{r}' = \mathbf{R}\mathbf{r}$ and for the lower jet $\mathbf{r}'' = \mathbf{R}^T\mathbf{r}$. (For brevity, we give only the solution for the upper jet when $\alpha < 0$, as shown in Figure A.6, the solution for $\alpha > 0$can be obtained by switching Θ_1 and Θ_2.) The integration domain at the inlet boundary has to be split into two different sections as shown on the left in Figure A.6: the inlet region where $x' < r_x$ so that the mean inlet velocity U_0 is directed towards r_x (colored in green, Ω_1 in velocity space) and that where $x' > r_x$ so that the flow will not pass r_x after leaving the inlet (hatched in blue, Ω_2 in velocity space). The corresponding domains in velocity space are shown in Figure A.6 on the right, where Ω_1 is limited by the direction vector between the upper boundary A and the studied point X shifted from the origin by $-U_0$ and a right angle, while Ω_1 is limited by the direction vector between the upper boundary B and the studied point X shifted from the origin by $+U_0$ and a right angle. In the other directions, the integration domain is unbounded. This can be transformed to polar coordinates, producing the limiting angles

$$\Theta_1 = \arctan\left(\frac{z' - \cos(\alpha)D/2}{x' + \sin(\alpha)D/2}\right), \tag{A.9}$$

$$\Theta_2 = \arctan\left(\frac{z' + \cos(\alpha)D/2}{x' - \sin(\alpha)D/2}\right). \tag{A.10}$$

The green integration domain Ω_1 is then given by

$$\Omega_1 : \Theta_1 < \Theta < \min\left(\frac{\pi}{2}, \Theta_2\right), \tag{A.11}$$

$$|\mathbf{V_1}| = \sqrt{(c_x + U_0)^2 + c_z^2}. \tag{A.12}$$

and the blue hatched integration domain Ω_2 by

$$\Omega_2 : \frac{\pi}{2} < \Theta < \Theta_2 , \tag{A.13}$$

$$|\mathbf{V_2}| = \sqrt{(c_x - U_0)^2 + c_z^2}. \tag{A.14}$$

All solution can be written as a function of the inlet speed ratio $S_0 = U_0/\sqrt{2k_B T/m}$ and the angles Θ_1, Θ_2. To switch between regions where only the green depicted integration domain Ω_1 and the one where also Ω_2 has to be considered, the Heaviside step function $H()$ is applied. The expressions for number density $n(x,z)$, velocities $u(x,z), w(x,z)$ and total energy $E_{tot}(x,z)$ of a single inclined plume then read

$$\begin{aligned}
\frac{n(x,z)}{n_0} = {} & \frac{\exp(-S_0^2)}{2\pi}(\Theta_2 - \Theta_1) \\
& + \frac{1}{4}\left[\operatorname{erf}(S_0 \sin\Theta_2) - \operatorname{sign}(\Theta_1)\operatorname{erf}(S_0 \sin\Theta_1)\right] \\
& + H\left(\Theta_2 - \frac{\pi}{2}\right)\frac{1}{2}\left[\operatorname{erf}(S_0) - \operatorname{erf}(S_0 \sin\Theta_2)\right] \\
& + \frac{S_0}{2\pi}\int_{\Theta_1}^{\Theta_2} \exp(-S_0^2 \sin^2\Theta)\cos\Theta \operatorname{erf}(S_0\cos\Theta)\,\mathrm{d}\Theta ,
\end{aligned} \tag{A.15}$$

$$\begin{aligned}
\frac{u(x,z)}{\sqrt{2k_B T_0/m}} = {} & \frac{\exp(-S_0^2)}{\pi n(x,z)} \cdot \\
& \left[\frac{S_0}{2}\left(\Theta_2 - \Theta_1 + H\left(\Theta_2 - \frac{\pi}{2}\right)(\pi - 2\Theta_2)\right)\right. \\
& + \frac{S_0}{4}\left(\sin(2\Theta_2) - \sin(2\Theta_1) - H\left(\Theta_2 - \frac{\pi}{2}\right)2\sin(2\Theta_2)\right) \\
& \quad + S_0^2\sqrt{\pi}\left(\int_{\Theta_1}^{\Theta_2} \cos^3\Theta\,(1 + \operatorname{erf}(S_0\cos\Theta))\exp(S_0^2\cos^2\Theta)\,\mathrm{d}\Theta\right. \\
& \qquad \left. - H\left(\Theta_2 - \frac{\pi}{2}\right)2\int_{\frac{\pi}{2}}^{\Theta_2} \cos^3\Theta \operatorname{erf}(S_0\cos\Theta)\exp(S_0^2\cos^2\Theta)\,\mathrm{d}\Theta\right) \\
& \quad + \frac{\sqrt{\pi}}{2}\left(\int_{\Theta_1}^{\Theta_2} \exp(S_0^2\cos^2\Theta)\cos\Theta\,(1 + \operatorname{erf}(S_0\cos\Theta))\,\mathrm{d}\Theta\right. \\
& \qquad \left.\left. - H\left(\Theta_2 - \frac{\pi}{2}\right)2\int_{\frac{\pi}{2}}^{\Theta_2} \exp(S_0^2\cos^2\Theta)\cos\Theta \operatorname{erf}(S_0\cos\Theta)\,\mathrm{d}\Theta\right)\right]
\end{aligned} \tag{A.16}$$

$$\begin{aligned}
\frac{w(x,z)}{\sqrt{2k_B T_0/m}} = {} & \frac{1}{4\sqrt{\pi}n(x,z)} \cdot \left[\exp\left(-S_0^2\sin^2\Theta_1\right)\cos\Theta_1\,(1 + \operatorname{erf}(S_0\cos\Theta_1))\right. \\
& - \exp\left(-S_0^2\sin^2\Theta_2\right)\cos\Theta_2\,(1 + \operatorname{erf}(S_0\cos\Theta_2)) \\
& \left. + H\left(\Theta_2 - \frac{\pi}{2}\right)2\exp\left(-S_0^2\sin^2\Theta_2\right)\cos\Theta_2 \operatorname{erf}(S_0\cos\Theta_2)\right]
\end{aligned} \tag{A.17}$$

$$E_{tot}(x,z) = \frac{T_0 \exp(-S_0^2)}{6n(x,z)\pi} \cdot \left[\left(3+S_0^2\right)(\Theta_2-\Theta_1) + S_0^2\left(\frac{1}{2}(\sin 2\Theta_2 - \sin 2\Theta_1)\right) + 2S_0\sqrt{\pi}\int_{\Theta_1}^{\Theta_2} \left(2\cos\Theta + S_0^2\cos^3\Theta\right)\exp(S_0^2\cos^2\Theta)\left(1+\operatorname{erf}(S_0\cos\Theta)\right)\mathrm{d}\Theta - H\left(\Theta_2-\frac{\pi}{2}\right)4S_0\sqrt{\pi}\int_{\Theta_2}^{\frac{\pi}{2}}\left(2\cos\Theta+S_0^2\cos^3\Theta\right)\exp(S_0^2\cos^2\Theta)\,\mathrm{d}\Theta\right] \quad \text{(A.18)}$$

(ii) Superposition of Two Inclined Jets

The number density of the interacting case is the superposition of number densities of two single jets given by

$$n(\mathbf{r}) = n_U(\mathbf{r}) + n_L(\mathbf{r})\,, \quad \text{(A.19)}$$

where the subscript U denotes the upper jet and L the lower one. The velocity vectors have to be rotated back into the original coordinate system by

$$\mathbf{u_U} = \mathbf{R}^T\,\mathbf{u'_U} \quad \text{and} \quad \mathbf{u_L} = \mathbf{R}\,\mathbf{u''_L}\,, \quad \text{(A.20)}$$

before applying their density-weighted average to obtain the velocity of the jet interaction

$$\mathbf{u}(\mathbf{r}) = \frac{n_U(\mathbf{r})\mathbf{u_U}(\mathbf{r}) + n_L(\mathbf{r})\mathbf{u_L}(\mathbf{r})}{n(\mathbf{r})}\,. \quad \text{(A.21)}$$

To obtain the temperature field, the thermal energy is calculated as the difference of the total energy of both jets E_{tot} and the macroscopic kinetic energy E_{kin} derived from the velocity and number density field:

$$E_{tot}(\mathbf{r}) = m\iiint_{\Omega_U\cup\Omega_L}\xi^2 f_0(\xi)\,\mathrm{d}\xi\,, \quad \text{(A.22)}$$

$$E_{kin}(\mathbf{r}) = m\,n(\mathbf{r})\,\mathbf{u}(\mathbf{r})^2\,. \quad \text{(A.23)}$$

The temperature field is then determined by

$$T = \frac{1}{3k_B n(\mathbf{r})}\left(E_{tot}(\mathbf{r}) - E_{kin}(\mathbf{r})\right)\,. \quad \text{(A.24)}$$

The same steps can be conducted to adapt the effusion solution for three-dimensional single plumes [232] to interacting three-dimensional plumes.

A.4. VERIFICATION RIEMANN SOLVER, SHOCK TUBE

We verified the approximate Riemann solver using a shock tube case, which is 1D domain initially split in a high and a low pressure section by a membrane. The sudden

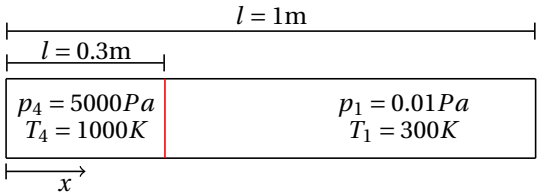

Figure A.7: Sketch of the shock tube. Driver section on the left; driven section on the right.

Table A.3: Overview of tested solvers.

	cells	temporal integration	CFL
sonicFoam (foam-extend 4.0)	50000	Euler	0.1
dbnsFoam (foam-extend 4.0)	150	Runge-Kutta 4	flux based
dbnsFoam hllc	150, 10000, 100000	Runge-Kutta 4	flux based
rhoCentralFoam (OpenFoam v18.06)	1000	Euler	0.1

destruction of the membrane yields an expansion wave travelling into the high pressure section (driver section) and a shock wave travelling into the low pressure region (driven section) until they reach their respective boundaries. The shock tube setup is often used to test compressible solvers and schemes, as it is simple, but still covers all fundamental phenomena in compressible flow, i.e., expansion wave, contact discontinuity and shock.

We tested multiple compressible solvers and schemes available in OpenFoam, as listed in Table A.3 and Table A.4. The classical Sod's shock tube test is driven by a pressure ratio of 10, for which most of the compressible solvers mentioned hereafter produced reasonable to accurate results [233, 234]. However, the tremendous pressure ratio due to the vacuum exacerbates the problem so that the shock is not captured accurately anymore. To verify the solver for the case of interacting jets, we adapted the shock tube test case to a pressure ratio of $5 \cdot 10^5$, which is an extreme version of the simulated cases. The computational domain and initial conditions are depicted in Figure A.7. No initial or inlet velocity is assumed. The high pressure ratio in the driven section may give rise to numerical instabilities,i.e., either oscillations or over-/undershoots. In addition, it should be noted that the smaller the sound speed ratio between the driver and driven section a_1/a_4 (below unity), the stronger the shock and the higher the minimum temperature in the expansion wave, which may yield negative temperatures for an insufficient discretization.

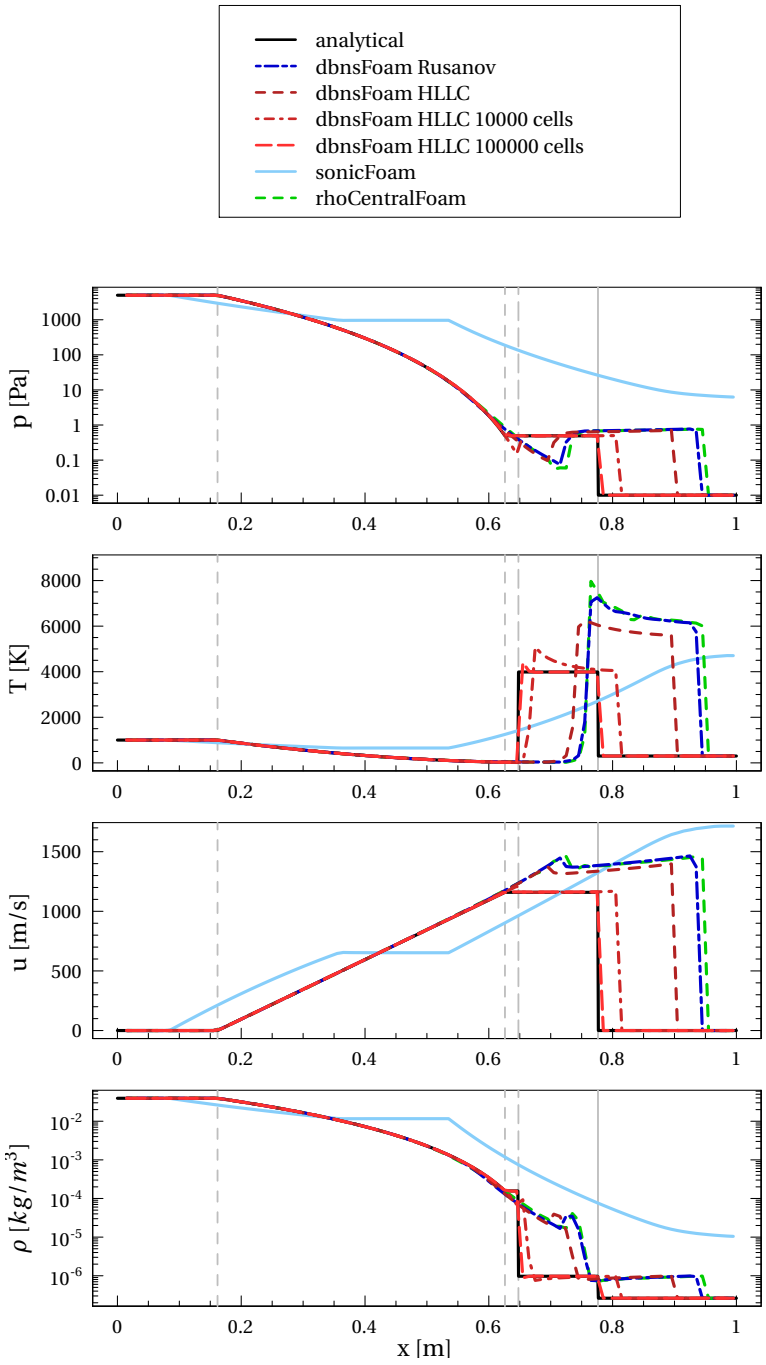

Figure A.8: Pressure, temperature, velocity and density profiles in the shock tube at $t = 0.0003$s from the analytical solution and different solvers. The thin gray lines mark from left to right: the expansion head, the expansion tail, the slip surface and the shock.

Table A.4: Overview schemes used in tested solvers.

	convective scheme	advective schemes	grad scheme
sonicFoam (foam-extend 4.0)	cellLimited linear 1	van Leer	cellLimited linear 1
dbnsFoam (foam-extend 4.0)	flux: rusanov, limiter: Barth-Jespersen	-	-
dbnsFoam hllc	flux: HLLC, limiter: Barth-Jespersen	-	-
rhoCentralFoam (OpenFoam v18.06)	flux: Tadmor	-	cellLimited leastSquares 1

Table A.5: Mesh parameters for mesh independence study for the approximate Riemann solver.

	cells	cells in x-direction	cells in z-direction
coarse	288000	1200	240
medium	1152000	2400	480
fine	1792000	3200	560

Figure A.8 shows the pressure, temperature, velocity and density profiles for the analytical solution [73] and different solvers at $t = 0.0003$s. The result of sonicFoam, which is a pressure-based solver, is far from the solution and does not capture the shock features even in qualitative terms (please note that this is the version in foam-extend 4.0, which differs from the in ESI OpenFoam versions). rhoCentralFoam, a solver based on Tadmor flux splitting, qualitatively captures the expansion and shock, but overpredicts shock speed. Further grid refinement produces oscillations around the discontinuities, which results in the divergence of the solver. dbnsFoam, an approximate Riemann solver, produces a result similar to rhoCentralFoam, when a Rusanov flux scheme is applied. When a HLLC flux is applied, the shock speed is reduced. Grid refinement further improves the prediction. However, to obtain a reasonably accurate solution, $100k$ cells are required, which is immense for a 1D problem and illustrates the difficulties in using CFD for high pressure ratios.

A.5. MESH INDEPENDENCE STUDY

The independence of the solution from the mesh was studied. The computational domain was chosen a bit longer than for the DSMC solution and was $0.012\,\text{m} \times 0.03\,\text{m}$. All tested meshes had a completely orthogonal and equidistant meshing to ensure perfect orthogonality and a fine resolution along the entire shock at the same time. The resolution for the studied meshes is listed in Table A.5. Figure A.9 shows the normalized density and deposition rate predicted on the three different meshes at $x = 15\,\text{mm}$. To highlight

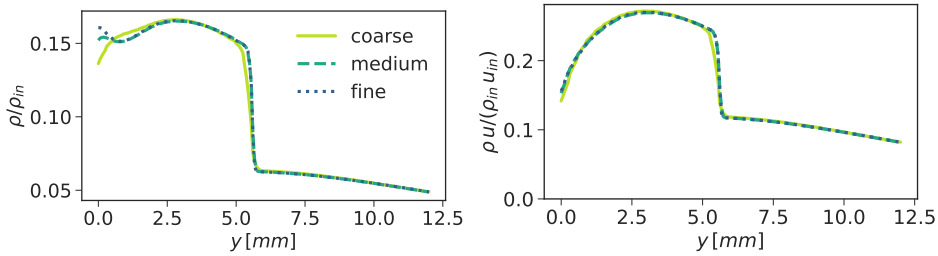

(a) Density at $x = 15\,\text{mm}$ (b) Deposition rate at $x = 15\,\text{mm}$

Figure A.9: Profiles of (a) normalized density and (b) normalized deposition rate for different mesh refinements at $x = 15\,\text{mm}$ for the inviscid continuum flow (Riemann solver, inlet density corresponds to the case $Kn_s = 8Kn_0$).

the small differences, only the region above the symmetry line is considered. The coarse mesh predicts the height of the two plateaus before and after the shock correctly, but calculates a lower steepness across the shock and a larger density drop around the symmetry compared with the medium and fine mesh. The solution on the medium and fine mesh match quite well. For the normalized deposition rate, the parameter which was of foremost importance in this study, the small deviations in density rate are mitigated producing a good match between all meshes and an excellent match between the medium and fine mesh. Hence, the medium mesh was chosen for all calculations.

A.6. SHOCK STRUCTURE

To validate the shock detection method and to gain a better understanding of the shock region, we analyze the changes the flow undergoes when passing through the shock. Figure A.10 compares the inviscid continuum solution and one rarefied solution for $Kn_s = 2Kn_0$. Figure A.10a and Figure A.10b show the subsonic region (red dots), the detected shock (blue solid line) and multiple streamlines crossing the shock. The changes the flow undergoes within the shock are shown for streamline No. 0 in Figure A.10c for the inviscid continuum solution and in Figs. A.10d for the transitional flow regime. The figures show the profiles of several flow variables $\Phi \in [n, T, M, ...]$ in the immediate vicinity of the shock, normalized by their local maximum and minimum values before (Φ_1) and after the shock (Φ_2), which reads

$$\tilde{\Phi} = \frac{\Phi - \Phi_1}{\Phi_2 - \Phi_1}.$$

First, we focus on the number density profile, as it is commonly used to define the shock position and shock thickness [131]. Before the shock, the number density declines due to expansion — which is more clearly visible in the transitional flow regime as the shown section covers a longer streamline length — and rises sharply in the shock. Its crossing of $\tilde{n} = 0.5$ is commonly picked as shock location and here marked by gray dashed lines. The blue vertical line marks the location where the shock was detected by our proposed approach using the MOC. The detected location varied between $\tilde{n} \approx 0.3 - 0.8$ for the streamlines shown, with the exception of streamline No. 0 for the continuum flow

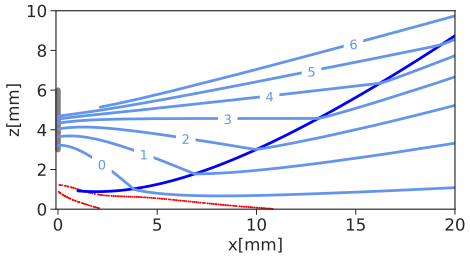

(a) Streamlines for $Kn_s = 2Kn_0$. Inviscid continuum solution. The gray solid line marks the inlet position, the light blue solid lines mark streamlines, the blue solid line denotes the detected shock position and the red dots represent the sonic line.

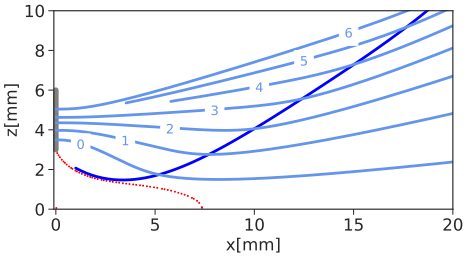

(b) Streamlines for $Kn_s = 2Kn_0$. DSMC solution. The gray solid line marks the inlet position, the light blue solid lines mark streamlines, the blue solid line denotes the detected shock position and the red dots represent the sonic line.

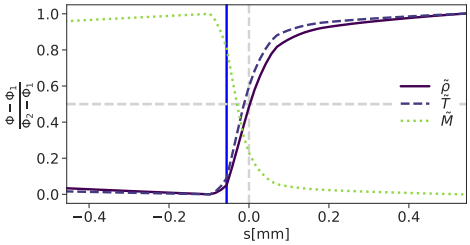

(c) Flow variables plotted over streamline No. 0 in subfigure (a) around the shock position for $Kn_s = 2Kn_0$ (Euler solution).

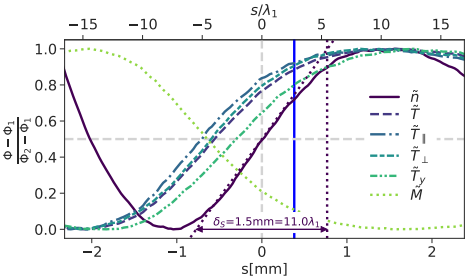

(d) Flow variables plotted over streamline No. 0 in subfigure (b) around the shock position for $Kn_s = 2Kn_0$ (DSMC solution).

Figure A.10: (a),(b) streamline positions. (c),(d) Profiles along the streamlines across the shock. The vertical blue line marks the detected shock location, the gray dashed lines mark the actual shock location, i.e., $\tilde{n} = 0.5$.

with $\tilde{n} \approx 0$, for which the broad region of converging characteristics around the subsonic region hampers localization.
The shock thickness δ_s is the distance it takes to go from pre-shock density to post-shock density when applying the highest slope of the density profile inside the shock, i.e.,

$$\delta_s = \left[\max\left(\frac{\mathrm{d}\tilde{n}}{\mathrm{d}s}\right)\right]^{-1}.$$

Since the change from pre-shock to post-shock state depends on the number of collisions undergone, the shock thickness is commonly expressed in terms of mean free path lengths from the pre-shock state, λ_1. (For inviscid continuum flow, the shock thickness vanishes, the continuity of the shown profiles is due to discretization.) Streamline No. 0 is near the subsonic region for both the continuum and the transitional flow regime. It enters the shock at a wide angle and bends more than the other depicted streamlines. For the case in the transitional flow regime, the shock thickness is $\delta_S = 1.5$mm, which corresponds to $11\lambda_1$. Considering that the shock is a weak oblique shock with a pre-shock

Mach $M_1 = 2.4$ and post-shock Mach $M_2 = 1.3$, the thickness compares reasonably well with typical thicknesses for weak normal shocks [235].
The Mach number drops and the temperature rises before the number density rise occurs. The shift between the temperature and density profile is about $5\lambda_1$ for the tansitional flow regime. While in a continuum only one equilibrium temperature is defined, the different temperature modes are shifted as well for transitional flow. We split the temperature in a temperature which is parallel to the local mean velocity, denoted as $T_\parallel$, one orthogonal to it (but in the solution plane), denoted as $T_\perp$, and one in the quasi-homogeneous out-of-plane direction, denoted as T_y. First the parallel temperature $T_\parallel$ rises, as the decrease in mean velocity due to the mixing of pre-shock and post-shock particles is reflected in a transfer from macroscopic kinetic energy to thermal energy. The orthogonal temperature follows closely, one reason being that the streamline bending breaks the alignment of particle velocities with the mean velocity. (If collisions played the dominant role in this initial rise of parallel and orthogonal temperatures, the equidistribution between modes would transfer the energy to the homogeneous direction immediately.) Only then does the temperature in homogeneous direction rise due to collisions, which transfer the energy from the parallel and orthogonal temperature mode into the homogeneous direction. This temperature-density separation of $2-3\lambda_1$ between temperatures is maintained across the shock, which indicates that the free movement of particles between two collisions introduces non-equilibrium, which can not be overcome by the redistribution due to collisions. (no comprehensive experimental measurements are available). The temperature-density separation in oblique shocks is expected to increase with the velocity component tangential to the shock.)

A.7. TIME STEP, MESH AND PARTICLE NUMBER INDEPENDENCE STUDY

The independence of the solution was tested exemplary for the case $Kn = 2Kn_0 = 0.025$ and $y_He = 0.5$. The results in the manuscript were drawn from a simulation containging a number of particles of $N_p = 3.27M$, a time step of $dt_0 = 2.5{\cdot}10^{-9}$ s and a number of cells of $No_c = 56784$. This corresponds to fulfilling the resolution criteria for time step $dt < \tau/10$, grid size $dx < 2\lambda/3$ everywhere and particle number per cell being at least 20 as described in **??**. The resolution was varied to study the independence of the solution on the discretization. The silver number density flux normalized by the silver inlet number density flux at a nozzle-to-plate distance of $x = 8$ mm is plotted for the different resolutions in Figure A.11. The time step was varied with $dt \in [0.5dt_0, dt_0, 2dt_0, 10dt_0, 40dt_0, 100dt_0]$. For a time step size of $dt = 40dt_0$ and $dt = 100dt_0$, the predicted normalized number density flux varies from the one at smaller time step sizes, whereas the deviations for $dt \in [0.5dt_0, dt_0, 2dt_0, 10dt_0$ are small to negligible (Figure A.11a). The grid cell size was refined by a factor of 2 (increasing the number of cells by a factor 4, so that the mesh globally fulfilled $dx < 1\lambda/3$. The particle number was adapted to keep the number of particles per cell constant. The resulting number density fluxes match for the different grid refinements (Figure A.11b). The particle number was varied to be 0.25, and 0.5 of the standard particle number. The results for the different particle numbers match each

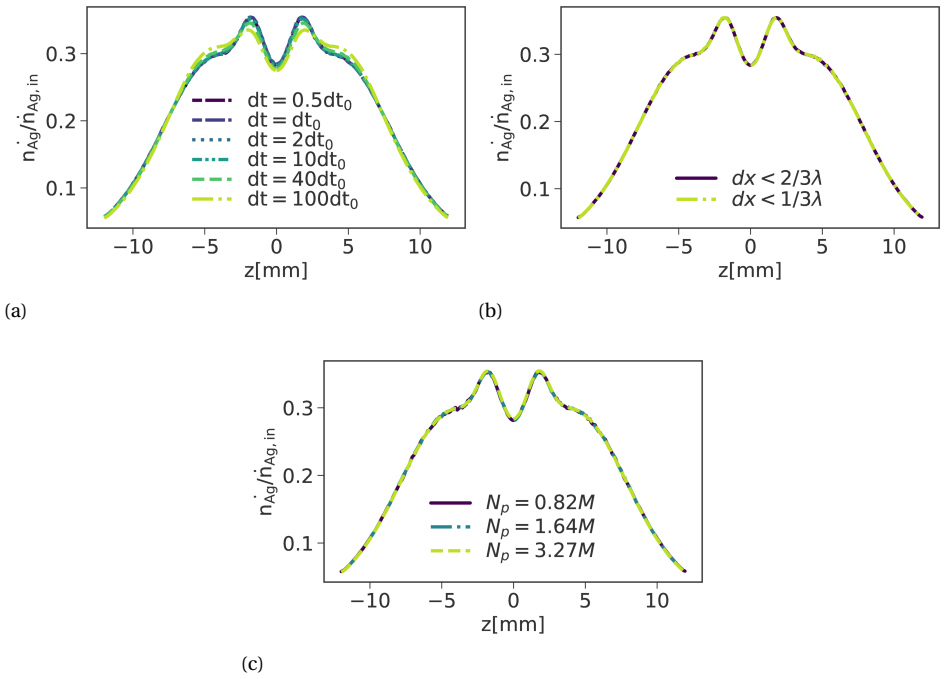

Figure A.11: Independence study for interacting plumes at $Kn = 2Kn_0 = 0.025$ and $y_He = 0.5$. Line plot of the silver number density flux normalized by the silver inlet number density flux at a nozzle-to-plate distance of $x = 8$ mm for (a) varying time step sizes, (b) varying mesh size and (c) varying particle number.

other (Figure A.11c). Based on these good results for the chosen resolution, we expect the fulfillment of the previously discussed and widely referenced resolution criteria to be sufficient for a discretization refinement independent solution. The actual time step size, grid and number of particles was adapted for each case individually to ensure the fulfillment of the criteria.

REFERENCES

[1] E. Fermi, *Thermodynamics By Enrico Fermi* (Snowball Publishing, 2010).

[2] N. Hosking, M. Ström, P. Shipway, and C. Rudd, *Corrosion resistance of zinc–magnesium coated steel,* Corrosion science **49**, 3669 (2007).

[3] T. Prosek, A. Nazarov, U. Bexell, D. Thierry, and J. Serak, *Corrosion mechanism of model zinc–magnesium alloys in atmospheric conditions,* Corrosion Science **50**, 2216 (2008).

[4] K. Bae, J. La, I. Lee, S. Lee, and K. Nam, *Effects of annealing heat treatment on the corrosion resistance of Zn/Mg/Zn multilayer coatings,* Metals and Materials International **23**, 481 (2017).

[5] J. Davies, C. Glover, J. Van de Langkruis, E. Zoestbergen, and G. Williams, *The effect of Mg concentration on the resistance of PVD Zn-Mg coatings to corrosion driven organic coating delamination,* Corrosion Science **100**, 607 (2015).

[6] S. Sabooni, E. Galinmoghaddam, H. Cao, R. Westerwaal, E. Zoestbergen, J. T. M. De Hosson, and Y. Pei, *New insight into the loss of adhesion of ZnMgZn bi-layered coatings on steel substrates,* Surface and Coatings Technology **370**, 35 (2019).

[7] E. Zoestbergen, T. Maalman, C. Commandeur, and M. Goodenough, *Influence of contamination on the thermal evaporation of a zinc melt,* Surface and Coatings Technology **218**, 108 (2013).

[8] J. Fan, I. D. Boyd, and C. Shelton, *Monte carlo modeling of electron beam physical vapor deposition of yttrium,* Journal of Vacuum Science & Technology A: Vacuum, Surfaces, and Films **18**, 2937 (2000).

[9] U. Helmersson, M. Lattemann, J. Bohlmark, A. P. Ehiasarian, and J. T. Gudmundsson, *Ionized physical vapor deposition (ipvd): A review of technology and applications,* Thin solid films **513**, 1 (2006).

[10] Y. Deng, W. Chen, B. Li, C. Wang, T. Kuang, and Y. Li, *Physical vapor deposition technology for coated cutting tools: A review,* Ceramics International **46**, 18373 (2020).

[11] L. Baptiste, N. van Landschoot, G. Gleijm, J. Priede, J. S. van Westrum, H. Velthuis, and T.-Y. Kim, *Electromagnetic levitation: A new technology for high rate physical vapour deposition of coatings onto metallic strip,* Surface and Coatings Technology **202**, 1189 (2007).

[12] P. Banaszak, D. Marneffe, E. Silberberg, and L. Vanhee, *Industrial vapour generator for the deposition of an alloy coating onto a metal strip,* (2011), US Patent App. 12/681,969.

[13] J. D. Anderson, *Modern compressible flow: with historical perspective*, Vol. 12 (McGraw-Hill New York, 1990).

[14] D. Lindley, *Boltzmann's atom: The great debate that launched a revolution in physics,* (2001).

[15] T. L. Heath *et al.*, *The works of Archimedes* (Courier Corporation, 2002).

[16] Vitruvius and M. H. Morgan, *The ten books on architecture* (Dover, 1914).

[17] T. Lucretius Carus, *De rerum natura / Welt aus Atomen* (Reclam Verlag, Germany, 1986).

[18] D. Bernoulli, *Hydrodynamica,* Dulsecker. Consultable en ligne http://imgbase-scd-ulp. u-strasbg. fr/displayimage. php **1738** (1738).

[19] L. Euler, *Principes généraux du mouvement des fluides,* Mémoires de l'académie des sciences de Berlin , 274 (1757).

[20] G. G. Stokes, *On the theories of the internal friction of fluids in motion, and of the equilibrium and motion of elastic solids,* (1845).

[21] J. J. Waterston and J. W. Strutt, *I. on the physics of media that are composed of free and perfectly elastic molecules in a state of motion,* Philosophical Transactions of the Royal Society of London.(A.) , 1 (1892).

[22] A. Krönig, *Grundzüge einer Theorie der Gase* (éditeur non identifié, 1856).

[23] R. Clausius, *Ueber die Art der Bewegung, welche wir Wärme nennen,* Annalen der Physik **176**, 353 (1857).

[24] A. Einstein, *Über die von der molekularkinetischen Theorie der Wärme geforderte Bewegung von in ruhenden Flüssigkeiten suspendierten Teilchen,* Annalen der physik **4** (1905).

[25] O. Reynolds, *Iv. on the dynamical theory of incompressible viscous fluids and the determination of the criterion,* Philosophical transactions of the royal society of london.(a.) , 123 (1895).

[26] W. Jones and B. E. Launder, *The prediction of laminarization with a two-equation model of turbulence,* International journal of heat and mass transfer **15**, 301 (1972).

[27] M. Knudsen, *Eine Revision der Gleichgewichtsbedingung der Gase. Thermische Molekularströmung,* Annalen der Physik **336**, 205 (1909).

[28] M. Knudsen, *Thermischer Molekulardruck der Gase in Röhren,* Annalen der Physik **338**, 1435 (1910).

[29] M. Knudsen, *Die Gesetze der Molekularströmung und der inneren Reibungsströmung der Gase durch Röhren,* Annalen der Physik **333**, 75 (1909).

[30] D. Enskog, *Kinetische Theorie der Vorgänge in mässig verdünnten Gasen. i. Allgemeiner Teil,* Uppsala: Almquist & Wiksells Boktryckeri (1917).

[31] S. Chapman and T. Cowling, *The mathematical theory of non-uniform gases. an account of the kinetic theory of viscosity, thermal conduction and diffusion in gases,* Cambridge: University Press (1970).

[32] S. Chapman, *The kinetic theory of simple and composite monatomic gases: viscosity, thermal conduction, and diffusion,* Proceedings of the Royal Society of London. Series A, Containing Papers of a Mathematical and Physical Character **93**, 1 (1916).

[33] G. Bird, *Approach to translational equilibrium in a rigid sphere gas,* The Physics of Fluids **6**, 1518 (1963).

[34] G. Bird, *Molecular gas dynamics and the direct simulation of gas flows,* (1994).

[35] S. V. Patankar and D. B. Spalding, *A calculation procedure for heat, mass and momentum transfer in three-dimensional parabolic flows,* in *Numerical prediction of flow, heat transfer, turbulence and combustion* (Elsevier, 1983) pp. 54–73.

[36] R. I. Issa, *Solution of the implicitly discretised fluid flow equations by operator-splitting,* Journal of computational physics **62**, 40 (1986).

[37] S. Godunov and I. Bohachevsky, *Finite difference method for numerical computation of discontinuous solutions of the equations of fluid dynamics,* Matematičeskij sbornik **47**, 271 (1959).

[38] U. Frisch, B. Hasslacher, and Y. Pomeau, *Lattice-gas automata for the Navier-Stokes equation,* Physical review letters **56**, 1505 (1986).

[39] N. Frapolli, S. S. Chikatamarla, and I. V. Karlin, *Entropic lattice Boltzmann model for compressible flows,* Physical Review E **92**, 061301 (2015).

[40] P. E. Hovsepian, Q. Luo, G. Robinson, M. Pittman, M. Howarth, D. Doerwald, R. Tietema, W. Sim, A. Deeming, and T. Zeus, *TiAlN/VN superlattice structured PVD coatings: a new alternative in machining of aluminium alloys for aerospace and automotive components,* Surface and coatings technology **201**, 265 (2006).

[41] T. Prosek, A. Nazarov, F. Goodwin, J. Šerák, and D. Thierry, *Improving corrosion stability of ZnAlMg by alloying for protection of car bodies,* Surface and Coatings Technology **306**, 439 (2016).

[42] Q. Mehran, M. Fazal, A. Bushroa, and S. Rubaiee, *A critical review on physical vapor deposition coatings applied on different engine components,* Critical Reviews in Solid State and Materials Sciences **43**, 158 (2018).

[43] M. Peters, C. Leyens, U. Schulz, and W. A. Kaysser, *EB-PVD thermal barrier coatings for aeroengines and gas turbines,* Advanced engineering materials **3**, 193 (2001).

[44] X. Zhang, K. Zhou, C. Deng, M. Liu, Z. Deng, C. Deng, and J. Song, *Gas-deposition mechanisms of 7YSZ coating based on plasma spray-physical vapor deposition,* Journal of the European Ceramic Society **36**, 697 (2016).

[45] S. Shahidi, B. Moazzenchi, and M. Ghoranneviss, *A review-application of physical vapor deposition (PVD) and related methods in the textile industry,* The European Physical Journal Applied Physics **71**, 31302 (2015).

[46] H. Sun, K. Cooke, G. Eitzinger, P. Hamilton, and B. Pollet, *Development of PVD coatings for PEMFC metallic bipolar plates,* Thin Solid Films **528**, 199 (2013).

[47] N. Selvakumar and H. C. Barshilia, *Review of physical vapor deposited (PVD) spectrally selective coatings for mid-and high-temperature solar thermal applications,* Solar energy materials and solar cells **98**, 1 (2012).

[48] S. Suman, M. K. Khan, and M. Pathak, *Performance enhancement of solar collectors – a review,* Renewable and Sustainable Energy Reviews **49**, 192 (2015).

[49] N. Barreau, S. Marsillac, D. Albertini, and J. Bernede, *Structural, optical and electrical properties of β-In2S3-3xO3x thin films obtained by PVD,* Thin Solid Films **403**, 331 (2002).

[50] K. Matsumoto, Y. Itoh, and T. Kameda, *EB-PVD process and thermal properties of hafnia-based thermal barrier coating,* Science and Technology of Advanced Materials **4**, 153 (2003).

[51] C. G. Soares, Y. Garbatov, A. Zayed, and G. Wang, *Influence of environmental factors on corrosion of ship structures in marine atmosphere,* Corrosion Science **51**, 2014 (2009).

[52] M.-J. Li, S.-Z. Tang, F.-l. Wang, Q.-X. Zhao, and W.-Q. Tao, *Gas-side fouling, erosion and corrosion of heat exchangers for middle/low temperature waste heat utilization: A review on simulation and experiment,* Applied Thermal Engineering **126**, 737 (2017).

[53] B. Schmitz, *Development of Zn-Mg alloy coatings by JVD,* steel research **72**, 522 (2001).

[54] D. Chaleix, D. Jacques, P. Sergio, E. Silberberg, B. Schmitz, and X. V. Eynde, *Painted steel sheet provided with a zinc coating,* (2019), US Patent 10,400,326.

[55] S. Blakey and S. Beck, *The effect of combined radiation and convection on hot dip galvanizing kettle wear,* Applied thermal engineering **24**, 1301 (2004).

[56] D. Mei, F. Xing, M. Wen, P. Lei, and Z. Fang, *Numerical simulation of mixed convection heat transfer of galvanized steel sheets in the vertical alloying furnace,* Applied Thermal Engineering **93**, 500 (2016).

[57] A. El Hajjami, M. Gigandet, M. De Petris-Wery, J. Catonne, J. Duprat, L. Thiery, F. Raulin, N. Pommier, B. Starck, and P. Remy, *Characterization of thin Zn–Ni alloy coatings electrodeposited on low carbon steel,* Applied surface science **254**, 480 (2007).

[58] R. Cresdee, W. Edwards, P. Thomas, and G. Voss, *Analysis of beam distortion during hot dip galvanising,* Materials science and technology **9**, 161 (1993).

[59] J. M. Kapopara, A. R. Mengar, K. V. Chauhan, and S. K. Rawal, *Cfd analysis of sputtered TiN coating,* Materials Today: Proceedings **4**, 9390 (2017).

[60] L. Nastac, W. Hanusiak, H. Dong, and F. Dax, *Modeling and simulating engineering processes with computational fluid dynamics,* JOM **56**, 43 (2004).

[61] W. He, G. Mauer, M. Gindrat, R. Wäger, and R. Vaßen, *Investigations on the nature of ceramic deposits in plasma spray–physical vapor deposition,* Journal of Thermal Spray Technology **26**, 83 (2017).

[62] G. Mauer and R. Vaßen, *Conditions for nucleation and growth in the substrate boundary layer at plasma spray-physical vapor deposition (ps-pvd),* Surface and Coatings Technology **371**, 417 (2019).

[63] S. Upadhye, S. Ramesh, M. Shah, M. Tendolkar, and J. Mukherjee, *Application of multicore processing and volume parallelization in EBPVD process simulated using dsmc,* in *International Conference on Advances in Thermal Systems, Materials and Design Engineering (ATSMDE2017)* (2017).

[64] X. Lu and J. Chai, *Direct simulation monte carlo study of metal evaporation with collimator in e-beam physical vapor deposition,* Chinese Physics B **28**, 074702 (2019).

[65] R. Dorsman, C. Kleijn, J. Velthuis, J. Zijp, and A. van Mol, *Zinc deposition experiments for validation of direct-simulation monte carlo calculations of rarefied internal gas flows,* Journal of Vacuum Science & Technology A: Vacuum, Surfaces, and Films **25**, 474 (2007).

[66] T. M. Rodgers, H. Zhao, and H. N. Wadley, *Thermal barrier coating deposition by rarefied gas jet assisted processes: Simulations of deposition on a stationary airfoil,* Journal of Vacuum Science & Technology A: Vacuum, Surfaces, and Films **31**, 061509 (2013).

[67] J. Balakrishnan, I. D. Boyd, and D. G. Braun, *Monte carlo simulation of vapor transport in physical vapor deposition of titanium,* Journal of Vacuum Science & Technology A: Vacuum, Surfaces, and Films **18**, 907 (2000).

[68] K. Bobzin, R. P. Brinkmann, T. Mussenbrock, N. Bagcivan, R. H. Brugnara, M. Schäfer, and J. Trieschmann, *Continuum and kinetic simulations of the neutral gas flow in an industrial physical vapor deposition reactor,* Surface and Coatings Technology **237**, 176 (2013).

[69] D. Ivchenko, T. Zhang, G. Mariaux, A. Vardelle, S. Goutier, and T. E. Itina, *On the validity of continuum computational fluid dynamics approach under very low-pressure plasma spray conditions,* Journal of Thermal Spray Technology **27**, 3 (2018).

[70] D. Ivchenko, G. Mariaux, A. Vardelle, S. Goutier, T. E. Itina, and P. André, *Feasibility study of an adaptive-pressure plasma coating process — part 1: Model description,* Journal of Thermal Spray Technology , 1 (2019).

[71] J. A. Moríñigo and J. H. Quesada, *Analysis of viscous heating in a micro-rocket flow and performance,* Journal of Thermal Science **17**, 116 (2008).

[72] N. S. Kumar and K. T. Ooi, *One dimensional model of an ejector with special attention to fanno flow within the mixing chamber,* Applied thermal engineering **65**, 226 (2014).

[73] J. D. Anderson, *Modern Compressible Flow with Historical Perspective* (McGraw-Hill, 2003).

[74] H. Jasak, A. Jemcov, Z. Tukovic, *et al.*, *Openfoam: A c++ library for complex physics simulations,* in *International workshop on coupled methods in numerical dynamics*, Vol. 1000 (IUC Dubrovnik Croatia, 2007) pp. 1–20.

[75] C. J. Smithells, *Metals reference book* (Elsevier, 2013).

[76] H. Hertz, *Über den Druck des gesättigten Quecksilberdampfes,* Annalen der Physik **253**, 193 (1882).

[77] M. Knudsen, *Experimentelle Bestimmung des Druckes gesättigter Quecksilberdämpfe bei 0 und höheren Temperaturen,* Annalen der Physik **334**, 179 (1909).

[78] J. Safarian and T. A. Engh, *Vacuum evaporation of pure metals,* Metallurgical and Materials Transactions A **44**, 747 (2013).

[79] D. Labuntsov and A. Kryukov, *Analysis of intensive evaporation and condensation,* International Journal of Heat and Mass Transfer **22**, 989 (1979).

[80] T. Ytrehus and S. Østmo, *Kinetic theory approach to interphase processes,* International journal of multiphase flow **22**, 133 (1996).

[81] H. S. Clair and M. Spendlove, *Rate of evaporation of zinc at low pressures,* JOM **3**, 1192 (1951).

[82] J. Song, X.-d. Ren, X.-s. Li, C.-w. Gu, and M.-m. Zhang, *One-dimensional model analysis and performance assessment of tesla turbine,* Applied Thermal Engineering **134**, 546 (2018).

[83] B. E. Launder and B. Sharma, *Application of the energy-dissipation model of turbulence to the calculation of flow near a spinning disc,* Letters in heat and mass transfer **1**, 131 (1974).

[84] S. El Tahry, *K-epsilon equation for compressible reciprocating engine flows,* Journal of Energy **7**, 345 (1983).

[85] Y. Bayazitoglu, F. Brotzen, and Y. Zhang, *Metal vapor condensation in a converging nozzle,* Nanostructured materials **7**, 789 (1996).

[86] J. Bian, X. Cao, W. Yang, D. Guo, and C. Xiang, *Prediction of supersonic condensation process of methane gas considering real gas effects,* Applied Thermal Engineering **164**, 114508 (2020).

[87] Y. Yang, J. H. Walther, Y. Yan, and C. Wen, *CFD modeling of condensation process of water vapor in supersonic flows,* Applied Thermal Engineering **115**, 1357 (2017).

[88] OpenCFD Ltd, *OpenFoam v1806,* https://develop.openfoam.com/Development/openfoam, commit: 71942d682 (2018).

[89] T. Uroić, H. Jasak, and H. Rusche, *Implicitly coupled pressure–velocity solver,* in *OpenFOAM®* (Springer, 2019) pp. 249–267.

[90] P. K. Sweby, *High resolution schemes using flux limiters for hyperbolic conservation laws,* SIAM journal on numerical analysis **21**, 995 (1984).

[91] T. Poinsot and S. Lelef, *Boundary conditions for direct simulations of compressible viscous flows,* Journal of computational physics **101**, 104 (1992).

[92] G. L. Martins, S. L. Braga, and S. B. Ferreira, *Design optimization of partial admission axial turbine for orc service,* Applied Thermal Engineering **96**, 18 (2016).

[93] J. E. Vesper, T. J. Broeders, J. Batenburg, D. E. van Odyck, and C. R. Kleijn, *The interaction of parallel and inclined planar rarefied sonic plumes—from free molecular to continuum regime,* Physics of Fluids **33**, 086103 (2021).

[94] G. Zukav, *The dancing wu li masters: An overview of the new physics,* (2012).

[95] B. Doncaster, J. Shulman, J. Bradford, and J. Olds, *Spaceworks' 2016 nano/microsatellite market forcast,* (2016).

[96] A. Z. Giovannini and R. S. Abhari, *Rarefied flow expansion in linear aerospikes,* Physics of Fluids **27**, 062003 (2015).

[97] E. Vesper, C. Obiji, R. Westerwaal, C. Bolesma, S. Kenjereš, and C. Kleijn, *Modeling of a continuous physical vapor deposition process, mass transfer limitations by evaporation rate and sonic choking,* Applied Thermal Engineering (in press).

[98] Z. Yang, Z.-Y. Tang, G.-B. Cai, and B.-J. He, *Development of a coupled NS-DSMC method for the simulation of plume impingement effects of space thrusters,* Thermophysics and Aeromechanics **24**, 835 (2017).

[99] K. H. Lee, *Plume simulation of liquid apogee engine for geo satellite using parallel DSMC method,* Computers & Fluids , 104612 (2020).

[100] A. Zilic, D. Hitt, and A. Alexeenko, *Numerical simulations of supersonic flow in a linear aerospike micro nozzle,* in *37th AIAA Fluid Dynamics Conference and Exhibit* (2007) p. 3984.

[101] K. H. Lee, *Numerical comparison of exhaust plume flow behaviors of small monopropellant and bipropellant thrusters,* PloS one **12**, e0176423 (2017).

[102] A. K. Chinnappan, R. Kumar, and V. K. Arghode, *Modeling of dusty gas flows due to plume impingement on a lunar surface,* Physics of Fluids **33**, 053307 (2021).

[103] V. Yarygin, Y. I. Gerasimov, A. Krylov, V. Prikhodko, A. Y. Skorovarov, and I. Yarygin, *Model and on-orbit study of the international space station contamination processes by jets of its orientation thrusters,* in *Journal of Physics: Conference Series*, Vol. 925 (IOP Publishing, 2017) p. 012003.

[104] V. Yarygin, V. Prikhodko, and I. Yarygin, *Modeling of space vehicle orientation thruster jets in vacuum chambers,* Journal of Applied Mechanics and Technical Physics **61**, 798 (2020).

[105] R. Jambunathan and D. A. Levin, *On the study of ion thruster plume characteristics and backflow contamination using fully-kinetic PIC-DSMC simulations.* in *AIAA Propulsion and Energy Forum and Exposition, 2019* (American Institute of Aeronautics and Astronautics Inc, AIAA, 2019).

[106] M. Grabe and C. E. Soares, *Status and future of research on plume induced contamination,* in *Proceedings of the International Astronautical Congress, IAC* (IAF, 2019).

[107] C. Cai and X. He, *Detailed flowfield and surface properties for high Knudsen number planar jet impingement at an inclined flat plate,* Physics of Fluids **28**, 056103 (2016).

[108] S. Cai, C. Cai, and J. Li, *Jet loads on a plate with different Knudsen numbers,* Physics of Fluids **30**, 127101 (2018).

[109] P. J. Herráiz, J. M. Fernández, and J. R. Villa, *Development of a matlab® plume impingement tool for fast system analysis.* (2019).

[110] B. Zitouni, F. Weber, and R. Kast, *CFD and DSMC methods for tracking gases and droplets behaviors within the plume,* in *Systems Contamination: Prediction, Control, and Performance 2020*, Vol. 11489 (International Society for Optics and Photonics, 2020) p. 114890C.

[111] J. Berg, D. Goldstein, P. Varghese, and L. Trafton, *DSMC simulation of Europa water vapor plumes,* Icarus **277**, 370 (2016).

[112] W. J. McDoniel, D. B. Goldstein, P. L. Varghese, and L. M. Trafton, *Simulation of Io's plumes and Jupiter's plasma torus,* Physics of Fluids **31**, 077103 (2019).

[113] W. A. Hoey, L. M. Trafton, P. C. Ackley, D. B. Goldstein, and P. L. Varghese, *Variations in the canopy shock structures of massive extraterrestrial plumes: Parametric DSMC simulation of 2007 Tvashtar observations,* Icarus **363**, 114431 (2021).

[114] T. Soga, M. Takanishi, and M. Yasuhara, *Experimental study of underexpanded free jets,* in *14th International Symposium on Rarefied Gas Dynamics, Tsukuba Science City, Japan* (1984).

[115] I. A. Chirokov, T. G. Elizarova, J.-C. Lengrand, I. Gibek, and I. A. Graur, *Experimental and numerical investigation of rarefied interacting plumes,* in *AIP Conference Proceedings*, Vol. 663 (AIP, 2003) pp. 572–579.

[116] G. Koppenwallner, *Scaling laws for rarefied plume interference with application to satellite thrusters,* in *International Symposium on Space Technology and Science, 14 th, Tokyo, Japan* (1984) pp. 505–512.

[117] L. Dagum and S. K. Zhu, *Direct Simulation Monte Carlo simulation of the interaction between rarefied free jets,* Journal of Spacecraft and Rockets **31**, 960 (1994).

[118] A. Holz, G. Dettleff, K. Hannemann, and S. Ziegenhagen, *Experimental investigation of two interacting thruster-plumes downstream of the nozzles,* Space Propulsion (2012).

[119] W. Li and F. Ladeinde, *Simulation and analysis of rarefied parallel interacting sonic jets,* in *44th AIAA Aerospace Sciences Meeting and Exhibit* (2006) p. 1192.

[120] S. Zhu and L. Dagum, *Self-similarity in rarefied jet interactions — a DSMC study,* in *30th Thermophysics Conference* (1995) p. 2030.

[121] A. Venkattraman and A. A. Alexeenko, *Direct Simulation Monte Carlo modeling of metal vapor flows in application to thin film deposition,* **2**, 654.

[122] A. V. Y. Baby *et al.*, *Experimental study on the interaction of under-expanded jets in rarefied flow regimes,* in *30th International Symposium on Shock Waves 2* (Springer, 2017) pp. 859–867.

[123] J. Allègre, A. Chaiz, I. Chirokov, N. Gorchakova, I. Graur, C. Purpura, I. Gibek, T. Elizarova, and J.-C. Lengrand, *Numerical and experimental investigation of plumes interacting with satellite walls,* in *Spacecraft Propulsion*, Vol. 465 (2000) p. 619.

[124] W. Li and F. Ladeinde, *Analysis of interacting, underexpanded, rarefied jets,* AIAA journal **49**, 2581 (2011).

[125] M. Grabe, G. Dettleff, and K. Hannemann, *Impact of nozzle separation on the plumes of two parallel thrusters,* in *AIP Conference Proceedings*, Vol. 1786 (AIP Publishing, 2016) p. 170005.

[126] C. Cai and I. D. Boyd, *Theoretical and numerical study of free-molecular flow problems,* Journal of Spacecraft and Rockets **44**, 619 (2007).

[127] R. Vos and S. Farokhi, *Introduction to transonic aerodynamics*, Vol. 110 (Springer, 2015).

[128] v. L. Crocco, *Eine neue Stromfunktion für die Erforschung der Bewegung der Gase mit Rotation.* ZAMM-Journal of Applied Mathematics and Mechanics/Zeitschrift für Angewandte Mathematik und Mechanik **17**, 1 (1937).

[129] M. J. Zucrow and J. D. Hoffman, *Gas dynamics. volume 2-multidimensional flow,* nyjw (1977).

[130] M. Silnikov, M. Chernyshov, and V. Uskov, *Analytical solutions for Prandtl–Meyer wave–oblique shock overtaking interaction,* Acta Astronautica **99**, 175 (2014).

[131] H. Alsmeyer, *Density profiles in argon and nitrogen shock waves measured by the absorption of an electron beam,* Journal of Fluid Mechanics **74**, 497 (1976).

[132] M. Kanamori and K. Suzuki, *Shock wave detection in two-dimensional flow based on the theory of characteristics from CFD data,* Journal of Computational Physics **230**, 3085 (2011).

[133] M. Kanamori and K. Suzuki, *Shock wave detection based on the theory of characteristics,* in *Shock Fitting: Classical Techniques, Recent Developments, and Memoirs of Gino Moretti*, edited by M. Onofri and R. Paciorri (Springer International Publishing, Cham, 2017) pp. 171–190.

[134] *foam-extend-4.0,* https://sourceforge.net/p/foam-extend/foam-extend-4.0/ci/master/tree/ReleaseNotes.txt (2016).

[135] E. F. Toro, M. Spruce, and W. Speares, *Restoration of the contact surface in the HLL-Riemann solver,* Shock waves **4**, 25 (1994).

[136] S. Dellacherie, *Analysis of Godunov type schemes applied to the compressible Euler system at low Mach number,* Journal of Computational Physics **229**, 978 (2010).

[137] E. F. Toro, *Riemann problems and the WAF method for solving the two-dimensional shallow water equations,* Philosophical Transactions of the Royal Society of London. Series A: Physical and Engineering Sciences **338**, 43 (1992).

[138] K. Xu and J.-C. Huang, *A unified gas-kinetic scheme for continuum and rarefied flows,* Journal of Computational Physics **229**, 7747 (2010).

[139] K. Xu, *Direct modeling for computational fluid dynamics: construction and application of unified gas-kinetic schemes*, Vol. 4 (World Scientific, 2014).

[140] Z. Guo, R. Wang, and K. Xu, *Discrete unified gas kinetic scheme for all Knudsen number flows. II. Thermal compressible case,* Physical Review E **91**, 033313 (2015).

[141] Y. Zhang, L. Zhu, R. Wang, and Z. Guo, *Discrete unified gas kinetic scheme for all Knudsen number flows. III. Binary gas mixtures of maxwell molecules,* Physical Review E **97**, 053306 (2018).

[142] X. Zhao, C. Wu, Z. Chen, L. Yang, and C. Shu, *Reduced order modeling-based discrete unified gas kinetic scheme for rarefied gas flows,* Physics of Fluids **32**, 067108 (2020).

[143] S. Chen, K. Xu, and Q. Cai, *A comparison and unification of ellipsoidal statistical and shakhov bgk models,* Advances in Applied Mathematics and Mechanics **7**, 245 (2015).

[144] B. N. Todorova, C. White, and R. Steijl, *Numerical evaluation of novel kinetic models for binary gas mixture flows,* Physics of Fluids **32**, 016102 (2020).

[145] L. Zhu, X. Pi, W. Su, Z.-H. Li, Y. Zhang, and L. Wu, *General synthetic iterative scheme for nonlinear gas kinetic simulation of multi-scale rarefied gas flows,* Journal of Computational Physics **430**, 110091 (2021).

[146] S. Plimpton, S. Moore, A. Borner, A. Stagg, T. Koehler, J. Torczynski, and M. Gallis, *Direct Simulation Monte Carlo on petaflop supercomputers and beyond,* Physics of Fluids **31**, 086101 (2019).

[147] C. White, M. K. Borg, T. J. Scanlon, S. M. Longshaw, B. John, D. Emerson, and J. M. Reese, *dsmcFoam+: An OpenFOAM based direct simulation Monte Carlo solver,* Computer Physics Communications **224**, 22 (2018).

[148] F. P. Boynton, *Highly underexpanded jet structure-exact and approximate calculations.* AIAA Journal **5**, 1703 (1967).

[149] P. Fialho, J. Fareleira, M. Ramires, and C. A. Nieto de Castro, *Thermophysical properties of alkali metal vapours part ia—prediction and correlation of transport properties for monatomic systems,* Berichte der Bunsengesellschaft für physikalische Chemie **97**, 1487 (1993).

[150] H. Struchtrup, *Macroscopic transport equations for rarefied gas flows,* in *Macroscopic transport equations for rarefied gas flows* (Springer, 2005) pp. 145–160.

[151] W. Stein and A. Alexeenko, *Application of the DSMC method for design of a coaxial microthruster nozzle,* in *44th AIAA/ASME/SAE/ASEE Joint Propulsion Conference & Exhibit* (2008) p. 4530.

[152] H. Liu, Y. Zhu, Q. Meng, X. Lu, S. Kong, Z. Huang, P. Jiang, and X. Bao, *Role of the carrier gas flow rate in monolayer MoS2 growth by modified chemical vapor deposition,* Nano Research **10**, 643 (2017).

[153] A. Drize and A. Settaouti, *Physical investigation of copper thin film prepared by sputtering,* Indian Journal of Pure & Applied Physics **56**, 434 (2018).

[154] A. Torgovkin, S. Chaudhuri, A. Ruhtinas, M. Lahtinen, T. Sajavaara, and I. Maasilta, *High quality superconducting titanium nitride thin film growth using infrared pulsed laser deposition,* Superconductor Science and Technology **31**, 055017 (2018).

[155] M. C. Schwille, T. Schössler, J. Barth, M. Knaut, F. Schön, A. Höchst, M. Oettel, and J. W. Bartha, *Experimental and simulation approach for process optimization of atomic layer deposited thin films in high aspect ratio 3D structures,* Journal of Vacuum Science & Technology A: Vacuum, Surfaces, and Films **35**, 01B118 (2017).

[156] S. Thiruppathiraj, S.-M. Ryu, J. Uh, and L. L. Raja, *Direct-simulation Monte Carlo modeling of reactor-scale gas-dynamic phenomena in a multiwafer atomic-layer deposition batch reactor,* Journal of Vacuum Science & Technology A: Vacuum, Surfaces, and Films **39**, 052404 (2021).

[157] J. F. Groves, S. Jones, T. Globus, L. Hsiung, and H. Wadley, *Directed vapor deposition of amorphous and polycrystalline electronic materials: Nonhydrogenated a-si,* Journal of the Electrochemical Society **142**, L173 (1995).

[158] D. D. Hass and B. Gogia, *Method and apparatus for applying a coating at a high rate onto non-line-of-sight regions of a substrate,* (2013), US Patent App. 13/178,135.

[159] A. Moarrefzadeh and M. Branch, *Simulation and modeling of physical vapor deposition (PVD) process,* WSEAS Trans. Appl. Theor. Mech **7**, 106 (2012).

[160] T. M. Rodgers, H. Zhao, and H. N. Wadley, *Microstructure of vapor deposited coatings on curved substrates,* Journal of Vacuum Science & Technology A: Vacuum, Surfaces, and Films **33**, 05E118 (2015).

[161] T. M. Rodgers, H. Zhao, and H. N. Wadley, *Vapor deposition on doublet airfoil substrates: Coating thickness control,* Journal of Vacuum Science & Technology A: Vacuum, Surfaces, and Films **33**, 061509 (2015).

[162] N. Bykov and V. Zakharov, *Binary gas mixture outflow into vacuum through an orifice,* Physics of Fluids **32**, 067109 (2020).

[163] N. Wei, Y. Feng, W. Sun, Y. Cheng, M. Dong, Y. Song, C. Wu, G. Liu, and Y. Qiu, *Experimental study on the conductance of pure and binary gas mixtures,* Vacuum **189**, 110277 (2021).

[164] A. Venkattraman and A. A. Alexeenko, *Direct simulation Monte Carlo modeling of e-beam metal deposition,* Journal of Vacuum Science & Technology A: Vacuum, Surfaces, and Films **28**, 916 (2010).

[165] T. Dutta, K. Sinhamahapatra, and S. Bandyopadhyay, *Numerical investigation of gas species and energy separation in the ranque–hilsch vortex tube using real gas model,* International Journal of Refrigeration **34**, 2118 (2011).

[166] S. Mohammadi and F. Farhadi, *Experimental and numerical study of the gas–gas separation efficiency in a ranque–hilsch vortex tube,* Separation and Purification Technology **138**, 177 (2014).

[167] J. Yun, Y. Kim, and S. Yu, *Feasibility study of carbon dioxide separation from gas mixture by vortex tube,* International Journal of Heat and Mass Transfer **126**, 353 (2018).

[168] S. Kuwatani, S. Watanabe, and N. Ono, *Study and development of a mini-tube gas separator utilizing the soret effect,* Journal of Thermal Science and Technology **7**, 31 (2012).

[169] T. Saiki, N. Ono, S. Matsumoto, and S. Watanabe, *Separation of a binary gas mixture by thermal diffusion in a two-dimensional cascade of many small cavities,* International Journal of Heat and Mass Transfer **163**, 120394 (2020).

[170] M. Sabouri and M. Darbandi, *Numerical study of species separation in rarefied gas mixture flow through micronozzles using DSMC,* Physics of Fluids **31**, 042004 (2019).

[171] T. Wu and A. Firoozabadi, *Molecular simulations of binary gas mixture transport and separation in slit nanopores,* The Journal of Physical Chemistry C **122**, 20727 (2018).

[172] A. D. Strongrich, A. J. Pikus, I. B. Sebastiao, D. Peroulis, and A. A. Alexeenko, *Low-pressure gas sensor exploiting the Knudsen thermal force: DSMC modeling and experimental validation,* in *2016 IEEE 29th International Conference on Micro Electro Mechanical Systems (MEMS)* (IEEE, 2016) pp. 828–831.

[173] R. Gatignol and C. Croizet, *Asymptotic modeling of thermal binary monatomic gas flows in plane microchannels — comparison with DSMC simulations,* Physics of Fluids **29**, 042001 (2017).

[174] A. Lotfian and E. Roohi, *Binary gas mixtures separation using microscale radiometric pumps,* International Communications in Heat and Mass Transfer **121**, 105061 (2021).

[175] H. Sugimoto, S. Takata, and S. Kosuge, *Gas separation effect of the pump driven by the thermal edge flow,* Rarefied gas dynamics , 1158 (2007).

[176] S. Takata, H. Sugimoto, and S. Kosuge, *Gas separation by means of the knudsen compressor,* European Journal of Mechanics-B/Fluids **26**, 155 (2007).

[177] S. Nakaye and H. Sugimoto, *Demonstration of a gas separator composed of knudsen pumps,* Vacuum **125**, 154 (2016).

[178] H. Trinks, *Gas species separation effects in exhaust plumes,* in *5th Joint Thermophysics and Heat Transfer Conference* (1990) p. 1734.

[179] K. H. Lee, *Multi-plume flow simulation of small bipropellant thrusters using parallel DSMC method,* Computers & Fluids **173**, 259 (2018).

[180] F. S. Sherman, *Hydrodynamical theory of diffusive separation of mixtures in a free jet,* The Physics of Fluids **8**, 773 (1965).

[181] D. E. Rothe, *Electron beam studies of the diffusive separation of helium-argon mixtures,* The Physics of Fluids **9**, 1643 (1966).

[182] A. Ramos, G. Tejeda, J. Fernández, and S. Montero, *Nonequilibrium processes in supersonic jets of N2, H2, and N2+ H2 mixtures:(i) zone of silence,* The Journal of Physical Chemistry A **113**, 8506 (2009).

[183] V. V. Riabov, *Kinetic phenomena in spherical expanding flows of binary gas mixtures,* Journal of thermophysics and heat transfer **17**, 526 (2003).

[184] V. Kosyanchuk and A. Yakunchikov, *Separation of a binary gas mixture outflowing into vacuum through a micronozzle,* Physics of Fluids **33**, 082007 (2021).

[185] J. Wu, G. Cai, B. He, and H. Zhou, *Experimental and numerical investigations of vacuum plume interaction for dual hydrogen/oxygen thrusters,* Vacuum **128**, 166 (2016).

[186] D. E. Rothe, *Electron beam studies of the diffusive separation of helium-argon mixtures in free jets and shock waves*, Tech. Rep. (Toronto University (Ontario) Institute for Aerospace Studies, 1966).

[187] A. Ramos, G. Tejeda, J. Fernández, and S. Montero, *Nonequilibrium processes in supersonic jets of N2, H2, and N2+ H2 mixtures:(ii) shock waves,* The Journal of Physical Chemistry A **114**, 7761 (2010).

[188] K. Koura and H. Matsumoto, *Variable soft sphere molecular model for air species,* Physics of Fluids A: Fluid Dynamics **4**, 1083 (1992).

[189] D. Valougeorgis, M. Vargas, and S. Naris, *Analysis of gas separation, conductance and equivalent single gas approach for binary gas mixture flow expansion through tubes of various lengths into vacuum,* Vacuum **128**, 1 (2016).

[190] I. W. Kokkinakis, D. Drikakis, K. Ritos, and S. M. Spottswood, *Direct numerical simulation of supersonic flow and acoustics over a compression ramp,* Physics of Fluids **32**, 066107 (2020).

[191] O. Tumuklu and D. A. Levin, *On the temporal evolution in laminar separated boundary layer shock-interaction flows using dsmc,* in *55th AIAA Aerospace Sciences Meeting* (2017) p. 1614.

[192] L. Boltzmann, *Über die mechanische Bedeutung des zweiten Hauptsatzes der Wärmetheorie:(vorgelegt in der Sitzung am 8. Februar 1866)* (Staatsdruckerei, 1866).

[193] N. Fougere, K. Altwegg, J.-J. Berthelier, A. Bieler, D. Bockelée-Morvan, U. Calmonte, F. Capaccioni, M. R. Combi, J. De Keyser, V. Debout, *et al.*, *Direct simulation Monte Carlo modelling of the major species in the coma of comet 67P/Churyumov-Gerasimenko,* Monthly Notices of the Royal Astronomical Society **462**, S156 (2016).

[194] M. Combi, Y. Shou, N. Fougere, V. Tenishev, K. Altwegg, M. Rubin, D. Bockelée-Morvan, F. Capaccioni, Y.-C. Cheng, U. Fink, *et al.*, *The surface distributions of the production of the major volatile species, H2O, CO2, CO and O2, from the nucleus of comet 67P/Churyumov-Gerasimenko throughout the Rosetta mission as measured by the ROSINA double focusing mass spectrometer,* Icarus **335**, 113421 (2020).

[195] M. A. Silva, D. C. Guerrieri, A. Cervone, and E. Gill, *A review of MEMS micropropulsion technologies for cubesats and pocketqubes,* Acta Astronautica **143**, 234 (2018).

[196] A. Baptista, F. Silva, J. Porteiro, J. Míguez, and G. Pinto, *Sputtering physical vapour deposition (PVD) coatings: A critical review on process improvement and market trend demands,* Coatings **8**, 402 (2018).

[197] K. M. Rafi, M. Deepu, and G. Rajesh, *Effect of heat transfer and geometry on micro-thruster performance,* International Journal of Thermal Sciences **146**, 106063 (2019).

[198] P. G. Spazzini and L. Fallerini, *Performance analysis of a microthruster for satellite applications,* Measurement **131**, 782 (2019).

[199] P. L. Bhatnagar, E. P. Gross, and M. Krook, *A model for collision processes in gases. i. small amplitude processes in charged and neutral one-component systems,* Physical review **94**, 511 (1954).

[200] L. H. Holway Jr, *New statistical models for kinetic theory: methods of construction,* The physics of fluids **9**, 1658 (1966).

[201] E. Shakhov, *Generalization of the Krook kinetic relaxation equation,* Fluid Dynamics **3**, 95 (1968).

[202] I. A. Graur and A. P. Polikarpov, *Comparison of different kinetic models for the heat transfer problem,* Heat and Mass Transfer **46**, 237 (2009).

[203] A. Shershnev and A. Kudryavtsev, *Kinetic simulation of near field of plume exhausting from a plane micronozzle,* Microfluidics and Nanofluidics **19**, 105 (2015).

[204] M. Pfeiffer, *A particle-based ellipsoidal statistical Bhatnagar–Gross–Krook solver with variable weights for the simulation of large density gradients in micro-and nano-nozzles,* Physics of Fluids **32**, 112009 (2020).

[205] F. Fei, H. Liu, Z. Liu, and J. Zhang, *A benchmark study of kinetic models for shock waves,* AIAA Journal **58**, 2596 (2020).

[206] T. Krüger, H. Kusumaatmaja, A. Kuzmin, O. Shardt, G. Silva, and E. M. Viggen, *The lattice Boltzmann method,* Springer International Publishing **10**, 4 (2017).

[207] M. Gallis and J. Torczynski, *The application of the BGK model in particle simulations,* in *34th Thermophysics Conference* (2000) p. 2360.

[208] M. Macrossan, *A particle simulation method for the BGK equation,* in *AIP Conference Proceedings*, Vol. 585 (American Institute of Physics, 2001) pp. 426–433.

[209] G. Bird, *Breakdown of translational and rotational equilibrium in gaseous expansions,* Aiaa Journal **8**, 1998 (1970).

[210] I. D. Boyd, *Predicting breakdown of the continuum equations under rarefied flow conditions,* in *AIP Conference Proceedings*, Vol. 663 (American Institute of Physics, 2003) pp. 899–906.

[211] A. L. Garcia and B. J. Alder, *Generation of the Chapman–Enskog distribution,* Journal of Computational Physics **140**, 66 (1998).

[212] R. Kumar, E. Titov, and D. Levin, *Development of a particle–particle hybrid scheme to simulate multiscale transitional flows,* AIAA journal **51**, 200 (2013).

[213] A. Alamatsaz and A. Venkattraman, *Characterizing deviation from equilibrium in direct simulation Monte Carlo simulations,* Physics of Fluids **31**, 042005 (2019).

[214] O. Ilyin, *Relative entropy based breakdown criteria for hybrid discrete velocity Bhatnagar–Gross–Krook and lattice Boltzmann method,* Physics of Fluids **32**, 112006 (2020).

[215] I. D. Boyd, G. Chen, and G. V. Candler, *Predicting failure of the continuum fluid equations in transitional hypersonic flows,* Physics of Fluids **7**, 210 (1995).

[216] R. Kumar, S. Saurav, E. Titov, D. Levin, R. Long, W. Neely, and P. Setlow, *Thermo-structural studies of spores subjected to high temperature gas environments,* International Journal of Heat and Mass Transfer **54**, 755 (2011).

[217] M. Pfeiffer, *Particle-based fluid dynamics: Comparison of different Bhatnagar-Gross-Krook models and the direct simulation monte carlo method for hypersonic flows,* Physics of Fluids **30**, 106106 (2018).

[218] J. C. Maxwell, *Vii. on stresses in rarified gases arising from inequalities of temperature,* Philosophical Transactions of the royal society of London , 231 (1879).

[219] H. Rezaei, M. Rahimi, S. Ovaysi, and A. Abdulaziz Alsairafi, *Computational fluid dynamics modeling of heat transfer and condensation in a modified laval nozzle,* Journal of Thermophysics and Heat Transfer , 1 (2022).

[220] S. A. Davari and D. Mukherjee, *Kinetic Monte Carlo simulation for homogeneous nucleation of metal nanoparticles during vapor phase synthesis,* AIChE Journal **64**, 18 (2018).

[221] L. Azzini, M. Pini, and P. Colonna, *Semi-analytical model for the prediction of the wilson point for homogeneously condensing steam flows,* International Journal of Heat and Fluid Flow **70**, 1 (2018).

[222] J. Wedekind, A.-P. Hyvärinen, D. Brus, and D. Reguera, *Unraveling the "pressure effect" in nucleation,* Physical Review Letters **101**, 125703 (2008).

[223] F. Römer and T. Kraska, *Homogeneous nucleation and growth in supersaturated zinc vapor investigated by molecular dynamics simulation,* The Journal of chemical physics **127**, 234509 (2007).

[224] F. Russo and N. T. Basse, *Scaling of turbulence intensity for low-speed flow in smooth pipes,* Flow Measurement and Instrumentation **52**, 101 (2016).

[225] ANSYS Inc., *ANSYS Fluent User's Guide,* ANSYS Inc., release 19.0 ed. (2018).

[226] N. Georgiadis, J. Drummond, and B. Leonard, *Evaluation of turbulence models in the PARC code for transonic diffuser flows,* in *32nd Aerospace Sciences Meeting and Exhibit* (1994) p. 582.

[227] T. Bogar, M. Sajben, and J. Kroutil, *Characteristic frequencies of transonic diffuser flow oscillations,* AIAA journal **21**, 1232 (1983).

[228] J. W. Slater, C. Towne, D. Yoder, S. Mohler, and J. Dudek, *Sajben Transonic Diffuser,* https://www.grc.nasa.gov/www/wind/valid/transdif/transdif.html (198x–2017), [Online; accessed 04-February-2021].

[229] B. Wüthrich, *Simulation and validation of compressible flow in nozzle geometries and validation of OpenFOAM for this application,* Master's thesis, ETH, Swiss Federal Institute of Technology Zurich, Institute of Fluid Dynamics (2007).

[230] J. Dudek and J.-R. Carlson, *Evaluation of full Reynolds stress turbulence models in fun3d,* in *55th AIAA Aerospace Sciences Meeting* (2017) p. 0541.

[231] J. W. Slater, J. C. Dudek, and K. E. Tatum, *The NPARC alliance verification and validation archive,* Proceedings of ASME FEDSM00 (2000).

[232] C. Cai and L. Wang, *Numerical validations for a set of collisionless rocket plume solutions,* Journal of Spacecraft and Rockets **49**, 59 (2012).

[233] A. R. Khodadadi, M. R. Malekbala, and A. F. Khodadadi, *Evaluate shock capturing capability with the numerical methods in OpenFOAM,* Thermal Science **17**, 1255 (2013).

[234] M. H. Arabnejad, R. Bensow, and C. Eskilsson, *Density-based compressible solver with equilibrium cavitation model in OpenFoam,* in *19th Numerical Towing Tank Symposium-NuTTS, At St Pierre d'Oleron, France* (2016).

[235] C. Cercignani, *Rarefied gas dynamics: from basic concepts to actual calculations*, Vol. 21 (Cambridge University Press, 2000).

CURRICULUM VITÆ

Judith Elin VESPER

30-01-1990 Born in Kassel, Germany.

EDUCATION

2008	Abitur Internatsschule Schloss Hansenberg (2005–2008), Geisenheim, Germany
2008–2012	Bachelor in Mechanical and Process Engineering Technische Universität Darmstadt, Germany
2012–2013	Exchange studies in the program of Thermal Science and Engineering, IIT Kharagpur, India
2013–2016	Master in Mechanics, Technische Universität Darmstadt, Germany
2017–2022	Ph.D. candidate, Faculty of Applied Sciences, Chemical Engineering, TU Delft, The Netherlands
Thesis:	Modeling of Continuous Physical Vapor Deposition: From Continuum to Free Molecular Flow
Promotors:	Prof. dr. ir. C. R. Kleijn Prof. dr. S. Kenjereš, Dipl.-Ing.
2021–	CFD Expert, Bayer AG, Leverkusen, Germany

LIST OF PUBLICATIONS

4. **Vesper, J. E.**, Obiji, C. S., Westerwaal, R., Boelsma, C., Kenjereš, S., & Kleijn, C. R. (2021). *Modeling of a Continuous Physical Vapor Deposition Process: Mass Transfer Limitations by Evaporation Rate and Sonic Choking.* Applied Thermal Engineering, 117099.

3. **Vesper, J. E.**, Broeders, T. J., Batenburg, J., van Odyck, D. E., & Kleijn, C. R. (2021). *The interaction of parallel and inclined planar rarefied sonic plumes — From free molecular to continuum regime.* Physics of Fluids, 33(8), 086103.

2. **Vesper, J. E.**, Tietjen, S. C., Chakkingal, M., & Kenjereš, S. (2022). *Numerical analysis of effects of fins and conductive walls on heat transfer in side heated cavities—Onset of three-Dimensional phenomena in natural convection.* International Journal of Heat and Mass Transfer, 122033.

1. **Vesper, J. E.**, Kenjereš, S., & Kleijn, C. R. (2022). *Diffusive Separation in Rarefied Plume Interaction.* Accepted for publication in Journal of Vacuum Science & Technology B.